IMPROVEMENT AND EVALUATION OF THE MESOSCALE METEOROLOGICAL MODEL MM5 FOR AIR-QUALITY APPLICATIONS IN SOUTHERN CALIFORNIA AND THE SAN JOAQUIN VALLEY

Final Report

by

Robert D. Bornstein, Co. P. I.
Dimitra Boucouvala
James Wilkinson
Anil Yadav
Department of Meteorology
San Jose State University
San Jose, CA 95192-0104

Nelson L. Seaman, Co. P. I.
David R. Stauffer
Glenn K. Hunter
Department of Meteorology
Pennsylvania State University
University Park, PA 16802
(SJSU Foundation Subcontract No. 22-1505-7384)

Douglas Miller
Department of Meteorology
Naval Postgraduate School
University Park, PA 16802
(SJSU Foundation Subcontract No. 22-1505-7384)

Prepared for the

California Air Resources Board
and
California Environmental Protection Agency

2020 L Street
P.O. Box 2815
Sacramento CA 95812

under
Contract No. 97-310

30 January 2001

Disclaimer

The statements and conclusions in the Report are those of the contractors and not necessarily those of the California Air Resources Board. The mention of commercial products, their source, or their use in connection with material reported herein is not to be constructed as actual or implied endorsement of such products.

Acknowledgements

Kathy Pagan of NASA supplied AVHRR satellite visual and infrared imagery that was specially enhanced to emphasize SJV low cloud and fog. At SJSU, Ruri Imamura helped with the SoCAB data analysis, David McCooey helped with the reformatting the SoCAB data, and Jennie Wu wrote software to produce time height data sections. We also wish to acknowledge the helpful guidance of Mr. James Pederson of the California Air Resources Board, who consistently sought to define and clarify the goals of the project, and who made available much of the special data needed to carry out this study. His continual willingness to offer help contributed much to the success of the project.

This report was submitted in fulfillment of the California Air Resources Board Contract No. 97-310, titled "Improvement and Evaluation of the Mesoscale Meteorological Model MM5 for Air-Quality Applications in Southern California and the San Joaquin Valley," by San Jose State University, Penn State University, and the Naval Postgraduate School under the sponsorship of the California Air Resources Board. Work was completed as of 31 January 2001. Funding to Penn State University and the Naval Postgraduate School for this project was provided by the California Air Resources Board through San Jose State University Foundation Subcontract No. 22-1505-7384.

Table of Contents

Page

Disclaimer ……. ii

Acknowledgements ……. iii

List of Figures ……. vii

List of Tables ……. xvi

Abstract ……. xviii

Executive Summary ……. xix

1. Introduction ……. 1

1.1 Background……... 1

1.2 Wintertime Climatology and Formation of Particulate Matter in SJV……. 2

1.3 Summertime Climatology and Formation of Sea Breeze Flows in SoCAB 4

1.4 Statement of Problem ……..……. 8

1.5 Report Organization ……. 8

2. Meteorological Modeling System ……. 9

2.1 PSU/NCAR MM5 Model ……. 9

2.2 FDDA System……. 10

2.3 Initialization and Lateral Boundary Conditions ……. 11

2.4 Extension of 1.5-order Turbulence Scheme for Moist Processes 12

3. Experimental Design of SJV Fog Experiments …… 14

4. Description of Observed Meteorology During SJV Fog Episode ……. 15

5. Results of SJV Numerical Fog Experiments…….. 18

5.1 Experiment GS-1 Results ……. 18

5.2 Experiment BLK-1 Results ……. 21

5.3 Experiment GS-2 Results …… 21

5.4 Experiment GS-3 Results …… 25

5.5 Statistical Evaluation of Fog Event …… 30

6. Experimental Design of SoCAB Sea Breeze Simulations ……. 32

6.1 SCOS97 Data …… 32

6.2 MM5 Modifications for SoCAB Simulations …….. 33

6.3 MAPS Statistical Analyses 35

7. Description of Observed Meteorology During SoCAB Sea Breeze Episode …… 38

7.1 Summary/Preview …… 38

7.2 Synoptic Scale Data……. 47

7.3 SoCAB Temperature Data……. 48

7.4 SoCAB Wind Data……. 54

7.5 SoCAB Ozone Data…….. 63

8. Results of SoCAB Numerical Sea Breeze Experiments ……. 64

8.1 Run 1 Results …… 64

8.2 Run 2 Results …… 65

8.3 Run 3 Results …… 66

8.4 Run 4 Results …… 67

8.5 Run 5 Results …… 67

8.6 Run 6 Results …… 69

9. Summary ……. 70

9.1 Conclusions of SJV Fog Study……. 70

9.2 Recommendations for Future SJV Fog Research ……. 71

9.3 Conclusions of SoCAB Sea Breeze Study……. 72

9.4 Recommendations for Future SoCAB Sea Breeze Research…… 73

REFERENCES ……. 75

Appendix A: List of Acronyms ……81

Appendix B: Modeling of the SCOS-97 Case of 26-30 September 1997……..82

List of Figures

Figure 1a. Location of special meteorological sites operated during the IMS-95 field campaign by STI.

Figure 1b. Topographic height values in SoCAB, with contour interval of 500 m.

Figure 2. Location of MM5 nested domains for the 7-12 December 1995 Case, where D01 is the 108-km domain, D02 the 36-km domain, D03 the 12-km Domain, and D04 the 4-km domain.

Figure 3. Terrain (m) on the 4-km domain for the 7-12 December 1995 episode, with contour interval of 100 m.

Figure 4. NCEP surface analysis of sea-level pressure (mb) for 1200 UTC, 7 December 1995, with isobar interval of 4 mb.

Figure 5. AVHRR infrared satellite image at 1027 UTC, 7 December 1995, where imagery has been processed so that low clouds and fog appear bright, while high clouds shown as darker gray shades.

Figure 6. NCEP surface analysis of sea-level pressure (mb) for 0000 UTC, 8 December 1995, with isobar interval of 4 mb.

Figure 7. Manual mesoscale surface analysis of sea-level pressure (- 1000 mb) for 1200 UTC, 8 December 1995. Isobar interval of 2 mb, with short dashed lines intermediate isobars at 1 mb interval. Medium gray shading indicates areas reporting fog.

Figure 8. AVHRR infrared satellite image at 1016 UTC, 8 December 1995. The imagery has been processed so that low clouds and fog appear to be bright, while high clouds are shown as darker gray shades.

Figure 9. Special radiosonde sounding plotted at Bakersfield, CA, for 1200 UTC (0400 PST), 9 December 1995 (created by Sonoma Technology, Inc.)

Figure 10. Manual mesoscale surface analysis of sea-level pressure (mb - 1000) for 1200 UTC, 9 December 1995. Isobar interval is 2 mb. Medium gray shading indicates areas reporting fog.

Figure 11. AVHRR visual satellite image at 1503 UTC, 9 December 1995. The imagery has been processed so that low clouds and fog appear to be bright, while high clouds are shown as darker gray shades.

Figure 12. Special radiosonde sounding plotted at Bakersfield, CA, for 0000 UTC, 10 December 1995 (1600 PST, 9 December)(created by Sonoma Technology, Inc.).

Figure 13. Special radiosonde sounding plotted at Bakersfield, CA, for 1200 UTC (0400 PST), 10 December 1995 (created by Sonoma Technology, Inc.).

Figure 14. Special radiosonde sounding plotted at Bakersfield, CA, for 0000 UTC, 11 December 1995 (1600 PST, 10 December)(created by Sonoma Technology, Inc.).

Figure 15. Manual mesoscale surface analysis of sea-level pressure (- 1000 mb) for 0000 UTC, 11 December 1995. Isobar interval is 2 mb. Medium gray shading indicates areas reporting fog. Light gray shading indicates areas reporting haze

Figure 16. AVHRR visual satellite image at 2119 UTC, 10 December 1995.

Figure 17. MM5 simulated winds (m s^{-1}) in the surface layer (6 m AGL) on the 4-km domain, valid for 0000 UTC, 8 December 1995, (+24 h) in Exp. GS-1. Isotach interval is 10 m s^{-1}.

Figure 18. MM5 simulated temperatures(C) in the surface layer (6 m AGL) on the 4-km domain, valid for 0000 UTC, 8 December 1995, (+24 h) in Exp. GS-1. Isotherm interval is 2 C.

Figure 19. MM5 simulated relative humidity (%) in the surface layer (6 m AGL) on the 4-km domain, valid for 0000 UTC, 8 December 1995, (+24 h) in Exp. GS-1. Contour interval is 10 %.

Figure 20. MM5 simulated temperatures(C) at 500 m AGL on the 4-km domain, valid for 0000 UTC, 8 December 1995, (+24 h) in Exp. GS-1. Isotherm interval is 2 C.

Figure 21. MM5 simulated relative humidity (%) at 500 m AGL on the 4-km domain, valid for 0000 UTC, 8 December 1995, (+24 h) in Exp. GS-1. Contour interval is 10 %.

Figure 22. MM5 simulated sounding plotted at Bakersfield, CA, for 0000 UTC, 8 December 1995, (+24 h) in Exp. GS-1.

Figure 23. Location of east-west cross section along 37 N, just north of Fresno, CA, overlaid on 4-km terrain (plotted with 500 m contour intervals).

Figure 24. MM5 simulated potential temperature, θ (K), on the 4-km domain Plot-

ted in the plane of the Fresno cross section, valid for 0000 UTC, 8 December 1995 (+24 h) in Exp. GS-1. Isentrope interval is 1 K.

Figure 25. MM5 simulated relative humidity, (%), on the 4-km domain plotted in the plane of the Fresno cross section, valid for 0000 UTC, 8 December 1995 (+24 h) in Exp. GS-1. Contour interval is 1 K

Figure 26. MM5 simulated sounding plotted at Fresno, CA, for 1200 UTC, 7 December 1995, (+12 h) in Exp. BLK-1.

Figure 27. MM5 simulated winds (m s^{-1}) in the surface layer (6 m AGL) on the 4-km domain, valid for 1200 UTC, 7 December 1995, (+12 h) in Exp. GS-2. Isotach interval is 10 m s^{-1}.

Figure 28. MM5 simulated temperatures(C) in the surface layer (6 m AGL) on the 4-km domain, valid for 1200 UTC, 7 December 1995, (+12 h) in Exp. GS-2. Isotherm interval is 2 C.

Figure 29. Location of east-west cross section along 36 N, between Fresno and Bakersfield, CA, overlaid on 4-km terrain (plotted with 500 m contour intervals).

Figure 30. MM5 simulated potential temperature, θ (K), on the 4-km domain plotted in the plane of the Fresno cross section, valid for 0000 UTC, 8 December 1995 (+24 h) in Exp. GS-2. Isentrope interval is 1 K.

Figure 31. MM5 simulated relative humidity, (%), on the 4-km domain plotted in the plane of the Fresno cross section, valid for 0000 UTC, 8 December 1995 (+24 h) in Exp. GS-2. Contour interval is 1 K.

Figure 32. MM5 simulated winds (m s^{-1}) in the surface layer (6 m AGL) on the 4-km domain, valid for 1200 UTC, 8 December 1995, (+36 h) in Exp. GS-2. Isotach interval is 10 m s^{-1}.

Figure 33. MM5 simulated relative humidity (%) in the surface layer (6 m AGL) on the 4-km domain, valid for 1200 UTC, 8 December 1995, (+36 h) in Exp. GS-2. Contour interval is 10 %.

Figure 34. MM5 simulated sounding plotted at Fresno, CA, for 1200 UTC, 8 December 1995, (+36 h) in Exp. GS-2.

Figure 35. MM5 simulated sounding plotted at Bakersfield, CA, for 1200 UTC, 8 December 1995, (+36 h) in Exp. GS-2.

Figure 36. MM5 simulated winds (m s^{-1}) in the surface layer (6 m AGL) on the 4-km domain, valid for 1200 UTC, 9 December 1995, (+60 h) in Exp. GS-2. Isotach interval is 10 m s^{-1}.

Figure 37. MM5 simulated sounding plotted at Fresno, CA, for 1200 UTC, 9 December 1995, (+60 h) in Exp. GS-2.

Figure 38. MM5 simulated sounding plotted at Bakersfield, CA, for 1200 UTC, 9 December 1995, (+60 h) in Exp. GS-2.

Figure 39. MM5 simulated sounding plotted at Fresno, CA, for 0000 UTC, 10 December 1995, (+72 h) in Exp. GS-2.

Figure 40. MM5 simulated sounding plotted at Bakersfield, CA, for 0000 UTC, 10 December 1995, (+72 h) in Exp. GS-2.

Figure 41. MM5 deep-soil temperatures (C) on the 4-km domain, generated for the model initialization and held constant through the simulation period. Valid for Exps. GS1, GS-2, and BLK-1. Isotherm interval is 1 C.

Figure 42. MM5 deep-soil temperatures (C) on the 4-km domain, generated for the model initialization and held constant through the simulation period. Valid for Exp. GS-3. Isotherm interval is 1 C.

Figure 43. MM5 simulated winds (m s^{-1}) in the surface layer (6 m AGL) on the 4-km domain, valid for 1200 UTC, 7 December 1995, (+12 h) in Exp. GS-3. Isotach interval is 10 m s^{-1}.

Figure 44. MM5 simulated temperatures (C) in the surface layer (6 m AGL) on the 4-km domain, valid for 1200 UTC, 7 December 1995, (+12 h) in Exp. GS-3. Isotherm interval is 2 C.

Figure 45. MM5 simulated potential temperature, θ (K), on the 4-km domain plotted in the plane of the Fresno cross section, valid for 0000 UTC, 8 December 1995 (+24 h) in Exp. GS-3. Isentrope interval is 1 K.

Figure 46. MM5 simulated relative humidity, (%), on the 4-km domain plotted in the plane of the Fresno cross section, valid for 0000 UTC, 8 December 1995 (+24 h) in Exp. GS-3. Contour interval is 1 K.

Figure 47. MM5 simulated winds (m s^{-1}) in the surface layer (6 m AGL) on the 4-km domain, valid for 1200 UTC, 8 December 1995, (+36 h) in Exp. GS-3. Isotach interval is 10 m s^{-1}.

Figure 48. MM5 simulated temperatures (C) in the surface layer (6 m AGL) on the 4-km domain, valid for 1200 UTC, 8 December 1995, (+36 h) in Exp. GS-3. Isotherm interval is 2 C.

Figure 49. MM5 simulated relative humidity (%) in the surface layer (6 m AGL)

on the 4-km domain, valid for 1200 UTC, 8 December 1995, (+36 h) in Exp. GS-3. Contour interval is 10 %.

Figure 50. MM5 simulated sounding plotted at Fresno, CA, for 1200 UTC, 8 December 1995, (+36 h) in Exp. GS-3.

Figure 51. MM5 simulated sounding plotted at Bakersfield, CA, for 1200 UTC, 8 December 1995, (+36 h) in Exp. GS-3.

Figure 52. MM5 simulated winds (m s^{-1}) in the surface layer (6 m AGL) on the 4-km domain, valid for 1200 UTC, 9 December 1995, (+60 h) in Exp. GS-3. Isotach interval is 10 m s^{-1}.

Figure 53. MM5 simulated relative humidity (%) in the surface layer (6 m AGL) on the 4-km domain, valid for 1200 UTC, 9 December 1995, (+60 h) in Exp. GS-3. Contour interval is 10 %.

Figure 54. MM5 simulated sounding plotted at Fresno, CA, for 1200 UTC, 9 December 1995, (+60 h) in Exp. GS-3.

Figure 55. MM5 simulated sounding plotted at Bakersfield, CA, for 1200 UTC, 9 December 1995, (+60 h) in Exp. GS-3.

Figure 56. MM5 simulated sounding plotted at Fresno, CA, for 0000 UTC, 10 December 1995, (+72 h) in Exp. GS-3.

Figure 57. MM5 simulated sounding plotted at Bakersfield, CA, for 0000 UTC, 10 December 1995, (+72 h) in Exp. GS-3.

Figure 58. MM5 simulated sounding plotted at Fresno, CA, for 1200 UTC, 10 December 1995, (+84 h) in Exp. GS-3.

Figure 59. MM5 simulated sounding plotted at Bakersfield, CA, for 1200 UTC, 10 December 1995, (+84 h) in Exp. GS-3.

Figure 60. MM5 simulated winds (m s^{-1}) in the surface layer (6 m AGL) on the 4-km domain, valid for 0000 UTC, 11 December 1995, (+96 h) in Exp. GS-3. Isotach interval is 10 m s^{-1}.

Figure 61. MM5 simulated sounding plotted at Fresno, CA, for 0000 UTC, 11 December 1995, (+96 h) in Exp. GS-3.

Figure 62. MM5 simulated sounding plotted at Bakersfield, CA, for 0000 UTC, 11 December 1995, (+96 h) in Exp. GS-3.

Figure 63. MM5 simulated sounding plotted at Fresno, CA, for 1200 UTC, 11

December 1995, (+108 h) in Exp. GS-3.

Figure 64. MM5 simulated sounding plotted at Bakersfield, CA, for 1200 UTC, 11 December 1995, (+108 h) in Exp. GS-3.

Figure 65. Selected SoCAB surface observational sites (Part I).

Figure 66. Selected SoCAB surface observational sites (Part II)

Figure 67a,b. SoCAB (a) rawinsonde (b) RWP/RASS profiler observational sites.

Figure 68. MM5 domains

Figure 69a,b. 700mb NWS weather charts (height contour interval of 30 m) at: (a) 05/00UTC and (b) 06/00UTC.

Figure 70. Surface NWS weather charts (isobar interval of 4 mb) at 06/00UTC.

Figure 71a-c. GDAS model 650 mb heights (height contour interval of 5 m) for: (a) 05/00UTC, (b) 05/12UTC, and (c) 06/00UTC.

Figure 72a-c. Rawinsonde temperature (^{0}C) time section at (a) SNIC, (b) UCLA, and (c) 29PA SoCAB sites.

Figure 73a-c. RASS 6-hourly SCL temperature (^{0}C) profiles on: (a) 4 August, (b) 5 August, and (c) 6 August.

Figure 74a-c. RASS 6-hourly LAX temperature (^{0}C) profiles on (a) 4 August, (b) 5 August, and (c) 6 August.

Figure 75a-c. RASS 6-hourly EMT temperature (^{0}C) profiles on: (a) 4 August, (b) 5 August, and (c) 6 August.

Figure 76a-c. RASS 6-hourly HPA temperature (^{0}C) profiles on: (a) 4 August, (b) 5 August, and (c) 6 August.

Figure 77a,b. Profiler temperature (^{0}C) cross-sections for 04/06UTC in: (a) coastal and (b) perpendicular planes.

Figure 78a,b. Profiler temperature (^{0}C) cross-sections for 04/18UTC in: (a) coastal and (b) perpendicular planes.

Figure 79a,b. Profiler temperature (^{0}C) cross-sections for 05/06UTC in: (a) coastal and (b) perpendicular planes.

Figure 80a,b. Profiler temperature (^{0}C) cross-sections for 05/18UTC in: (a) coastal and (b) perpendicular planes.

Figure 81a,b. Profiler temperature (^{0}C) cross-sections for 06/06UTC in: (a) coastal and (b) perpendicular planes.

Figure 82a,b. Profiler temperature (^{0}C) cross-sections for 06/18UTC in: (a) coastal and (b) perpendicular planes.

Figure 83a-f. Surface interpolated temperatures (K) on: (a) 04/12, (b) 04/18, (c) 05/00, (d) 05/18, (e) 06/00, and (f) 06/18UTC.

Figure 84a-e. Interpolated RASS temperatures (K) at 300m AGL on: (a) 04/12, (b) 05/00, (c) 05/12, (d) 06/00, and (e) 06/12UTC.

Figure 85a-e. Interpolated RASS temperatures (K) at 800 m AGL on: (a) 04/12, (b) 05/00, (c) 05/12, (d) 06/00, and (e) 06/12UTC.

Figure 86a-c. Winds (full barb is 1 m s^{-1}) for (a) SNIC, (b) UCLA, and (c) 29PA rawinsonde sites from 04/12 or 04/20UTC to 07/06 or 07/20UTC.

Figure 87a-c. SCE profiler winds (flag is 5 m s^{-1}) on: (a) 4 August, (b) 5 August, and (c) 6 August.

Figure 88a-c. LAX profiler winds (flag is 5 m s^{-1}) on: (a) 4 August, (b) 5 August, and (c) 6 August.

Figure 89a-c. HPA profiler winds (flag is 5 m s^{-1}) on: (a) 4 August, (b) 5 August, and (c) 6 August.

Figure 90a,b. Profiler wind (speed proportional to arrow length) cross-sections at 04/06UTC in (a) coastal and (b) perpendicular directions.

Figure 90c,d. Profiler wind (speed proportional to arrow length) cross-sections at 04/18UTC in (a) coastal and (b) perpendicular directions.

Figure 90e,f. Profiler wind (speed proportional to arrow length) cross-sections at 04/22UTC in (a) coastal and (b) perpendicular directions.

Figure 91a,b. Profiler wind (speed proportional to arrow length) cross-sections at 05/06UTC in (a) coastal and (b) perpendicular directions.

Figure 91c,d. Profiler wind (speed proportional to arrow length) cross-sections at 05/22UTC in (a) coastal and (b) perpendicular directions.

Figure 92a,b. Profiler wind (speed proportional to arrow length) cross-sections at 06/06UTC in (a) coastal and (b) perpendicular directions.

Figure 92c,d. Profiler wind (speed proportional to arrow length) cross-sections at 06/22UTC in (a) coastal and (b) perpendicular directions.

Figure 93: Vertically interpolated 3800m AGL profiler winds (flag is 5 m s^{-1}) on (a) 04/18, (b) 05/00, (c) 05/06, (d) 05/12, (e) 05/20, (f) 06/00, and (g) 06/12UTC.

Figure 94. Observed surface (6 m AGL) winds (flag is 5 m s^{-1}) on: (a) 04/12, (b) 04/16, (c) 04/23, (d) 05/02, (e) 05/03, (f) 05/12, (g) 05/22, (h) 06/03, and (i) 06/23UTC.

Figure 95. Vertically interpolated 800m AGL profiler winds (flag is 5 m s^{-1}) on: (a) 04/12, (b) 04/16, (c) 04/23, (d) 05/02, (e) 05/03, (f) 05/12, (g) 05/16, (h) 05/22, (i) 06/06, (j) 06/10, (k) 06/15, and (l) 06/22UTC.

Figure 96. Interpolated observed surface ozone concentrations (pphm) on: (a) 04/20, (b) 04/23, (c) 05/06, (d) 05/14, (e) 05/17, (f) 05/22, and (g) 06/02UTC.

Figure 97 Run 1 first level temperature (^{o}C) contours for (a) 05/09UTC and (b) 05/21UTC.

Figure 98. Run 1 spatial mean temperature (^{o}C) without height correction for the full domain. Solid line represents predicted and dotted line observed values.

Figure 99. Run 1 first level winds for (a) 05/09UTC and (b) 05/21UTC.

Figure 100. Run 2 spatial mean temperature (^{o}C) with (a) no height correction and (b) corrected to 2 m AGL for the full domain. Solid line represents predicted and dotted line observed values.

Figure 101. Run 3 spatial mean temperature (^{o}C) corrected to 2 m AGL for the full domain. Solid line represents predicted and dotted line observed values.

Figure 102. Run 3 first level winds for (a) 05/09UTC and (b) 05/21UTC.

Figure 103. Run 3 mean (a) scalar and (b) vector wind speeds (m/s) for full domain, uncorrected for heights. Solid line is predicted and dotted line observed speeds.

Figure 104. Run 4 spatial mean temperature (^{o}C) corrected to 2 m AGL for the full domain. Solid line represents predicted and dotted line observed values.

Figure 105. Run 5 first level temperature contours for (a) 05/09UTC and (b) 05/21UTC.

Figure 106. Run 5 spatial mean temperature (^{o}C) corrected to 2 m AGL for the full domain. Solid line represents predicted and dotted line observed values.

Figure 107. Model performance sub-domains: (1) South Central Coast, (2) South Coast (3) Foothills, (4) South Central Valley, (5) Interior, (6) Desert, and (7) Mountains.

Figure 108. Run 5 spatial mean temperature (^{o}C) corrected to 2 m AGL for (a) Desert, (b) Foothills, (c) Interior, (d) Mountains, (e) South Central Coast, (f) South Central Valley and (g) South coast sub-domain for RUN5. Solid line represents predicted and dotted line observed values.

Figure 109. Run 5 first level winds for (a) 05/09UTC and (b) 05/21UTC.

Figure 110. Run 5 scalar mean wind speed (m/s) for full domain, uncorrected for heights. Solid line is predicted and dotted line observed values.

Figure 111. Run 5 scalar mean wind speed (m/s) for (a) Desert, (b) Foothills, (c) Interior, (d) Mountains, (e) South Central Coast, (f) South Central Valley, and (g) South coast sub-domain, uncorrected for height.

Figure 112. Run 5 mean vector wind speed (m/s) for full domain, uncorrected for height. Solid line is predicted and dotted line is observed.

Figure 113. Run 5 vector mean wind speed (m/s) for (a) Desert, (b) Foothills, (c) Interior, (d) Mountains, (e) South Central Coast, (f) South Central Valley, and (g) South coast sub-domain, uncorrected for heights.

Figure 114. Run 5 average wind direction for full domain. Black line with black squares is predicted and gray line with gray triangles is observed.

Figure 115. Run 5 average wind direction for (a) Desert, (b) Foothills, (c) Interior, (d) Mountains, (e) South Central Coast, (f) South Central Valley, and (g) South Coast sub-domains.

Figure 116. Run 6 spatial mean temperature (^{o}C) corrected to 2 m AGL for the full domain. Solid line represents predicted and dotted line observed values.

Figure 117. Run 6 scalar mean wind speed (m/s) for full domain, uncorrected for heights. Solid line is predicted and dotted line observed values.

Figure 118. Run 6 mean vector wind speed (m/s) for full domain, uncorrected for height. Solid line is predicted and dotted line is observed.

Figure 119. Run 6 average wind direction for full domain. Black line with black squares is predicted and gray line with gray triangles is observed.

List of Tables

Table 1a,b. SoCAB modeling studies.

Table 2. Vertical layer definitions for SJV MM5 Experiments. Model layers are numbered, following the MM5 convention, from the top of the domain (layer 1) downward to the surface (layer 40). Heights (m) and pressures (mb) apply at the center of the layers, where the prognostic variables u, v, T, q_v q_c, q_r and p' are calculated. For preparation of the table, the surface pressure was assumed to be 1000 mb, while the model top is at 100 mb.

Table 3. Design of the MM5 SJV model experiments for the case of 7-12 December 1995.

Table 4. MM5 wintertime soil moisture availability for the SJV. Exps. GS-1, BLK-1, and GS-2 use the standard moisture, while Exp. GS-3 used the modified soil moisture to reflect recent rainfall associated with a recent frontal passage. Soil moisture can range from 0.0 (dry) to 1.0 (water surface).

Table 5. Conversion of temperature between Celsius (C) and Fahrenheit (F) scales.

Table 6. Frequency of occurrence of fog (block numbers) and haze (*italic numbers*) summed over all NWS stations in Sacramento and San Joaquin Valleys for 7-11 December 1995 as a function of dew-point depression. Data are based on surface observations at 3-h intervals. Depressions in Celsius scale are reported to the nearest 0.5 C. In the frequency displays (lines 3 and 4) **bold block numbers** indicate idealized range assumed to apply for fog, while ***bold italic numbers*** indicate idealized range assumed for haze.

Table 7. Model Verification at Bakersfield in Exp. GS-2. Characteristics of stratus, fog and haze for the IMS-95 Case of Dec. 9-11, 1995. Verifications are based on surface and radiosonde observations versus MM5, based on criteria developed from Table 6.

Table 8. Model Verification at Fresno in Exp. GS-2. Characteristics of stratus, fog and haze for the IMS-95 Case of Dec. 9-11, 1995. Verifications are based on surface and radiosonde observations versus MM5, based on criteria developed from Table 6.

Table 9. Model Verification at Bakersfield in Exp. GS-3. Characteristics of stratus, fog and haze for the IMS-95 Case of Dec. 9-11, 1995. Verifications are based on surface and radiosonde observations versus MM5, based on criteria developed from Table 6

Table 10. Model Verification at Fresno in Exp. GS-3. Characteristics of stratus, fog and haze for the IMS-95 Case of Dec. 9-11, 1995. Verifications are based on surface and radiosonde observations versus MM5, based on criteria developed from Table 6.

Table 11. Summary of statistical evaluations for fog-related variables at the two IMS-95 sites having special 6-hrly radiosonde data (Bakersfield and Fresno) from 9-11 December 1995. Statistics are based on "model minus observations".

Table 12a. SCOS97 surface sites used in current simulations.

Table 12b. SCOS97 rawinsonde sites.

Table 12c. SCOS97 profiler sites.

Table 13. Vertical layer definitions for the SoCAB MM5 Experiments. Model layers are numbered, following the MM5 convention, from the top of the domain (layer 1) downward to the surface (layer 30). Heights (m) apply at the center of the layers, where the prognostic variables u, v, T, q_v q_c, q_r and p' are calculated. For preparation of the table, the surface pressure was assumed to be 1000 mb, while the model top is at 100 mb.

Table 14. SoCAB MM5 cases.

Table 15. Original and modified SoCAB surface roughness length values for different land use types.

Table 1a

Reference	Models	Phenomenon	Resolution (km) Nesting	Notes
Schultz and Warner (1982)	2D vertical section	summertime circulation and ventilation in LA Basin	2.5 no	> sea-breeze dominates local circulation, which is reinforced by local winds > small urban heat island effect > fairly good agreement with monthly avg obs
Glandening (1989)	(x-y) vertically averaged model	daytime BL variation in LA Basin	5 no	> qualitative agreement with obs > mixing heights overpredicted > detrainement increases accuracy > compensating errors in equations
Ulrickson and Mass (1990a)	CSUMM hydrostatic	mesoscale circulations over LA basin	5 no	> spatial variability of surface winds not very well captured > nightime wind prediction poor > mean BL temp peak later than obs
Ulrickson and Mass (1990b)	CSUMM trajectory model	synoptic influences on pollutant trajectories	5 no	> daytime simulation only > large scale effects stronger in winter > pollutants lofted and transported
Kessler and Douglas (1991)	CSUMM	Santa Barbara eddy	10 (larger at boundaries) no	> relatively good agreement with obs > off-shore winds exaggerated > large scale wind change restricts simulation time
Ueyoshi and Roads (1993)	Ueyoshi and Han	Catalina eddy	25 yes one-way	> pressure gradients not very well represented (grid too coarse) > BL structure in region of S flow not well represented. SST(x,y)
Harley et al. (1993)	CIT airshed model	photochemical study of SCAQS	5 no	> peak O_3 concentrations underpredicted > NO_2 and HC overprediction at night at coastal sites > limited physics

Reference	Models	Phenomenon	Resolution (km) Nesting	Notes
Lu and Turco (1994)	SMOG (meteorological) hydrostatic	2D simulations of LA sea breeze and mountain effects on χ	2.5 (larger at boundaries) no	> sea breeze and mountain flows create vertical mixing, which causes elevated pollution layers. > pollutants are injected into inversion layer in evening
Lu and Turco (1995)	SMOG (meteorological) trajectory model	air pollution transport in LA basin	4.6 by 5 no	> elevated pollution layers due to : convergence zones, BL stabilization, and complex terrain effects > no observations
Ulrickson et al. (1995)	CSUMM	Catalina eddy	13.9 no	> eddy caused by N-NW geostrophic flow interacting with topography > sea-breeze delays onset of eddy > no observations
Taha (1996)	CSUMM UAM-IV	impacts on O_3 of increased urban vegetation	5 no	> net basin-wide reduction of O_3 if trees are low emitters of biogenic hydrocarbons
Jacobson et al. (1996)	MMTD GATOR	air quality in LA basin	4.6 by 5	> overall ozone prediction accuracy decrease F70 in time > nighttime temperature underprediction causes causes errors in predicted ozone
Lu and Turco (1996)	SMOG (coupled) (meteorological, transport and chemistry)	air quality in LA basin	4.6 by 5 smaller domain for air quality	> O_3 vertical structure quite accurately reproduced > layers of O_3 in free troposphere > highest levels of O_3 in eastern basin
Lu and Turco (1997a, b)	SMOG (coupled)	air quality in LA basin	4.6 by 5 smaller domain for air quality	> nightime winds not accurately predicted (grid too coarse) > mixing layer overpredicted in the afternoon > O_3 distribution overall good but details poor

Reference	Models	Phenomenon	Resolution (km) Nesting	Notes
Thompson et al. (1997)	NORAPS hydrostatic vertically nested	Catalina eddy	20 yes fully interactive	> model includes cloud radiation interaction > SST(x,y) > BL vertical structure satisfactory > deep MBL in region of S flow
Taha (1997)	CSUMM UAM	effects on O_3 of albedo increase	5 no	> locally positive or negative impacts > albedo increase produces O_3 reduction
Hegarty et al. (1998) I Pai (1998) II	MM5 SAQM	meteorological simulations and air quality in LA basin	45 15 5 yes, two-way	> not so accurate predictions after 48 hours >synoptic scale error growth > FDDA may impove results > air quality simulations not completed
Jackobson (1998)	GATORM	effects on meteorology and O_3 of soil moisture	4.6 by 5	> low soil moisture case: predicted O_3 higher temperatures hotter, winds faster > high soil moisture case: predicted O_3 higher temperatures colder, winds slower

Table 1b

Reference	Initial Conditions	Upper BC	Surface temperature	SBL	Turbulence Closure
Schultz and Warner (1982)	> composite of Tand T_D sounding > zero synoptic pressure gradient	constant	ground surface slab model		space and time variable l (Busch)
Glandening (1989)	> obs BL heights over land and sea > free atmosphere temperature gradient > zero synoptic pressure gradient	steady free atmosphere parameterized values	no	>bulk transfer mom.flux > specified sfc heat flux	vertical average fluxes
Ulrickson and Mass (1990a)	> θ ,q and wind sounding > dymamic initialization	constant	multilayer soil model	Businger Dyer	TKE (TL modified)
Ulrickson and Mass (1990b)	> large scale forcing for composite of smog events	constant	multilayer soil model constant soil moisture	Businger Dyer	TKE (TL modified)
Kessler and Douglas (1991)	> T, q and wind sounding > dynamic initialization	constant	multilayer soil model constant soil moisture	Businger Dyer	TKE (TL modified)
Ueyoshi and Roads (1993)	> global model interpolation	constant	force restore	Louis	Blackadar
Harley et al. (1993)	> interpolation of measurements	constant			analytical expression

Reference	Initial Conditions	Upper BC	Surface temperature	SBL	Turbulence Closure
Lu and Turco (1994)	> composite of Tand T_D sounding > zero synoptic pressure gradient	constant	force restore	Monin Obukhov (Louis)	multi-layer hybrid BL 1 st order Blackadar
Lu and Turco (1995)	> monthly averaged T and Td sndgs > zero synoptic pressure gradient	constant	force restore	Monin Obukhov (Louis)	multi-layer hybrid BL 1 st order Blackadar
Ulrickson et al. (1995)	> T and wind sounding > dynamic initialization	constant	multilayer soil model	Businger Dyer	TKE (TL modified)
Taha (1996)	> single T and wind sounding	constant	multilayer soil model	Businger Dyer vegetation bulk layer	TKE
Jacobson et al. (1996)	> single T, Td, pressure > zero initial winds	constant	force restore	Monin Obukhov (Louis)	multi-layer hybrid BL 1 st order Blackadar
Lu and Turco (1996)	> interpolation of T, wind ,q soundings over grid domain	reinitialized meteorological fields every morning	multilayer soil model	Monin Obukhov (Louis)	multi-layer hybrid BL 1 st order Blackadar
Lu and Turco (1997a and b)	> interpolation of T, wind, q soundings over grid domain	reinitialized meteorological fields every morning	multilayer soil model	Monin Obukhov (Louis)	hybrid BL(used) or 2.5 level M-Y

Reference	Initial Conditions	Upper BC	Surface temperature	SBL	Turbulence Closure
Thompson et al. (1997)	> global model interpolation	mesoscale data assimilation (update every 12 hours)	force restore	Louis (sfc) Liu (water)	3 level M-Y
Taha (1997)	> single T and wind sounding	constant	multilayer soil model	Businger Dyer vegetation bulk layer	TKE
Hegarty et al. (1998) Pai (1998)	> surface observations and upper air soundings blended into ECMWF-TOGA analysis > NAVY SST 5-days average		force restore explicit moisture prediction		multi layer Blackadar scheme
Jackobson (1998)	> single T, Td, pressure > zero initial winds	constant	multilayer soil model	Monin Obukhov (Louis)	multi-layer hybrid BL 1 st order Blackadar
Stauffer et al. 2000	> NCEP/GDAS	analysis nudging FDDA	force restore		Gayno Seaman 1.5 TKE order

Table 2. Vertical layer definitions for MM5 SJV experiments. Model layers are numbered, following the MM5 convention, from the top of the domain (layer 1) downward to the surface (layer 40). Heights (m) and pressures (mb) apply at the center of the layers, where the prognostic variables u, v, T, q_v q_c, q_r and p' are calculated. For preparation of the table, the surface pressure was assumed as1000 mb, while the model top is at 100 mb.

Grid Level	Height (m)	Pressure (mb)	Grid Level	Height (m)	Pressure (mb)
1	14,888	116.2	21	1,208	865.9
2	13,496	149.5	22	1,079	879.4
3	12,259	184.6	23	982	889.75
4	11,138	221.5	24	894	899.20
5	10,130	259.3	25	814	907.84
6	9,229	297.1	26	740	915.94
7	8,414	334.9	27	669	923.77
8	7,652	373.6	28	599	931.51
9	6,919	414.1	29	531	939.12
10	6,226	455.5	30	464	946.59
11	5,582	496.9	31	398	954.06
12	4,979	538.3	32	332	961.53
13	4,413	579.7	33	267	969.00
14	3,890	620.2	34	206	976.02
15	3,383	661.6	35	153	982.14
16	2,892	703.9	36	108	987.36
17	2,433	745.3	37	71	991.63
18	2,023	784.0	38	43	994.96
19	1,684	817.3	39	21	997.48
20	1,408	845.2	40	6	999.28

Table 3. Design of the MM5 model experiments for the case of 7-12 December 1995.

Exp. Name And Length (h)	Turbulence Sub-Model	Lower Bndry Conditions	FDDA
GS-1 (120 h)	Std. Gayno-Seaman, plus moist buoyancy production term	Std. Time avg'd T_m using 00 UTC and 12 UTC 108-km surface temp. analyses; Std. Moisture availability	Analysis nudging on 108 & 36-km domains above 1.5 km AGL (Shoran et al. 2000), G=3X10^{-4} s^{-1}
BLK-1 (36 h)	Std. Blackadar	Std. Time avg'd T_m using 00 UTC and 12 UTC 108-km surface temp. analyses; Std. Moisture availability	Analysis nudging on 108 & 36-km domains above 1.5 km AGL (Shoran et al. 2000), G=3X10^{-4} s^{-1}
GS-2 (120 h)	Extended Gayno-Seaman as in Sec. 2.4	Std. Time avg'd T_m using 00 UTC and 12 UTC 108-km surface temp. analyses; Std. Moisture availability	Analysis nudging on 108 & 36-km domains above 1.5 km AGL (Shoran et al. 2000), G=3X10^{-4} s^{-1}
GS-3 (120 h)	Extended Gayno-Seaman as in Sec. 2.4	T_m based on observed surface max. and min. temps. In SJV; Enhanced moisture availability	Analysis nudging on 108 & 36-km domains above 1.5 km AGL (Shoran et al. 2000), G=3X10^{-4} s^{-1}

Table 4. MM5 wintertime soil moisture availability for the SJV. Exps. GS-1, BLK-1, and GS-2 use the standard moisture, while Exp. GS-3 used the modified soil moisture to reflect recent rainfall associated with a recent frontal passage. Soil moisture can range from 0.0 (dry) to 1.0 (water surface).

Land Use No.	Land Use Description	Standard Soil Moist.	Modified Soil Moist.
1	Urban	0.10	0.25
2	Agriculture Cropland	0.60	0.75
3	Rangeland/Grassland	0.30	0.45
14	Vineyards/Orchards	0.60	0.75

Table 5. Conversion of temperature between Celsius (C) and Fahrenheit (F) scales.

Celsius	Fahrenheit	Celsius	Fahrenheit
21	70	10	50
20	68	9	48
19	66	8	46
18	64	7	45
17	63	6	43
16	61	5	41
15	59	4	39
14	57	3	37
13	55	2	36
12	54	1	34
11	52	0	32

Table 6. Frequency of occurrence of fog (block numbers) and haze (*italic numbers*) summed over all NWS stations in SJV and Sacramento Valley for 7-11 December 1995 as a function of dew-point depression. Data are based on surface observations at 3-h intervals. Depressions in Celsius scale are reported to the nearest 0.5 C. In the frequency displays (lines 3 and 4) **bold block numbers** indicate idealized range assumed to apply for fog, while ***bold italic numbers*** indicate idealized range assumed for haze.

Dew Pt. Depression (C)	0.0	0.5	1.0	1.5	2.0	3.0	3.5	4.0	4.5	5.0	5.5	6.0	6.5
Dew Pt. Depression (F)	0	1	2	3	4	*5*	*6*	*7*	*8*	*9*	*10*	*11*	*12*
Frequency Of Fog	**48**	**34**	**24**	**36**	**24**	10	2	2	1	0	0	0	0
Frequency of Haze	*0*	*0*	*1*	*0*	*1*	*7*	*7*	***8***	*7*	***4***	*1*	*0*	*2*

Table 7. Model Verification at **Bakersfield** in Exp. GS-2. Characteristics of stratus, fog, and haze for the IMS-95 Case of Dec. 9-11, 1995. Verifications are based on surface and radiosonde observations versus MM5, based on criteria developed from Table 5.

			Obs'd WX			MM5 WX			Obs'd Ts(C) & Td(C)			MM5 Ts(C) & Td(C)		
Date	**GMT**	**LST**	**Type**	**Vis. (mi)**	**Depth (m)**	**Type**	**Vis. (mi)**	**Depth (m)**	**Surface Report [Raob. Report]**		**Fcst Hrs**	**Surface Report**		**Fcst Hrs**
09	1200	09/04	Fog	4	600	Fog	---	300	7.0 [6]	6.0 [6]	60 h	11.5	10.5	60 h
09	1800	09/10	Fog	0	400	Fog	---	400	8.0 [9]	8.5* [8]	66 h	11.0	11.0	66.h
10	0000	09/16	Haze, Strat.	1	250	Haze, Strat.	---	300	11.5 [10]	9.0 [10]	72 h	13.0	10.5	72 h
10	0600	09/22	Fog	0.125	250	Fog	---	150	4.0 [7]	4.0 [7]	78 h	12.0	10.5	78 h
10	1200	10/04	Fog	0	250	Haze	---	100	4.5 [7]	4.5 [7]	84 h	12.5	9.5	84 h
10	1800	10/10	Fog	0.125	200	Clear	---	---	6.5 [6]	6.5 [6]	90 h	15.0	7.0	90 h
11	0000	10/16	Haze	3	150	Clear	---	---	15.5 [15]	9.0 [11]	96 h	17.5	9.0	96 h
.11	0600	10/22	Haze	4	125	Clear	---	---	10.0 [11]	6.5 [11]	102 h	NA	NA	102 h
11	1200	11/04	Clear	---	---	Clear	---	---	11.0	2.0	108 h	NA	NA	108 h

- **Warning: Sfc. report at 9 Dec., 1800 GMT, has Td > Ts**

Table 8. Model Verification at **Fresno** in Exp. GS-2. Characteristics of stratus, fog and haze for the IMS-95 Case of Dec. 9-11, 1995. Verifications are based on surface and radiosonde observations versus MM5, based on criteria developed from Table 5.

			Obs'd WX			MM5 WX			Obs'd Ts(C) & Td(C)			MM5 Ts(C) & Td(C)		
Date	**GMT**	**LST**	**Type**	**Vis. (mi)**	**Depth (m)**	**Type**	**Vis. (mi)**	**Depth (m)**	**Surface Report [Raob. Report]**		**Fcst Hrs**	**Surface Report**		**Fcst Hrs**
09	1200	09/04	Fog	0.188	700	Fog	---	400	5.5 [5]	5.5 [5]	60 h	11.5	10.5	60 h
09	1800	09/10	Fog	0.188	300	Fog	---	400	8.5 [8]	8.0 [7]	66 h	11.0	11.0	66.h
10	0000	09/16	Haze, Strat.	2.5	275	Haze	---	250	13.5 [11]	10.0 [11]	72 h	12.5	10.0	72 h
10	0600	09/22	Fog	0.188	400	Fog	---	200	9.5 [9]	9.5 [9]	78 h	11.5	10.0	78 h
10	1200	10/04	Fog	0.063	300	Fog	---	150	8.0 [7]	8.0 [7]	84 h	11.0	10.5	84 h
10	1800	10/10	Fog	0.063	200	Haze	---	50	7.5 [7]	7.5 [7]	90 h	13.5	10.0	90 h
11	0000	10/16	Haze	2	175	Clear	---	---	15.5 [14]	9.0 [10]	96 h	17.0	8.0	96 h
11	0600	10/22	Haze	5	150	Clear	---	---	13.5 [12]	7.0 [9]	102 h	NA	NA	102 h
11	1200	11/04	Haze	3	---	Clear	---	---	11.5	9.0	108 h	NA	NA	108 h

Table 9. Model Verification at **Bakersfield** in Exp. GS-3. Characteristics of stratus, fog and haze for the IMS-95 Case of Dec. 9-11, 1995. Verifications are based on surface and radiosonde observations versus MM5, based on criteria developed from Table 5.

			Obs'd WX			MM5 WX			Obs'd Ts(C) & Td(C)			MM5 Ts(C) & Td(C)		
Date	**GMT**	**LST**	**Type**	**Vis. (mi)**	**Depth (m)**	**Type**	**Vis. (mi)**	**Depth (m)**	**Surface Report [Raob. Report]**		**Fcst Hrs**	**Surface Report**		**Fcst Hrs**
09	1200	09/04	Fog	4	600	Fog	---	450	7.0 [6]	6.0 [6]	60 h	9.5	9.5	60 h
09	1800	09/10	Fog	0	400	Fog	---	400	8.0 [9]	8.5* [8]	66 h	9.0	9.0	66.h
10	0000	09/16	Haze, Strat.	1	250	Fog	---	300	11.5 [10]	9.0 [10]	72 h	9.5	9.0	72 h
10	0600	09/22	Fog	0.125	250	Fog	---	200	4.0 [7]	4.0 [7]	78 h	8.5	8.5	78 h
10	1200	10/04	Fog	0	250	Fog	---	100	4.5 [7]	4.5 [7]	84 h	8.5	7.5	84 h
10	1800	10/10	Fog	0.125	200	Haze	---	100	6.5 [6]	6.5 [6]	90 h	11.0	6.5	90 h
11	0000	10/16	Haze	3	150	Haze	---	100	15.5 [15]	9.0 [11]	96 h	13.5	8.5	96 h
11	0600	10/22	Haze	4	125	Haze	---	150	10.0 [11]	6.5 [11]	102 h	10.5	8.0	102 h
11	1200	11/04	Clear	---	---	Haze	---	100	11.0	2.0	108 h	11.0	6.5	108 h

- **Warning: Sfc. report for 9 Dec., 1800 GMT, has Td > Ts**

Table 10. Model Verification at **Fresno** in Exp. GS-3. Characteristics of stratus, fog and haze for the IMS-95 Case of Dec. 9-11, 1995. Verifications are based on surface and radiosonde observations versus MM5, based on criteria developed from Table 5.

			Obs'd WX			MM5 WX			Obs'd Ts(C) & Td(C)			MM5 Ts(C) & Td(C)		
Date	**GMT**	**LST**	**Type**	**Vis. (mi)**	**Depth (m)**	**Type**	**Vis. (mi)**	**Depth (m)**	**Surface Report [Raob. Report]**		**Fcst Hrs**	**Surface Report**		**Fcst Hrs**
09	1200	09/04	Fog	0.188	700	Fog	---	500	5.5 [5]	5.5 [5]	60 h	9.0	8.0	60 h
09	1800	09/10	Fog	0.188	300	Fog	---	400	8.5 [8]	8.0 [7]	66 h	9.5	8.0	66.h
10	0000	09/16	Haze, Strat.	2.5	275	Haze	---	300	13.5 [11]	10.0 [11]	72 h	10.5	8.0	72 h
10	0600	09/22	Fog	0.188	400	Fog	---	225	9.5 [9]	9.5 [9]	78 h	8.5	8.5	78 h
10	1200	10/04	Fog	0.063	300	Fog	---	200	8.0 [7]	8.0 [7]	84 h	8.5	8.5	84.h
10	1800	10/10	Fog	0.063	200	Haze	---	100	7.5 [7]	7.5 [7]	90 h	11.0	8.0	90 h
11	0000	10/16	Haze	2	125	Haze	---	50	15.5 [14]	9.0 [10]	96 h	15.0	8.5	96 h
11	0600	10/22	Haze	5	150	Haze	---	100	13.5 [12]	7.0 [9]	102 h	12.5	8.5	102 h
11	1200	11/04	Haze	3	---	Haze	---	100	11.5	2.0	108 h	12.0	8.5	108 h

Table 11. Summary of statistical evaluations for fog-related variables at the two IMS-95 sites having special 6-hrly radiosonde data (Bakersfield and Fresno) from 9-11 December 1995. Statistics are based on "model minus observations".

Verification Category	Exp. GS-2	Exp. GS-3
Bakersfield		
Type of Weather (no. of correct predictions out of 9)	5	6
Mean Error (m) for depth of fog/haze	-70 m	-53 m
Mean Abs. Error (m) for depth of fog/haze	120 m	72 m
Mean Error of Sfc. Temperature (C)	5.07 C	1.44 C
Mean Abs. Error of Sfc. Temperature (C)	5.07 C	2.33 C
Mean Error of Sfc. Dew Point (C)	2.79 C	1.89 C
Mean Abs. Error of Sfc. Dew Point (C)	2.79 C	2.00 C
Fresno		
Type of Weather (no. of correct predictions out of 9)	5	8
Mean Error (m) for depth of fog/haze	-121 m	-78 m
Mean Abs. Error (m) for depth of fog/haze	154 m	109 m
Mean Error of Sfc. Temperature (C)	2.86 C	0.39 C
Mean Abs. Error of Sfc. Temperature (C)	3.14 C	1.61 C
Mean Error of Sfc. Dew Point (C)	1.79 C	0.11 C
Mean Abs. Error of Sfc. Dew Point (C)	2.07 C	1.00 C
COMPOSITE FOR BOTH SITES		
Type of Weather (no. of correct predictions out of 18)	**10**	**14**
Mean Error (m) for depth of fog/haze	**-99 m**	**-41 m**
Mean Abs. Error (m) for depth of fog/haze	**139 m**	**92 m**
Mean Error of Sfc. Temperature (C)	**3.97 C**	**0.92 C**
Mean Abs. Error of Sfc. Temperature (C)	**4.11 C**	**1.97 C**
Mean Error of Sfc. Dew Point (C)	**2.29 C**	**1.00 C**
Mean Abs. Error of Sfc. Dew Point (C)	**2.43 C**	**1.50 C**

TABLE 12
Currently used SCOS97 Surface Sites

CODE	SPONSOR	UTMN (m)	UTME (m)	Lat/deg	min	sec	Long/deg	min	sec
ACTN		3812.048	389.759	34	26	45	118	12	0
AGRN		3899.528	187.516	35	11	31	120	25	54
ALPN	SDAQMD	3630.8	523.403	32	49	58	116	45	0
ANAH	SCAQMD	3741.999	416.706	33	49	11	117	54	46
ANZA		3712.671	530.351	33	33	18	116	40	23
ARVN	CARB	3896.481	337.652	35	12	28	118	47	2
ATAS	SLOCO	3932.63	167.308	35	29	27	120	40	4
BEAR	BLM	3971.317	405.223	35	53	3	118	3	6
BKWC	CIMIS	3947.09	232.854	35	38	59	119	57	30
BLHT	CIMIS	3715.238	716.645	33	33	24	114	39	59
BRBK	SCAQMD	3781.205	380.176	34	10	33	118	18	57
BRST	CIMIS	3859.99	501.523	34	53	3	116	59	0
BURN	BLM	3784.203	535.318	34	12	30	116	37	15
CALB	AVES	3779.614	351.313	34	8	55	118	36	46
CAMB	CIMIS	3655.928	649.42	33	2	37	115	24	56
CARL	NWS	3664.061	475.121	33	7	42	117	16	48
CARR	BLM	3885.589	247.754	35	5	47	119	46	22
CASE		3700.538	461.143	33	26	43	117	25	5
CATA	AVES	3701.349	362.252	33	26	40	118	28	55
CATH	CIMIS	3743.611	549.35	33	50	33	116	28	44
CMFS	USFS	3620.338	550.318	32	43	17	116	27	47
CONV	USFS	3782.323	507.653	34	11	1	116	55	1
CPGB	CHVRON	3809.034	274.784	34	24	10	119	27	28
CUYA	CIMIS	3866.69	262.472	34	55	54	119	36	17
DEVO		3786.551	462.875	34	13	16	117	24	11
ECAJ	SDAQMD	3627.079	506.243	32	47	27	116	56	31
EDSN	CARB	3911.381	331.858	35	20	45	118	51	3
ELDO	CIMIS	3738.467	399.699	33	47	50	118	5	38
ELRO	VCAPCD	3791.74	303.549	34	15	53	119	8	2
EMMA	VCAPCD	3795.806	286.748	34	17	23	119	19	50
ESCD	CIMIS	3660.334	503.111	33	5	24	116	58	52
ESCO	SDAQMD	3664.031	493.78	33	7	40	117	4	26
FAMS	CIMIS	3942.059	299.579	35	36	14	119	12	45
FAWN	USFS	3791.472	509.308	34	15	58	116	53	56
FISH	BLM	3649.649	588.765	32	59	0	116	3	28
FSPR		3973.488	327.156	35	53	32	118	54	54
FVML	BLM	3969.904	417.097	35	52	18	117	55	6
FVPT	CIMIS	4025.182	221.737	36	20	11	120	6	47
GOLE	SBAPCD	3813.523	244.235	34	26	41	119	47	38
GRAN	BLM	3821.097	498.471	34	32	8	117	1	33
HAWH	SCAQMD	3753.563	373.661	33	55	51	118	22	8
HORS	BLM	3958.427	599.436	35	46	14	115	54	33
IRVI	CIMIS	3727.083	433.571	33	41	19	117	43	14
JOSH	NPS	3769.525	556.905	34	4	15	116	23	27

CODE	SPONSOR	UTMN (m)	UTME (m)	Lat/deg	min	sec	Long/deg	min	sec
JULI		3659.577	538.191	33	4	33	116	35	27
KEEN	USFS	3728.74	527.802	33	42	47	116	42	48
KETT	CIMIS	3972.8	239.654	35	52	8	119	53	39
LANM	SCAQMD	3770.04	386.188	34	4	1	118	14	31
LAPZ		3919.776	210.433	35	22	52	120	11	15
LIND	CIMIS	4024.519	316.042	36	21	26	119	3	31
LOST	NPS	3764.11	575.405	34	1	4	116	11	16
LPHP	UNOCAL	3847.027	185.714	34	43	8	120	25	54
LPSH	SBAPCD	3837.602	183.708	34	38	16	120	27	21
LRLM	BLM	3926.115	436.596	35	28	42	117	41	56
LSF		3683.278	444.909	33	17	20	117	35	30
LTAB		3952.639	144.82	35	39	20	120	55	22
MBLD	SDAPCD	3788.458	439.756	34	14	14	117	39	15
MELO	CIMIS	3630.011	646.692	32	48	24	115	26	46
MID	BLM	3890.652	645.746	35	9	58	115	24	55
MILL	USFS	3804.98	401.936	34	23	0	118	4	0
MOJP	CARB	3878.977	396.64	35	3	3	118	8	45
MRCP	SJVUCD	3881.024	281.102	35	3	14	119	24	14
NAFB	CARB	3778.991	476.954	34	9	12	117	15	0
NIPO	UNOCAL	3880.511	174.522	35	1	19	120	34	8
NLGB	SCAQMD	3742.264	390.482	33	49	26	118	11	20
OAKG	USFS	3694.72	519.066	33	23	36	116	47	42
OASS	CIMIS	3709.669	578.545	33	31	32	116	9	15
OCEA	SDAQMD	3673.327	465.824	33	12	10	117	22	1
OCSD	CIMIS	3678.855	470.501	33	15	21	117	19	11
OJAI	VCAPCD	3812.339	291.723	34	26	49	119	16	11
OLDL	CARB	3922.739	318.448	35	26	20	119	0	57
OPAL	BLM	3889.495	483.301	35	9	15	117	10	32
PFLD		3977.977	190.227	35	53	56	120	25	55
PICO	SCAQMD	3762.458	403.031	34	0	46	118	3	32
PIRU	CIMIS	3804.058	336.011	34	22	30	118	47	20
PLVD	CIMIS	3695.922	712.399	33	23	15	114	43	21
POTR		3607.5	536.777	32	36	22	116	36	29
PSRB	CARB	3947.484	166.348	35	37	55	120	41	23
PTCL	CHVRON	3817.26	183.013	34	27	7	120	27	28
RAMO	CIMIS	3654.793	506.226	33	2	58	116	56	18
RANC		3674.732	546.104	33	12	44	116	30	19
ROSE	USFS	3823.262	299.621	34	32	35	119	11	3
SANB	SCAQMD	3773.081	475.402	34	6	28	117	16	22
SCLA	SCAQMD	3806.024	358.986	34	23	16	118	32	2
SCLR	SCAQMD	3806.024	358.986	34	23	16	118	32	2
SDOV	SDAQMD	3630.779	489.079	32	49	40	117	7	58
SELY	CIMIS	3624.111	620.227	32	45	34	115	43	54
SHFT	CARB	3930.657	294.407	35	30	14	119	16	19
SLOM	CARB	3910.379	168.001	35	17	2	120	39	14
SLTE	CIMIS	3676.031	633.576	33	13	12	115	34	48
SLTW	CIMIS	3686.693	597.739	33	19	38	115	57	0
SNTM	CIMIS	3872.531	191.008	34	57	16	120	23	3

CODE	SPONSOR	UTMN (m)	UTME (m)	Lat/deg	min	sec	Long/deg	min	sec
SNTY	CIMIS	3829.068	218.64	34	34	59	120	4	41
SQUA	BLM	3913.655	448.521	35	22	0	117	34	5
STAM	CIMIS	3766.627	364.601	34	2	28	118	28	34
STRA	CIMIS	4004.149	243.585	36	9	27	119	51	0
SVAL	VCAPCD	3792.811	345.024	34	16	40	118	41	5
SVLM	CARB	3795.671	334.533	34	17	27	118	47	52
TEME	CIMIS	3704.7	479.871	33	29	25	117	13	20
THER	CIMIS	3721.572	571.105	33	38	47	116	14	30
TME2	CIMIS	3755.67	497.189	33	33	24	117	1	49
TOMP	VCAPCD	3785.712	328.007	34	12	35	118	52	8
TUST	NWS	3728.999	424.316	33	42	0	117	49	48
UCR	CIMIS	3756.468	469.199	33	57	54	117	20	8
UHL		3963.979	355.443	35	48	0	118	36	0
VLYC		3676.162	500.725	33	13	34	116	59	32
VSLA	CIMIS	4019.302	300.957	36	18	3	119	13	23
VTRV	CIMIS	3813.733	477.039	34	28	42	117	15	40
WALK	BLM	3945.438	404.946	35	39	53	118	3	25
WARM	USFS	3827.733	357.837	34	35	0	118	33	0
YCAV		3775.794	554.614	34	7	24	116	24	28

Table 13. Half Sigma levels for the SCOS97 simulations

Grid Level	Height (m)	Sigma value	Grid Level	Height (m)	Sigma value
1	14,737	0.023	16	2,480	0.713
2	13,075	0.069	17	2,095	0.753
3	11,706	0.115	18	1,779	0.787
4	10,536	0.161	19	1,478	0.820
5	9,509	0.207	20	1,207	0.851
6	8,592	0.253	21	976	0.878
7	7,763	0.299	22	784	0.901
8	7,004	0.345	23	624	0.921
9	6,304	0.391	24	490	0.937
10	5,654	0.437	25	378	0.951
11	5,046	0.483	26	283	0.963
12	4,475	0.529	27	201	0.974
13	3,936	0.575	28	131	0.983
14	3,426	0.621	29	73	0.990
15	2,942	0.667	30	23	0.997

Table 14: MM5 Simulations

Run No	**Land Use**	**Deep Soil**	**Analysis nudging**	**Observational nudging**
Run 1: Hands Off	Original	Original	None	None
Run 2: Analysis Nudging	Original	Original	Outer three domains	None
Run 3: Cool Soil	Original	4 K cooler	Outer three domains	None
Run 4: FDDA	Original	4 K cooler	Outer three domains	Surface and upper air
Run 5: Urban Extended	Modified	4 K cooler	Outer three for T, and outer one for wind	Surface and upper air
Run 6 : Surface FDDA	Modified	4 K cooler	Outer three for T, and outer one for wind	Surface

Table 15: Modified Roughness Lengths for different Landuse types

Land use integer Identification	Landuse description	Old Roughness length	New Roughness length
1	Urban	50	150
7	Grassland	0.12	10
8	Sgrubland	10	20
9	Mix Shrb./Grs.	11	30
10	Savanna	15	40
11	Decids. Broadlf	50	100
14	Evergrn. Needlf.	50	100
16	Water Bodies	0.01	1

Abstract

The objective of the Penn State University (PSU) part of the study was to investigate the MM5's ability to simulate wintertime fog in the San Joaquin Valley (SJV) and summertime sea breeze flows in the South Coast Air Basin (SoCAB). For the SJV work the MM5 was configured with four nested grids and an advanced turbulence sub-model. Applied to the event of 7-12 December 1995, observed during the IMS-95 program, the model's innermost domain used 40 vertical layers and a 4-km mesh. Several experiments were performed to improve the turbulence sub-model for saturated conditions and to provide more accurate initial conditions for soil temperature and moisture. Results showed the MM5 correctly predicted the type of visibility obscuration (fog, haze, stratus, or clear) in 14 out of the 18 events. Fog depth was estimated by the MM5 with a mean absolute error of only 92 m and a mean error of -41 m. Mean errors for both the surface temperature and dew point were within +1 C, while the mean absolute errors were ~1.5-2.0 C. As a consequence, the mean error for dew-point depression is very small. Thus, the MM5 was shown to simulate fog and haze in the SJV with considerable accuracy. Extension of the turbulence sub-model to include saturation effects and the specification of accurate soil temperature and moisture were important for simulating fog characteristics in this case. Additionally, MM5 was able to simulate the light and variable winds in the Sacramento and San Joaquin Valleys that prevailed duri
ng this event. Moreover, the winds responded quite well to the slowly changing synoptic-scale weather, as well, as confirmed by the observations.

The objectives for the San Jose State University (SJSU) work included use of SCOS97 data and MM5 simulations to understand meteorological factors in the formation of high ozone concentrations during 4-7 August 1997. Meteorological data for the case study included observations at 110 SCOS97 surface sites and upper air measurements from 12 rawinsonde and 26 RWP/RASS profilers. The MM5 version contained the PSU Marine Boundary Layer Initialization (MBLI) scheme, quadruple nested grids (horizontal resolutions of 135, 45, 15, and 5 km), 30 vertical layers, minimum sigma level of 46 m, USGS global land-use, GDAS global gridded model analyses and SSTs, analysis nudging, observational nudging, force-restore surface temperature, 1.5 order TKE, one-way continuous nesting, and a MAPS statistical evaluation. Analysis showed the ozone episode resulting from a unique combination of large-scale upper level synoptic forcings that included a weak local coastal 700 mb anticyclone. Its movement around SoCAB rotated the upper level synoptic background flow from its normal westerly onshore direction to a less common offshore easterly flow during the nighttime period preceding the episode. The resulting easterly upper level synoptic background winds influenced surface flow directions at inland sites, so that a surface frontal convergence zone resulted where the easterly flow met the westerly onshore sea breeze flow. The maximum inland penetration of the convergence zone was about to the San Gabriel Mountain peaks, the location of daytime maximum ozone-episode concen-trations. The current MM5 simulations reproduced the main qualitative features of the evolution of the diurnal sea breeze cycle in the SoCAB with reasonable accuracy. The position of the sea breeze front during its daytime inland penetration and nighttime retreat could be determined from the simulated wind fields. The accuracy of predicted MM5 surface winds and temperatures over SoCAB were improved by the modifications of its deep-soil temperatures, interpolation of predicted temperatures and winds to SCOS97 observational levels, use of

updated urban land-use patterns, and use of corrected input values for ocean and urban surface roughness parameter values.

Executive Summary

SJV Background: The primary objective of this study was to investigate the ability of the MM5 mesoscale model to simulate wintertime high-acid fog events in the San Joaquin Valley (SJV). Unlike fogs that form as a result of rain falling into sub-cloud layers or from stratus-cloud decks that expand downward to the surface, the acidic fogs of the SJV are mostly associated with surface cooling caused by long-wave radiation flux divergence (i.e., radiation fogs). An important motivation for the study of these fogs is that future studies are planned by the ARB with the intent of better understanding the formation of aerosols and acidic particulate matter in the Valley. In particular, it is important to learn if the MM5's physical parameterizations can reproduce the major characteristics of the fog events, including its formation, depth, dissipation and density (expressed as visibility), and the evolution of the weather pattern in which the fog forms.

SJV Methodology: For this work the MM5 was configured with four nested grids and a turbulence sub-model that explicitly predicts the profiles of turbulent kinetic energy (TKE). The model was applied for the event of 7-12 December 1995 that had been observed during the IMS-95 field program. This event was characterized by an frontal passage in the first 12 h, followed by the establishment of a cool moist Pacific air mass in the Sacramento and San Joaquin Valleys. Following the early dissipation of a marine stratus-cloud layer, fog formed at the surface through long-wave radiational cooling. Over the final four days of the case, the fog gradually thinned and acidic haze began to dominate the SJV. To simulate this complex event, the model's innermost domain used 40 vertical layers and a 4-km mesh. Five layers were placed in the lowest 108 m, with the first calculation level at 6 m above the ground. Several experiments were performed to improve the turbulence sub-model for saturated conditions and to provide more accurate initial conditions for soil temperature and moisture. Four-dimensional data assimilation (FDDA) was used only on the outer two (synoptic-scale) domains, which had 108- and 36-km resolution. Thus, the purpose of the FDDA was to improve the accuracy of the lateral boundary conditions applied to the innermost domains (12 and 4-km resolution), but it was not allowed to have any direct impact on the development of the fog.

SJV Results: The MM5's output fields were carefully compared to the observations reported by the NWS and to special radiosondes collected during the IMS-95 field program. Examination of the model fields showed that the MM5 correctly simulated the post-frontal stratus clouds that followed the cold front southwards through the Sacramento and San Joaquin Valleys in the first 12 h of the study period. As observed, the stratus deck in the model dissipated and was followed by the development overnight of ground-based radiation fog. A simple post-processing method was developed, based on the observations in the SJV, to diagnose fog, haze and clear air conditions from the model's dew-point depression. Using this diagnostic tool, it was clear that the model simulated the tendency for fog to become widespread overnight, while it partially dissipated in the daytime to leave haze in many areas. As the episode continued into its fourth and fifth days, the haze became more general in the model, with fog gradually ending, just as observed. The model was also able to simulate the increasing surface winds, and the warm and moist advection aloft that accompanied the approach of a new Pacific storm from the west. The increasing winds and growing dew-point depressions predicted by the MM5 were verified quite well by observations over all of CA and the eastern Pacific Ocean.

Statistical evaluation of the experiments showed that the MM5 correctly predicted the type of visibility obscuration (fog, haze, stratus, or clear) in 14 out of the 18 events. The fog depth was estimated by the MM5 with a mean absolute error of only 92 m and a mean error of -41 m. Mean errors for both the surface temperature and dew point were within +1 C, while the mean absolute errors were ~1.5-2.0 C. As a consequence, the mean error for dew-point depression is very small. This is especially important for the correct simulation of fog and haze.

SJV Conclusions: The principal conclusions are as follows. The MM5 is capable of simulating the evolution of fog and haze in the SJV with considerable accuracy. The model's simulated fields of temperature and dew-point depression are accurate enough to allow the type of obscuration to be diagnosed in most events. The MM5 also shows reasonably good skill in simulating the depth of the fog and haze layer, and whether or not it is topped by stratus. The extension of the TKE-simulating turbulence sub-model to include the effects of saturation on the buoyancy production of TKE was important for the simulation of fog characteristics. The very high vertical resolution used in these experiments also appears to be helpful for resolving the fog-and-haze-sensitive processes close to the ground. It learned that the model solutions for fog and haze are quite sensitive in this case to the specification of the deep-soil temperature and soil moisture. Finally, the MM5 was able to simulate the very light and variable winds in the Sacramento and San Joaquin Valleys in the post-frontal maritime polar air mass. The model appears to reproduce these light winds for the correct reasons. That is, the presence of a shallow, but strong inversion decouples the cool low-level air mass from the high-momentum flow above the level of the mountain ranges surrounding the Valleys. Throughout the episode, the winds in the MM5 responded quite well to the slowly changing synoptic-scale weather patterns, as well, as was confirmed by the observations.

Based on the results of the model experiments and evaluations, the following steps are recommended for future research. First, the objective approach developed here for diagnosing fog and haze is only a prototype. However, it would not be difficult to extend it by expanding the database over more observed cases. Additionally, the effects of other predictors can be included, such as the wind speed and age of the air mass. The result would be a more reliable, automated approach for objectively diagnosing fog and haze in wintertime over the entire model domain from the MM5 fields, even for situations for which an aerosol model is not available. Second, the specification of temporally constant fields for deep-soil temperature and moisture is unsatisfactory for multi-day episodes, especially in cases with significantly changing conditions. Therefore, it recommended that the TKE-predicting turbulence sub-model be coupled with a more sophisticated land-surface scheme that allows for a more realistic evolution of the soil temperature and moisture. The MM5 system already has at least one interactive land-surface sub-model available for use with several other boundary-layer schemes. It should not be difficult to adapt that sub-model for use with the turbulence scheme used in this investigation. Third, it is recommended that the algorithms developed and successfully applied in this study be used in new simulations for a larger number of cases.

SoCAB Background: The problem addressed by SJSU in this study is whether or not the surfce specifications of the current MM5 is fully adapted for the simulation of important meteorological conditions associated with poor air quality in the SoCAB during the summer. In particular, it is

important to learn if MM5 can reproduce the major characteristics of the sea breeze flow, including its formation, depth, and dissipation. It will be useful for the success of future investigations of air quality in the SoCAB if a selected meteorological modeling tool be extended, tested, and evaluated to ensure that accurate simulations are possible for these conditions. Previous SoCAB modeling studies were performed by 3-D models with constant boundary conditions, without nesting, and/or with simple PBL schemes. The current SJSU effort thus first involves an analysis of the meteorological conditions during a data-rich SCOS97 summer ozone episode, and then numerical simulations of the case by use of a sophisticated version of MM5 that combines analysis nudging and FDDA techniques. Objectives of the current study include use of SCOS97 data and MM5 simulations to understand meteorological factors in the formation of high ozone concentrations in the SoCAB. The period of 4-7 August was selected for study, as maximum SCOS97 surface ozone concentrations (187 pphm) were found during the afternoon of 5 August at 2200 UTC (1500 PDT), Pacific Daylight Time.

SoCAB Methodology: Rawinsonde and profiler data were vertically interpolated (by a linear scheme) to key AGL levels (e.g., within the sea breeze and synoptic flows). These values, and the hourly surface meteorological data, were then interpolated horizontally to a regular grid in the Lambert conformal space used for plotting MM5 output and then smoothed, and plotted in various planes. Horizontal plots were constructed based on observation levels near the surface (2 m for temperature and 6 m for wind) and at the predetermined key AGL levels. Rawinsonde and profiler time-height sections for selected sites for either the entire study period or for each day were plotted and contoured. Arbitrarily oriented vertical cross sections using profiler data were constructed for selected times. Sections present data in an MSL format that included a topography profile along straight lines running parallel and perpendicular to the SoCAB coast. Values were then contoured.

A series of six five-day simulations were carried out using an MM5 version that contained the PSU Marine Boundary Layer Initialization (MBLI) scheme, quadruple nested grids (horizontal resolutions of 135, 45, 15, and 5 km), 30 vertical layers, minimum sigma level of 46 m, USGS global land-use, GDAS global gridded model analyses and SSTs, analysis nudging, observational nudging, force-restore surface temperature, 1.5 order TKE, one-way continuous nesting, and a statistical evaluation package.

SoCAB Results: Analysis showed that the 3-7 August ozone episode resulted from a rare combination of large-scale upper level synoptic forcings. A weak local coastal 700 mb anticyclone first moved from a position on the central SoCAB coast to a position at the southern SoCAB coast, and then to a position at the northern SoCAB coast. The latter movement resulted in a rotation of the upper level (> 3000 m MSL) synoptic back-ground flow from its normal westerly onshore direction to a less common offshore easterly flow during the nighttime period preceding the ozone episode. The offshore movement of the high also produced a warming aloft and at the surface on the episode day, as well as a sinking and strengthening of the associated elevated subsidence in-version over SoCAB. The resulting easterly upper level synoptic background winds influenced surface wind flow directions at inland sites, so that a surface frontal convergence zone resulted where the easterly flow met the inland moving westerly onshore sea breeze flow. The maximum inland penetration of the convergence zone was about

to the San Gabriel Mountain peaks, the location of daytime maximum ozone-episode concentrations.

The current MM5 simulations reproduced the main qualitative features of the evolution of the diurnal sea breeze cycle in the SoCAB with reasonable accuracy. The position of the sea breeze front during its daytime inland penetration and nighttime retreat could be determined from the simulated wind fields. In particular, MM5 showed reasonable skill in the simulation of the diurnal variation of coastal temperature gradients that produce the diurnal sea breeze cycle, opposing easterly flow, inland movement of the sea breeze front, retreat of land breeze front, and spatial wind velocity distributions.

The accuracy of predicted MM5 surface winds and temperatures over SoCAB were improved in the current simulations by the following sequential modifications of MM5 and/or its input parameters: use of the PSU MBLI scheme, use of the Gayno-Seaman turbulence scheme, analysis nudging with NCAR GDAS model output, a new specification of deep-soil temperatures, interpolation of predicted MM5 temperatures and winds to SCOS97 observational levels, observational nudging with SCOS97 surface and upper level coarse RWP and rawinsonde winds and RASS temperatures, use of updated urban land-use patterns, use of corrected input surface roughness parameter values for ocean and urban areas, and proper limitation of MM5 diagnosed mixing depth values. The current MM5 simulations were less successful in the reproduction of some quantitative aspects of the diurnal evolution of the SoCAB sea breeze cycle, including the low-speed nighttime wind speeds (1 ms^{-1} observed versus 3 ms^{-1} predicted), and the times (shifted by about two hours) and magnitudes of some sea and land breeze frontal wind shifts.

SoCAB Conclusions: Although the evaluations of the SCOS97 observations and MM5 model results indicate mostly positive results, it is clear that a complete understanding of the meteorology of the 3-7 August ozone episode requires additional data analysis and model simulations. Now that higher QA-level SCOS97 upper air data sets will be available, additional analyses of the episode should be carried out to refine our understanding of the complex interactions between the upper level synoptic and surface mesoscale meteorological forcings that produced it. A review of the NCAR Reanalysis large-scale model wind fields for this SCOS97 case revealed that its upper level nighttime winds were lower than those in the currently used NCAR GDAS. It thus might be useful to carry out a simulation with Reanalysis model fields instead, to see if this would reduce the current nighttime over predicted wind speeds. As the current simulations show an increase in over-predicted nighttime wind speeds when SCOS97 upper air winds were used in the observational nudging scheme, it would be useful to carry out a simulation with a reduced vertical nudging coefficient. This change would reduce impacts from upper level high-speed layers on over-predicted nighttime surface speeds. As the MM5 configuration for an optimum SoCAB sea breeze simulation involves several important formulation and input choices, a series of parametric MM5 simulations (in which only one input parameter is systematically varied in each run) should be carried out to determine the optimum combination of: first vertical grid spacing (perhaps the 6 m value used in the current SJV study), westward movement of the Domain 4 lateral boundary position, reduced Domain 4 horizontal grid spacing (to perhaps 1.67 km), updated land use boundaries and parameters, and better determined deep soil temperature. The Blackadar turbulence scheme in MM5 should be tested

against the currently used TKE scheme, and vertical TKE cross sections should be plotted, as should computed and observed wind and temperature soundings. The proposed simulations will build upon the understanding and results obtained to date from the current effort. A more complete understanding will allow for a more accurate simulation of the complex meteorological conditions producing the 3-7 August 1997 ozone episode, and those results will allow for more accurate air quality simulations.

1. INTRODUCTION

1.1. Background

The current project encompassed in Contract 97-310 from the California Air Resources Board (CARB, where all acronyms are listed in the Appendix) was originally designed to address a number of perceived weaknesses and areas of unknown performance skill in the Penn State University/National Center for Atmospheric Research (PSU/NCAR) Mesoscale Model, widely known as MM5 (Dudhia 1993, Grell et al. 1994). This three-dimensional (3-D) meteorological model, dedicated to the public domain by its developing institutions, is based on the nonhydrostatic primitive equations for atmospheric flow and is designed for general applications in atmospheric research and forecasting.

Over the past decade, MM5 has been used in studies to investigate conditions over California during poor air quality episodes. For example, it was applied by Seaman et al. (1995) to represent meteorological conditions in the San Joaquin Valley (SJV) during two 1990 summer episodes for which special observations were collected for the SJV Air Quality Study (SJVAQS) and Atmospheric Utility Signatures, Predictions, and Experiments (AUSPEX). Subsequently, meteorological numerical modeling was conducted under the direction of the SJVAQS/AUSPEX Regional Modeling Adaptation Project (SARMAP) sponsored by the SJV-wide Air Pollution Study Agency (Seaman and Stauffer 1996, Seaman et al. 1995). Later, under Contract No. 94-730 from CARB, MM5 was used to study wind flow and mixed-layer depth in the Los Angeles Basin during the 1987 Southern California Air Quality Study (SCAQS) (Seaman and Stauffer 1998). This study was used to help design the distribution of measurement sites in the Basin in preparation for the 1997 summertime Southern California Ozone Study (SCOS97) (Stauffer et al. 2000a, Tanrikulu et al. 2000).

These studies showed that the MM5, especially with the assistance of four-dimensional data assimilation (FDDA), could reproduce observed mixing depth and boundary layer winds with considerable accuracy. In the SJV, the model also simulated the nocturnal low-level jet and the Fresno Eddy, along with several other well-observed mesoscale circulations. In the Los Angeles Basin, although boundary layer depth was represented rather well during the October SCAQS episode, it was recognized that improvement of the simulated evolution of boundary layer winds could benefit future air quality studies performed with MM5. In particular, the mid-level return branch of the mesoscale flow that re-circulates air from the Basin to areas over the Ocean was found to be too weak and intermittent.

Another concern was related to the fact that these earlier studies were conducted for high-ozone periods observed during the warm season. However, in California, cases having high concentrations of pollutants can occur in the wintertime, as well. For example, highly acidic fogs and aerosols can form during foggy episodes in the SJV. These acid fogs occur in a season when photochemistry is relatively unimportant, but their simulation is more dependent on the correct handling of moist processes that are mostly missing from summer episodes. Therefore, it was believed that MM5 must be tested and evaluated specifically for its ability to simulate moist processes associated with SJV fog cases.

Based on concerns raised following the earlier MM5 studies, CARB requested that Project No. 97-310 be developed with the following *three objectives*. First, experimentation was to be performed with the MM5 to further test and, if need be, improve its performance for simulating the diurnal *evolution of the complex boundary-layer winds in the South Coast Air Basin (SoCAB)*. These re-circulation patterns, of special interest for pollution transport, are driven mostly by a combination of the sea breeze and orographic forcings. Second, it was requested that the ability of MM5 to simulate *wintertime fog in the* SJV be examined. Third, it was requested that the ability of MM5 to simulate *summertime coastal fog in the* SoCAB be also examined. An important motivation for the study of fog is that future studies are planned by CARB with the intent of better understanding the formation of aerosols and particulates in the Valley. The formation of these aerosols is strongly influenced by moist chemistry processes acting in the stable valley fogs that are common in the winter months. Thus, a need exists need for a specialized study on this subject.

Under CARB Contract No. 97-310, the first objective was pursed by San Jose State University (SJSU), with the second and third pursed by PSU. This final report thus focuses on the PSU study of MM5 wintertime fog predictability and on the SJSU study of SoCAB sea breeze flows.

1.2 Wintertime Climatology and Formation of Particulate Matter in SJV

MM5 contains a 1.5-order turbulence parameterization that was proposed by PSU as potentially helpful for the simulation of fog (Gayno 1994, Gayno et al. 1994). Although this parameterization had been tested in a variety of cases over other parts of the U.S., the unusual topography of the SJV presents a new and unique environment in which the simulation of fog characteristics may be difficult. Some fog cases are strongly cyclic, with fog patches forming at night and burning off during the day. In other cases, the fog may be more widespread and persistent. In these latter cases, the topography of the SJV becomes more important. For example, the mountain ranges surrounding the SJV often lead to trapping of low-level air in the valley following the passage of a wintertime cold front.

Rain accompanying the frontal system moistens the soil, increasing surface evaporation and maintaining high humidity. Long wave radiation from fog or clouds leads to additional cooling and stagnation of the air mass. Thus, the fog may deepen over time, sometimes becoming nearly 1000 m in depth. Although visibility may become less or greater with the diurnal cycle, these stagnant foggy conditions can persist for days during which there can be a steady build-up of pollutants. The moist conditions foster aqueous chemical reactions in the fog droplets, and when these evaporate, they leave behind a thick acidic haze of secondary, potentially harmful pollutants. Consequently, the ability of a numerical model to reproduce the complex interplay of orography, radiation, and moist boundary-layer processes during these post-frontal synoptic conditions is of great interest. In particular, it is important to learn if the model's 1.5-order turbulence parameterization can simulate the timing, extent, and depth of these persistent SJV fogs.

The meteorology associated with fog formation, especially in the SJV, deserves a more complete review before proceeding. Technically, fog is a stratus cloud at the ground. However, fog also can involve some complex phenomena unique to the boundary layer. It can form in a variety of

ways, either (1) when low-level air cools to its dew point, or (2) if initially unsaturated air becomes saturated by the evaporation of water into it. Examples of the former include radiation fog, upslope-advection fog, and advection of moist air over a cold surface. Examples of the latter occur due to evaporation from the surface or from warm rainfall falling into cool air behind an advancing cold front.

As discussed by Gayno (1994) radiation fog is a result of nocturnal cooling of air near the surface. In mid-latitude regions, it is most common in the fall or winter, when nights increase in length. Initially, radiation fog forms as patches where the coldest air collects in low points over irregular terrain. Eventually, as the cold air deepens, the fog fills in to become a continuous layer. Fog can have an emissivity approaching 1.0, whereas the surface emissivity may range from 0.88 to 0.98 for typical soils and vegetation. Thus, enhanced longwave-radiation loss from the fog top becomes an important factor that can accelerate cooling and contribute to deepening of the fog layer. Because most radiation fogs remain less than 100 m in depth, they typically dissipate a few hours after sunrise, when enough sunlight reaches the ground to warm the air above its dew point.

Turbulent mixing is a critical element for the formation of most fogs, especially radiation fog. Nocturnal boundary layers tend to grow in depth as shear-induced turbulent mixing transfers heat from potentially warmer layers aloft downward toward the cooler ground. Therefore, for conditions of moderate shear, light surface winds and turbulent mixing are helpful to accelerate the cooling aloft and to increase the depth of a fog layer. If the mean wind is too strong, however, intense turbulent mixing will prevent the formation of a temperature inversion and the fog. The intense mixing will efficiently transport moisture upward, thereby hindering fog formation and promoting the development of a low-lying stratus deck instead. These turbulently generated stratus clouds are often observed behind cold fronts. On the other hand, if the nocturnal boundary layer is very stable and calm, shear-induced turbulence will be minimal. In such conditions, only the air within several meters of the ground may be able to cool to its dew point, resulting in patchy ground fog that dissipates quickly following sunrise (Gayno 1994).

In the SJV fog is common in winter, because seasonal rains, which occur with the passage of cold fronts, raise soil moisture levels, while stable maritime polar air masses frequently invade the Valley behind the fronts. These maritime polar air masses are cold high-pressure systems originating over the North Pacific Ocean. The unique topography of the SJV and Sacramento Valley (Fig. 1a) favor air stagnation in these cases, especially when the subsidence inversion is lower than the height of the Coast Ranges to the west (about 1 km above ground level, AGL). Then, the only outlet for the trapped air is through the Sacramento Delta region. The long wintertime nights lead to strong outgoing long wave radiation, which cools the stagnant surface air and leads to the formation of stratus and/or fog.

A study by Holets and Swanson (1981) documented the principal characteristics of the major post-frontal fog episodes occurring in the central California valleys from 1954 to 1980. These so-called "high-inversion" fog events lasted up to 13 days, and in many cases failed to burn off during the day. They have also been referred to as "Tule fogs" by Gilliam (1970). Typically, stratus clouds first formed following the passage of a cold front and arrival of a maritime polar air mass. In this early stage, it is likely that wind shear still is fairly large, so that low-level

turbulent mixing is quite strong. As discussed by Gayno (1994), these conditions favor upward transport of water vapor from the moist surface, so that stratus forms instead of fog.

Once the high-pressure systems become well established, however, geostrophic winds and vertical shear decrease, and a strong subsidence inversion usually settles into the Valley (the mean inversion height is between about 200-700 m AGL). In these cases solid stratus decks prevent much of the solar energy from reaching the surface, while long-wave radiative flux divergence rapidly cools the top of the stratus layer. This cooling induces turbulent mixing and a gradual downward thickening of the cloud layer until it fills the entire sub-inversion layer, becoming a deep spatially extensive fog. Mean surface wind speeds during these fog events are about 1-2 m s^{-1}, but are sometimes only 0.5 m s^{-1}. Mean diurnal visibility is about 3 km, with daily minimum visibility (usually during the night or early morning) around 1 km or less. Holets and Swanson (1981) report that, once the fog layer forms it tends to persist until a major change occurs in the synoptic pattern.

Note that these high-inversion fogs are distinct from the normal description of a radiation fog. The latter builds upward from the surface as a nocturnal surface inversion forms and grows, but usually does not exceed 100-200 m in depth. On the other hand, the SJV inversion fog builds downward from the stratus deck. In the SJV, if the maritime polar air mass is too dry for stratus to form, then two inversions may be present: (1) the subsidence inversion and (2) a surface-based radiation inversion.

Fog episodes in the SJV, having very high concentrations of secondary aerosols and particulates, are less likely to have thick fog layers that persist through the diurnal period (S. Tanrikulu, CARB, personal communication). Continuous thick fogs can lead to comparatively rapid wet deposition of soluble species due to settling of the large fog droplets. If, on the other hand, the droplets mostly evaporate during the day due to insolation or stronger mixing than is typical in the classic high-inversion events described by Holets and Swanson, then the smaller aerosol particulates can remain suspended for longer periods. In such cases, the particulates can be recycled into fogs on the following evenings, while fresh emissions add to the pollutant concentrations. Thus, these "high-acid fogs" (aerosols and particulates in the SJV have high concentrations of nitrate and sulfate) tend to be more shallow and patchy than those discussed by Holets and Swanson. They are also more likely to form as radiation fogs, rather than downward-building stratus.

Pandis and Seinfeld (1989) reported typical liquid water contents in high-acid fog events of about 0.25 g m^{-3}. Peak liquid water deposition rates were about 25 g m^{-2} h^{-1}, falling to zero during afternoons when the fog had dissipated at the surface. In some cases, fog conditions can be associated with aged Great Basin high-pressure systems, rather than recently arrived maritime polar air masses from the Pacific Ocean.

1.3 Summertime Climatology and Formation of Sea Breeze Flows in SoCAB

Ozone is a difficult secondary tropospheric pollutant to control, and the U. S. area generally with the most severe problem is the SoCAB area of California in summer. Peak SoCAB ozone concentrations arise from a combination of extensive precursor emissions, mountain ranges on

three sides of the Basin, complex photochemical processes, and complex meteorological patterns that involve General Circulation (GC) and mesoscale (i.e., coastal, topographic, and urban) factors.

The SoCAB lies in the coastal plain between the Pacific Ocean to the west and the surrounding high terrain (maximum elevations of 3000 m) on its northern, eastern, and southern edges (Fig. 1b). The Santa Monica and San Gabriel Mountains form the northern edge of the Basin, the San Bernardino and San Jacinto mountains its eastern boundary, and the Santa Ana Mountains are southeast of the Basin.

The Basin is divided into western and eastern halves by the Puente Hills at its northern end and the Santa Ana Mountains at its southern edge. Both the western and eastern basins are essentially flat, with the eastern basin about 250 m higher. Terrain channeling affects the typical daytime sea-breeze flows, particularly between the Puente Hills and San Gabriel Mountains and at the southern entrance to the San Fernando Valley (Glendening 1990).

During summer, the GC Pacific High is located offshore north of the basin, and it acts to deflect rain producing storms northward, producing a dry summer climate in the area. Subsidence from the High produces warm, dry air, which caps cool moist air near the surface, creating a marine boundary layer (MBL). The resulting elevated subsidence temperature inversion layer is stable and generally prevents the vertical diffusion of polluted moist air. Onshore airflow from the High produces the cold southward flowing California ocean current by upwelling, when cold deep water is brought to the surface. When moist marine air from the High flows onshore over this cold water, it cools and produces coastal fog and/or stratus clouds.

The fog-stratus layer evaporates before it penetrates far into the SoCAB, consistent with inland daytime temperatures that are much higher than coast values. The high temperatures create a thermal low-pressure system, and resulting daytime pressure differences between coastal and inland areas create a cool onshore mesoscale sea breeze flow that augments the normally onshore flow from the GC Westerlies. This flow is further augmented by inland directed, thermally driven upslope flows associated with the ringing mountain ranges. During nighttime hours, land surfaces cool more quickly than the sea, and thus air over the land becomes cooler than over the sea. This reversed temperature difference produces an offshore mesoscale land breeze flow that reverses the normal west to east flow of the GC Westerlies. This flow is also augmented by a seaward directed, downslope flow from the ringing mountain ranges.

During many daytime periods, when the inland flow hits the ringing mountains, a recirculation develops aloft, in which the flow is opposite in direction to the onshore sea breeze flow below (Wakimoto and McElroy 1986). Surface ozone and particulate matter (PM) carried aloft in such flows can produce elevated pollutant layers, which then sequentially: decouple from surface polluted layers during the evening transition period (when the turbulent boundary layer collapses), persist throughout the nighttime stable period, and then are fumigated to the surface during the morning transition period. Such effects have also been observed over Tokyo (Wakamatsu et al. 1983), Athens (Lalas et al. 1983), and Lake Michigan (Fitzner et al. 1989). The daytime onshore flow can rise over the mountains and thus blow further inland (Wakimoto

and McElroy 1986), as convective heating of air over the slopes can raise the inversion to produce a chimney effect that allows polluted air to exit the Basin.

Pollutant concentrations in the SoCAB thus vary significantly in time and space. A large fraction of primary pollutants (from traffic and industrial sources) are emitted in the western region of the Basin during morning rush hours. Peak surface ozone concentrations are, however, mostly found during afternoon hours in the eastern part of the basin, due to ongoing photochemical reactions during eastward advection by the sea breeze flow. Measured vertical concentration profiles of ozone often show maximum values within the elevated stable layer, rather than at the surface (Lu and Turco 1996). During late afternoon hours, these layers blanket the entire western basin, while by evening they extend over the eastern basin as well (due to return flows aloft), albeit at lower concentrations (Wakimoto and McElroy 1986).

Field measurement campaigns have yielded an increased understanding of the mesoscale flow patterns critical for SoCAB ozone episodes. Airborne downward-looking lidar data were collected by over the SoCAB during the summer of 1982 (McElroy et al. 1983). Analysis by McElroy and Smith (1986) showed that the two or more distinct offshore aerosol layers were eliminated a short distance inland by afternoon heating and mechanical turbulence.

The August 1984 Project BASIN (Basic Studies on Airflow, Smog, and Inversions) included enhanced surface and upper air monitoring. Analysis by Wakimoto (1987) found that the offshore atmospheric cyclonic Catalina Eddy was thermally and topographically induced, and that it resulted in deepened MBLs. Associated transport patterns reduced ozone concentrations at Glendora, but increased values northeast of Los Angeles.

The primary objective of the autumn 1985 SCCCAMP (South-Central Coast Cooperative Aerometric Monitoring Program) was detailed meteorological and ozone concentration databases for use in air quality models of offshore oil and gas activities in the Santa Barbara channel. Analysis by Scire and Chang (1991) showed high ozone concentrations in Santa Barbara related to the simultaneous occurrence of high 850 mb temperatures (reflecting subsidence and thus limited mixing) and pressure gradients consistent with moderate easterly or southerly synoptic flow. The first of these relationships was previously noted by Smith (1984) and Moore and Reynolds (1986), while the second had been found by Smith and Lehrman (1987).

SCCCAMP data were used by McElroy and Smith (1991) to study MBL structure, whose shallow offshore depth ranged from 100-200 m. The sharp boundary surface between this layer and the heated land-surface convective layer resembled a cold front, across which mixing layer thickness increased to 1800 m. Moore et al. (1991) used SCCCAMP wind trajectories to show that most ozone exceedances in Ventura and Santa Barbara Counties resulted from westerly or northerly transport of Los Angeles air. Inter-comparison by Baxter (1991) of mixing height values (determined from lidar, rawinsonde, doppler acoustic radar, and aircraft data) showed that while doppler radar were generally the most accurate, rawinsondes were more useful in the surface boundary layer (SBL), the atmospheric layer below 50m AGL. Aircraft soundings were useful, only when they penetrated the SBL. The extensive 1987 SCAQS was conducted during 11 summer and six fall days (Lawson 1990). Observations generally showed mid-afternoon peak

ozone concentrations, with those on 27 August at Riverside reaching 240 ppb at 1500 PST (Lu et al. 1997).

The vertical observational components of the summertime SCOS97 were the most complete and intensive ever undertaken in the SoCAB, as they contained 12 rawinsode and 26 profiler sites. It was hoped that this data set would allow for an analysis of the early morning fumigation of ozone trapped in the residual return flow layer aloft. Preliminary results and Quality Control (QA) efforts on its vast database were discussed at a recent workshop (CARB 2001).

While the above observational studies have provided a general understanding of the complex meteorological and chemical processes producing high ozone concentrations in the SoCAB, 3-D mesoscale meteorological modeling studies using these various databases have provided additional details. A summary of many of them is given in Tables 1a,b. Ulrickson and Mass (1990a) used the prognostic hydrostatic Colorado State University Mesoscale Model (CSUMM) to simulate summertime flows in SoCAB. Simulated daytime onshore, upslope winds were generally more accurately reproduced than were nighttime low speed, spatially variable wind patterns. Output meteorological fields from additional winter and summer simulations by Ulrickson and Mass (1990b) were input into a pollution trajectory model, which showed entrainment and upward motion producing planetary boundary layer (PBL) growth that mixed pollutants into the elevated subsidence inversion layer.

The mass-consistent wind model of Douglas and Kessler (1991) used SCCCAMP data to analyze SoCAB mesoscale flow patterns associated with the Catalina Eddy, but such diagnostic models cannot correctly reproduce its evolution in conjunction with the limited number of observations. While results were better with the prognostic CSUMM (Kessler and Douglas 1991), off shore area winds were sometimes overestimated, as the uniform CSUMM initial wind fields could not include many large-scale details. Taha (1997) also used CSUMM to simulate effects from urban-induced albedo increases on SoCAB flow patterns, with results input into the photochemical Urban Airshed Model (UAM). Results showed that increased albedo sequentially: lowers surface temperatures and mixing depths; affects emission and reaction rates; but finally produces reduced peak ozone concentrations.

Mesometeorolgical output from the hydrostatic UCLA model was input into a passive tracer model by Lu and Turco (1995) to simulate typical summertime SoCAB pollution transport. The models qualitatively reproduced many observed features of the polluted MBL over the Basin, such as the San Fernando convergence zone that lifts pollutants into the elevated inversion. This resulted in a residual elevated reservoir of daytime polluted air that survived throughout the night.

Hegarty et al. (1998) used MM5 to simulate SCAQS data with: two way nesting in three domains, Blackadar (1979) PBL scheme, initial conditions from ECMWF-TOGA analyses, and five-day averaged U. S. Navy sea surface temperatures (SSTs). Predictions after 48 hours were not accurate, however, due to a lack of analysis nudging. Stauffer at al. (2000b) also simulated a six-day high SCAQS ozone period using MM5 with: three nested domains; two-way interaction between the outer two domains, one-way nesting between the two inner domains, and FDDA in the two outer domains. Although general agreement exists with the observations, model under-

estimation of afternoon over-land wind maxima by 1-2 m s^{-1} was attributed to the coarse NCEP SST analyses that produced too warm values.

1.4 Statement of Problem

The above discussion of the local meteorology associated with SJV high-acid fog episodes and the unknown ability of the MM5 numerical model for simulating them can be summarized into a statement of the problem to be addressed by PSU in this study. That is, that the physical parameterizations of the current MM5 may or may not be fully adapted for the simulation of these important meteorological conditions associated with poor winter air quality in central California. In particular, it is important to learn if MM5 can reproduce the major characteristics of SJV fog, including its formation, depth, dissipation, and density (expressed as visibility and/or liquid water content). It is imperative for the success of future investigations of air quality in the SJV that the meteorological modeling tool, MM5, be extended, tested, and evaluated to ensure that accurate simulations are possible for these conditions.

The above discussion of the local meteorology associated with SoCAB ozone episodes and the still incomplete ability of MM5 to simulate them can also be summarized into a statement of the problem to be addressed by SJSU in this study. That is, that the surface specifications of the current MM5 may or may not be fully adapted for the simulation of the important summer meteorological conditions associated with poor air quality in the SoCAB. In particular, it is important to learn if MM5 can reproduce the major characteristics of the sea breeze flow, including its formation, depth, and dissipation. It is imperative for the success of future investigations of air quality in the SoCAB that the meteorological modeling tool, MM5, be extended, tested, and evaluated to ensure that accurate simulations are possible for these conditions. Previous SoCAB modeling studies were performed by 3-D models with constant boundary conditions, without nesting, and/or with simple PBL schemes. The current SJSU effort thus first involves an analysis of the meteorological conditions during a data-rich SCOS97 summer ozone episode, and then numerical simulations of the case by use of a sophisticated version of MM5 that combines analysis nudging and FDDA techniques.

1.5 Report Organization

Section 2 of this report describes the MM5 numerical modeling system used in the SJV fog-and SoCAB sea breeze simulation studies. Section 3 describes the design of the PSU SJV numerical fog experiments. Section 4 gives an overview (based on available observations) of the SJV fog case of 7-12 December 1995, with results (including evaluation of the most critical modeled fields) from the experiments described in Section 5.

Section 6 describes the design of the SJSU SCOS97 numerical sea breeze experiments. Section 7 gives an overview (again based on available observations) of the SCOS97 sea breeze case of 2-7 August 1997, with results (again including evaluation of the most critical modeled fields) from these experiments described in Section 8. Finally, Section 9 summarizes the conclusions of both the SJV and SoCAB numerical studies, along with suggestions for future research.

An appendix to this report is currently in preparation in the form of a PSU SoCAB simulation of a sea breeze episode in which the new fog algorithms are applied to a sea breeze flow case in which coastal fog is an important factor.

2. METEOROLOGICAL MODELING SYSTEM

2.1 PSU/NCAR MM5 Model

The model used for this study of fog in the SJV is the non-hydrostatic 3-D PSU/NCAR mesoscale model (Dudhia 1993), widely known as MM5, Version 2. This model, and its pre-and post-processors, have been described in detail by Grell et al. (1994) and Haagenson et al. (1994), and hence only an abbreviated description is provided here.

Briefly, the model uses the terrain following "σ" vertical coordinate (non-dimensional zed pressure) and a split semi-implicit temporal integration scheme. The terrain following vertical coordinates are an advantage for applications in areas having steep terrain, such as are common in California. The split-semi-implicit time integration allows for the use of relatively long time steps for advective terms [usually the time step Δt is set to $3 * \Delta x(km)$]. Meanwhile, those terms of the primitive equations responsible for the propagation of sound waves and fast gravity waves are treated with much shorter time steps. Prognostic primitive equations are used to predict the three wind components (u, v, and w), temperature (T), water-vapor mixing-ratio (q_v), and perturbation pressure (p') in three dimensions. Perturbation pressure is the departure from a temporally invariant and hydrostatically balanced reference-state pressure (p^*), so that the total pressure at any location on the 3-D grid is given by

$$p(x, y, \sigma, t) = p^*(x, y, \sigma) + p'(x, y, \sigma, t) .$$

Use of the constant reference-state pressure increases the accuracy of gradient calculations in the vicinity of steep terrain and ensures that the location of the σ levels does not change during the model integration. MM5 has the capability for defining up to 10 different nested-grid domains at a time, with a 3:1 mesh ratio between successive nested grids. Otherwise, the horizontal and vertical resolutions of the model are arbitrary. The exchange of information between domains and grid interfaces can be chosen as either one- or two-way interactive.

For this study, turbulent processes and mixed-layer depth are represented in most experiments using a type of Mellor-Yamada (1974) 1.5-order parameterization. Known in MM5 as Gayno-Seaman, it explicitly predicts the 3-Dfield of turbulent kinetic energy (TKE) (Gayno 1994, Shoran et al. 2000). Eddy diffusivity is diagnosed from the local TKE, while the boundary layer depth is diagnosed from the vertical profile of the TKE. In one additional SJV experiment, the Blackadar PBL parameterization is used (Zhang and Anthers 1982, Grell et al. 1994). The Blackadar PBL uses a non-local closure for convectively unstable conditions and a first-order closure for stable and neutral conditions.

A force-restore prognostic surface energy budget equation is used to predict the ground temperature (T_g) (Zhang and Anthers 1982). The surface physical properties (albedo, roughness length, moisture availability, emissivity, and thermal inertia) are defined as a function of land use for 14 categories via a look-up table (Grell et al. 1994), but for applications at fine resolutions over California, PSU added an additional category for orchards and vineyards (Seaman and Stauffer 1996).

Other important physical processes include precipitation and radiation. Resolved-scale precipitation is represented using a parameterization described by Dudhia (1989) that has explicit prognostic equations for suspended cloud water or cloud ice (q_c) and for rainwater or snow (q_r). In the Dudhia precipitation scheme, no mixed-phase precipitation or cloud states exist, and freezing occurs at an arbitrary temperature (defined as 0 C). Convective precipitation, although not important in the wintertime case investigated in this study, is represented using the Kain-Fritsch (1990) cumulus parameterization. Finally, the effects of long-wave and short-wave radiation at the surface and at all levels in a column are treated with a single broad-band two-stream radiation parameterization (Dudhia 1989).

The code of MM5 is written in Fortran 90 and Fortran 77, and its structure is highly modularized, so that physical parameterizations can be easily exchanged. All parameterizations discussed above are found in the official supported public-release version of MM5 (available through the NCAR Mesoscale and Microscale Meteorology Division), and several options exist for each parameterization type. The model is easily ported to a variety of supercomputers, workstations, and PCs, and a parallelized version of the code is available for use on distributed-memory massively parallelized computers.

2.2 FDDA System

The FDDA technique used in this study is based on the Newtonian relaxation approach, or nudging, described by Stauffer and Seaman (1990) and Seaman et al. (1995). Nudging is a continuous form of FDDA that relaxes the model state toward the observed state by adding to one or more of the prognostic equations artificial tendency terms based on the difference between the two states. It is said to be continuous because the nudging term is applied at every time step, thereby minimizing "shock" to the model solutions that may occur in intermittent assimilation schemes. In this study the analysis nudging approach described by Stauffer and Seaman (1990) and modified by Shoran et al. (2000) is also applied. In analysis nudging, the assimilation uses 3-D gridded analyses based on synoptic observations (see Sec. 2.3), which are interpolated to the model's current time step. The alternative nudging approach developed by Stauffer and Seaman (1994) is not included in the present PSU SJV study because there were not sufficient special observations in the Valley during the study period to warrant its use. It is, however, used in the SJSU SoCAB study in conjunction with the SCOS97 data set. The modification introduced by Shoran et al. (2000) to FDDA prevents application of analyses below an arbitrary level (1.5 km AGL in these cases) to avoid weakening mesoscale features generated in response to lower-boundary forcing. Such features, such as low-level jets and channeling around orography, are not defined well by the synoptic upper-air observing network, but can be simulated by MM5, are thus not inadvertently smoothed out of the model solutions.

Clearly, retention of the analysis nudging above 1.5 km directly influences the model solutions in the mid and upper layers of the atmosphere. However, it is important to note that by the analysis nudging to about 85 % of the atmospheric mass, the normal hydrostatic and gravity-wave adjustments naturally lead to similar adjustments below 1.5 km. Thus, the modified analysis-nudging strategy remains effective for reducing large-scale errors, such as phase speed errors in the deep synoptic-scale flow, through the entire model column. At the same time, it reduces the potential for detrimental interference with the model's physical and orographic solutions close to the surface.

2.3 Initialization and Lateral Boundary Conditions

Initial conditions (ICs) and lateral boundary conditions (BCs) for MM5 are specified from large scale (108-km for the SJV study and 135 km for the SoCAB study) objective analyses performed on pressure levels at 12-h intervals (Benjamin and Seaman 1985). Over the data-sparse oceans the analyses are essentially those supplied through the first guess (background) fields obtained from archives of the global spectral analyses performed by the National Centers for Environmental Predictions (NCEP) for the Global Tropospheric Analysis (GDAS) by the Medium-Range Forecast (MRF) Model. Surface and upper-air observations used in the objective analyses are quality-inspected by MM5 pre-processors using automated gross-error checks and "buddy" checks. In addition, rawinsonde soundings undergo vertical consistency checks.

Following the objective analysis on pressure levels, the fields are interpolated vertically to model sigma levels to complete the ICs for the 108 or 135 km analysis domain. For the model's other three finer-resolution domains (see Sec. 3), the initial fields are obtained by interpolation from the 108 or 135 km analyses. SST and snow-cover analyses are obtained from NCEP and values are held constant for the duration of each experiment. In addition, based on satellite imagery and climatology, snow is assumed to exist on mountainous areas above 2600 m (~8000 ft).

Another initial field that must be defined for MM5 is the deep-soil temperature below the surface, T_m. It is nominally defined at ~25 cm depth, where the soil temperature is assumed to be approximately invariant between day and night. The value of T_m is calculated by the data preprocessor as the averaging of all of the 12-hour interval surface-layer temperature analyses (at 0000 and 1200 UTC) for the entire episode. This averaged T_m field is held constant through the model simulation.

A special characteristic of the PSU analysis scheme, not available in the standard NCAR pre-processors, is that low-level coastal temperature and moisture observations are not used uniformly in the onshore and offshore directions, because they are generally not representative of both regimes simultaneously. The analysis scheme used thus first analyzes the wind direction at stations within the coastal zone and determines whether onshore or offshore flow exists. The temperature and moisture data are then applied only in that portion of the standard area of influence around those coastal sites that lies upwind (i.e., either over land or ocean, depending on

wind direction). This approach is applied only in the lowest kilometer and can be important for preserving the low-level coastal gradients that characterize the near-shore zone of California.

Lateral boundary information is introduced into the model using the Davies and Turner (1977) relaxation technique. Relaxation is applied in the outermost five rows and columns of the outer (synoptic scale) domain (defined below in Sec. 3), with boundary values defined by interpolation between successive 12-h analyses of the same type used to define ICs. This approach gradually and continuously imposes the observed state at boundaries without generating large imbalances between the observed and modeled states. One-way interface conditions are used in this study between the 36-km domain and the 12-km domain, and also between the 12-km and 4-km domains (and on the 45, 15, and 5 km inner domains in the SoCAB study), so the values of the prognostic variables at the interior interfaces are supplied from the next coarser grid. No feedback of information is allowed from the finer grids to the coarser grids in these domains. However, two-way grid nesting is used between the 108-km and 36-km domains, which are run simultaneously.

2.4 Extension of the 1.5-order Turbulence Scheme for Moist Processes

Ensemble-averaged turbulence sub-models (or, parameterizations) that include a prognostic equation for TKE must account for differences in the buoyant production (BP) of TKE in saturated and non-saturated conditions (Munoz et al. (2000). In fact, this same requirement applies for all ensemble-averaged turbulence sub-models used in mesoscale models, such as first-order schemes and non-local mixing schemes. Unfortunately, a survey of several well-known models in widespread use today reveals that many current turbulence sub-models do not account for the effects of saturation on the generation of turbulence. An example is the Blackadar PBL parameterization of MM5 (Grell et al. 1994, Zhang and Anthers 1982). One result of the absence of this saturation effect is the development of dry-adiabatic or other absolutely unstable profiles in saturated layers (Stauffer et al. 2000). This can be a very damaging circumstance for a model that is applied to cases involving the formation of fog because vertical mixing and correct representation of thermal profiles in saturated layers are important components of fog formation and evolution (see Sec. 1.2).

The expression for BP of TKE in fully saturated layers was derived in the 1970s (e.g., Someria and Deardorff 1977). As described in Shoran et al. (2000), the Gayno-Seaman turbulence sub-model includes a prognostic equation for TKE, comprised of source and sink terms due to buoyancy, shear, transport and dissipation. In this scheme, the MM5 temperature and moisture fields are first transformed into variables that are conservative during condensation and evaporation processes. The TKE sub-model converts the potential temperature (θ), water vapor mixing ratio (q_v), and liquid water mixing ratio (q_l) into liquid water potential temperature (θ_l) and total water mixing ratio (q_t), following Betts (1973) and given by

$$\theta_l = \theta - \frac{\theta}{T}\frac{L_{lv}}{c_p} q_l \qquad (1)$$

$$q_t = q_v + q_l \quad , \tag{2}$$

where L_{lv} is the latent heat of vaporization and c_p is the specific heat at constant pressure. The turbulence calculations for TKE and the vertical mixing are then performed on the liquid water potential temperature and total-water mixing ratio. Finally, the θ_l and q_t fields are converted back to the native MM5 variables at the end of the time step.

Implementation of the vertical mixing using conservative variables helps to somewhat reduce the possibility of model generated unrealistic thermal profiles in saturated layers. However, moist-adiabatic profiles in cloud layers are still not assured in the Gayno-Seaman sub-model because the buoyancy production term in the TKE equation was based on the standard eddy-diffusivity formulation for the virtual potential temperature flux, and this formulation is valid only in a cloud-free environment. Following Deardorff (1972), Stauffer et al. (2000b) implemented an alternative formulation for the buoyancy production of TKE in saturated layers in terms of the conservative variables defined by (1) and (2).

Because the TKE is defined at the full MM5 layers (at the boundaries of the layers where the temperature and moisture fields are defined), a problem occurs when computing the buoyancy production at a vertical boundary between saturated and unsaturated air. Neither formulation for buoyant production of TKE is strictly correct in this boundary region. They decided to use the dry formulation in boundary zones (that is at the top and bottom of saturated zones) based on experimental results using both methods. Stauffer et al. (2000b) also reformulated the dissipation of TKE to include moisture effects in saturated layers in the stability parameter, N^2, the Brunt-Vaisala frequency. The computation of the Blackadar length scale used in the dissipation was also redesigned to better represent the vertical turbulent scales in saturated and unsaturated layers, based on the TKE profile and local minima.

Another limitation of the original version of the TKE sub-model described by Shoran et al. (2000) is that cloud ice cannot be treated properly using liquid water potential temperature and total water defined by (1) and (2). Therefore, Stauffer et al. (2000b) replaced θ_l in the scheme by an ice-liquid water potential temperature, θ_{il}, as described by Tripoli and Cotton (1981).

$$\theta_{il} = \theta\left[1 - \frac{L_{lv} q_l}{c_p \max(T,253.0)} - \frac{L_{iv} q_i}{c_p \max(T,253.0)}\right] \quad , \tag{3}$$

where all symbols are as above, q_i is the cloud ice mixing ratio, L_{iv} is the latent heat for ice-vapor phase changes, and the $\max(T,253.0)$ is an empirical correction that improves diagnosis of θ from θ_{il} at temperatures colder than 253 K. The total water mixing-ratio, modified to account for the cloud-ice mixing ratio, is given by

$$q_t = q_v + q_l + q_i \quad . \tag{4}$$

The ability to account for phase changes in saturated layers below 273 K is potentially important for wintertime conditions, such as those simulated for the SJV in the present study. As of summer 2000, all of these changes to the original TKE-predicting turbulence scheme of Shoran et al. (2000) have been incorporated into the public-release MM5 Version 3 at NCAR.

3. EXPERIMENTAL DESIGN OF SJV FOG EXPERIMENTS

In the SJV study, MM5 was configured with four nested grids (Fig. 2). All four nested domains used 40 layers in the vertical, with the lowest layer having a thickness of ~12 m (Table 2). The top of the model is placed at 100 mb. Because the model design detailed by Grell et al. (1994) has a staggered mesh system in the vertical (and horizontal), the computation level for most of the prognostic variables (except w and TKE) is at the middle of each layer. This places the height of the lowest computation level at ~6 m AGL. Above the surface layer, the grid gradually telescopes to create thicker layers farther aloft. Thus, there are 21 layers in the lowest 1.4 km of the column, with five layers concentrated in the lowest 108 m, providing excellent vertical resolution for the representation of low-lying fog.

The outermost (synoptic-scale) grid of the four domains has 49 x 61 points and 108-km resolution (domain D01 in Fig. 2). Next, a regional-scale grid of 55 x 55 points is located over the western states, using a 36-km horizontal resolution (domain D02). The third grid covers most of California with a domain of 79 x 64 points on a 12-km grid that extends well off the Pacific Coast to improve the accuracy of simulated low-level winds in the vicinity of various capes and bays (domain D03). Finally, a 4-km domain of 151 x 121 points encompasses the SJV and Sacramento Valley (domain D04), where the development fog is the focus of the study. This grid also is designed to include the California coastline for almost the entire north-south extent of the 4-km domain. All four domains are centered at 37.0 N and 120.5 W in the northern SJV. The terrain field for the 4-km grid is shown in Fig. 3.

Four primary numerical experiments are discussed in this report. Additional short experiments were run to test various intermediate software developments over the course of the project, but they are not important for understanding the main results and conclusions. Three experiments were run for the full episode from 0000 UTC, 7 December through 0000 UTC, 12 December 1995, observed during the 1995 Integrated Monitoring Study (IMS-95) field campaign (see Sec. 4 for details). A fourth experiment was run only for the first 36 h of the period.

The first experiment (Exp. GS-1) was run using an almost standard public-release code for MM5v2 (Version 2), including the option for analysis nudging above 1.5 km AGL (Shoran et al. 2000) and a nearly standard version of the Gayno-Seaman turbulence sub-model. That is, most of the extensions to the Gayno-Seaman TKE-predicting turbulence scheme described in Sec. 2.4 were *not* included in this experiment, except for an early form of the buoyancy adjustment for saturated conditions. However, it should be noted that a non-standard option was used when creating the 108-km analyses for the *ICs in all four experiments*. The non-standard option in the analysis pre-processor allowed coastal observations to be used only in the upwind direction (over either land or sea), depending on low-level flow direction (see Sec. 2.3). Although not supported

by the official pre-processors released through NCAR, this option was considered potentially important for conserving the integrity of coastal gradients in the ICs and was used in all four experiments discussed in this report. The experiment design for Exp. GS-1 is summarized in Table 3.

Next, Exp. BLK-1 used the same general conditions as Exp. GS-1, but replaced the Gayno-Seaman turbulence sub-model with the Blackadar PBL. Although Shoran et al. (2000) showed that the Blackadar PBL did not produce mixed-layer depths that are as accurate as those of the Gayno-Seaman scheme, their tests were performed in summer. Since the Blackadar PBL has been widely used for almost 20 years with considerable success, it was believed appropriate to perform one experiment for inter-comparison using this scheme. The third experiment (Exp. GS-2) returned to the Gayno-Seaman PBL, but with the addition of modifications described in Sec. 2.4 to better account for buoyancy effects associated with saturation. All other aspects of Exp. GS-2 were identical to those in Exp. GS-1. Finally, Exp. GS-3 was similar to Exp. GS-2 (extended Gayno-Seaman turbulence sub-model), but with the addition of two refinements to lower boundary conditions.

Based on evaluation of the first three experiments (see Sec. 5), Exp. GS-3 used a more accurate estimate of deep-soil temperature, T_m, than the standard approach (Sec. 2.3) by averaging the observed maximum and minimum surface temperatures in the SJV on the 12-km and 4-km domains. This refined analysis for T_m replaced the standard approach that was based on the much coarser 108-km analysis of 0000 and 1200 UTC surface temperatures that could not adequately resolve the SJV. In addition, Exp. GS-3 used a somewhat higher value for moisture availability in the SJV than is calculated through the standard look-up table from the land use (Sec. 2.3). The justification for the increase of the moisture availability in the case of 7-12 December 1995 is that a cold front had just passed through the SJV preceding development of the fog episode (see Sec. 4). Thus, frontal rain showers would have raised the soil moisture above the average wintertime values for the four SJV land-use categories(Table 4).

4. DESCRIPTION OF OBSERVED METEOROLOGY DURING SJV FOG EPISODE

An example of an acidic fog event in the southern SJV during the 1995 Integrated Monitoring Study (IMS-95) occurred in the period December 7-12, 1995. This episode was chosen by CARB as the focus for the numerical investigation using the MM5.

Conditions leading up to the fog episode began on the morning of 7 December 1995, when a weak cyclone, its cold front, and associated rain showers pushed southeastward across California. Precipitation totals were generally less than 0.1 inch. The position of the surface front at 1200 UTC and the accompanying surface reports are shown in the NWS analysis (Fig. 4). At 1027 UTC, an infrared image shows post-frontal stratus clouds and fog across the entire Sacramento Valley (Fig. 5). The NWS analysis at 0900 UTC, just before the time of the satellite image, places the cold front between Sacramento and Stockton (not shown). This is in good agreement with the leading edge of the post-frontal stratus clouds. Between 0900 and 1200 UTC, the surface analyses indicate that the cold front and cloud cover moved rapidly southward

and were already past Bakersfield by 1200 UTC. Over the next 12 h, the front weakened as it traveled farther southward and eventually dissipated about 0000 UTC on 8 December 1995 (Fig. 6). The initial post-frontal fog burned off during the afternoon of 7 December and SJV temperatures rose to 16-22 C by 2100 UTC (not shown). Dew points in the Valley at this time were around 10-13 C.

As evening began, shortly after 0000 UTC on 8 December, a broad ridge became established across the Northeast Pacific Ocean and northern CA. In the wake of the dissipating front, cool Pacific air entered central California on northwesterly winds and became entrenched in the Sacramento Valley and SJV. The weak high-pressure ridge became quasi-stationary and persisted throughout the rest of the episode, leading to generally light surface wind speeds. Skies over the region became mostly clear by 0300 UTC, 8 December, but observed winds in the Valleys at this time were still from the northwest at about 2.5 m s^{-1} (not shown). Unfortunately, the special radiosondes and wind profilers deployed in the SJV for IMS-95 did not start operating until 1200 UTC, 9 December, so no vertical wind shear data are available during this evening. Nevertheless, the observations of surface winds at 2.5 m s^{-1} for several hours after sunset, and the dissipation of the stratus clouds and fog at this time, suggest that the shear was rather strong (also see Sec. 1.2).

As the night progressed and the weak ridge settled into the area, the surface winds became calm in the southern SJV and temperatures fell to about 9-11 C by 1200 UTC, 8 December (Fig. 7). [For easier interpretation of the National Weather Service (NWS) data shown in Fig. 7 and other figures, Table 5 provides temperature conversions between the Celsius and Fahrenheit scales in the range of interest.] The drop in surface temperatures, coupled with moderate dew points in the post-frontal maritime polar air mass, caused radiation fog to form overnight. An infrared satellite image at 1016 UTC, 8 December 1995, shows that the radiation fog had become fairly extensive in the SJV toward morning (Fig. 8). The figure also shows fairly widespread fog and stratus extending from the coastal region westward over the Pacific Ocean at this time.

Once the fog had formed in the Sacramento Valley and SJV, conditions changed little for the following three days. The gentle winds in the weak quasi-stationary ridge kept the air mass relatively stagnant. The ridge was too weak to experience much subsidence-induced heating. Meanwhile, radiation flux divergence from the fog top caused long-wave cooling and reflected short-wave energy during the day. Thus, surface temperatures maxima in the SJV remained in the 12-15 C range and the fog tended to persist through much of the daytime during 8-10 December 1995. By late afternoon of each day, the fog often dissipated into haze in many areas, but would generally reform at night. Mesoscale manual analyses performed at 3-h intervals through the period show that sea-level pressures in the SJV and Sacramento Valley tended to be 1-2 mb higher than along the coast or over eastern California and Nevada. This mesoscale high in the central Valleys is likely caused by the higher density of the cold-air pool that collected in the lower levels due to radiational cooling from the fog and from cold-air drainage from the slopes of the flanking mountain ranges.

Examination of data from these three days reveals the basic patterns of the acidic-fog episode. Figure 9 shows a radiosonde profile at Bakersfield for 0400 PST (1200 UTC), 9 December 1995, taken from the IMS-95 Final Data Report by STI (Lindsey et al. 1996). It indicates a weak

subsidence inversion at 1700 m MSL (just above 850 mb), marked by strong drying aloft. Lower down, fog (saturated conditions) has formed all the way from the surface (at 117 m) to 750 m MSL. The fog layer is also characterized by higher dew points (due to the surface evaporative flux), cool temperatures through the layer, and a moderate capping inversion due to the radiation flux divergence from the fog top. Winds within the fog layer are from the southeast at about 2.5 m s^{-1}, according to Fig. 9, but the NWS observations at other stations in the southern SJV indicate mostly calm winds (Fig. 10).

The thermal profile in the upper portion of the observed fog layer appears to be close to moist adiabatic (~350-750 m MSL), suggesting some turbulent mixing exist in that layer (probably induced by the strong radiational cooling at the fog top). Meanwhile, the lowest 250 m is stable, so turbulence should be minimal there. This suggests that the southeast wind at Bakersfield may represent cold-air drainage (advection) from the sloping elevated terrain of the Sierra Nevada and Tehachapi Mountains southeast of Bakersfield. Thus, it appears likely that the radiation-induced cloud-top mixing does not reach down to the surface in this particular case.

Meanwhile, surface observations from the NWS in the southern SJV indicate that Bakersfield had a visibility of 4 miles at this time, while Raisin City and Fresno had calm winds and visibilities of 1/16 mile (Fig. 10). Three hours later at 1500 UTC (0700 PST), temperatures had fallen about 2 C and visibility at Bakersfield had dropped to 1/16 mi (not shown). A visible-range satellite image close to sunrise at 1503 UTC (Fig. 11) indicates that the brightest area in the central valleys was in the south near Bakersfield, suggesting that the fog is deepest in this region. North of Fresno, the fog is apparently shallower, because the fog shows up in the satellite picture as darker shades of gray. This demonstrates two characteristics of the fog event. First, strong spatial variability that can occur in depth and visibility. Second, quite rapid changes can take place in the local visibility as cooling activates more and more condensation nuclei.

As 9 December progressed, surface temperatures gradually rose at Bakersfield from 6 C at 1200 UTC to a maximum of 9 C by at 0000 UTC (1600 PST). Fig. 12 shows that the fog persisted on this afternoon, although its depth had decreased to about 250 m by 0000 UTC, 10 December. A similar thinning of the fog depth occurred at Fresno, the other IMS-95 sounding site (not shown). Overnight and through the early morning hours of 10 December, there was strong drying aloft in the ridge due to advection (Fig. 13). It is clear that the drying mechanism cannot be subsidence, because that would have led to both drying and adiabatic heating of the column. Despite overnight radiational cooling in the low levels, the morning sounding at 1200 UTC shows that the fog at Bakersfield is still only ~250 m in depth (Fig. 13). Therefore, solar radiation was able to penetrate to the surface more easily on this day and the fog gradually dissipated during the late afternoon, as shown at 0000 UTC (1600 LST), 11 December (Fig. 14). However, even though Fig. 14 shows a dew-point depression of about 4 F (~2 C) at 0000 UTC, the NWS surface observations in the mesoscale manual analysis (Fig. 15) indicate widespread haze in the SJV, including Bakersfield. There are also a few patches of fog remaining in the Valley, as shown in Fig. 15. Finally, Fig. 16 shows a visual satellite image taken less than 3 h earlier at 2119 UTC, 10 December. The picture corroborates the haze and patchy fog in the SJV at this time, but also shows widespread clouds overspreading the Pacific Ocean and already entering northern CA. The clouds are associated with an approaching storm system, whose pressure gradient and advancing rain can be seen along the northern CA coast in Fig. 15. With the approach of the

new storm, southeasterly winds increased in the SJV on 11 December, ending the air stagnation and foggy conditions. This brought the episode to a close.

To better understand the occurrence of fog and haze in the SJV during this episode, it is useful to further examine the NWS observations. The goal is to identify the ranges of dew-point depressions that can be associated with fog versus haze. Considering the data available at all stations in the SJV and Sacramento Valley, Table 6 gives the frequency distributions for reports of fog and haze. (No fog or haze was reported with depressions greater than 12 F, or 6.5 C.) First, examination of the frequency distributions reveals that fog reports are 4.5 times more common than haze reports. Normalizing for this factor, the distributions indicate that fog is associated mostly when the dew-point depressions of 0-4 F (0-2 C) and haze exists mostly for depressions of 5-9 F (3-5 C). These ranges are useful for interpreting the predictions of the MM5 mesoscale model (Sec. 5), which provides temperature and water vapor mixing ratio as its output variables. For this type of case, visibility would have to be computed using a separate aerosol model capable of representing chemical reactions, aqueous processes, droplet growth, and deposition. Therefore, in this study model verification for fog and haze must be done by matching the model-predicted dew-point depressions with the observed depressions associated with those visibility-related quantities, as summarized in Table 6.

5. RESULTS OF SJV FOG NUMERICAL EXPERIMENTS

5.1 Experiment GS-1 Results

For brevity, all model results shown in this final report are taken from solutions on the 4-km domain. First, we examine the results of Exp. GS-1, described in Table3.

At 1200 UTC, 7 December 1995 (+12 h into the simulation), the cold front had recently pushed south of Bakersfield in the southern SJV (Fig. 4). At this time, the MM5 model produced 2.5-5.0 m s^{-1} northwesterly surface winds in the SJV and Sacramento Valley (not shown), similar to those observed. Strong shear was predicted above the surface layer, with winds at 500 m reaching 10-15 m s^{-1} (not shown). Northwesterly surface winds of 4-7 m s^{-1} prevailed in the coastal and offshore areas of the 4-km domain, as observed, with higher winds of 7-13 m s^{-1} located in "expansion fans" downwind of prominent land features (e.g., Cape Mendocino, Pt. Arena, and Monterey Peninsula).

In this post-frontal environment at 1200 UTC, 7 December, the model developed a stratus cloud layer over the SJV and Sacramento Valley in Exp. GS-1 (not shown), which agrees with the reports of cloud at all the surface observing sites in the Valleys (Fig. 4). The model's stratus cloud tops were at ~600 m AGL. At a few places in the SJV and Sacramento Valley, they extended all the way down to the surface, which also agrees with observations of local areas of fog. However, inspection of the simulated surface temperatures in the Valleys (not shown) indicated that they were much too cold, only ~1-4 C, whereas the observed temperatures at this time were ~11.5-13.5 C, as shown in Fig. 4.

Further development of the most critical solutions in Exp. GS-1 is revealed best by examining the model fields at 0000 UTC, 8 December 1995, after the first 24 h of the MM5 simulation.

Figure 17 shows the horizontal wind field at this time in the model's lowest layer (at ~6 m AGL). It indicates that the winds offshore are still mostly from the northwest, as reported in Fig. 6. In the SJV and Sacramento Valley, however, Fig. 17 shows only very weak winds (0-2 m s^{-1}) and highly variable directions. This contradicts the observations in the Valleys at this time. The actual winds behind the dissipating cold front were still from the northwest at 2.5 - 5.0 m s^{-1} (Fig. 6). Meanwhile, Figs. 18 and 19 show the MM5 surface-layer temperature and relative humidity at 0000 UTC, 8 December, respectively. Fig. 19 shows only a very few points in the SJV and Sacramento Valley with 100 % humidity, suggesting that there is little fog at this time (which is correct). However, the surface temperatures in the model are still much too cold, with wide-spread areas in the range of 3-6 C, while the observations were ~15-20 C (compare Figs. 6 and 18). Aloft at 500 m AGL, Figs. 20 and 21 confirm that there are serious problems in the thermal and humidity fields of Exp. GS-1. Temperatures at this level over the Valleys are about 8 C colder than in the immediate surrounding areas. Fig. 21 reveals that the area experiencing this excessive cooling aloft is also completely saturated. Thus, the cold bias persists upward from the surface through at least 500 m, which in turn promotes the continuation of the stratus cloud deck, even though the observations indicate that the clouds had begun to break up by this time (compare to Fig. 6).

To better understand the solutions shown in these horizontal fields, a set of model-generated soundings was created at the 24-h time of the Exp. GS-1 simulation. In Fig. 22, the model sounding at Fresno for 0000 UTC, 8 December clearly reveals the stratus cloud lying between ~200-850 m AGL, with very cold temperatures in the cloud layer. However, notice that despite the cloud cover and the colder-than-observed surface layer temperature, the sub-cloud layer is actually superadiabatic. Taken together, these results strongly imply that the superadiabatic surface layer is caused primarily by excessive cooling in the cloud layer, rather than by strong heating at the surface. Excessive spurious cooling in the cloud layer would also explain the very light winds found at the surface in Fig. 17. That is, the cooling in and below the cloud generates the low-level cold pool and the strong thermal inversion layer found near 900 mb in Fig. 22. The inversion, in turn, causes the momentum below the level of the mountains surrounding the SJV to become effectively decoupled from the strong northwesterly flow aloft (Fig. 22 shows 50 m s^{-1} winds at 500 mb). Thus, the low-level winds in the SJV become very weak and variable about 6-9 h too early in Exp. GS-1, while the observed stagnation of the surface flow occurs somewhat later at ~0300 UTC, 8 December.

As another check of the model simulation in Exp. GS-1, an east-west cross section was calculated at this time along a vertical plane along 37 N just north of Fresno (location shown in Fig. 23). Figures 24 and 25 show the potential temperature, θ, and the relative humidity along this cross section. In Fig. 24, notice that the air beneath the strong inversion layer is mostly well mixed (that is, the isentropes are nearly vertical). Examination of the *TKE* in the cross section (not shown) confirmed that the entire sub-inversion layer is turbulent at 0000 UTC, 8 December, with a maximum *TKE* of ~0.4-0.5 J kg^{-1}. This moderate turbulence is also consistent with the unstable surface layer found in Fig. 22. Meanwhile, Fig. 25 shows that the clouds over the valley are quite extensive and extend westward over Pacheco Pass to the west of the SJV (one of the few significant gaps in the Coast Range Mountains). In fact, the cloud tops coincide roughly with the top of the dominant ridgeline of the Coast Ranges. However, at the surface, the relative

humidity across most of the Valley is only 80-85%, suggesting that fog is not extensive at this time in Exp. GS-1.

The model errors that developed in the first 24 h dominated the subsequent evolution of the solutions through the remainder of the episode. By 36 h into the model simulation, at 1200 UTC, 8 December 1995, the cold low-level temperatures and the stratus cloud had reached a quasi-steady state (not shown). During the daytime on 8 December, conditions finally began to change in Exp. GS-1 until the stratus cloud dissipated completely by about 2100 UTC. This change occurred for three reasons. First, the turbulence induced in the cloud layer by the radiational cooling from the cloud tops gradually mixed drier air from aloft into the layer (similar to cloud-top entrainment instability). During this period mid-level advection of dry air was occurring above the cloud layer at 850 mb, as evidenced by the observed soundings shown in Figs. 9, 12 and 13. This drying was not associated with subsidence, because that would also have caused significant adiabatic heating, which is not evident in the figures. The steady drying would tend to make any turbulent mixing at the cloud top more effective for depleting the cloud water. Second, the auto-conversion microphysical process in the model's explicit cloud moisture scheme (Dudhia 1989) gradually depleted some of the liquid water from the long-lived stratus clouds as light precipitation.

Third, the absorption of solar radiation by the clouds gradually warmed the layer. Once the stratus clouds dissipated, the model's surface temperatures in the SJV began to recover, rising to 7-10 C by 0000 UTC, 9 December (+48 h). However, the cold temperatures predicted earlier in the stagnant air mass entrenched in the Valleys had significantly lowered the dew points (causing nearly 0.25 inch of drizzle and light rain before the stratus cleared). Thus, as temperatures slowly recovered, the relative humidity fell because there was almost no advection of moister air into the Valleys from the Pacific Ocean. Despite surface evaporation over the following three days, the dew points remained lower than the gradually warming temperatures, so that fog never formed in the SJV throughout the rest of Exp. GS-1.

Even though the Exp. GS-1 clearly produced seriously unrealistic fields for some of the key variables, there are still some rather positive results to be found in the MM5 solutions. First, although they became too extensive, the model did produce the post-frontal stratus clouds that were observed in Fig. 5. Second, the model was able to expand the stratus down to the surface, as is typically observed in so-called "high-inversion" fog events, or "Tule fogs", described by Gilliam (1970). Even though this was not a high-inversion fog episode, it does demonstrate that the model has the necessary physical processes to develop such a fog. Third, this experiment demonstrates that the model is able to simulate the weak low-level winds and air-stagnation conditions that are common in SJV wintertime fog episodes, when cold air is trapped in the SJV and Sacramento Valley by the surrounding mountains. Fourth, the model was able to dissipate the stratus deck later on, although the clearing occurred about 24 h later than observed. Despite the error in the timing of this development, the stratus dissipation occurred due to local physical processes, rather than by advecting the cloud out of the region. These are all processes and characteristics that are common for many of the fog events observed in the SJV and are necessary for the model to eventually produce more accurate solutions.

5.2 Experiment BLK-1 Results

Since the MM5 does not have a history of producing extreme rates of cooling at the top of cloud layers, it was suspected that the errors found in Exp. GS-1 might be related to the Gayno-Seaman (G-S) turbulence scheme. On the other hand, the G-S sub-model had already been in use for daily real-time forecasting at PSU for at least two years prior to the time that Exp. GS-1 was performed (summer 1999), without such obvious errors in the temperature field. So it seemed unlikely that the errors were inherent to the sub-model in its original form. It was hypothesized that another possible source of error was related to the very fine vertical resolution used in this study. Such fine vertical resolution, along with the expectation of saturated conditions in those very thin layers, was unusual for prior MM5 applications. Thus, as a check, the next experiment (Exp. BLK-1) was run with the same Dudhia (1989) radiation scheme used in all the experiments, but with the Blackadar PBL parameterization replacing the Gayno-Seaman turbulence sub-model.

Figure 26 shows the MM5-simulated sounding at Fresno in Exp. BLK-1 for 1200 UTC, 7 December 1995 (+12 h). The surface temperature in the sounding is 13 C (55 F), with a dew-point depression of ~1 C. This agrees very well with the observed temperatures and dew points in the SJV at this time (e.g., see Fig. 4), while Exp. GS-1 had produced a surface temperature of 3 C at this location. Also, Exp. BLK-1 has developed the stratus cloud deck, much like Exp. GS-1, but without the excessive cooling in the cloud layer. From these results, we conclude that the radiation scheme is working correctly, despite the very fine vertical resolution in these experiments. However, because the Blackadar PBL scheme used in this experiment cannot account for the effects of saturation on buoyancy in cloud and fog layers, the model cannot maintain a realistic thermal profile in these layers. Thus, although Exp. BLK-1 was mostly successful in the first 36 h of the study period, it is not suitable for the overall goals of the project.

5.3 Experiment GS-2 Results

Based on the positive results from Exp. BLK-1, it was considered probable that the source of the temperature errors in Exp. GS-1 was associated with the numerical formulations in the standard Gayno-Seaman turbulence scheme. Further inspection and experimentation uncovered a flaw in the numerical methodology used to convert the model's thermal field back to the original form, θ, from the conservative variable, θ_l, following completion of the turbulence calculations (see Sec. 2.4). In the original numerical approach, the recovery of θ included a linearized form of one equation, which caused a small systematic error (cooling) for saturated environments. This error was easily overlooked, at least on mesoscale grids of 36-km resolution or greater. However, on very fine-mesh domains having much smaller time steps (as in the case of the 4-km domain used here), these systematic errors accumulated much faster and led to large spurious cooling in saturated layers, as found in Exp. GS-1.

Because this error was related to the moisture terms in (1) and (3), it only occurred in cloudy layers and was most significant in the low to mid layers of the atmosphere, where the cloud water concentrations are greatest. Therefore, the error had no significant impact on earlier MM5

applications in summertime air-quality episodes that used the Gayno-Seaman turbulence scheme, because those cases had very few resolved-scale clouds. Once the problem was identified, it was easily corrected by simply inverting (1) or (3) to solve directly for θ. Although this approach is slightly less efficient computationally, it is far more accurate than the earlier formulation. The correction was immediately reported to NCAR in August 1999 and installed in the public-release version of MM5.

For Exp. GS-2, the MM5 model was run using the extended version of the TKE-predicting turbulence sub-model (as described in Section 2.4), including the corrected θ-recovery algorithm. These modifications to the Gayno-Seaman scheme led to significant improvements in the MM5-simulated conditions in the Valleys during the episode of 7-12 December 1995. First, Fig. 27 shows northwesterly surface-layer winds of 3-6 m s^{-1} simulated at ~6 m AGL throughout the Valleys in Exp. GS-2 at 1200 UTC, 7 December (+12 h). At this time the observed front was analyzed just south of Bakersfield (Fig. 4) with similar northwesterly winds across the interior region of the SJV and Sacramento Valley. Somewhat faster northwesterly winds are found off the coast, with 7-11 m s^{-1} maxima near the capes and peninsulas. On average, the surface winds in the Valleys are about 1-2 m s^{-1} faster in Exp. GS-2 at this time than in Exp. GS-1. This is likely a result of the elimination of the false low-level cold pool produced in Exp. GS-1, which prevents early decoupling of the winds in the valley from the faster winds aloft. The correction of the thermal structure is confirmed by the simulated surface temperatures in Exp. GS-2, which are generally 12-15 C across the SJV at this time (Fig. 28). Compared with the surface observations of 11.5-13.5 C (Fig. 4), the MM5 solution in Exp. GS-2 is actually slightly warm, instead of being ~10 C too cold.

Next, it is instructive to examine briefly the vertical structure of the MM5 solutions in Exp. GS-2 at +24 h (0000 UTC, 8 December), about the time the stratus cloud should dissipate. This structure is represented along an east-west cross section located along 36 N in the southern SJV (Fig. 29), about mid-way between Fresno and Bakersfield (the two sites at which special sounding observations are available later in the period). Figures 30 and 31 show the potential temperature, θ, and the relative humidity, respectively, in the plane of the cross section. First, notice that the thermal inversion at the top of the turbulent boundary layer (Fig. 30) is much weaker and more realistic than in Exp. GS-1 (Fig. 24). The surface temperatures in the figure are simulated as ~13 C (55 F). This is still too cold by ~3 C, but it represents an increase of the surface temperatures compared to Exp. GS-1 by ~10 C. Meanwhile, Fig. 31 shows that the surface relative humidity in the SJV has fallen to ~85% (little or no fog), while the stratus clouds (indicated by 100 % contours just below the inversion) clearly are breaking up. Thus, the model solution appears to be fairly reasonable after the first 24 h.

In Fig. 32, a horizontal plot at 1200 UTC (0400 PST), 8 December (+36 h) shows that the early morning winds have become nearly calm (0-1 m s^{-1}) and variable in most of the southern SJV. Farther north, in the region from Modesto to Sacramento, light southeasterly winds of 1-3 m s^{-1} are predicted. Meanwhile, the model continues to simulate moderate, but gradually weakening northwesterly winds off the coast. This wind pattern in Exp. GS-2 is in excellent agreement with the observed winds shown in the mesoscale analysis (Fig. 7). Careful examination of Fig. 32 also reveals light downslope winds along the flanks of the major mountain ranges, which is consistent with nocturnal cold-air drainage expected for this pre-dawn time period. The MM5-

simulated surface temperatures at this time in the Valleys are in the range of 9-13 C (48-55 F) (not shown), which agrees well with the observed temperatures in Fig. 7.

The generally favorable simulations of the light and variable low-level winds and moderately cool surface temperatures in Exp. GS-2 are very positive developments for the goal of simulating an evolving fog episode in the SJV. However, the difference between fog, haze, stratus and clear skies can be difficult to diagnose from a model's prognostic fields, especially when the existence of particles such as sulfates can lead to the formation of aerosol droplets at humidities well below 100%. Therefore, to diagnose fog from the model fields, it was helpful to make use of the frequency distributions calculated from observed reports of fog and haze as a function of dew-point depression in the central Valleys (Table 6). The table showed that, in this region, wintertime fog appeared to be associated with surface dew-point depressions of 0-2 C, while haze was correlated well with surface depressions of 3-5 C. For surface temperatures that are typical during this episode, a dew-point depression of 2 C corresponds to a relative humidity of ~87%, while a depression of 5 C corresponds to ~70%. Under normal conditions, a humidity of 70% may be high enough to activate a few of the most hydroscopic condensation nuclei. However, it is unlikely to be responsible for seriously hazy conditions, except perhaps in a polluted environment such as the SJV or in a high sea-salt environment such a coastline. Realistically,, it must be recalled that visibility observations are not made strictly in the horizontal direction, but the observer may include a variety of low angles to the true horizon over distances of at least several miles. Therefore, when haze develops, it can be associated with the humidities through the lowest 100-500 m of the atmosphere, not only the local surface humidity.

Figure 33 shows the surface-layer relative humidity at ~6 m AGL for 1200 UTC, 8 December (+36 h) in Exp. GS-2. The figure indicates that the simulated humidities between 90-100 % extend from slightly north of Sacramento southward to Bakersfield, and around San Francisco Bay. Comparison with the specially processed infrared image at 1016 UTC (Fig. 8) and the mesoscale analysis (Fig. 7) on this morning shows generally good agreement with this pattern. Thus, the area covered by the humidities that include the approximate range of humidities associated with fog (87-100 %) appears to fit the observed fog pattern quite well in this case.

Further insight can be gained by applying these humidity criteria in conjunction with the corresponding model-simulated soundings at Fresno and Bakersfield, which are shown for this time in Figs. 34 and 35, respectively. In Fig. 34, at Fresno, the surface dew-point depression is about 2.5 C, which suggests a borderline case were fog and haze are almost equally likely. Also, the same sounding shows that the layer at 910 mb is nearly saturated, so that the humidity a few hundred meters aloft is plenty high enough to activate many of the hygroscopic nuclei, and maybe produce some low-water-content stratus. This assessment of the model solution is verified by the Fresno observation at this time (see Fig. 7), which indicates fog, 2 1/2-mile visibility and obscured sky (cloud cover or deep fog). However, in a common bit of ambiguity, the NWS surface station at Fresno also reported a dew-point depression of 0 C, so the agreement of the model to the data is not perfect.

Meanwhile, at Bakersfield, Fig. 35 fails to indicate any saturated layer below the inversion in the model sounding from Exp. GS-2. Nevertheless, the surface dew-point depression is only ~1.5 C, while above the surface the depression averages just ~1.0 C up to 930 mb. Since this

corresponds to humidities in the range of 87-95%, it is likely that many of the hygroscopic particles are activated, even though technical saturation is never reached. Using the criteria from Table 6, this suggests fog should be present, but no overlying solid stratus layer. Consistent with this interpretation of the model sounding, the NWS surface report for Bakersfield in Fig. 7 indicates fog, 4-mile visibility, and broken skies aloft. The dew-point depression reported by the NWS at Bakersfield is ~0.5 C, which is less than that simulated by the MM5, but not unreasonable. Thus, diagnosis of the model-simulated visibility class (fog, haze, stratus and clear skies) in the SJV cannot be based solely on the model-predicted *surface* variables. It is also important to consider the sounding characteristics all the way up to the inversion layer. As a result, the model-simulated and observed soundings, along with surface reports, were adopted in this study as the primary data for verifying the MM5 fog predictions.

At +60 h into the simulation (1200 UTC, 9 December 1995), the MM5 solutions in Exp. GS-2 can be compared to special IMS-95 observations, as well as NWS surface reports and satellite images. First, the surface winds at 1200 UTC, 9 December, are shown in Fig. 36. Again, the winds are light and variable in much of the southern SJV. However, weak southeasterly winds of 1-2 ms^{-1} prevail in most of the central part of the region from Fresno to Redding, and also in the vicinity around Bakersfield. This pattern is verified reasonably well by the NWS surface observations in Fig. 10. It should also be pointed out that the northwesterly flow off the CA coast in Fig. 36 is beginning to change by this time, with some southeasterly winds appearing northward from Pt. Reyes. This change in the flow over the ocean is also confirmed by the observations in Fig. 10, and is a prelude to the approach of the Pacific storm that later on brings an end to the acidic-fog event on 11 December.

Surface relative humidities simulated at 1200 UTC on this morning are above 90 % throughout the SJV and Sacramento Valley in Exp. GS-2, implying that fog is widespread at this time (not shown). This agrees well with the mesoscale surface analysis and satellite image shown in Figs. 10 and 11. Furthermore, the model-predicted soundings at Fresno and Bakersfield are very helpful for understanding the continuing evolution of the solutions in this experiment (Figs. 37 and 38). Both figures clearly indicate the presence of fog because the model-simulated dew point depressions at the surface are ~1 C, with overlying saturated layers of ~300-400 m. These profiles should not be interpreted as very low stratus lying above a shallow hazy layer, because the model layers near the ground, although unsaturated, do not have a dew-point depression large enough to make haze a reasonable possibility (Table6). This diagnosis of the model results pointing to deep fog is confirmed by the NWS observations plotted in Fig. 10, with both stations reporting fog (Fresno has a visibility of 1/16 mile and Bakersfield has a visibility of 4 miles). At Fresno, the sky is reported as obscured by the deep fog.

The verification at Bakersfield at +60 h is more difficult to interpret. The special IMS-95 sounding at Bakersfield at this time (Fig. 9) shows complete saturation from the ground to 600 m AGL. This is about twice as deep as simulated by the model (Fig. 38) and it also does not seem to agree with the NWS report of broken clouds and a dew point depression of 1 C at Bakersfield. Thus, it is not always clear just what the observed conditions are like, even in a small area. For the purpose of objective verification of the model results (also see Sec. 5.5), we must resolve ambiguities that arise between the NWS and special IMS-95 observations. Therefore, in cases where the NWS observation does not agree with the special sounding, the differences in

observed surface temperature and dew point will be noted, but the observed present weather conditions (fog, haze, stratus, clear) will be based on the explicit reports given in the NWS reports.

Despite the fairly good agreement between model-simulated and observed fog characteristics at this time (+60 h), there are some accumulating errors that point to a growing problem during the second half of the study period in Exp. GS-2. That is, too little fog and haze is predicted by the MM5 in the last 2-3 days of the episode. Closer inspection of the fields from Exp. GS-2 showed that, once the radiation fog dissipated in the MM5 around 72 h, the surface temperatures became too warm during both day and night by 2-8 C. Analysis of the model results suggests two possible explanations.

First, it is possible that warm, dry air from above the inversion reaches the surface in the model simulation, thereby diminishing the fog. The inversion level predicted in the model in the southern SJV (Figs. 37 and 38) is clearly lower than observed at +60 h (Fig. 9). However, this trend did develop eventually in the observations, although it occurred somewhat later than in the model (Figs. 12-14). Thus, if the warm dry air from aloft reached the surface in Exp. GS-2, it may have contributed to larger-than-observed dew-point depressions, and hence less fog and haze than were observed in the last two days of the period. Fig. 12 indicates that the observed fog persisted through the afternoon at Bakersfield until 0000 UTC, 10 December 1995, but in the model's soundings (Figs. 39 and 40) the profiles indicate only haze and low stratus at Fresno and Bakersfield. However, in this case the discrepancy is reconciled by the NWS surface observations (not shown), which reported only haze at both sites, with obscured sky (stratus) at Bakersfield. Thus, the observed Bakersfield sounding shown in Fig. 12 once more contradicts both the NWS surface observations and the model soundings. Moreover, the inversion actually persists in the model soundings at later times, even though it comes very close to the ground (not shown), which is consistent with the observations (e.g., Fig. 13). So, it does not appear that the shallow inversion level can be the *primary* cause of the warm surface-temperature errors found in the model.

Second, it is possible that the model's surface sensible heat flux is too large, while the surface latent heat flux is too small. A large sensible heat flux could be explained during the *daytime* by excessive solar radiation reaching the ground, rather than being reflected or absorbed by the fog. At night, this argument does not help. However, another possible source of sensible heat is from the deep soil. That is, if the deep-soil temperature, T_m (which is constant in time), is specified to be too warm in the model's initial conditions, it can serve as an infinite heat reservoir during the simulation (see Sec. 2.3). There is also a possibility that the surface evaporation flux is underestimated in the model because the rain that occurred with the recent frontal passage could have raised the soil moisture above its wintertime average for the land-use types in the SJV (Table4).

5.4 Experiment GS-3 Results

As discussed above, the analysis of results from Exp. GS-2 led to the conclusion that errors in the surface fluxes for sensible and latent heat were the most probable cause of errors in the

simulated low-level temperature and moisture fields. Those errors, in turn, could have a significant impact on the ability of the model to simulate the fog and haze characteristics in the SJV. Consequently, before experimentation was continued, the T_m field used in the initialization of Exps. GS-1, GS-2 and BLK-1 was examined. In these experiments, the standard MM5 approach for assigning T_m on the 4-km domain was simply to interpolate in the horizontal from the T_m field developed for the outermost 108-km domain (Sec. 2.3). The original T_m field for these three experiments is shown in Fig. 41. Notice that this field has deep-soil temperatures in the southern SJV exceeding 16 C at Bakersfield and 13 C around Fresno. This is clearly much too high, since the surface air temperature at Bakersfield never once became that warm during the entire episode. Based on examinations of Fig. 41 and the surface temperature observations across the domain, it was concluded that the T_m analysis is reasonably accurate over the Pacific Ocean, in the coastal regions, over the Coast Range Mountains, and in Nevada. Therefore, corrective measures could be concentrated in the Sacramento Valley and SJV.

To take corrective action for the errors found in the original T_m field, the surface air temperatures at five stations in the Valleys first were plotted as a function of time for every 6 h during the four days following the frontal passage, from 8-11 December 1995 (not shown). (The five stations selected were Redding, Sacramento, Stockton, Fresno and Bakersfield.) During this period, the surface temperatures showed the familiar diurnal pattern of variability, although the widespread fog and haze tended to limit the average diurnal range from 4 C at Stockton to 8 C at Bakersfield. Overall, the maximum and minimum temperatures during the period were 18 C (at Redding, 0000 UTC, 8 December) and 4 C (at Bakersfield, 0600 UTC, 10 December). Most of the stations had an average temperature for the four-day period of ~10 C. Therefore, for Exp. GS-3, the deep-soil temperature field was modified so that T_m in the SJV and Sacramento Valley was no greater than 10 C (Fig. 42). Finally, for Exp. GS-3 the soil moisture availability was adjusted upward by 0.15 (Table 4) for all the land use categories that apply in the Valleys to account for the effects of recent rainfall.

The MM5 model solutions in Exp. GS-3 that result from specifying this moderately lower T_m and higher soil-moisture availability in the SJV and Sacramento Valley are different from the solutions in Exp. GS-2 (Sec. 5.3) in subtle, but important ways. For the most part, we shall follow the steps of examination of horizontal and vertical structures used in that previous experiment. First, Fig. 43 presents the surface-layer wind field at +12 h (1200 UTC, 7 December 1995), when the cold front had just passed through Bakersfield (compare to Fig. 4). Comparison of these surface winds with those produced in Exp. GS-2 (Fig. 27) indicates virtually no difference at all. The surface-layer temperatures in the Valleys for Exp. GS-3 are in the range of 10.0-13.5 C (Fig. 44), which is about 2 C cooler on average than in Exp. GS-2 (Fig. 28), and quite close to the observations in Fig. 4. Thus, the primary surface fields in Exp. GS-3 look very reasonable in the earliest part of the study period as the maritime polar air mass was just beginning to become established in the Valleys.

Figures 45 and 46 present the vertical structure of potential temperature and relative humidity simulated by Exp. GS-3 at +24 h (0000 UTC, 8 December) in the plane of the cross section

located along 36 N between Fresno and Bakersfield (refer to Fig. 29 for location). For the potential temperature, a brief comparison of Figs. 30 and 45 shows that both Exps. GS-2 and GS-3 had very similar vertical stability structures at this time. The moderate thermal inversion over the SJV is in the same location in both experiments, capping a fairly well-mixed boundary layer. However, the minimum surface temperature of 11 C in the SJV shown in Fig. 40 (Exp. GS-3) is about 2 C cooler than in Fig. 30, and is about 4-5 C cooler than observed (Fig. 6).

This cool temperature bias at +24 h in Exp. GS-3 can be explained by two factors. First, it has been shown that the cooler values of T_m used in Exp. GS-3 are certainly quite representative of the four days of the episode following 0000 UTC, 8 December. However, since the frontal system had just passed through the SJV shortly before this time, the actual soil temperatures are probably still in the process of cooling. That is, the actual soil temperature cannot remain constant in nature at a depth of ~25 cm if the atmospheric conditions change significantly. Thus, the transition to post-frontal cool conditions and establishment of the stagnant air mass in the Valleys would favor a cool bias in the surface temperatures simulated by the model during the first 24 h of the simulation. Consequently, this result demonstrates that a more sophisticated multi-layer soil model is a better choice for a mesoscale model in cases where atmospheric conditions are expected to change significantly over the course of time. Second, Fig. 46 (Exp. GS-3) has higher humidities near the surface than found in Fig. 31 (Exp. GS-2), and somewhat more extensive areas of 100 % humidity just beneath the potential temperature inversion. This implies greater cloud cover in Exp. GS-3 and reduced solar heating at the surface. In summary, the low-level temperatures have somewhat less accuracy at this time in Exp. GS-3, compared to the previous experiment.

Moving forward to +36 h (1200 UTC, 8 December), Fig. 47 shows that the surface-layer wind field in Exp. GS-3 is mostly similar to the winds in Fig. 32 from Exp. GS-2. Both figures can be compared to the surface observations in the mesoscale analysis presented in Fig. 7. As found in Fig. 32, the wind pattern in Fig. 47 matches very well with the observations. Specifically, this includes light and variable winds in the southern SJV, southeasterly winds from Modesto to the region north of Sacramento, downslope winds on the western flanks of the Sierra Nevada Mts., and even the northwesterly winds near Redding (northern interface of the domain, near 40.5 N, 122.5 W). Fig. 48 indicates that the pre-dawn temperatures in the Valleys at this time are about 8-11 C (46-52 F), which agrees well with the observations in Fig. 7. These temperatures in Exp. GS-3 are about 1-2 C cooler than in Exp. GS-2 (not shown), but most of the model error noted for Exp. GS-3 at +24 h has disappeared. From this time forward, the surface temperatures in Exp. GS-3 usually remained in fairly good agreement with the observations for the rest of the episode. Fig. 49 shows that the surface-layer relative humidity at +36 h has about the same pattern as in Fig. 33 (which was consistent with the satellite image in Fig. 8). So, it appears that the overall temperature and moisture fields in the low levels for Exp. GS-3 are reasonable and should be suitable for the prediction of fog and haze characteristics.

As discussed in Sec. 5.3, an evaluation of the model simulations, the observations, and statistical correlations between observed visibility characteristics and the temperature and dew-point data produced a reasonable methodology for interpreting the obscuration type implied in the MM5 solutions. That methodology was applied to the MM5-generated soundings for Fresno and

Bakersfield at +36 h (1200 UTC, 8 December), shown in Figs. 50 and 51. At Fresno, the sounding indicates saturation from just above the surface to about 950 m AGL (Fig. 50). The surface temperature is ~10 C (50 F) and the dew point depression is only ~0.5 C. Therefore, Table 6clearly implies that this sounding represents a deep fog layer. Although the period covered by the IMS-95 special soundings had not yet begun, the NWS surface observation at Fresno for this time (Fig. 7) reported fog, 10.5 C temperature, cloudy or obscured sky, and a dew-point depression of 0 C. Thus, the cooler surface temperature at this site in Exp. GS-3, compared to Exp. GS-2, is approximately correct. The model-simulated conditions at Bakersfield are also fairly reasonable. Figure 51 shows that the surface temperature is ~10 C. Near-saturated conditions prevail between the surface and 700 m AGL, indicating a rather deep fog layer. In contrast, Fig. 35 from Exp. GS-2 showed a 1.5-2.5 C dew-point depression in this fog layer. The observation at Bakersfield in Fig. 7 confirms the presence of fog, a temperature of 50 F (10 C), a surface dew-point depression of just 0.5 C, and broken clouds. However, in Fig. 51, the saturated layer near 950 mb indicates that the model is predicting a thin, but solid stratus layer at this time. Therefore, despite some remaining minor flaws, it appears that the changes in the surface conditions defined for Exp. GS-3 are having an overall positive impact on the fog and haze simulations at these two stations by + 36 h.

Moving ahead to the mid-point of the five-day simulation, at +60 h (1200 UTC, 9 December), the surface-layer wind field for Exp. GS-3 is shown in Fig. 52. This wind field can be compared with Exp. GS-2 (Fig. 36) and the observed winds (Fig. 10). Examination of Fig. 52 reveals characteristics similar to those in Fig. 36. There are weak southeasterlies around Bakersfield, with chaotic directions in much of the remaining SJV. Interestingly, the model shows weak northeasterly winds at Davis and San Francisco, suggesting that the accumulated cold air in the Valleys is draining out through the Carquinez Strait. The observation at Davis in Fig. 10 also has a northeasterly wind, implying that this drainage is real. Meanwhile, the surface-layer relative humidity is above 90 % throughout the SJV and Sacramento Valley (Fig. 53), indicating that radiation fog in Exp. GS-3 is very widespread on this morning. The simulation is confirmed by the widespread observed fog shown in the mesoscale analysis (Fig. 10) and by the satellite picture at this time (Fig. 11).

The MM5-simulated soundings for Fresno and Bakersfield in Exp. GS-3 at +60h are shown in Figs. 54 and 55, respectively. These can be compared to the simulations from Exp. GS-2 (Figs. 37 and 38) and the observed Bakersfield sounding (Fig. 9). The observed sounding had revealed 600-m deep fog at Bakersfield, with a surface temperature of 6.5 C, even though Fig. 10 showed an NWS surface observation of 7.0 C, fog with broken clouds, and a dew-point depression of 1 C. The NWS report suggested that perhaps the sounding should not have been saturated through such a deep layer, but it is not necessary to dispute the observed sounding. In Fig. 55, the MM5-simulated sounding in Exp. GS-3 shows a saturated fog layer ~450 m deep and with a surface temperature of ~9 C. This is cooler than the surface temperature in Exp. GS-2 by 2.5 C, but is still somewhat warmer than the observed temperature. At Fresno, the surface temperature in Fig. 54 is also 9 C, but the fog is a bit deeper (~500 m) with a surface dew point depression of ~1 C. The observed surface temperature at this time is especially cold (5.5 C), so the model simulation is certainly too warm. Thus, the colder values of T_m used in Exp. GS-3 are helpful in reducing the low-level temperature errors, but they have still not been eliminated.

For the rest of the study period, from + 72 h through +120 h, the evaluation of the model simulation in Exp. GS-3 will concentrate mostly on the soundings at Fresno and Bakersfield. Figures 56 and 57 present the MM5 soundings for the following afternoon, at +72 h (0000 UTC, 10 December). The Fresno sounding in Fig. 56 contains the characteristic signature for shallow fog, with a dew-point depression of 1.5 C, while the NWS surface observation indicated haze and a dew-point depression of 3 C. The mean humidity in the fog layer appears to be higher in Exp. GS-3 than simulated in Exp. GS-2 (compare to Fig. 39). Meanwhile, Fig. 57 shows that in Exp. GS-3 the model simulated an obvious fog layer at Bakersfield, while in Exp. GS-2, the model predicted haze with a possible thin stratus cloud. At this location and time, the observations are somewhat contradictory. The observed sounding (Fig. 12) indicates a saturated fog layer, much like Fig. 57. On the other hand, the NWS surface observation at Bakersfield reported haze and obscured sky (possible thin stratus deck). As stated earlier, when a contradiction arose between the two sources of observed data, the NWS report is accepted for the visibility type, unless there is clearly a evidence that that report is faulty. So, even though the Bakersfield special sounding data indicate fog, in agreement with the MM5, we will use the NWS surface report during the statistical evaluation in Sec. 5.5.

Next, Figs. 58 and 59 show the MM5-simulated soundings for these two sites at +84 h (1200 UTC, 10 December). Both model-generated soundings indicate a very shallow inversion layer and shallow radiation fog on this morning. Figure 59, for Bakersfield, can be compared with the observed sounding at the same time (Fig. 13). The observed sounding shows a very dry atmosphere above a 250 m fog layer, which is clearly deeper than the foggy layer implied in Fig. 59. At this time, the NWS surface reports at both Fresno and Bakersfield confirmed dense fog, obscured sky and very low visibilities (1/16 mile and 0 mile, respectively). The low visibility at this time, despite the dry air above the very shallow inversion, may have been the result of an accumulation of sulfates and other hygroscopic pollutants in the stagnant air mass through the previous 2-3 days of the episode.

By that afternoon, at +96 h (0000 UTC, 11 December), conditions in the SJV and Sacramento Valley were changing more rapidly as the Pacific storm approached the California coast. Recall that Fig. 15 showed mostly southeasterly winds in the Valleys at this time, with fog giving way to widespread haze in most areas (also see Fig. 16). In Exp. GS-3, the model did rather well in capturing this important change, even though the simulation had been running for four full days. Figure 60 shows that the surface-layer winds at +96 h throughout the Valleys has become southeasterly, except for some highly variable wind directions around Bakersfield. Speeds in Fig. 60 range from about 1-2 ms^{-1} between Bakersfield and 36 N. North of Fresno the wind in the Valleys increases to 2-4 ms^{-1}. Southeasterly flow also prevails in most of the near-coastal areas (both onshore and offshore), with southerly winds farther west over most of the Pacific Ocean. Comparison with the wind data in Fig. 15 reveals very good agreement between Exp. GS-3 and the observations. The wind speeds and directions at stations in the Valleys mostly confirm the model simulation, except that the MM5 failed to produce the southwesterly flow through the Carquinez Strait at this time. The coastal and ocean wind reports also confirm the patterns predicted by the model to the westward.

Also at +96 h, Figs. 61 and 62 show the model-simulated soundings at Fresno and Bakersfield. Notice that the winds in the model on this afternoon are south to southwesterly from the inversion layer to the tropopause. This reflects a deep zone of warm moist advection and the figures already show the impact of that moistening, especially above 500 mb. At the surface, the fog has definitely broken up in Exp. GS-3 at both stations. The simulated dew point depressions at this time are 6.5 C at Fresno and 5.0 C at Bakersfield, with surface temperatures of 15 C and 13.5 C, respectively. These simulated surface values indicate haze is probable at Fresno, but is marginal at Bakersfield (see Table 6). Nevertheless, the NWS surface observations at these stations both indicated haze, with identical temperatures of 15.5 C and dew-point depressions of 6.5 C. Apparently, in this case, the accumulation of pollutants allowed haze despite the rather large dew-point depression, relative to those that were common earlier in the study period. Thus, these results show that the model has done a remarkably good job at simulating the visibility characteristics at this time, along with the temperature and moisture conditions that influenced them. The observed sounding at Bakersfield (Fig. 14) also confirms a shallow inversion with a dew-point depression of ~5.5 C, although the low-level moist layer is about 300 m deep in the observation. Notice that Figs. 13 and 14 confirm the model prediction of significant moistening during the previous 12 h, even though these soundings do not extend high enough to capture the most moist layers aloft.

Finally, Figs. 63 and 64 show the MM5-simulated soundings in Exp. GS-3 at +108 h (1200 UTC, 11 December) shortly before the end of the model run (and after the last special IMS-95 soundings). The winds aloft now have shifted into the west and the profiles are rapidly approaching saturation. The model already has predicted saturation between 900 and 630 mb at Sacramento and Stockton, along with a saturated surface layer (fog) and rainfall (not shown). At this same time, the model's profiles in Figs. 63 and 64 indicate that, although clouds are just starting to overspread Fresno at 700 mb, rain has not yet begun either at Fresno or Bakersfield. This simulation by MM5 in Exp. GS-3 is confirmed by the NWS surface observations at this time (not shown), that show rain and fog at Sacramento, Stockton, Davis and other stations in the Delta region, but only broken skies and no rain at Fresno and Bakersfield. However, there is another surface observation in the SJV just 50 km southwest of Fresno (probably Lemoore Naval Air Station) that already is reporting rain. In the next several hours, the approaching rains and accelerating winds accompanying the Pacific storm brought an end to the SJV fog and haze episode in the model, very similar to the observed pattern. Overall, it is clear that Exp. GS-3 performed fairly well, although some modest errors were certainly noticeable, as well.

5.5 Statistical Evaluation of Fog Event

The model evaluations of the individual experiments described in Sec. 5.1-5.4 provide a tremendous amount of information about specific details in the model simulations at individual times. These time-specific evaluations are very important for determining whether or not the various model fields are consistent with the observations and with one another. As shown in several places, careful examination of these results was valuable for understanding which features were simulated well or poorly, and hence were critical to determining the most likely sources of errors found in the solutions. However, despite the obvious value of such detailed inspections, the amount of information can be overwhelming. This can make it difficult to

determine the overall accuracy of the experiments. Consequently, in this section, an objective statistical analysis of the MM5 results is presented.

Because the MM5 has been extensively evaluated against observations in many prior studies, including several for cases in CA, it is not necessary to compute statistical scores for winds, temperatures and mixed-layer depths in this case. Not only would that be redundant, but there were very few special upper-air sounding available in IMS-95 (two radiosondes at 6-h intervals and two wind profilers at 1-h intervals). Therefore, because the primary objective of the present study is to evaluate and understand the MM5's capability for simulating haze and fog conditions in the SJV, the statistical evaluations have been focused to examine thoroughly that particular capability.

The MM5-simulated soundings were collected at 6-h intervals and compared carefully to the IMS-95 special radiosondes and NWS surface reports at both the Fresno and Bakersfield sites. These observed soundings were available on 9-11 December 1995 through the peak period of the fog and haze episode. Because Exp. GS-1 had serious errors in its temperature simulations and Exp. BLK-1 was run for only 36 h, they were not subjected to the statistical evaluations. However, the remaining experiments (Exps. GS-2 and GS-3) were evaluated in detail. Tables 7-10 show the observed and model-simulated conditions at each individual site and for both experiments. Table 11 provides an overall statistical summary (mean errors and mean-absolute errors) comparing the two experiments, based on the data compiled in Tables 7-10. The estimates of visibility types for the model experiments are derived on the basis of Table 6.

For the observed weather conditions, Tables 7-10 show composite drawn from the surface observations (for obscuration type and visibility) and the special radiosondes (for depth of the obscuring layer). From the model, the type and depth of the visibility obscuration can be determined, but no attempt is made to estimate a visibility range. That type of determination would be possible, but only by developing an empirical relationship based on a much greater amount of raw observations for the SJV than is available in this period. Generalized fog visibility statistics from other sources are unlikely to be successful in this area because of the unusual nature of the SJV wintertime fog events that are influenced by a combination of anthropogenic pollutants and topographically related air stagnation. The difficulty of relating model-simulated conditions to visibility is in this area is accentuated by widely differing values of observed visibility reported with similar dew-point depressions. In at least one report, the visibility at Fresno was reported as only two miles during hazy conditions, even though at the time the dew-point depression was 12 F (relative humidity of ~63 %).

To aid in interpretation of possible ambiguous cases, the two right hand columns of Tables 7-10 give the observed and model-simulated values of surface temperature and dew-point. There are two separate values for the *observations* at each time because both the reports from the NWS and the special radiosondes are shown (the radiosonde report is shown in brackets).

The principal statistical results are tabulated in Table 11. Combining information from both sites, this table demonstrates that in Exp. GS-3, the MM5 was able to correctly estimate the type of visibility obscuration that was reported for 14 out of the 18 events occurring in the period 9-11 December 1995. (An "event" is an individual place and time during the 3-day evaluation

period.) The fog depth in Exp. GS-3 was estimated with a mean absolute error of only 92 m and a mean error of -41 m. Mean errors for the surface temperature and dew point were within 1 C, while the mean absolute errors were ~1.5-2.0 C. This is a very good result, considering that temperature and dew point are generally more difficult to predict at the surface than anywhere else in the troposphere. Comparison of the statistics between the two experiments also shows clearly that the modifications to the surface characteristics introduced in Exp. GS-3 (moderately lower T_m and higher soil-moisture availability) led to significant improvement in the simulation of the fog and haze characteristics. The primary problems in Exp. GS-2, according to the table, were that the surface temperatures were too high (+3.97 C mean error), while the mean error of the dew points were too high by a smaller amount (+2.29 C). Thus, not only were the temperatures too warm, but the dew-point depression was over-estimated by an average of ~1.7 C. This inevitably causes a decrease of fog and haze occurrence and severity. The mean errors for temperature and dew point in Exp. GS-3 are considerably smaller, but almost as important, they are both about the same size. Thus, the mean error of the dew-point *depression* in Exp. GS-3 is only ~0.1 C. This is an obvious advantage for simulating fog and haze.

6. EXPERIMENTAL DESIGN OF SoCAB SEA BREEZE SIMULATIONS

6.1. **SCOS97 Data**

Objectives of the CARB sponsored observational summertime SCOS97 study include (Fujita et al. 2000) an*:* updated database; new understanding of relationships between emissions, transport, and ozone exceedances; and plans for further emission reductions needed to attain the ozone NAAQS in the SoCAB.

Objectives of the current study include use of SCOS97 data and MM5 simulations to understand meteorological factors in the formation of high ozone concentrations in the SoCAB. Particular emphasis is placed on early morning boundary layer growth and its effects on downward fumigation of residual layer ozone. The period of 4-7 August was selected for study by CARB, as maximum SCOS97 surface ozone concentrations (187 pphm) were found during the afternoon of 5 August at 2200 UTC (1500 PDT, Pacific Daylight Time). Somewhat lower concentrations (121 pphm) were found at 1000 and 1100 PDT at a few sites on this day, indicative of possible fumigation processes.

Meteorological data for the case study (Fujita et al. 2000) include hourly measurements of wind, temperature, and relative humidity from 259 surface sites and ozone from 116 sites. After a CARB QA analysis, the 110 most reliable surface meteorological sites were selected (Figs. 66a,b and Table 12a). SCOS97 is also rich in upper air meteorological measurements, including wind, temperature, and humidity profiles every six hours (starting at 0500 PDT) from 12 rawinsonde sites (Fig. 67a) and hourly averaged (centered on the half hour) wind and temperature profiles from 26 RWP/RASS profilers (Fig. 67b). Rawinsonde data were QAed at CARB and SJSU, while profiler data were QAed at NOAA ERL by Wolfe and Weber (1999). Note that few surface and upper air sites are, in fact, located at high elevations.

Rawinsonde (Table 12 b) and profiler data (Table 12c) were vertically interpolated (by a linear scheme) to key AGL levels (e.g., within the sea breeze and synoptic flows). These values, and the hourly surface meteorological data, were then interpolated horizontally to a regular grid in the Lambert conformal space used for plotting MM5 output using the inverse distance-square weighting objective-analysis scheme of Daley (1991). Interpolated data were then smoothed using a four-point scheme developed by Lin (2000), and then finally plotted in various planes by the NCAR, MATLAB, or SURFER graphics software packages. Horizontal plots were constructed at the surface (i.e., at 2 m, except at 5 m for winds) and at the predetermined key AGL levels. Rawinsonde and profiler time-height sections for selected sites, for either the entire study period or for each day, were plotted and contoured by MATLAB.

Arbitrarily oriented vertical cross sections using profiler data were constructed using SURFER for selected times. Sections present data in an MSL format that included a topography profile along straight lines running parallel and perpendicular to the SoCAB coast in regions with a maximum station density. Horizontal distance in these charts is proportional to the actual straight-line distance between adjacent sites along the accordion shaped path that connected adjacent profilers located close to the straight line of the cross sectional plane. They do not represent distances between projections from adjacent sites to the cross sectional plane. Values were contoured using SURFER.

6.2. MM5 Application for SoCAB Simulations

MM5 Version 2.12+ was used to simulate the 1997 five-day SoCAB ozone episode period that began on 0500 PDT on 2 August. This version contained the PSU Marine Boundary Layer Initialization (MBLI) scheme of Leidner et al. (1999), not yet in NCAR MM5 releases. The scheme, used during a 13-hour spin-up period, quickly establishes a realistic MBL in generally data-sparse marine regions. Establishment of such a simulated layer during summertime GC Pacific High conditions normally requires about 48 hours, because the cool marine surface produces only weak near-surface shear-induced turbulence that is mostly suppressed by subsidence-induced stability. Only the latter four simulation days of the five-day simulation were thus used for model performance evaluation.

Quadruple nested grid domains were used, based on a Lambert conformal-projection. Domain 1 (outermost) is centered at 34.5N, 118W (Fig. 68), has a horizontal resolution of 135 km, and 41 x 33 horizontal grid points in the E-W and N-S directions, respectively. The domain possesses a large upwind fetch that includes the Pacific High. Domain 2 has a grid resolution of 45 km and dimensions of 67 x 61; Domain 3 has a resolution of 15 km and dimensions of 91 x 85; and the inner domain (Domain 4) has a grid resolution of 5 km and dimensions of 121 x 85. All domains have 30 vertical layers (Table 13), with a minimum sigma level closest to the surface that corresponds to 46 m; wind and temperatures are calculated at half sigma levels.

The new 25-category U. S. Geological Survey (USGS) global land-use distribution in MM5 was used for the SoCAB simulations (Dudhia et al. 1999), with 10 min (of latitude and longitude) resolution in Domains 1 and 2, 5 min in Domain3, and 30 sec in Domain 4. Grid averaged topographic height values in MM5 for the SoCAB were obtained from: PSU/NCAR for Domain 1, Geophysical Data Center for Domains 2 and 3, and Defense Mapping Agency for Domain 4.

GDAS global gridded model analyses and SSTs, both at resolutions of 2.5 x 2.5 degrees, were obtained from the NCAR Mass Storage System. Both provided initial and boundary conditions, the latter at 12-hour intervals with linear interpolation for intermediate time steps. In MM5, the input integration time step for the coarsest domain is set to three times its horizontal grid size, producing a value of 405 s in the current application. Time step sizes for the remaining domains are likewise internally computed.

Low-resolution Domain 1 input GDAS fields were improved by assimilation of data from about 70 upper air and several hundred surface sites (via the MM5 RAWINS preprocessor). Initial conditions for the inner three domains are obtained via sequential interpolation of values from its encompassing coarser domain. Analysis nudging (with NCAR GDAS fields) and/or observational nudging, (with SCOS97 observations) are used only in the three outer domains for most of the current simulations and only in the outermost domain for the last two simulations (reasons discussed below). As NCAR GDAS values (available at 12-hour intervals) were thus linearly interpolated in time and space, smaller scale events produced by upper-level forcing may not thus be captured.

Analysis nudging terms in the MM5 momentum, temperature, and moisture prognostic equations "relaxes" grid point model values towards nearby interpolated NCAR GDAS values. The nudging terms are linear and thus assumed proportional to a "nudging function" times the difference between MM5 simulated and NCAR-GDAS values at each grid point. Analysis nudging in the SoCAB was only carried out above the PBL (assumed at 850 mb) in Domains 1-3.

Each "nudging function" is the product (Grell et al. 1994) of a: nudging factor (or coefficient), weighting function, and analysis factor. As nudging terms must not dominate governing equation terms, they are scaled by the slowest model adjustment-process (i.e., inertial effects). The nudging factor (determines impact of new terms) is thus defined as similar in magnitude to the Coriolis parameter. Its values are user-selected, and in the current application they were set to $1x10^{-5}$ for Domains 1-3 for moisture and for Domain 3 for wind and temperature. They were also set to $2.5x\ 10^{-5}$ for wind and temperature for Domains 1 and 2 (Stauffer 2001).

The internally specified weighting function is the product of horizontal, vertical, and time weighting functions. The temporal weighting function is set to unity, except at the end of a dynamic-initialization period. Horizontal weighting-function components are internally set to unity, while the vertical weighting function is internally set to: zero in the PBL, 0.1 in the next vertical grid layer, and 1.0 aloft. Finally, the also internally set analysis factor (from 0 to 1) depends on the data used to produce the input gridded analysis.

Observational nudging terms in MM5 are similar to analysis nudging terms, but use only SCOS97 observations that fall within a preset radius of influence and within a predetermined two-hour time window centered about each model time step. Observational nudging for wind was carried out throughout the vertical model extent in Domains 3 and 4, while temperature and moisture were again only nudged above the PBL. Based on an average distance of 20 km between SCOS97 surface observational sites, Stauffer (2001) recommended a 75 km radius of influence. With increasing height, the number of SoCAB measurement sites decreases, and thus

the distance between observational sites increases. Hence, the recommended radius of influence was doubled, but this is not a problem as upper level gradients are smoother than those at the surface. Horizontal weighting functions are inverse-square distance types, while the vertical component uses an inverse distance function. The temporal function is unity for one-quarter of the time window period, and then decays to zero.

Other options selected for the current SoCAB simulations include: Deardorff (1972) force-restore surface temperature, Dudhia (1989) simple ice, Kain and Fritch (1993) cumulus parameterization in the outer three domains (none in inner domain), Gayno (1994) 1.5 order TKE (only normally available in MM5 Version 3), and one-way continuous (Lozej and Bornstein 1999) nesting. With this nesting option, only one MM5 simulation is required and information is fed to the inner domains each time step, and there is no feedback from inner to outer domains. With "normal" one way nesting, each domain is simulated in a separate run, outputs are kept at hourly intervals, and information is feed to inner domains at that interval. Two-way nesting is like continuous one-way nesting, but there is feedback from inner to outer domains.

6.3.. MAPS Statistical Analyses

Statistical evaluation of model results was conducted using the Model Performance Evaluation, Analysis, and Plotting System (MAPS), developed for (urban and regional scale) meteorological, emission, and photochemical model evaluation (Tesche 1994). MAPS uses a variety of statistical and graphical methods recommended for use in model performance evaluations by various air quality control agencies (e.g. Tesche and Lyons 1991, Tesche and Roth 1998).

Performance evaluation is a method to develop confidence in a model's ability to adequately simulate physical phenomena. Though specific model performance-evaluation statistics are commonly used with air quality models (EPA 1996), no such standards exist for meteorological models. It is still, however, possible to evaluate meteorological model performance for a given episode against historical data sets.

Model performance evaluation tests the ability of a model to estimate observed meteorological data over a range of conditions. It thus guides model development and data collection, as well as model analysis, testing, and re-testing. The "model" includes not only predictions, but also supporting input databases and related analytical and numerical procedures that produce model results. In fact, model performance may be more sensitive to input values than to its formulation. Inherent spatial variability also produces significant deviations between evaluation point measurements and spatially averaged simulated phenomena.

Operational evaluation is an assessment of model ability to estimate correct answers, whether or not processes described in the model are accurate. Scientific evaluation examines the accuracy of the physical and chemical process within the modeling system. Scientific evaluation is comprised of diagnostic, mechanistic, and comparative evaluations. Diagnostic evaluation assesses model ability to simulate processes (e.g., development of the CBL or fog). Diagnostic evaluation uses tests designed to stress the model science, while mechanistic evaluation assesses module ability to reproduce specific observed phenomena (e.g., advection or wet deposition). When applied to all process modules in the full model, mechanistic evaluation represents an

accuracy test of its underlying science. Comparative evaluation inter-compares models or modules against observed data.

The desired outcome of a complete model performance evaluation is validation, attained when minimum acceptable levels of agreement between model predictions and observations are achieved. Validation is achieved only through successful completion of various model performance evaluations, diagnostic analyses, and model modifications. Despite continued progress in model performance evaluation, current practice is hindered by (Tesche 1991):

> Lack of adequate databases to provide thorough performance testing. Seldom are high-resolution databases, similar to that collected for SCOS97, available for intensive mechanistic evaluation.

> Lack of consistency among performance evaluations conducted by different groups. For example, various definitions of wind speed cutoff level or time period over which model performance is quantified have been used. Further, results are presented in a variety of graphical formats that lead to difficulty when inter-comparison is attempted.

> Use of conflicting definitions of key performance measures, such as bias, peak estimation accuracy, skill, and correlation.

> Inability of most statistical measures to clearly reveal model flaws, data base deficiencies, and compensatory errors in models and/or data.

> Lack of agreed upon criteria to judge acceptable model performance.

Regardless of shortcomings, it is still possible to provide quantitative insight into MM5 performance for the 3-6 August 1997 SCOS97 episode through use of statistical measures that compare meteorological observations to MM5 predictions. Definitions of these measures are understood, but their interpretation is subjective and hence open to debate. The current model performance evaluation focused on the ability of MM5 to reproduce observed surface wind speed, wind direction, and temperature, ergo an operational evaluation.

Mean observation is given by

$$M_o = \frac{1}{N} \sum_{i=1}^{N} \Phi_{oi} \quad ,$$

where N is the product of the numbers of observed hours and ground-level monitoring locations providing hourly-averaged data, and Φ_{oi} represents observations at hour i. A cutoff level may be applied to observed values, below which both estimated and observed values are excluded from the statistic. In this study, a 1 m s^{-1} wind speed was used, as a number of anemometers used during SCOS97 had such a measurement threshold.

Mean model-estimate is given by

$$M_e = \frac{1}{N} \sum_{i=1}^{N} \Phi_{ei} \quad ,$$

where Φ_{ei} represents a model estimate at hour i.

Mean bias error is given by

$$MBE = \frac{1}{N} \sum_{i=1}^{N} (c_e(x, t) - c_o(x, t)) \quad ,$$

where c_e is an estimated value at position x and time t; and where c_o is the concurrent observed value.

Mean gross error, given by

$$MAGE = \frac{1}{N} \sum_{i=1}^{N} | c_e(x, t) - c_o(x, t) | \quad ,$$

is a robust measure of overall model performance.

$$RMSE = \left[\frac{1}{N} \sum_{i=1}^{N} | \Phi_{ei} - \Phi_{oi} |^2 \right]^{1/2} \quad ,$$

Root mean square error, given by.

is also a good overall measure of model performance. However, since large errors are weighted heavily, a few such values can produce a large *RMSE*.

Model linear bias (or systematic error) is given by

$$RMSE_s = \left[\frac{1}{N} \sum_{i=1}^{N} | \hat{\Phi}_{ei} - \Phi_{oi} |^2 \right]^{1/2} \quad ,$$

where $\hat{\Phi}_{ei}$ is estimated by the following regression of predictions on observations

$$\hat{\Phi}_{ei} = m\Phi_{oi} + b \quad .$$

Model noise (or unsystematic error) is given by

$$RMSE_u = \left[\frac{1}{N} \sum_{i=1}^{N} | \Phi_{ei} - \hat{\Phi}_{ei} |^2 \right]^{1/2} ,$$

which measures the discrepancy due to random influences.

A "good" model run produces low *RMSE* values and thus explains most observational variations. As the systematic $RMSE_s$ error should approach zero, the unsystematic $RMSE_u$ error should approach the *RMSE,* since:

$$RMSE^2 = RMSE_u^2 + RMSE_s^2 \quad .$$

If the *RMSE* consists largely of bias, it might be removed, but if it consists largely of noise, this indicates further error reduction may require model refinement and/or data acquisition. It also provides error bars for inputs for subsequent sensitivity analyses.

Following Wilmont (1981), the index of agreement I, which condenses all model-observation differences, is given as

$$I = 1 - \left[\frac{N \ (RMSE)^2}{\sum_{i=1}^{N} (| \Phi_{ei} - M_o | + | \Phi_{oi} - M_o |)^2} \right] .$$

I is thus the ratio of the cumulative difference between model estimates and observations to the sum of the differences between estimates and the observed mean and between observations and the observed mean. It is thus a measure of model estimate departure from observed mean matches, and it thus ranges between 0 and 1, with the latter suggesting perfect agreement. Finally, the boundaries of the currently assumed SoCAB MM5 performance sub-domains (Fig. 68) were selected based on similar geographic features, but are open to refinement.

7. DESCRIPTION OF OBSERVED METEOROLOGY DURING SoCAB SEA BREEZE EPISODE

7.1. Summary/Preview

This section presents a summary and synthesis of observed meteorological conditions during the simulated 3-7 August SCOS97 ozone episode, for which a preliminary analysis was presented by Bornstein and Boucouvala (2000). Details and supporting data are shown in the following sections. For readability, SCOS97 date-hour specifications generally will be abbreviated, so that

0500 UTC on 06 August 1997 will be noted as 06/05UTC, and its PDT equivalent of 2200 PDT on 05 Aug 1997 will be given by 05/22PDT.

Weak and only slightly changing anticyclonic synoptic forcing existed over the SoCAB throughout the test period. NWS 300 mb charts did show that a high over the western U. S. kept both the GC long wave trough and Polar Front jet far from SoCAB. They also showed a: cut off low west of Vancouver Island, strong ridge over the western U. S., weak local coastal high over SoCAB, and low upper level wind speeds. By 06/00UTC (05/17PDT, near the time of the surface ozone episode), the upper-level coastal high reached its maximum intensity, and upper level temperatures increased as the GC subsidence inversion-base lowered. A surface inverted i.e., south to north pointing) thermal low-pressure trough and a coastal high also did not changed much over southern California throughout the test period, and surface wind speeds were also minimal. Given a synoptic scale data scarcity, however, NWS charts cannot show the fine details of the above synoptic forcings.

Use of NCAR GDAS reanalysis 650 mb pressure charts and AGL RWP profiler winds at the 3800 m allowed for a more accurate assessment of the 700 mb coastal-high and the associated changes in synoptic forcings and upper level wind flows. These charts first showed a small scale high over the SoCAB high at 05/00UTC. It then moved slightly southward and enlarged westward during the next 12 hours, moved back northwest ward past its original coastal location by 06/00UTC (05/17PDT, time of ozone episode), and then dissipated by 06/12UTC. The north to south movement changed the synoptic background flow over SoCAB from (westerly) onshore to (easterly) offshore.

Offshore rawinsondes showed a persistent strong (10 K) subsidence inversion with a top at about 600-800 m AGL. Inversion-top temperature and intensity peaked at 06/06UTC (05/23PDT, six hours after the surface ozone peak). The peaks resulted from increased subsidence from the upper level high (seen on NWS charts), which warmed upper level temperatures and strengthened (and lowered) the inversion base. Patterns were similar at coastal sites, except that inversion intensity peaked one launch (i.e., six hours) earlier, implying a westward movement of the synoptic high (see NWS discussion above). Temperatures at the inland sites showed little influence from the high, but did show maximum temperatures aloft at the same times as SNIC and UCLA.

The more frequent RASS temperature profiles were generally consistent with those from rawinsonde sites. The vertical variation of the warming on 4 August at coastal sites was reversed from that produced by normal upward progression of surface heating, as subsidence-induced warming started at the inversion top during the nighttime period. An additional day of subsidence warming left the PBL warmer by up to 5.5 K, while absolute maximum offshore temperatures were reached at 500 m AGL on 06/06UTC, when the inversion base had fallen rapidly over the preceding six hours. Profiles at coastal sites on 4 August also show (as did coastal rawinsonde data) a persistent strong inversion, whose top is at about 600 to 800 m AGL (as at SCL). The vertical variation of warming on this day was not reversed from that produced by upward progression of surface heating, and thus subsidence produced warming was not yet a major influence at coastal sites (as offshore). A shallow sub-inversion MBL, was evidence of coastal sea breeze penetration.

RASS profiles at inland sites on western slope of San Gabriel Mountains on 4 August showed maximum subsidence warming 48 and 24 hours earlier than at offshore and coastal sites, respectively, again consistent with a westward moving synoptic high. Note that the 300 m AGL deep daytime mixed layer at was not present at offshore and coastal sites, and was probably due to convective heating. Profiles further inland on the eastern slope of the San Gabriel Mountains continued the trend of weakening subsidence inversion strength with inland distance from the offshore synoptic high and showed almost no elevated inversion layers and only minimum synoptic forcing aloft. These inland sites again reached maximum temperatures at 06/00UTC (about time of peak ozone), and showed values generally warmer than the other sites.

The near-midnight, "along-coast" RASS section on 04/06UTC showed a strong inversion over the Los Angeles Basin, with a top at 800 m MSL, base at 200 m MSL, and strength of 4-9^{0}C. The concurrent "perpendicular to coast" section shows the inversion confined to the Los Angeles coastal plain, with a top sloping upward to the east to a maximum height of 1000 m MSL. Its base likewise slopes upward from 200 to 450 m AGL (550 m MSL), with two shallow embedded non-inversion layer "holes" at 700 and 800 m over ONT. Within these layers, non-inversion lapse rates exist.

The daytime "along coast" section on 04/18UTC again showed a strong inversion over the Basin, but with a top 200 m below that 12 hours before. This sinking again resulted from the westward movement of the Pacific High, which also increased maximum temperatures (near inversion top) and inversion strength (to 7.0-8.5^{0}C). In the concurrent "perpendicular to coast" section the inversion is again confined to the Basin. Its top does not, however, slope upwards to the east (as 12 hours before), but is fairly uniform at 600 m MSL. No holes (layers without an inversion lapse rate) in the inversion existed (as they did12 hours before).

The near-midnight, along coast section on 05/06UTC showed an even stronger inversion over the Basin, with a top 150-350 m lower than 24 hours before. Maximum temperatures near its top have increased 1-3^{0}C, and inversion strength has become more uniform. The concurrent perpendicular section shows the inversion now extending across the entire section, with a top that again slopes upwards (following the topography) from 650 to 1100 m MSL. Its base is 250 m AGL, and its intensity decreases from 10^{0}C at the coast to about 1^{0}C inland. The non-inversion layer hole grew to extend over all sites west of the San Gabriel Mountains, and its elevation also follows the topography.

The daytime, along-coast section at 05/18UTC showed that continued westward movement of the synoptic high producing a more widespread, deeper (900 vs. 600 m MSL), and warmer (about 3-4^{0}C) elevated inversion layer. The concurrent perpendicular section shows a now irregular inversion top (1100 to 700 m MSL), base now generally following the topography, and a more organized embedded non-inversion layer.

The coastal section on 06/06UTC shows that maximum temperatures near the inversion top have increased by about an additional 3.0-3.5^{0}C, while those near the surface have warmed somewhat less than that, thus slightly increasing inversion strength. The concurrent perpendicular section again shows the inversion sloping upwards westward from 400 to 1400 m MSL, or about 300 m

higher than 24-hours previous. Inversion top temperatures are now even warmer by about 2.5^{0}C, but inversion intensity has decreased substantially from that 24-hours previous.

The daytime, along-coast section at 06/18UTC still shows a deeper top (up to 1050 m). The warming trend is now a cooling trend, in which inversion top and bottom values have decreased by about 3^{0}C. The isothermal layers embedded within the inversion have now strengthened into weak lapse layers embedded (at 400 and 700 m MSL) within the inversion over LAX and LAS, and at 800 m MSL at CBD. The concurrent perpendicular section shows the inversion also outside Basin at HPA and BTW. Its top (temperatures still 32^{0}C) has lowered near the coast and has become more regular (at 850 m MSL). Its base, however, has risen to 400 m AGL over the basin, and the non-inversion layer hole is the inversion is gone. Rawinsonde patterns were similar at coastal sites, except that inversion intensity peaked one launch (i.e., six hours) earlier, showing the same westward movement of the synoptic high seen on the GDAS charts. Temperatures at inland rawinsonde sites showed little influence from the coastal high, but did show concurrent maximum temperatures aloft.

The more frequent RASS temperatures were generally consistent with rawinsonde values. The vertical variation of the warming on 4 August at offshore sites was reversed from that produced by the normal upward progression of surface heating, as subsidence-induced warming started at the inversion top during the nighttime period. One day of subsidence warming increased PBL temperatures by up to 5.5 K, with maximum values again (as at the rawinsonde sites) reached at 500 m AGL on 06/06UTC, after the inversion base had fallen rapidly over the preceding six hours. Subsidence produced warming at coastal sites was not a major influence until the 5th, while its effects were not felt at inland sites on the western slope of San Gabriel Mountains until the 6th, again consistent with a westward moving synoptic high. Profiles further inland on the eastern slope of the San Gabriel Mountains showed almost no elevated inversion layers and only minimum synoptic forcing aloft.

The near-midnight "along-coast" RASS vertical cross section on 04/06UTC showed a strong inversion over the Basin, with a top at 800 m MSL, base at 200 m MSL, and strength of 4-9^{0}C. The concurrent "perpendicular to coast" section shows the inversion confined to the coastal plain, with a top sloping upward (following the topography) to the east to a maximum height of 1000 m MSL. Its base likewise sloped upward from 200 to 450 m AGL, with two shallow embedded non-inversion layer holes (700 and 800 m).

The daytime coastal section on 04/18UTC also showed a strong inversion, but with a top 200 m below that 12 hours before. This sinking again resulted from the westward movement of the Pacific High, which also increased maximum temperatures (near the inversion top) and inversion strength to 8^{0}C. In the concurrent perpendicular section, the inversion top was fairly uniform at 600 m MSL and showed no layers with non-inversion lapse rates.

The near-midnight coastal section on 05/06UTC showed a still stronger inversion, with tops 150-350 m lower than 24 hours before. Maximum temperatures near its top had increased 1-3^{0}C, and inversion strength had become more uniform. The concurrent perpendicular section showed the inversion now across the entire section, a top again sloping upwards from 650 to 1100 m MSL, a base at 250 m AGL, an intensity that decreased from 10^{0}C at the coast to about 1^{0}C inland, and a

non-inversion hole over all sites west of the San Gabriel Mountains. The daytime coastal section at 05/18UTC showed that the continued westward movement of the synoptic high had produced a more widespread, 300 m deeper, and warmer (about 3-4^{0}C) elevated inversion layer. The concurrent perpendicular section showed a now: irregular inversion top, base that generally following the topography, and more organized embedded non-inversion layer.

The nighttime coastal section on 06/06UTC shows maximum temperatures near the inversion top increased by an additional 3^{0}C, while those near the surface have warmed somewhat less, thus increasing inversion strength. The concurrent perpendicular section again showed the inversion sloping upwards westward at about 300 m higher than 24-hours previous, but its intensity decreased substantially. The daytime coast section at 06/18UTC shows a deeper top (up to 1050 m), cooling (and no longer warming), inversion top and bottom values decreased by about 3^{0}C, and strengthened non-inversion holes. The concurrent perpendicular section shows its top lowered near the coast and more regular (at 850 m MSL), its base higher, and the non-inversion holes gone.

Rawinsonde wind velocity time-height cross-section over the entire period at an offshore site shows smoothly varying patterns, and in particular a prevailing westerly flow from 04/20UTC to 05/06UTC throughout its entire 3000 m AGL depth. The first sign of a shift to an easterly flow (associated with the westward movement of the synoptic high) is seen in the upper levels of the 05/12UTC sounding, and the shift reaches the surface two hour later. Easterly flow persists in the upper layers of the section throughout the episode day until 07/00UTC, after which it returns to a more normal westerly flow.

A coastal rawinsonde section showed the prevailing westerly flow shift more slowly. Its 3000 m AGL flow first became northerly at 05/00UTC, but took 18 hours to reach down to 1500 m AGL. Easterly flow persisted in the upper layers of the section throughout the episode day until 06/18UTC, after which it returned to a more normal westerly flow over the next 12 hours. During the 4th and 7th, its onshore sea breeze flows were in much the same direction as the synoptic flow, while on the 5th (episode day) it was perpendicular the then easterly prevailing flow. On the 4th the sea breeze depth is about only 550 m AGL, above which is a chaotic transition layer up to about 2000 m AGL, with the easterly return flow layer above. The shallow nighttime offshore land breeze at 05/06 and 05/12UTC only extends up 200 m AGL, and a northerly transition layer at 400 m AGL appears to coincide with the non-inversion hole.

On the 5th (episode day) the sea breeze depth flow direction was from the south, while at 05/18UTC it was only 400 m deep, six hours later it reaches to either 1700-2300 m. A land breeze at 06/06 was about 400 m AGL deep and was capped by a 600 m deep northerly transition layer. As the return flow aloft was now in a direction opposite to the now easterly offshore synoptic flow, it was possible to discern the boundary between the two at 2200 m AGL. On the 6th the sea breeze depth flow direction was again (as on the 4th) from the northwest. The land breeze at 07/06UTC was uncharacteristically strong and deep (about 1000 m AGL), and had almost no northerly transition layer.

At an inland site on the eastern side of the San Bernardino Mountains (too far inland for coastal sea breeze influences), lower level winds were a complex combination of topographic influences.

During nighttime hours, shallow (southerly or westerly) down-slope flows dominated near the surface, while during daytime hours shallow (easterly or southerly) upslope flows predominated.

The profiler section at an offshore site on 4 August showed that the prevailing generally southerly synoptic flow (above 15000 m AGL) shifted to a westerly flow between 04/13UTC and 04/19UTC. The onshore near-surface generally westerly marine flow lasted until about 05/08UTC (or 05/01PDT), was generally about 1400 m deep, and was generally capped by a shallow chaotic layer of about 200 m in depth, which deepened after 04/17UTC due to establishment of an early morning easterly return flow layer. The prevailing generally northerly synoptic flow on 5 August started to weaken at 05/00UTC. From 05/07UTC to 05/11UTC, the synoptic flow turns to an easterly flow, which raised its base up to 2200 m AGL (from 1600 m on the previous day). After the synoptic direction change, the near-surface westerly marine flow weakens and was replaced by a weak chaotic layer of about 1000 m in depth, above which the marine flow continued to about 2000 m AGL.

Offshore easterly flow seems to have reached the island site during the four-hour period from about 05/14UTC, as it was apparently able to overcome (with help from the still easterly upper level synoptic forcing) the weak pressure gradients existing during the previous five hours. Onshore marine flow then returned, was again about 900 m deep and capped by a shallow weak chaotic transition layer and by the still easterly synoptic flow, whose based had lifted to about 2000 m AGL by 06/00UTC. The westerly marine flow near the surface lasted until about 06/10UTC, when the flow in an ever-deepening surface based layer become southerly and by 06/22UTC grew up to 1100 m AGL.

The section at a coastal site on 4 August showed an onshore generally westerly coastal sea breeze flow lasted near the surface until about 04/04UTC (03/21PDT) to a depth of about 1400 m deep. The layer was capped by: a shallow chaotic layer of about 300 m in depth, a shallow (100 m) southeasterly return flow layer, and the prevailing southerly synoptic flow discussed above. The nocturnal downslope offshore combination (drainage and land breeze) flow at this coastal site started about 04/05UTC, was about only 600 m deep, and was apparently capped by a westerly return flow region up to about 1400 m AGL and by the still southerly synoptic flow. The sea breeze that replaced this nocturnal flow on the following morning at about 04/18UTC (04/11PDT) after a few hours of chaotic transition was about the same depth as 24 hour pervious.

The prevailing generally northerly synoptic flow on 5 August first weakened at 05/00UTC and then was undercut at 05/02UTC by a layer of easterly flow (discussed below) that raised its base up to 3500 m AGL (from 2000 m 24 hours previous). The synoptic flow was then turned easterly at about 05/09UTC. The onshore westerly sea breeze was similar (in start time, intensity, depth, and duration) as 24 hours previously. It was again capped by a: chaotic layer to about 2200 m AGL (and thus was about 200 m deeper than on the previous day), an easterly return flow layer to about 3000 m AGL, and the then prevailing northwesterly synoptic flow discussed above. Note that the return layer on this day was deeper and stronger than that on the 4th, as the stronger synoptic flow on that day could mostly suppress a return layer. The nocturnal offshore flow again started about 0600 UTC, was again about only 700 m deep, and was capped by a now northerly return flow region up to about 2000 m AGL and then by the now easterly synoptic flow.

The prevailing generally easterly synoptic flow appears to persist throughout the 6th. The onshore westerly sea breeze flow that began at 05/18UTC (05/11PDT) on his episode day lasted until about 06/05UTC (05/22PDT). While this approximated the sea breeze period of the previous day, this westerly breeze was deeper (above top of data at 2700 m AGL vs. 1400 m AGL) and faster (7 vs. 5 m s^{-1}) than on the two previous days. This strengthening was probably associated with the above discussed strengthening of the high aloft, which increased onshore pressure gradients aloft due to its effect on coastal land temperatures.

In summary, a first synoptic wind shift over the SoCAB was consistent with a westward movement of the synoptic high. The Basin was thus no longer on its northern side (with a generally southerly flow), but was now on its northeastern side (with a generally westerly flow). The second shift was consistent with a northwestward movement of the high, with the Basin no longer on its northeastern side, but now on its eastern side (with a generally northerly flow). This final shift was consistent with a northeastward movement of the high, which means that the Basin was no longer on its eastern side, but was now on its southern side (with generally easterly flow).

In the near-midnight coastal vertical section of total horizontal profiler winds over the Los Angeles Basin on 04/06UTC, lower level flow (below 2000 m AGL) had a generally westerly (onshore) component, while that south of the basin generally had a northerly (offshore) component. This is consistent with flow around the northeastern edge of a coastal high located just offshore of the basin, i.e., the flow would change from westerly to northerly as one goes southward along the coast. In the concurrent perpendicular section, offshore nocturnal drainage and/or land breeze flows were seen at the western sites, while the most inland sites showed onshore westerly flow. The depth of the offshore flow about equals the depth of the marine and elevated inversion layers over the Basin, and all Basin sites showed what could be a westerly return flow layer (centered at about 1000 m AGL) in between the offshore and synoptic flows.

The 04/18UTC (04/11PDT) coastal section showed that the offshore nocturnal drainage flow has been replaced by an onshore westerly-component sea breeze flow with a depth of about 500 m AGL. This flow is thus restricted to the sub-inversion layer, and several sites showed the beginning of a weak return flow layer above the sea breeze layer. By 04/22UTC the northerly section of the upper level synoptic flow had enlarged northward over the Basin. The sea breeze flow, however, is now stronger, deeper (up to about 900 m AGL), and over the entire Basin. The return flow layer was also stronger, deeper (centered at about 2000 m AGL), and extended over more sites. The concurrent perpendicular section also shows initiation of sea breeze flow at all sites west of the San Gabriel Mountains. While the return flow layer was about several 100 m deep at several sites, at some locations it appeared only as a low speed layer in which both flows cancel each other.

The near-midnight coastal section on 05/06UTC showed that the easterly synoptic flow had penetrated westward past the coast. The lower level flow (below 2000 m AGL) over the Basin had a generally offshore component (easterly in the northern part of the Basin and northerly in its southern part. This is consistent with flow around the southern edge of a coastal high located mostly onshore in the basin, i.e., the flow changes from easterly to northerly as one goes

southward along the coast. Most basin sites the concurrent perpendicular section showed the beginning of a shallow (about 200 m AGL) weak offshore flow, capped by a somewhat stronger westerly flow that could be a combination of sea breeze remnants and/or a return flow.

The 05/22UTC (05/15PDT) coastal section (time of the peak ozone) showed that both the easterly synoptic and onshore sea breeze flows covered the entire Basin. The sea breeze is somewhat stronger and deeper than 24 hours previous, extending to about 1000 m AGL in the northern part of the Basin and to about 2000 m AGL in its southern part. The concurrent perpendicular section again shows a deep sea breeze flow at all sites west of the San Gabriel Mountains (up to 2000 m AGL). The near-midnight coastal section on 06/06UTC showed stronger easterly synoptic flow. The lower level flow (below 2000 m AGL) over the Basin again has a generally weak and shallow (600 m MSL) offshore component. The 06/22UTC coastal section shows that that the easterly synoptic flow had become southerly at the northern end of the Basin, as the high has moved inland. The sea breeze is weaker than 24 hours previous, and had a southerly component

Horizontal distributions of profiler and rawinsonde winds at key flow levels can provide additional insights into temporal variations of the complex interactions between synoptic and mesoscale effects on spatial flow patterns. As discussed above, 3800 m AGL is optimum (in terms of data density and lack of mesoscale forcing) to look for purely synoptic flow field patterns.

The 04/18UTC flow field at 3800 m AGL thus showed onshore flow over the SoCAB that became more along-shore during the next fours. By 05/00UTC, the offshore synoptic high discussed above seems to have produced offshore flow in the southern half of the Basin. Six hours later, while the high is still offshore, it has moved north of Basin, thus producing offshore flow over the entire Basin. Another six hours later, it started to move back to the south and inland, producing offshore flow in the southern Basin, along-shore flow from the south in the middle of the Basin, and the beginnings of onshore flow at the northern edge of the Basin. By 05/20UTC, the high must have again moved back north, as the flow showed mostly easterly offshore flow over the entire SoCAB. While the flow six hours later was still offshore over the Basin, it now is more northeasterly, but also now along-shore at coastal sites on the northern edge of the Basin, consistent with a more northerly position of the high. By 06/12UTC, only the southern part of the basin still showed offshore flow, a pattern that continued to the end of the period.

The nighttime surface flow pattern at 04/12UTC shows a complex combination of low speed flows. While some downslope flow could be seen, no clearly defined land breeze existed. By 04/16UTC, surface wind speeds increased and become organized into an onshore surface sea breeze flow from the west-southwest. The inland opposing synoptic flow was also ore organized and at higher speeds. By 04/23UTC, the sea breeze reached its maximum intensity, with an inland penetration that extends to the line of inland high elevation areas. By 05/02UTC, the sea breeze weakened, and was at its maximum inland penetration. By 05/03UTC, it had retreated significantly back to the coast, especially in the northern Basin.

The nighttime surface flow pattern at 05/12UTC shows a similar (to that at same time on 4th) complex flow pattern. Wind speeds, however, are somewhat faster and more organized than on the 4th. By 05/16UTC speeds were again organized into an onshore sea breeze flow, but with less inland penetration than 24 hours previous due to the stronger offshore opposing flow component on this day at inland sites. By 05/22UTC, the sea breeze again reaches its maximum intensity and again has an inland penetration that generally extends to the same inland distance as on the 4th. Winds on the east side of the San Bernardino Mountains were now, however, from the north-northeast, and thus more oppose the sea breeze flow. This produces a more extensive and stronger convergence zone along all of inland ridge tops in the basin. The low speeds within such convergence zones allow concentrations to increase. The maximum penetration of the sea breeze on the 5th was, as expected, less than on the previous day (because of the stronger opposing synoptic flow), and by 06/03UTC the sea breeze again (as on the 5th) had retreated back to the coast.

On 06/23UTC, the sea breeze flow direction along the coast was more southerly than on the previous two days, while the off shore directed winds on the mountain ridges had the same direction as on those days. Sea breeze penetration, however, was more inland in the area of the San Bernardino Mountains, as compared to the previous days. This resulted because of the reduced opposing wind speeds in that area, in association with the above mentioned reduction in the speed of the easterly opposing synoptic flow aloft.

The nighttime 800 m AGL flow pattern at 04/12UTC shows a somewhat less complex combination of faster speed flows than in the concurrent surface chart. While some areas of inland downslope flow are seen, no clearly defined land breeze flow existed as coastal sites show generally along coast flows. By 04/16UTC, while 800 m AGL wind speeds have increased as they did at the surface, they have not yet organized into an onshore sea breeze flow as at the surface. An offshore opposing synoptic flow is likewise also not organized at inland sites. By 04/23UTC, the sea breeze has reached its maximum intensity, with an inland penetration that also (as at the surface) extends to the line of the inland high elevation areas. By 05/02UTC, the sea breeze has not weakened as at the surface. By 05/03UTC, the sea breeze at this level has not retreated back to the coast, as at the surface, consistent with sea breeze remnants found aloft in the profiler time-height sections discussed above.

Nighttime surface flow speeds at 05/12UTC are faster, more organized, and more northerly (due to the changing synoptic flow) than on the 4th. By 05/16UTC speeds have not organized into an onshore sea breeze flow (as at the surface), due to the stronger offshore opposing flow component on this day at inland sites that resulted from the new northeasterly upper level synoptic flow direction. By 06/00UTC (later than on the previous day), the sea breeze reaches its maximum intensity, because of the stronger land-sea temperature gradient on this day (as discussed above). The flow then turns, and remains, more along-shore (from the northwest) over most of the Basin, while it is offshore from the north at its northern edge until 06/06UTC. For the next four hours, the offshore flow turned more northeasterly and its area expanded southward into the Basin. By 06/15UTC, the 800 m AGL flow direction had become a southeasterly along-coast flow. It remained this way, until an onshore sea breeze flow started at 06/18UTC at the southern edge of the Basin, which after four hours existed over the entire Basin.

Supporting NWS synoptic scale and SOCAB mesoscale data for the above summary are now presented.

7.2. **Synoptic Scale Data**

Surface and upper air NWS weather charts showed only slightly changing weak anticyclonic synoptic forcing throughout the four-day test period (Sterbis 2000). A strengthening 300 mb high over the western U. S. throughout the test period kept both the GC long wave trough and Polar Front jet far from areas that could affect the SoCAB. NWS charts did thus show a: 500 mb cut off low west of Vancouver Island, strong ridge over the western U. S., and weak local coastal high over the SoCAB region. Its exact location cannot be determined from the sparse NWS data, but will be located in the mesoscale analyses presented below using the high density SCOS97 data. By 06/00UTC (05/17PDT, near the time of peak surface ozone concentrations), the 500 mb coastal high reached its maximum intensity, thus increasing temperatures as the subsidence inversion base lowered. During the following 48 hours, the high slightly weakened.

At 700 mb, the coastal high over the SoCAB also strengthened, and its 3120 m MSL height contour line enlarged northward and westward from 05/00UTC (Fig. 69a) until 06/00UTC (Fig. 69b). Its exact 700 mb location (and hence wind direction over the SoCAB) still cannot be determined, but its winds were also low throughout the test period. Temperatures again increased at 06/00UTC, increased until 06/06UTC, but slightly decreased thereafter.

Surface pressure changes were minimal over the cloud free SoCAB for the test period. An inverted thermal low-pressure trough over southern California (Fig. 70) was drawn inland by daytime heating, and then at night weakened slightly and moved back toward the coast at night. The small offshore Pacific High west of Central California strengthened from 1024 mb on 05/00UTC to 1026 mb on 06/00UTC. While it continued to slowly strengthen to the end of the period, the low intensified only until 06/00UTC (time of peak 700 mb ridge strength and surface ozone). Horizontal pressure gradients over the California coast thus increased until 06/12UTC, when the high shifted northward and westward from the coast. Even then, surface gradients were relatively weak, and thus only weak SoCAB flows existed.

More accurate positions of the 700 mb coastal high discussed above were determined by use of NCAR GDAS reanalysis pressure charts (available at 12-hour intervals) and RWP profiler data, which extends to about 4000 m AGL. As 3500 m AGL is the height average of the 700 mb pressure level, the 650 mb (average height of 3800 m AGL) GDAS chart is thus optimum to investigate changes in upper level synoptic forcing.

While 650 mb charts first showed a closed (3860 m AGL height contour) coastal high over the (north to south) center of SoCAB at 05/00UTC (Fig. 71a), 12 hours later it had moved slightly southward and enlarged westward (Fig. 71b). It moved back northward past its original coastal location by 06/00UTC or 05/17PDT (Fig. 71c), when a weak coastal low (also seen above in corresponding NWS 700 mb chart) formed to the north. The high and low both essentially dissipated by 06/12UTC. The north to south movement changes the synoptic background flow over SoCAB from onshore to offshore, as deduced from Figs. 71a-c and as will be seen in the RASS wind data.

Surface (1.5 m) and (constant AGL) upper-level horizontal temperature sections also showed physically consistent (in space, altitude, and time) patterns. On 04/12UTC (04/05PDT), 1.5 m values showed expected maximum in the low desert area just north of the Mexican boarder and a secondary maximum in the inland plateau east of the San Gabriel Mountains. Minimum temperatures occur (as expected) on mountain peaks (when observations are available). The average nighttime 1.5 m coastal to inland difference is about 8 K, which increases at midday to 10 K, and at late afternoon to 15 K. Throughout the 5th, while most areas warmed by about 2-3 K (consistent with synoptic changes seen above on NWS charts), spatial patterns remained similar to those during corresponding hours on the previous day. The coastal-inland gradient on 05/18UTC was about 2-3 K stronger than on the 4th, and this larger gradient thus helped form the stronger onshore sea breeze flow on this day. The gradient was, however, weaker by that amount by 06/00UTC, the time of full sea breeze development. Throughout the daytime hours of the 6th, temperatures over the basin cooled to almost the values of the 4th.

The 300 m AGL early morning temperature distribution at 04/12UTC also (as did the corresponding surface distribution) shows cool air in coastal regions and warm air at inland locations. Note the lack of upper-air mountain top observations. Mid-afternoon values on this day shows a similar pattern, but with somewhat warmer values (as expected). The distribution at 05/12UTC likewise shows a similar pattern to the previous day, but also shows the general synoptic warming discussed above. The mid-afternoon field at 06/00UTC also still shows synoptic warming. While the final early morning distribution at 06/12UTC still shows warm air (relative to that on the 4th) over the northern SoCAB, it also now shows relatively cool air over the southern part of the Basin.

The 800 m AGL early morning temperature distribution at 04/12UTC shows warmer air in coastal regions and cooler air at inland locations, the reverse of the corresponding 1.5 and 300 m AGL distributions. Over the coast, temperatures are warmer by about 2 K at the 800 m AGL level than at the 300 m AGL level, while the reverse is true over inland sites. The mid-afternoon field shows a similarly reversed pattern, but with somewhat warmer values than 12 hours before (as expected). The distribution at 05/12UTC no longer shows a reversed pattern, but shows the general synoptic warming discussed above, but with more warming over the southern Basin than over northern sections. The mid-afternoon field at 06/00UTC shows more synoptic warming, but over the entire Basin. The final early-morning distribution at 06/12UTC shows cooling over the entire Basin.

7.3. SoCAB Temperature Data

The rawinsonde temperature time-height cross-section at the off shore SNIC island site (Fig. 72a) showed a persistent (throughout study period) daytime and nighttime strong (10 K) subsidence inversion with a top at about 600-800 m AGL. While its base seems only a few 10s of meters above the surface, near surface isotherms in these sections are not accurate. This is true as the lowest observations are at about 100 m AGL and as surface (really 2 m) temperatures were not included in the sections, as the two were generally inconsistent. The MATLAB graphics package, however, extrapolates to the ground even in the absence of data. These

sections thus will be used to determine inversion top characteristics, but with bases only discussed when observations are available.

Inversion-top temperature and intensity peaked at 06/06UTC (05/23PDT), i.e., around six hours after the surface ozone peak. The peak intensity resulted from increased subsidence from the upper level high discussed above, which warmed upper level temperatures and also strengthened and lowered the inversion base. The inversion layer capped the near-adiabatic morning MBL, formed as cool sea breeze air advects onshore.

Rawinsonde temperature patterns are similar at coastal UCLA (Fig. 72b, except that inversion intensity peaked one launch (i.e., six hours) earlier, implying the westward movement of the synoptic high (see NWS discussion above), which thus impacts coastal areas before offshore areas. Temperatures at the more-inland site of 29PA site shows little influence from the high (Fig. 72c). It shows no elevated inversion, but shows maximum temperatures at 1000 m AGL at about 06/00UTC to 06/06UTC (about times at SNIC and UCLA) only a weak nocturnal surface inversion existed on the episode day.

While RASS sites are more numerous, and their profiles more frequent, they do not provide data much below 200 m AGL. Temperature patterns are, however, generally consistent with those from nearby rawinsonde sites, e.g., those from the offshore SCL show similar inversion depths and peak temperature values compared to those at the SNIC rawinsonde site discussed above. SCL profiles on 4 August (Fig. 73a) also show (as did SNIC rawinsonde data) a persistent (daytime and nighttime) strong inversion, whose top is at about 600 to 800 m AGL, but whose base is unknown. Profiles show normal diurnal PBL cooling until 04/06UTC, followed by expected warming until 04/1800UTC. The warming is, however, reversed from that produced by normal upwards progression of surface heating, as subsidence warming started at the inversion top (700 m) during the 0600 to 1200 UTC night-time period. Surface temperatures warmed only six hours later (when solar heating reinforced the subsidence), increased to a peak at 05/00UTC (04/17PDT), and then cooled to 05/06UTC (04/23PDT).

Instead of cooling for the first six hours of 5 August (episode day), subsidence warming again overcame diurnal cooling, and thus temperatures at all levels warmed from 05/06UTC to 05/12UTC (Fig. 73b) by an amount even larger than on the previous day. Warming continued until 06/00UTC (time of maximum ozone), so that 600 m AGL values (Fig. 73c) were about 3.5 K warmer than 48 hours previous. Cooling during the next 12 hours (except for weak warming during the last six hours from 200 to 400 m) shows a now weaker subsidence warming that no longer could counter PBL cooling, as during the previous two nights. Two days of warming, however, has left the PBL warmer than 48 hours before, e.g., at 1200 m AGL values warmed by over 4 K. Absolute maximum SCL temperatures of 37^0C were reached at 500 m AGL on 06/06UTC, by when the subsidence inversion base had fallen rapidly over the preceding six hours. Values at that level thus were warmer by 5.5 K over those 48 hours previous.

RASS temperature profiles at coastal LAX on 4 August (Fig. 74a) also show (as did UCLA rawinsondes) a persistent (daytime and nighttime) strong inversion, whose top is at about 600 to 800 m AGL (as at SCL). The profiles show a normal diurnal PBL cooling until 04/06UTC, followed by expected warming until 04/18UTC (04/11PDT). Note that the vertical variation of

the warming on this day is not reversed from that produced by the normal upwards progression of surface heating, as subsidence warming is not yet a major influence (as at SCL). Note that the subsidence inversion only reaches down to about 200 m AGL, and that no surface based radiation inversion forms at this coastal site. A shallow sub-inversion MBL, persistent from 04/06UTC (03/23PDT) to 04/18UTC (04/11PDT), is evidence of sea breeze frontal penetration. This produces a morning increase in inversion-base elevation and/or a decrease in surface temperatures relative to values observed during the previous nighttime period (Sterbis 2000).

Instead of warming for first six hours of 5 August (episode day) as seen at SLC, weak surface and PBL cooling occurred at LAX until 05/00UTC (Fig. 74b). The exceptionally strong subsidence warming aloft (weaker version of that seen on the previous day at SCL) occurred above 400 m AGL during the six-hour period ending at 05/06UTC. Values above 400 m AGL (top unknown) that remained constant over at least the next 12 hours represent a deep warm pool (maximum values within LAX RASS profiles) over the coast during the episode day. Note the 24-hour time lag between the 05/06UTC time of maximum subsidence at coastal LAX and the time at offshore SCL, again due to the implied westward movement of the synoptic high discussed above. A comparable 4 K warming occurred below 400 m AGL during the next six hours, while surface values warmed by about 5 K over the 24-hour period ending at 05/18UTC.

Only small temperature changes occurred during the next six hours, 06/00UTC (Fig. 74c, note change in temperature scale). Warmer near-surface evening temperatures at 06/06UTC (05/23PDT, six hours past the time of the maximum ozone) are indicative of sea breeze frontal retreat during the previous six hours. Thus 200 m AGL temperatures are now about 2 K warmer than 48 hours previous. PBL and surface temperatures cooled during the next six hours until 06/12UTC (as at SCL), showing subsidence warming no longer able to counter PBL cooling. The inversion base is, however, at about 200 m AGL, and not at the surface (as expected with inland nocturnal radiative cooling). Two days of subsidence warming has thus left the surface warmer than 48 hours before by almost 4 K at 06/12UTC (06/05PDT). During the next six hours (until 06/18UTC), the inversion base lifted another 300 m and most of the layer (to sounding top at about 800 m AGL) warmed due to solar heating. Only a shallow layer centered at 400 m AGL cooled (as at SCL).

RASS temperature profiles at inland EMT (on western slope of San Gabriel Mountains) on 4 August (Fig. 75a) also show a persistent strong inversion, whose top is again at about 600 to 800 m AGL. Profiles show a normal diurnal near surface (below 200 m AGL) cooling until 04/12UTC and a large subsidence warming aloft (up to 800 m AGL). This is followed by an intense combined subsidence and diurnal warming at all levels, especially throughout the lowest 300 m AGL, until 04/18UTC (04/11PDT). Note that subsidence warming at this inland site is thus maximum 48 and 24 hours earlier, respectively, than at offshore SCL and coastal LAX, again consistent with a westward moving synoptic high.

Note that the 300 m AGL deep daytime mixed layer at EMT at 04/18UTC (04/11PDT) until 05/00UTC is not present at coastal LAX and offshore SCL. As the sea-breeze front has probably not yet penetrated inland to this site at 04/18UTC, the warm (compared to previous two RASS sites) mixed layer is probably due to convective heating. While the next two nighttime profiles show no surface based mixed layer (Fig. 75b), they do show a deep (600 m) surface inversion

that probably represents a combined subsidence and radiative layers. The surface mixed layer again forms at 05/18UTC and still remains at 06/00UTC (Fig. 75c), time of maximum EMT temperatures and about that of the peak ozone. Note that the inland EMT temperatures are, as expected, warmer than at LAX and SCL. The normal diurnal pattern is repeated on the remainder of 6 August.

RASS temperature profiles at HPA, further inland on the eastern slope of the San Gabriel Mountains, on 4-6 August (Figs. 76a-c, respectively) again show normal diurnal PBL temperature cycles. Continuing the trend of weakening subsidence inversion strength with inland distance from the center of the offshore synoptic high, this site is the first to show almost no elevated inversion layers and only minimum synoptic forcing aloft. The exceptions in one daytime profile on each day are weak inversion layers aloft (300-400 m in one daytime profile on each AGL),day which could have resulted from surface heating and/or weak subsidence aloft. Once again, this inland site reaches its maximum temperatures at 06/00UTC (about time of peak ozone) and shows values generally warmer that at any of the other three sites.

Review of the remaining RASS data by Sterbis (2000) showed that only coastal PHE and LAS with an elevated inversion base at 04/12UTC (04/07PDT), although by 05/00UTC (04/17PDT) the sea breeze front had also passed USC, SMI, LAX, and TTN. By 05/12UTC, however, only coastal LAX still showed evidence of marine air penetration (as the front had retreated), but by 06/00UTC (time of maximum ozone) the front again moved inland past EMT, SMI, USC, and TTN.

The near-midnight, "along coast" RASS vertical section on 04/06UTC (Fig. 77a) shows a strong inversion over the Los Angeles Basin (i.e., GLA southeastward to BFD). While the inversion extends to VAN (northwestward of Basin), it is not over ECO (southeast of Basin). Here and in subsequent figures of this type, while the data do not show an inversion, the SURFER graphics package has produced an isopleth patterns that seems to show such a layer (as described above). While the inversion top is fairly uniform at about 800 m MSL, it is again not possible to discern its base at most sites. At three sites where it is discernable (i.e., GLA, LAX, and PLM), it is fairly uniform at about 200 m MSL, producing an inversion depth of about 600 m. While maximum temperature values near the inversion top are about 31^0C, and as base values range from 22 to 27^0C, inversion strength is about 4-9^0C.

In the concurrent "perpendicular to coast" nighttime section starting at coastal LAX (Fig. 77b), the inversion is confined to the Los Angeles Basin, and is not west of the San Gabriel Mountains. Its top (temperature still about 31^0C) slopes upwards eastward to a maximum height of about 1000 m MSL. Its base at the two sites where discernable (i.e., LAX and EMT) likewise slopes upward from about 200 m AGL to about 450 m AGL (equal to 550 m MSL). Note two shallow embedded non-inversion layer holes at 700 and 800 m over ONT.

The daytime along coast section on 04/18UTC (Fig. 78a) again shows a strong inversion over the Basin, but now not over VAN and ECO. Its top is again clearly discernable and uniform in elevation, but about 200 m below that 12 hours before. The sinking does not result from diurnal heating (which would raise it), but again results from the westward movement of the Pacific High. It is again only possible to discern its base at the same three sites, where it ranges from

about 200 to 350 m MSL, producing a depth of about 250-400 m. Maximum temperature values near the inversion top are now a bit warmer (at about 31.5^{0}C) due to the sinking. As values along the base now range from 23 to 24.5^{0}C, inversion strength increased somewhat to about 7.0-8.5^{0}C. In the concurrent "perpendicular to coast" daytime section (Fig. 78b), the inversion is again confined to the Basin. Its top (temperature still about 31^{0}C) does not slope upwards to the east (as 12 hours before), but is fairly uniform at about 600 m MSL. Its base at the two sites where discernable (again LAX and EMT) does slope upward from about 100 m AGL to about 500 m MSL (equal to about 350 m AGL). No non-inversion layer holes exist, as did 12 hours before.

The near-midnight, along coast section on 05/06UTC (Fig. 79a) shows an even stronger inversion over the Basin and VAN, but again not ECO. Inversion tops rise from about 450 m MSL over GLA to about 650 m, i.e., about 150-350 m lower than 24 hours before; its base also seems somewhat lower. Maximum temperatures near its top have increased about 1-3^{0}C, while its strength has increased to a more uniform value, close to the maximum 24 hours before. The concurrent perpendicular section (Fig. 79b) shows it now extending across the entire section (except inland HPA), with a top (temperature still about 31^{0}C) that again slopes upwards (following the topography) from a minimum of about 650 m MSL to a maximum of about 1100 m MSL. Its base at the only two sites where discernable (i.e., ONT and BTW) is about 250 m AGL, and its intensity decreases from about 10^{0}C at coastal LAX to about 1^{0}C at inland ONT, NTN, and BTW. The non-inversion layer hole, visible at only one site 24 hours previous, now extends over all five sites west of the San Gabriel Mountains and its elevation follows the topography. Thus over 24 hours, the inversion became more widespread, lowered, and warmed, and enlarged its non-inversion hole over the Basin.

The along-coast daytime section at 05/18UTC (Fig. 80a) shows (relative to 24 hours before) the continued westward movement of the synoptic high producing a more widespread (now also over VAN), deeper (900 vs. 600 m MSL), and warmer (top and bottom, by about 3-4^{0}C) elevated inversion layer. Note that two shallow isothermal layers appear at about 500 and 700 m MSL over PHE, LAX, and CBD. The concurrent perpendicular section (Fig. 80b) again shows the inversion confined to the Basin. Its top (temperature still about 32^{0}C) is now irregular (ranging from 1100 to 700 m MSL), its base now generally follows the topography, and a more organized cool, non-inversion (weak lapse) layer is now embedded within it.

The coastal section on 06/06UTC (Fig. 81a) shows an inversion mainly over the Basin, with weak, seemingly isolated, inversions at VAN and ECO. Inversion tops and slope are similar to that 24-hours before, although soundings do not extend to its top at both ends of the Basin. Maxi-mum temperatures near its top have increased by an additional 3.0-3.5^{0}C, while those near the surface have warmed somewhat less, thus slightly increasing inversion strength.

The concurrent perpendicular section (Fig. 81b) again (as 24-hours previous) shows the inversion extending across the Basin. It again slopes upwards westward from a minimum of about 400 m MSL to a maximum of about 1400 m MSL, about 300 m higher than 24-hours previous. Inversion top temperatures are now warmer by about 2.5^{0}C, ranging from about 36^{0}C at the coast to about 34^{0}C inland. Inversion intensity has decreased substantially from that 24-hours pre-

vious, and it still decreases from about 3^0C at coastal LAX to about 1^0C inland. Thus over 24 hours, the inversion top has continued to warm, the inversion has weakened.

The along-coast daytime section at 06/18UTC (Fig. 82a) still shows a widespread (now even over ECO), deeper top (now up to 1050 m MSL at BFD), which means that it may extend over the top of the San Hancito Mountains. The warming trend of 24-hour previous is now a cooling trend, in which top and bottom values have decreased by about 3^0C. The isothermal holes in the inversion seen 24-hours ago have now strengthened into weak lapse layers embedded at about 400 and 700 m MSL over LAX and LAS, and at 800 m MSL over CBD. The concurrent perpendicular section (Fig. 82b) shows the inversion also outside of the Basin at HPA and BTW. Its top (temperatures still about 32^0C) has lowered near the coast and has become more regular (about 850 m MSL). Its base, however, has risen to about 400 m AGL over the basin, but its non-inversion hole is gone.

Surface and (constant AGL) upper-level horizontal temperature sections also showed physically consistent (in space, altitude, and time) patterns. On 04/12UTC (04/05PDT), interpolated and smoothed 1.5 m temperatures (Fig. 83a) showed expected absolute maximum in the low desert area just north of the Mexican border and a secondary maximum in the inland plateau east of the San Gabriel Mountains. Minimum temperatures occur (as expected) on mountain peaks (when observations are available).

The average nighttime 1.5 m coastal to inland difference is about 8 K (299 vs. 291 K), which increases to a midday (Fig.83b) 10 K difference at 04/18UTC (309 vs. 299 K), and to a late afternoon (Fig. 83c) difference of 15 K difference at 05/00UTC (312 vs. 297 K). Throughout the 5th, while most areas warmed by about 2-3 K (consistent with synoptic changes seen above on NWS charts), spatial patterns remained similar to those during corresponding hours on the previous day. The coastal-inland gradient on the 05/18UTC (Fig. 83d) was about 2-3 K stronger than on the 4th, and this stronger gradient thus helped form a stronger onshore sea breeze flow seen on this day (see below). The gradient again weakened, however, by that same amount by 06/00UTC (Fig. 83e), when the sea breeze was most development. Throughout the daytime hours of the 6th, temperatures over the entire basin cooled to almost the values of the 4th. In addition, the gradient at 06/18UTC was smaller than those on the two preceding days (Fig. 83f).

The 300 m AGL (rawinsonde plus profiler) early morning temperature distribution at 04/12UTC (Fig. 84a) was similar to that at the surface, with cool air in coastal regions and warm air at inland locations. Note the lack of upper-air mountain top observations. Mid-afternoon values on this day (Fig. 84b) shows a similar pattern, but with somewhat warmer values (as expected).

The distribution at 05/12UTC (Fig. 84c) likewise shows a similar pattern to that on the previous day, but it also shows the general synoptic warming discussed above. The mid-afternoon field at 06/00UTC (Fig. 84d) also still shows effects of synoptic warming. While the final early-morning distribution at 06/12UTC (Fig. 84e) still shows warm air (relative to that on the 4th) over the northern SoCAB, it also now shows relatively cool air over the southern part of the Basin.

The 800 m AGL early morning temperature distribution at 04/12UTC (Fig. 85a) shows warmer air in coastal regions and cooler air at inland locations, the reverse of the corresponding 1.5 and

300 m AGL distributions. Values are actually warmer over the coast by about 2 K than at the 300 m AGL level, while the reverse is true over inland sites. The mid-afternoon field on this day (Fig. 85b) shows a similarly reversed pattern, but with somewhat warmer values than 12 hours before (as expected).

The following distribution at 05/12UTC (Fig. 85c) no longer shows a reversed pattern like on the previous day. It does show the general synoptic warming discussed above, but with larger rates of warming over the southern half of the Basin than over the northern sections. The following mid-afternoon field at 06/00UTC (Fig. 85d) shows still more synoptic warming, but now over the entire Basin. The final early-morning distribution at 06/12UTC (Fig. 85e) shows cooling over the entire Basin.

In summary, rawinsonde and RASS temperature profiles have been used to describe the temporal and spatial variations of synoptic and radiative forcing across the SoCAB. The next section describes the corresponding wind flow patterns.

7.4. SoCAB Wind Data

The rawinsonde wind velocity time-height cross-section over the entire period at the SNIC offshore site (Fig. 86a) shows smoothly varying patterns during almost all hours (as do most, but not all, of the other sites). In particular a prevailing westerly flow from 04/20UTC to 05/06UTC is seen throughout its entire 3000 m AGL depth. The first sign of the dramatic shift to an easterly flow (associated with the westward movement of the synoptic high) is seen in the upper 100 m of the 05/12UTC. The shift complete, reaching the surface, in the next rawinsonde sounding, and the shift reaches the surface two hours later. The northerly flow in the layer from 1500-2000 m AGL at 05/06UTC is probably due to a local topographic flow. Easterly flow persists in the upper layers of the section throughout the episode day until 07/00UTC, after which it turns to a more normal westerly flow. As SNIC is an island site (and not in the SoCAB basin), its lower level winds are mostly locally produced and not necessarily related to those over the basin, and thus will not be discussed further.

The rawinsonde velocity time-height cross-section at UCLA (Fig. 86b) does not show (because of its multitude of SoCAB topographic forcings) a smoothly varying pattern. The prevailing westerly flow shifts slower at UCLA that it did at SNIC, as its 3000 m AGL flow first became northerly at 05/00UTC. It took 18 hours for the shift to work its way down to1500 m AGL, so that by 05/18UTC the flow had shifted to easterly at all heights above 1500 m AGL. Easterly flow persisted in the upper layers of the section throughout the episode day until 06/18UTC, after which it returned to a more normal westerly flow over the next 12 hours.

As UCLA is a coastal site in the SoCAB basin, its lower level winds are a complex combination of coastal influences. During the 4th and 7th, its onshore sea breeze flows were in much the same direction as the synoptic prevailing flow, while on the 5th (episode day) it was perpendicular the then easterly prevailing flow. Thus without a strong upper level offshore return flow, the sea breeze and westerly onshore flows would blend, making it difficult to determine the top of sea breeze layer.

On the 4th the sea breeze depth appears to be about only 550 m AGL, above which is a chaotic transition layer up to about 2000 m AGL, with the easterly return flow layer above that. The shallow nighttime offshore land breeze at 05/06 and 05/12UTC only extends up 200 m AGL, and a northerly transition layer at 400 m AGL appears to coincide with the non-inversion layer hole in Fig.72b. As any return flow aloft is now in the direction of the still westerly onshore synoptic flow at these times, it is not possible to discern the boundary between the two.

On the 5th (the episode day) the sea breeze depth flow direction is from the south (and not the northwest, as on the 4th), except for the lowest at 05/12UTC, which is from the west at 05/12UTC. While at 05/18UTC, it is only up to 400 m deep, six hours later it reaches up to either 1700 or 2300 m (depending on the interpretation of the southerly flow layer at 2000 m AGL). The easterly flow above this level is probably a combination of the return flow and synoptic background flow layers. The land breeze at 06/06 is about 400 m AGL deep, while at 06/12UTC it extends up about 600 m AGL. Both layers are capped by a 600 m deep northerly transition layer, which does not coincide to a non-inversion layer hole (as none existed over the coast at this time). As the return flow aloft is now in a direction opposite to the now easterly offshore synoptic flow at these times, it is now possible to discern the boundary between the two, which is located at 2200 m AGL at both times.

On the 6th the sea breeze depth flow direction is again (as it was on the 4th) from the northwest. At 06/18UTC, it is only up to 300 m AGL, and six hours later no data exists below 600 m AGL. The easterly flow aloft is again probably the combination of the return and background flows, but note that a westerly background flow comes back at about 2700 m AGL at 07/00UTC. The land breeze at 07/06UTC is uncharacteristically strong and deep (about 1000 m AGL), and has almost no northerly transition layer. As the return flow aloft would now again be in the same direction as the now again westerly onshore synoptic flow, it is not possible to discern the boundary between the two.

At 29PA, an inland site on the eastern side of the San Bernardino Mountains (too far inland for coastal sea breeze influences), lower level winds are a complex combination of topographic influences (Fig. 86c). Note its westerly prevailing flow has completely turned to an easterly one by 05/06UTC, about the time of the change at coastal UCLA and six hours before offshore SNIC. During nighttime hours, shallow (southerly or westerly) down-slope flows dominate near the surface (Fig. 86c), while during daytime hours shallow (easterly or southerly) upslope flows predominate.

On 04/12UTC, the still southerly (down-slope) flow to about 800 m AGL is capped by then still westerly synoptic flow. At 04/18UTC, a layer of easterly upslope flow extends up to the transition to the still westerly background flow (at 2000 m AGL). The lowest 1400 m of the 05/00UTC sounding is missing, but by 05/06UTC, the typical southerly (lowest 500 m) and westerly (another 800 m) -slope flows had formed. These slope flows are capped by the now northeasterly prevailing flow. Six hours later, only a shallow (300 m) remnant of the westerly downslope flow remained, and this was capped by the westerly synoptic flow to the top of the sounding (except for a shallow unexplained northerly flow at 2000 m). By 05/18UTC, the now easterly upslope flow blended into the still westerly synoptic flow, making it difficult to discern their boundary. The limited near surface northerly winds at 06/00UTC are still upslope, gut the

westerly flows during the next 12 hours are downslope.. The surface down-slope near flows transitions to the still easterly flow aloft at 800 m AGL at 06/06UTC and at 1500 m AGL six hours later.

By 06/18UTC, the again present westerly (near the surface) upslope flow shifts into a southerly transition (and/or return) flow layer from 1000-1700 m AGL and then into the still easterly synoptic flow aloft. Note the unexplained shallow westerly layer at about 400 m AGL. The limited near surface northerly winds at 07/00UTC (06/17PDT) show a transition (because it is too early for down-slope flows begin) to westerly down-slope flows during the next six hours. The transition from near surface downslope flows to the still easterly flow aloft is clearly shown to occur at 1900 m AGL at 07/06UTC.

The profiler wind time-height cross-section at offshore SCE on 4 August (Fig. 87a) shows that the prevailing generally southerly synoptic flow (always only above 15000 m AGL) shifted around to a westerly flow during the period between 04/13UTC and 04/19UTC. The onshore near-surface generally westerly marine flow lasted until about 05/08UTC (or 05/01PDT), and was generally about 1400 m deep, and was generally capped by a shallow chaotic layer of about 200 m in depth, which deepened after 04/17UTC due to establishment of an early morning easterly return flow layer.

The prevailing generally northerly synoptic flow on 5 August (Fig. 87b) starts to weaken at 05/00UTC. During the period from 05/07UTC to 05/11UTC, the synoptic flow turns to become an easterly flow, which also raises its base up to 2200 m AGL (from 1600 m on the previous day). After the synoptic flow direction change, the near-surface westerly marine flow weakens and is replaced by a weak chaotic layer of about 1000 m in depth, above which the marine flow seems to continue to about 2000 m AGL.

Offshore easterly flow seems to have reached this island site during four-hour period from about 05/14UTC, as it was apparently able to overcome (with help from the still easterly upper level synoptic forcing) the weak pressure gradients existing during the previous five hours. The onshore marine flow then returned, was again about 900 m deep, and was again capped by a shallow weak chaotic transition layer and by the still easterly synoptic flow, whose based had lifted to about 2000 m AGL by 06/00UTC (Fig. 87c). The westerly marine flow near the surface lasted until about 06/10UTC, when the flow in an ever-deepening surface based layer turned to become southerly, and by 06/22UTC it had grown up to 1100 m AGL.

The profiler section at coastal LAX on 4 August (Fig. 88a) shows that the prevailing generally southerly synoptic flow always had a base at about 2000 m AGL, or about 500 m above that at off-shore SCE. This flow first turned into a westerly flow sometime during the no-data period between 04/11UTC and 04/16UTC. It is not possible to know at which site this shift occurred first, given the missing data at both sites. The synoptic flow then became northerly at about 04/20UTC, a shift that could have also occurred at SCE during the period, but again this cannot be determined due to its data-gap at this time. The onshore generally westerly coastal sea breeze flow lasted near the surface until about 04/04UTC (or 03/21PDT), but apparently (see next paragraph) persisted aloft for about eight additional hours. It was generally about 1400 m deep throughout the entire period, except during 04/06UTC to 04/08UTC (period surrounded by

missing profiles), which shows westerly flow up to 2500 m AGL (above which data are missing). Throughout most of its existence the sea breeze layer was capped by: a shallow chaotic layer of about 300 m in depth, a shallow (100 m) southeasterly return flow layer, and the prevailing southerly synoptic flow discussed above.

The nocturnal down-slope offshore combination drainage and land flow at this coastal site started about 04/05UTC, was about only 600 m deep, and was apparently capped by a westerly return flow region up to about 1400 m AGL, and by the still southerly synoptic flow. Note that the westerly flow region above the combination drainage-land breeze layer could, in fact, be a combination of a persistent sea breeze flow (as discussed in the above paragraph) and of a true return flow region. Upwind topographic effects should not influence this layer, given the southerly synoptic flow. The sea breeze that replaced this nocturnal flow on the following morning at about 04/18UTC (or 04/11PDT) after a few hours of chaotic transition was about the same depth as it was 24 hour pervious.

The prevailing generally northerly synoptic flow on 5 August first weakens at 05/00UTC (Fig. 88b), and then is undercut at 05/02UTC by a layer of easterly flow (discussed below) that raises its base up to 3500 m AGL (from 2000 m, 24 hours previous). This is about 1300 m higher than the concurrent value at offshore SCE, due to its lack of an undercutting layer. The synoptic flow is then completely turned to an easterly flow at about 05/09UTC, during a transition period that is somewhat more erratic than that seen at SCE. The onshore westerly sea breeze flow was similar (in start time, intensity, depth, and duration) as 24 hours previously. It was again capped by a: chaotic layer to about 2200 m AGL (and thus was about 200 m deeper than on the previous day), an easterly return flow layer to about 3000 m AGL, and the then prevailing northwesterly synoptic flow discussed above. Note that the return layer on this day is deeper and stronger than that on the 4th, as the stronger synoptic flow on that day could mostly suppress a return layer.

The nocturnal offshore flow again started about 0600 UTC, was again about only 700 m deep, and was capped by a now northerly return flow region up to about 2000 m AGL, and then by the now easterly synoptic flow. The northerly return flow region could, in fact, also include upwind topographic effects, given the now generally offshore synoptic flow.

The prevailing generally easterly synoptic flow appears to persist throughout the 6th (Fig. 88c). Although a data-gap exists from 06/00UTC until 06/12UTC, the above SCE analysis also showed this. The onshore westerly sea breeze flow that began at 05/18UTC (or 05/11PDT) on this episode day lasted until about 06/05UTC (or 05/22PDT). While this approximated the sea breeze period of the previous day, this mid-afternoon westerly breeze was deeper (above top of data at 2700 m AGL vs. 1400 m AGL) and faster (7 vs. 5 m s^{-1}) than on the two previous days. This strengthening is probably associated with the above discussed strengthening of the high aloft, which increased onshore pressure gradients aloft due to its effect on coastal over-land temperatures. The sea breeze layer was not capped by a chaotic layer (as on the previous days), and a possible easterly return flow layer would blend in with the prevailing easterly synoptic flow, which could be seen in the concurrent SCE section.

The nocturnal offshore flow again started about 06/06UTC, but now grew to about 1300 m AGL (vs. the approximately 700 m of the previous two days). In addition, on this night, the offshore

flow was faster, better organized, and lasted four hours longer at the 100 m AGL level that during the previous two days at the 100 m AGL level (until 2100 UTC or 1400 PDT). This nocturnal flow was capped by (sequentially northerly, easterly, and westerly) return flow regions up to roughly 2500 m AGL, and then by the still easterly synoptic flow. These variable return-flow directions are again associated with small changes in the generally offshore synoptic flow directions, which places LAX downwind of different topographic features.

The inland valley HPA site, at an elevation close to 1 km MSL, is surrounded by even higher peaks. Its flow patterns are thus not affected by the MBL, but by a complex interaction of near-surface up-and downslope flows. Its lack of data-gaps at the key times of changes in the upper level synoptic flow (discussed above), makes it an ideal site to more accurately pinpoint the times of these changes.

The HPA profiler section on 4 August (Fig. 89a) shows that the prevailing southerly synoptic flow turned into a westerly flow at 04/01UTC. This is the first site so far at which this shift did not occur in a data-gap region, and it thus occurred at 04/01UTC, or at least 10-12 hours earlier than at the more westward sites of SCE and LAX. The synoptic flow then became northerly at about 04/23UTC, which is now about three hours later than the same change at LAX (a reversal of order for first two sites). Although the sea breeze front cannot generally cross the elevation needed to reach HPA, the synoptic wind velocity still also cannot reach it at the surface due to mesoscale topographic flows. The base of the synoptic layer is thus about 1300 m AGL over the entire period (Fig. 89a-c), with the largest variations on 5 August. This elevation is about equal to that at coastal LAX and about 700 m below that at offshore SCE.

Nocturnal downslope flows at complex topography sites like HPA are dependent on synoptic wind direction to determine upwind topographic features. On the ozone episode day, a northerly nocturnal near-surface drainage flow existed until 1800UTC (or 05/11PDT). This flow was then superceded by five hours of northeasterly flow, which given the inland mountain location of HPA, thus formed a barrier to the further inland penetration of the sea breeze frontal convergence zone. Peak ozone values occurred within that period (at 05/22UTC) just upwind of HPA, right within the convergence zone. On the days preceding and following the episode day, late afternoon winds had the same generally westerly flow direction as the sea breeze flow, and thus polluted air could flow past HPA. As these winds were slower and less organized on the day preceding the episode day (as compared to those on the day following the episode), less ozone was carried away and some remained to contribute to the peak ozone values found the next day.

In summary, the first synoptic wind shift over the SoCAB was consistent with a westward movement of the synoptic high. The Basin was thus no longer on its northern side (with a generally southerly flow), but was now on its northeastern side (with a generally westerly flow). The second shift was consistent with a now northwestward movement of the high, which means that sites within the Basin no longer on its northeastern (with generally westerly flow), but now on its eastern side (with a generally northerly flow). The final shift was consistent with a northeastward movement of the high, which means that sites in the Basin was no longer on its eastern side (with generally westerly flow), but now were on its southern side (with generally easterly flow).

In the near-midnight coastal vertical section of total horizontal profiler winds over the Los Angeles Basin (i.e., from GLA southeastward to BFD) on 04/06UTC (Fig. 90a), winds with a generally southerly component are about 45 deg south of the generally northwest to southeast plane of the section. As discussed above, 3800 m AGL is the optimum level to look for purely synoptic flow field patterns, and thus the synoptic flow direction over the Basin cannot be determined due to a lack of data.

The lower level flow (below 2000 m AGL) over the Basin does, however, have a generally westerly (or onshore) component, while that south of the basin (at PLM and BFD) generally has a northerly (offshore) component. This is consistent with flow around the northeastern edge of a coastal high located just offshore of the basin, i.e., the flow would change from westerly to northerly as one goes southward along the SoCAB coast.

In the concurrent nighttime perpendicular section starting at coastal LAX (Fig. 90b), winds with a generally southwesterly component are in the inland direction of the section. Both sites with synoptic level data (USC and ONT) show the southerly synoptic flow discussed above in the concurrent LAX time height section for this period. Offshore nocturnal drainage and/or land breeze flows are seen at the three most western sites (LAX, USC, and EMT), while the most inland of the four sites shows an onshore westerly flow. The depth of the offshore flow is almost equal to the depth of the marine and elevated inversion layers over the Basin. All three sites show what could be a westerly return flow layer (centered at about 1000 m AGL) in between the offshore and synoptic flows. The lack of low level wind data at ONT and temperatures at NTN makes it impossible to compare these variables at the two SoCAB sites showing low level onshore flow, while no inversion was found at the two outside the Basin sites (HPA and BTW).

The 04/18UTC (04/11PDT) coastal section now has enough data at 3800 m AGL (Fig. 90c) to also show the upper level westerly synoptic flow, while the lower level the offshore nocturnal drainage flow has now been replaced by an onshore westerly-component sea breeze flow (at PHE to PLM) with a depth of about 500 m AGL. This flow is thus restricted to the sub-inversion layer of Fig. 77a. Several of these sites also show the beginning of a weak return flow layer, located above the sea breeze layer. The concurrent perpendicular section (Fig. 90d) also shows the westerly sea breeze flow merging with the westerly upper level synoptic flow.

By 04/22UTC, the northerly section of the upper level synoptic flow has enlarged northward over the Basin to now include all sites, except PHE and GLA (Fig. 90e). The sea breeze flow, however, is now stronger, deeper (up to about 900 m AGL), and over virtually the entire Basin (PHE to BFD). The return flow layer is also stronger, deeper (centered at about 2000 m AGL), and extends over more sites (all but LAS and TTN).

The concurrent perpendicular04/18UTC section (Fig. 90f) now also shows initiation of sea breeze flow at all sites west of the San Gabriel Mountains. Three hours later (not shown), the sea breeze is stronger and deeper (ranging from 1200 m AGL to 2000 m AGL). The return flow layer is about several 100 m deep at several sites, but at some locations it appears only as a low speed layer in which both flows just about cancel each other.

The along coast near-midnight vertical coastal section on 05/06UTC (Fig. 91a) shows that the easterly synoptic flow has penetrated to the northwest to a location beyond LAX. The lower level flow (below 2000 m AGL) over the Basin has a generally offshore component (easterly in the northern part of the Basin and northerly in the southern part of the Basin), except for the westerly onshore component at LAX to TTN. This is consistent with flow around the southern edge of a coastal high located mostly onshore over the basin, i.e., the flow changes from easterly to northerly as one goes southward along the coast.

Most basin sites in the concurrent perpendicular section (Fig. 91b) show the beginning of a shallow (about 200 m AGL) weak off shore flow, which is capped by a somewhat stronger westerly flow that could be a combination of sea breeze remnants and/or a return flow. Inland BTW again shows onshore westerly flow, as it did 24 hours previous.

The 05/22UTC (05/15PDT) coastal section (Fig. 91c) is at the time of the peak ozone, and it shows that both the easterly synoptic flow and onshore sea breeze flows now cover the entire Basin. The sea breeze is somewhat stronger and deeper than 24 hours previous, now extending to about 1000 m AGL in the northern part of the Basin and to about 2000 m AGL in its southern part. Several sites also show the beginning of a weak return flow layer, centered at about 2500 m AGL.

The concurrent perpendicular05/22UTC section (Fig. 91d) again shows a deep sea breeze flow at all sites west of the San Gabriel Mountains that is again deeper, as it now extends up to 2000 m AGL at all Basin sites. The return flow layer is again several hundred meters deep at a few sites, but its top is hard to discern at several other sites as it blends into the now easterly synoptic flow.

The near-midnight coastal vertical section on 06/06UTC (Fig. 92a) shows stronger easterly synoptic flow. The lower level flow (below 2000 m AGL) over the Basin again has a generally weak and shallow (600 m MSL) offshore component. This flow was capped by the remnants of the daytime westerly sea breeze, which became particularly strong later in the evening (e.g., see Fig. 88c from LAX).

Most Basin sites in the concurrent perpendicular section (Fig. 92b) now show a deeper than 24 hours prior offshore flow. While the previous flow was only about 200 m AGL deep, this flow is about 500 m deep at the coast and until about 1500 GMT rises to about 1500 m AGL at NTN. It is again capped by a strong westerly flow that near the coast is a combination of sea breeze remnants and a return flow. Inland BTW again shows onshore westerly flow.

The 06/22UTC coastal section (Fig. 92c) shows that that the easterly synoptic flow has become southerly at the northern end of the Basin (PHE to VAN), as the high has moved inland. The sea breeze is weaker than 24 hours previous, and now has a southerly component at most SoCAB sites (except CBD). It does, however, extend to about 2000 m AGL over most of the Basin, and any return flows present have blended in with the upper synoptic flow.

The concurrent perpendicular 06/22UTC section (Fig. 92d) again shows a coastal southerly sea breeze flow, but an inland westerly one at all sites west of the San Gabriel Mountains. It again

generally extends up to 2000 m AGL. The capping transition layer is several 100 m deep, but its top is hard to discern as it again blends into the still easterly synoptic flow.

Horizontal distributions of RASS hourly profiler winds at key flow levels, in combination with six hourly rawinsonde winds, can provide additional insights into temporal variations of the complex interactions between synoptic and mesoscale effects on spatial flow patterns. As discussed above, 3800 m AGL is the optimum level (in terms of data density and lack of mesoscale forcing) to look for purely synoptic flow field patterns.

The 04/18UTC flow field at 3800 m AGL (Fig. 93a) thus shows onshore flow over the SoCAB that became more along-shore during the next fours. By 05/00UTC (Fig. 93b), the offshore synoptic high discussed above seems to have produced off shore flow in the southern half of the Basin. Six hours later, while the high is still offshore, it has moved north of Basin, thus producing offshore flow over the entire Basin (Fig. 93c). Another six hours later (Fig. 93d), the high has started to move back to the south and inland, producing offshore flow in the southern Basin, along-shore flow from the south in the middle of the Basin, and the beginnings of onshore flow at the northern edge of the Basin. By 05/20UTC, the high must have again moved back north, as the flow field (Fig. 93e) at the few stations available at this time shows mostly easterly offshore flow over the entire SoCAB. By 06/00UTC enough stations are shown (Fig. 93f), so that the high is again visible. While the flow at this time is still offshore over the Basin, it now is more northeasterly, but it is also now along-shore at coastal sites on the northern edge of the basin. This is all consistent with a more northerly position of the high. By 06/12UTC (Fig. 93g), only the southern part of the basin still shows offshore pattern that continued to the end of the test period.

Now that the upper level synoptic forcing has been described, the following section reviews mesoscale effects at various key levels, starting with the surface. The nighttime surface flow pattern at 04/12UTC shows a complex combination of low speed flows (Fig. 94a). While some areas of down-slope flow can be seen, no clearly defined land breeze flow exists. By 04/16UTC, surface wind speeds have increased (Fig. 94b) and have become organized into an onshore surface sea breeze flow from the west-southwest (almost perpendicular to coast). Note, that the inland opposing synoptic flow is also now more organized and at higher speeds.

By 04/23UTC, the sea breeze reaches its maximum intensity, with an inland penetration that extends to the line of the inland high elevation areas (Fig. 94c). The southeasterly up-slope winds on the inland side of the north to south oriented San Ana Mountains are probably due to local topographic effects, and not to the upper level synoptic flow, which at this time is from the southwest. Thus these surface winds do not really oppose the sea breeze flow, although a weak north to south oriented convergence zone is seen along the ridgeline of the Santa Ana Mountains.

By 05/02UTC (Fig. 94d), the sea breeze has weakened, and is at its maximum inland penetration (note that winds on eastern slope of the Santa Bernardino Mountains are now also more westerly). By 05/03UTC, the sea breeze has retreated significantly back to the coast, especially in the northern Basin (Fig. 94e).

The nighttime surface flow pattern at 05/12UTC shows a similar (to that at the same time on the 4th) complex flow pattern (Fig. 94f). Wind speeds, however, are somewhat faster and more organized than on the 4th. By 05/16UTC (not shown) speeds have again organized into an onshore sea breeze flow, but with less inland penetration than 24 hours previous. The reduced penetration is due to the stronger offshore opposing flow component on this day at inland sites, which resulted from the southwesterly upper level synoptic flow direction on the 4th changing to its current northeasterly direction.

By 05/22UTC, the sea breeze again reaches its maximum intensity (Fig. 94g) and again has an inland penetration that generally extends to the same places as on the 4th (Fig. 94c). Winds on the east side of the San Bernardino Mountains are now, however, from the north-northeast, and they now thus more oppose the sea breeze flow than on the 4th.flow. This produces a more extensive and stronger convergence zone along all of the inland ridge tops in the basin. The low speeds within such convergence zones allow concentrations to increase, and the resulting chimney effect ejects pollutants upward. The maximum penetration of the sea breeze on the 5th was, as expected, less than on the previous day (because of the stronger opposing synoptic flow component), and by 06/03UTC the sea breeze again (as on the 5th) had retreated back to the coast (Fig. 94h).

On 06/23UTC, the sea breeze flow direction along the coast was more southerly than on the previous two days (Fig. 94i), while the off shore directed winds on the mountain ridges had the same direction as on those two days. Sea breeze penetration, however, was more inland in the area of the San Bernardino Mountains, as compared to the two previous days. This resulted because of the reduced opposing wind speeds in that area, in association with the above mentioned reduction in the speed of the easterly opposing synoptic flow aloft.

The nighttime 800 m AGL flow pattern at 04/12UTC shows a somewhat less complex combination of faster speed flows (Fig. 95a) than in the concurrent surface chart. While some areas of inland down-slope flow can be seen, no clearly defined land breeze flow exists, as coastal sites show generally along coast flows. By 04/16UTC, while 800 m AGL wind speeds have increased (Fig. 95b) as they did at the surface, they have not yet organized into an onshore sea breeze flow, as they had at the surface. An offshore opposing synoptic flow is also not yet organized. at inland sites.

By 04/23UTC, the sea breeze has formed and reached its maximum intensity, with an inland penetration that also (as it did at the surface) extends to the line of the inland high elevation areas (Fig. 95c). The opposing synoptic flow cannot be determined, due to the lack of inland observations.

By 05/02UTC (Fig. 95d), the sea breeze has not weakened as generally it had at the surface. While it seems to have the same maximum inland penetration as three hours before, its flow is stronger and more northerly than at the surface (as expected from PBL theory). By 05/03UTC, the sea breeze at this level has not retreated back to the coast (Fig. 30e), as it did at the surface. This is consistent with sea breeze remnants found aloft in the profiler time-height sections discussed above.

The nighttime surface flow speeds at 05/12UTC (Fig. 30f) are now faster, more organized, and more northerly (due to the changing synoptic flow) than on the 4th. By 05/16UTC (Fig. 30g) speeds have not organized into an onshore sea breeze flow (as occurred at the surface), due to the stronger offshore opposing flow component on this day at inland sites that resulted from the new northeasterly upper level synoptic flow direction.

By 05/22UTC (one hour earlier than on the previous day), the sea breeze reaches its maximum intensity (Fig. 95h), because of the stronger land-sea temperature gradient on this day (as discussed above). The exact nature of the opposing flow at this level is unknown, due to too few observations. The flow then turns, and remains, more along-shore (from the northwest) over most of the Basin, while it is offshore from the north at the northern Basin edge until 06/06UTC (Fig. 95i). For the next four hours (Fig. 95j), the offshore flow turned more to the northeast and its area expanded southward into the Basin.

By 06/15UTC, the 800 m AGL flow direction had turned to become a southeasterly along-coast flow (Fig. 95k). It remained this way, until an on shore sea breeze flow started to form at 06/18UTC at the southern edge of the Basin, and which after four hours, a sea breeze flow existed over the entire Basin (Fig. 95l).

The interpolated and smoothed upper level temperature sections show a consistent structure. At 800m, the gradients between coastal and inland areas are weaker than 300m. Comparing the 300m levels for 0000 5th and 0000 6th, the temperatures of 6th 0000 are 2-3 degrees higher.

7.4. SoCAB Ozone Data

Afternoon surface ozone concentrations at 04/20UTC (or 04/13PDT) have increased above 80 ppbV in the San Gabriel Mountains (Fig. 96a). Later in the afternoon, the high values were advected southwestward, while photochemical production pushed values up to 130 ppbV south of San Bernardino at 04/23UTC (Fig. 96b) and at 04/24UTC. Values then gradually decreased and were transported northeastward, but with significant concentrations still found at 05/06UTC (Fig. 96c).

In the early morning hours of the 5 August, surface ozone concentrations had fallen below 50 ppbV everywhere in the SoCAB (Fig. 96d). This decrease is partly due to early evening offshore land and drainage breezes that swept the western basin clean and to the nocturnal NO titration of ozone. Ozone concentration then increased again over the Basin, as light morning boundary layer winds are not effective in dispersing emitted primary pollutants from their source regions. By 05/17UTC, however, the mixed layer deepened and ozone concentrations again rose to 100 ppbV in the southwest basin near San Diego (Fig. 96e), where emissions of primary pollutants are relatively small. A site near the San Fernando Valley reported concentrations above 120 ppbV one hour later, perhaps due to the downward fumigation of aged pollutant aloft.

As the sea breeze developed, precursor pollutants were carried eastward (inland), and up the mountain and ozone was generated by photochemical processes driven by NO_x and NMHC emissions. A sharp gradient in ozone concentration thus forms from the coast toward the inland mountains by the afternoon. The regional mountains act as a barrier, however, confining ozone

within the extended coastal plain, and thus peak ozone concentrations develop along the southern slopes of the San Gabriel Mountains.

The ozone episode (Fig. 96f) reaches a peak at 05/22UTC (or 05/15PDT), when five sites reported concentrations above 120 ppbV. After a maximum of 187 ppbV was reached at a site southeast of San Gabriel, ozone was advected slowly towards the east. Values decreased more abruptly than on the previous day, perhaps due to the then stronger winds aloft. By 06/02UTC (or 05/19PDT) they were already low (Fig. 96g). Throughout the afternoon and evening, polluted air was transported upslope through mountain passes into the desert regions beyond, while some was also vented into the free troposphere. Later at night, ozone concentrations near the surface were thus generally low. Along the mountain slopes, however, high ozone concentrations can still be found, due to elevated layers of pollution formed over the basin during the afternoon and stabilized in the elevated thermal inversion layer.

8. RESULTS OF SoCAB NUMERICAL SEA BREEZE EXPERIMENTS

A series of six MM5 simulations of the 2-7 August SCOS97 episode was carried out, as described in Table 14. A preliminary description of the first two simulations also appears in Boucouvala et al. (2000). As it is necessary to obtain accurate temperature simulations before it is possible to obtain accurate wind simulations (Bornstein et al. 1996), discussion of the first few simulations will mainly focus on predicted temperature values. For brevity, again only MM5 results from Domain 4 (inner, 5 km resolution) will be presented. The lowest temperature and wind prediction level at 23 m AGL in the inner 5 km resolution Domain 4 will be compared to observed 2 m temperatures and 7 m winds.

8.1. Run 1: Hands Off Simulation

Run 1 was carried out without either analysis or observational nudging, and thus it is not expected that it would produce acceptable results. Its results are presented, however, so as to provide a baseline against which results from the remaining five simulations can be compared. In fact, this simulation did reproduce many observed features of the spatial and temporal temperature and wind patterns over the SoCAB, but did not, however, correctly reproduce all their quantitative aspects.

MM5 temperatures (Fig. 97a) at 05/09UTC (05/02PDT), the nighttime period prior to the following daytime ozone episode, reproduced the observed nighttime cool coastline (18^0C), warm coastal plane (24^0C), warmer inland areas (34^0C), and cool mountain-peak (17^0C) areas (few observations available). The distribution at 05/21UTC (05/14PDT), an hour before peak ozone, also reproduced the observed pattern (Fig. 97b). This pattern was similar to that the night before, except that values had increased as expected to 23^0C at the coast, 34^0C on the coastal plane, 40^0C at inland areas, and 18^0C on the mountain peaks. While modeled coastal temperature gradients are significantly larger than those 12 hours before, they are, however, larger than observed, although accurate assessment of coastal gradients is difficult.

Domain-wide average observed versus first-level predicted MM5 domain-wide average diurnal temperature waves were similar to observed values, as evaluated by the MAPS statistical

package for the simulation period for Run 1 (Fig. 98). Results show a maximum under prediction of daytime temperatures of 5 K and a maximum over prediction of nighttime temperatures of 2 K. The cyclic equilibrium in the predicted diurnal temperature waves is an expected good result from this simulation, given the lack of cloud cover on any of the days and given the small day to day variation in solar forcing during such a short simulation period. The observations, however, show a general warming on the 5 August (episode day) due to the previously discussed westward movement and intensification of the GC anticyclone.

The domain 4 MM5first sigma level spatial nighttime wind pattern at 05/09UTC (05/02PDT) reveals a similar complex flow pattern (Fig.99a) as seen in the observations. While some down slope flow is seen, no clearly defined land-breeze flow exists. By 05/16UTC (05/09PDT), observed and simulated surface wind speeds had increased and organized into an onshore sea breeze flow.

By 05/21UTC on 5 August (one hour before peak ozone levels), the inland penetration of the simulated near-surface sea breeze flow (Fig. 99b) generally extended to the ridgeline of the first inland chain of high elevation areas. While predicted directions in the coastal zone over the northern and central SoCAB generally match the observed westerly flow direction, those near San Diego to the south generally have a more northwesterly component than do the observed values. By 06/03UTC (05/20PDT), the sea breeze retreated back to the coast (not shown). MAPS wind speed comparisons will be not shown (as was done in Fig. 98 for temperature) until 2 m temperatures are correctly reproduced in a subsequent simulation. The rationale for this is that the spatial distribution of these temperatures provides the mesoscale forcing, which in conjunction with the synoptic forcing aloft, controls the near surface flows.

This simulation was thus able to qualitatively capture the diurnal effects of the mesoscale surface forcing. But as it could not reproduce effects due to the observed changes in the upper level synoptic forcing, the Analysis Nudging Run 2 simulation was next carried out.

8.2. Run 2: Analysis Nudging Simulation

Run 2 was like Run 1 (Table 14), but with the addition of analysis (but not observational) nudging). As discussed above, analysis nudging as carried out in these first simulations involves use of NCAR GDAS fields to nudge solutions in the three outer domains.

Domain-wide average observed versus MM5first level predicted diurnal temperature waves, again calculated by MAPS, for this run (Fig. 100a) now show the anticipated simulated warming on the 5 August episode day. The maximum under prediction of daytime temperatures has been reduced to only 3 K, while the maximum over prediction of nighttime temperatures is still, however, about 2 K.

While temperatures are observed at a height of about 2 m, MM5 first-level predicted temperatures in the current simulations are calculated at a height of 23 m. A log-law height correction to 2 m was thus made to simulated MM5 values in a post-simulation processing procedure. This correction made use of the computed MM5 SBL scaling friction potential temperature simulation processing procedure (Fig. 100b) at each grid point at each hourly output interval. While the

correction worked well for daytime values (Fig. 100b) as it almost completely eliminated all differences, it had virtually no effect on nighttime values, and thus the Cool Soil Run 3 simulation was next carried out.

8.3. Run 3: Cool Soil Simulation

As an analysis of the force restore temperature prediction scheme by Bornstein et al. (1996) showed nighttime minimum temperatures dependent on deep soil temperature, and thus Run 3 specified a deep soil temperature reduced by 4 K from that used in Runs 1 and 2 (Table 14). This parameter represents the "restore" part of the temperature scheme, as it pulls nighttime values lower after daytime values are "forced" upwards by solar heating.

While use of the lower deep soil temperature resulted did in MM5 produce generally good nighttime results (Fig. 101), daytime maximum temperatures on the episode day were reduced to a level slightly below observed values. As deep soil temperature is only arbitrarily estimated in MM5 (as the simulation period average of input 0000 and 1200 UTC NCAR GDAS surface values), the current adjustment procedure suggests a need for better determination of this not normally measured parameter.

As 2 m MM5 temperatures are correctly simulated for the first time in Run 3, MM5 predicted near surface wind fields should also be reviewed. The MM5 nighttime wind pattern at 05/09UTC (05/02PDT) in this analysis nudged run again reveals a complex flow pattern (Fig.102a) similar to those of Run 1 (Fig. 99a). Downslope flows are again correctly simulated, and the observations and simulation still agree that no clearly defined land breeze flow exists. Differences do exist between the two simulations, however, as the organized moderate speed westerly onshore flow has moved north from the southern Los Angeles basin to the northern Los Angeles basin, as a result of the analysis nudging. This movement is consistent with the northward movement of the coast high discussed above in the observation section. In addition, the random flow in Run 1 in the inland areas on both sides of the Mexican boarder has become an organized northerly flow.

By 05/16UTC, simulated surface wind speeds increased and were organized into an onshore sea breeze flow (not shown). But by 05/21UTC (hour before peak ozone levels), the inland penetration of both the Run 3 observed and simulated near-surface sea breeze flow (Fig. 102b) generally extended to the ridgeline of the first inland chain of high elevation areas, again similar to that of Run 1. Differences do exist again, however, as analysis forcing has increased daytime wind speeds over the ocean (area with few flow speed observations). Onshore flow speeds have thus also increased, thereby correctly producing an earlier (about 1-2 hr) and stronger (about 1-2 m s^{-1}) sea breeze front. Daytime speed differences with observations are again largest in the northwestern part of the domain, where the synoptic forcing was still too large. The opposing off shore flow at the sea breeze front over the San Bernardino Mountains is also now stronger and more organized than in Run 1, and thus in better agreement with the observed winds in the area.. By 06/03UTC (05/20PDT), the sea breeze retreated back to the coast (not shown).

Domain-wide average observed versus MM5first-level predicted diurnal scalar wind speeds calculated by the MAPS statistical package for the simulation period for Run 3 (Fig. 103a) show

daytime peaks correctly simulated on 3 and 6 August, but overestimated on 4 and 5 August. While daytime speeds generally first peak near the correct time, predicted maxima remain well into the nighttime period, resulting in large over predictions, i.e., 2 m s^{-1} (with the 1 m s^{-1} observational cut off discussed above) versus 4.3 m s^{-1}. These high speeds are due to the synoptic forcing in the analysis nudging, as discussed above. Predicted nighttime speeds eventually do decrease, and the time of their minimum correctly corresponds to the end of each observed nighttime low speed period.

Concurrent vector observed (without the observational cut off) and predicted wind , as expected, are both lower (Fig. 103b) than the scalar speeds of Fig. 103a, as opposing-flow speeds cancel in vector averaging. Vector speeds are thus good for showing flow direction discontinuities, such as sea or land breeze fronts, as speed minima. The predicted midday speed minima in Fig. 103b thus correspond to sea breeze passages, which show up stronger in the MM5 results than in the observations. The magnitude of the nighttime MM5 vector speed minimum magnitudes agree better relative to the observed values, as compared to corresponding scalar values. Thus while the Analysis Nudging Run 3 has improved MM5 performance with respect to synoptic warming on the episode day, it has increased wind speeds. Additional simulations are, hence, required to improve its performance with respect to wind, and hence the FDDA Run 4 was next carried out.

8.4. Run 4: FDDA Simulation

Run 4 was same as Run3, but also included the FDDA of data from the extensive SCOS97 surface and upper air (rawinsonde and profiler) observational network (Table 14). As surface and PBL temperatures are not nudged, MAPS domain-average predicted temperature waves for this run (Fig. 104) did not change much relative to the good results of Run 3. Peak temperatures on the 5 August episode day, however, were simulated even slightly better. Subsequent analyses, however, showed that Run 4 upper air rawinsonde and profiler data were erroneously assimilated at MSL elevations and not at required AGL levels, and thus Run 4 surface winds will not be discussed. Since Run 3 nighttime near-surface winds were still too fast, the Run 5 Urban Extended Simulation was next carried out.

8.5. Run 5: Urban Extended Simulation

Run 5 was like the Run 4 FDDA simulation, except that: (1) upper air data were assimilated at the correct AGL heights, (2) wind analysis nudging was performed only in the outermost domain and not also in the middle two domains, as had been done in Runs 2-4, (3) Los Angeles urban boundaries were extended, and (4) surface roughness values z_0 were increased for a number of land use types. In addition, rawinsonde site PLM and profiler site ECO were excluded from the FDDA input files, as their winds seemed irregular.

Change (2) was initiated because nighttime wind speeds errors for Runs 2 and 3 (which included analysis nudging) were larger than those of Run 1 (which did not include it), while change (3) was carried out as urban areas with their large z_0 values act to reduce wind speeds. Change (4) was initiated because the analysis nudging of Runs 2 and 3 produced wind speeds off the Ventura coast that seemed excessive (Figs. 99 and 102). While off shore observations are not available to be certain of this, the excessive winds were advected onto the Ventura coast (perhaps

located too close to the western boundary of Domain 4), where observations did show over predicted speeds.

While the assumed sea surface z_0 value in the MM5 was only 0.01 cm, this value is internally increased as a function of increasing wind speed using the formulation of Charnock (1955). This formulation, however, is only valid under "complete equilibrium" conditions that rarely "exist over lakes and oceans" (Arya 1988). The more general formulation of Kitaigorodski (1970), which relates sea surface z_0 values to wave height, yields values of up to 10 cm. A value of 1 cm was thus selected for use in Runs 5 and 6. In addition, the urban z_0 value in MM5 of 50 cm is too low for a city the size of Los Angeles, as urban values in the literature range up to 4-5 m (Arya 1988). A value of 1.5 m was thus selected for Runs 5 and 6, and given the rough topography of the SoCAB domain, several other z_0 values were likewise increased (Table 15).

The Run 5 spatial temperature pattern (Fig. 105a) at 05/09UTC (05/02PDT) is generally similar to that of Run 1. Major changes were not expected, as surface and PBL temperatures are not directly effected by either analysis or observational nudging. The overall lower nighttime temperatures of Run 5 (relative to those of Run 1) are expected, however, given the demonstrated direct effects of the lowered deep soil temperature first introduced in Run 3. These changes have produced a steeper coastal gradient (as compared to Fig. 97a), especially in mountain areas northwest of the Los Angeles Basin. At 05/21UTC the temperature field is also generally similar to that of Run1 (Fig. 97b), but the higher temperatures and steeper coastal gradient on this day are due to the analysis nudging induced warming of Run 3.

While the magnitude of the above temperature changes may be difficult to quantify from the spatial patters, the domain-wide MAPS temperature wave (Fig. 106 vs. 101) shows results that are even better (for the maximum values on the episode day) than for Run 3 (last correct run). The full domain-average curves, however, can mask compensating errors in different areas across the SoCAB. To investigate this effect, the SoCAB was divided into the following seven sub domains (Fig. 107): (1) South Central Coast, (2) South Coast, (3) Foothills, (4) South Central Valley, (5) Interior, (6) Desert, and (7) Mountains.

In the important (has many comparison sites and sea breeze passages) Sub-domain (2), which includes the Los Angeles Basin, nighttime temperatures are well simulated, but daytime temperatures are under-predicted by about 4 K. In Sub-domain (1) to the north (also with many comparison sites), daytime temperatures are over-predicted by about 5 K on all but the episode day (when they are well predicted); nighttime values are also generally over-predicted by about 4 K. The remaining five Sub-domains contain fewer comparison sites. The Desert and Foothills areas (Figs. 108c and d, respectively) show 2 K under-predicted daytime and nighttime temperatures, while the Interior area (Fig. 108e) shows only under predicted nighttime temperatures. Finally, the Mountain areas (Fig. 108f) show 3 K under-predicted daytime and 2 K over predicted nighttime temperatures, while the South Central Valley area (Fig. 108g) shows good agreement throughout the day.

The nighttime wind pattern at 05/09UTC (05/02PDT) again reveals a complex flow pattern (Fig.109a). There are, however, some changes from Run 1, as observed winds now nudge the PBL and above, and as GDAS winds nudge only above. While down slope Katabatic flows are

now stronger (perhaps too strong in the mountain areas north of the SoCAB), a clearly defined land-breeze flow still does not exist. Wind directions in the northeast part of the SoCAB have completely reversed, and now are now northerly (due to the observed temporal changes in the assimilated synoptic conditions discussed above). Speeds over the ocean are now correctly lower and less organized, due to the increased z_0 over the water. They are also lower over the urban Los Angeles Basin, due to its expansion to its also increased z_0.

On 05/21UTC on 5 August (one hour before peak ozone levels), the onshore sea breeze wind is slower than in Run1 over the rougher urbanized areas (with their new larger z_0 values) than in Run1 and in the areas between the San Gabriel and San Bernardino Mountains. The opposing offshore winds from the mountains are again (as in Run 3) also more organized and stronger (due to the analysis and observational nudging) than in Run 1, and thus sea breeze penetration is less than that of Run 1. Their convergence with the sea breeze flow will cause the peak ozone accumulation on this day.

Domain-wide MM5first-level predicted scalar wind speeds calculated by MAPS for Run 5 (Fig. 110) again (as in Run 3) show daytime peaks correctly simulated on 3 and 6 August, but overestimated on 4 and 5 August. Daytime maxima again remain well into the nighttime period, resulting in even larger (than in Run 3) over predictions (>5 m s^{-1} vs. 4.3 m s^{-1} in Run 3). These higher Run 5 speeds are due to the observational nudging. The general over-prediction is also found in the four following sub-domains: South Coast, South Central Coast, Desert, and Mountains (Fig. 110a-d, respectively). In the remaining three areas (Foothills, Interior, and South Central Valley), MM5 better reproduces better reproduce their observed speeds (Figs.110e-g, respectively).

Concurrent vector observed and predicted wind are, as expected, again (as in Run 3) lower (Fig. 112) than their corresponding scalar speeds, but are faster than those of Run 3 on the episode day, once again due to the observational nudging. They are more variable than the scalar speeds, and due to the inherent compensations built into their calculation, they better match the low speed observations. Hence only the South Coast and South Central Coast areas show over-predictions on 5 and 6 August, while the remaining five areas do show relatively good agreement with the observations (Figs.113a-g).

The MAPS domain-averaged wind direction analysis for Run 5 (Fig. 114) show some agreement with observations, in that the direction shifts associated with the onset and cessation of the sea breeze flow are simulation, although the exact timing and directions may not be reproduced exactly. The same is true for the seven sub-domains (Figs. 115a-g)

Thus while the observational nudging (with both surface and upper air data) of Run 5 still results in an over-predicted nighttime winds, the final Surface-Only Analysis Nudging Run 6 was carried out next.

8.6. Run 6: FDDA Surface-Only Simulation

Run 6 was like Run 5 (Table 14), except that observational nudging was done only with surface data, so that the source (surface versus upper air) of the nighttime over-predicted wind speeds

might be identified. Observational analysis again did not much impact domain averaged near-surface temperatures, which remained well predicted (Fig.116). Domain averaged nighttime scalar (Fig. 117) and vector (Fig. 118) wind speeds were both, however, better predicted (i. e, lower) than those of Run 5. This demonstrates that it was the high-speed upper-level profiler and especially the rawinsonde winds that over-influenced the surface wind speeds of Run 5. The same was true for wind direction (Fig. 119).

9. SUMMARY

9.1 Conclusions of SJV Fog Study

The principal conclusions from the SJV fog investigation are summarized below:

(1) The MM5 is capable of simulating the evolution of fog and haze in the SJV with considerable accuracy. This type of obscuration can be diagnosed from the model's simulated fields of temperature and dew-point depression. The accurate prediction of the dew-point depression is a key factor allowing for an aerosol model to work correctly. The MM5 also shows reasonably good skill in simulating the depth of the fog and haze layer, and whether or not it is topped by stratus.

(2) The extension of the Gayno-Seaman TKE-simulating turbulence sub-model to include the effects of saturation on the buoyancy production of TKE was important for the simulation of fog characteristics. The very high vertical resolution used in these experiments appears to be helpful for resolving the fog-and-haze-sensitive processes close to the ground. It would have been difficult for a boundary-layer parameterization that does not account fully for the effects of saturation (e.g., the Blackadar PBL scheme) to produce the correct vertical structure of the thermodynamic variables in the saturated layers.

(3) It was quite important in this case to use soil temperatures and soil moistures that are as accurate as possible. These surface characteristics can have a profound effect on the evolution of fog and haze, especially in multi-day episodes. Models that are intended for fog and haze simulations should use a land-surface sub-model that can account for changes in the deep soil characteristics as atmospheric conditions evolve.

(4) The MM5 was able to simulate the very light and variable winds in the SJV and Sacramento Valley in the post-frontal maritime polar air mass. The model appears to reproduce these light winds for the correct reasons, especially by decoupling the cool low-level air mass from the higher momentum flow above the level of the mountain ranges surrounding the Valleys. The winds responded quite well to the slowly changing synoptic-scale weather patterns, as well, so that the wind direction sometimes became organized over part or all of the Valley floor, much similar to the response to observed patterns.

(5) The FDDA (analysis nudging) used in the MM5 experiments reported here was not applied to either the 12-km and 4-km domains. Therefore, FDDA only served to improve the quality of the lateral boundary conditions on the target domain, but it did not play any

direct role on the evolution of simulated fog characteristics reported in Sec. 5. The use of FDDA was probably valuable in this set of simulations of an historical event because it reduces the possibility of phase errors in the synoptic pattern and other large-scale problems in the model solutions. Such errors could have masked the development of fog in the SJV and made interpretation of the results much more difficult.

9.2 Recommendations for Future SJV Fog Research

Even though the evaluations of the model solutions and observations summarized in this report indicate mostly positive results, it is clear that the findings of this study can be generalized only through additional work. Therefore, the following steps for future research are recommended:

(1) It would not be difficult to write software to objectively diagnose fog, haze, stratus, and clear skies from the MM5 output fields, using the criteria developed in this study. The statistical correlations developed here can be improved by expanding the database over more observed cases. Correlations should also be calculated for dew-point depressions associated with clear skies. Additionally, the effect of wind speed on visibility in the SJV can be included. The result would be a more reliable, automated approach for objectively diagnosing fog from the meteorological model outputs in wintertime applications of the MM5, even for situations for which an aerosol model is not available. These objectively diagnosed fields can be generated for the entire domain. It would then be quite simple to verify the model predictions against individual NWS observations every 3 h at all reporting reporting stations in the Valleys, and also by using satellite images (when available). This research would be a logical way to begin evaluating and refining the techniques developed here, and it could eventually lead to more reliable real-time forecasts of haze and fog conditions in the SJV.

(2) The specification of temporally constant fields for T_m and soil moisture is not satisfactory for multi-day episodes with significantly changing conditions. Even when the T_m field is specified more carefully than in the standard public-release version of the MM5 pre-processors, as done in this study, a time invariant T_m can lead to errors in the low-level temperature and relative humidity fields. Such errors in the surface-layer fields could be very damaging for the simulation of fog and haze, whether or not an aerosol model is coupled to the meteorological model. Similar errors can occur when the soil-moisture fields are held constant in time. Therefore, it recommended that the Gayno-Seaman turbulence sub-model be coupled with a more sophisticated land-surface scheme that allows for a more realistic evolution of the soil temperature and moisture through the simulation period. The MM5 system already has at least one interactive land-surface sub-model available for use with several other boundary-layer schemes. It should not be difficult to extend the Gayno-Seaman sub-model accordingly.

(3) Since this study was based on only one case, there was insufficient data to develop a realistic algorithm to estimate visibility distance (km or miles) as a function of the MM5-simulated variables (temperature, dew point, TKE, wind, etc.). Diagnosing the type of low-level obscuration (fog, haze, stratus, or clear skies) was within the possibility of the

data base, and that prediction was shown to be quite successful. Clearly, simulation of additional fog and haze cases in the SJV is needed to further evaluate and extend the diagnostic approaches begun here.

9.3 Conclusions of SoCAB Sea Breeze Study

Principal conclusions from the SoCAB sea breeze investigation are summarized below:

(1) The SCOS97 3-7 August surface ozone episode resulted from a rarely occurring large-scale upper level synoptic forcing. NWS synoptic weather charts showed the SoCAB area protected during the episode period from large-scale synoptic forcings by the offshore position of the General Circulation Pacific High. A weak local coastal 700 mb anticyclone, too small to be resolved on NWS charts, was however resolved by the NCAR GDAS model simulations used to initialize, provide boundary conditions for, and nudge MM5 solutions via FDDA.

(2) The coastal 700 mb anticyclone first moved from a position on the central SoCAB coast to a position at the southern SoCAB coast, and then to a position at the northern SoCAB coast. The latter movement resulted in a rotation of the upper level (> 3000 m MSL) synoptic background flow from its normal westerly onshore direction to a less common offshore easterly flow during the nighttime period preceding the ozone episode. This direction change was clearly visible in the NCAR GDAS model winds and in the SCOS97 RWP and rawinsonde observed winds. The offshore movement of the high also produced warming aloft and at the surface on the episode day, as well as a sinking and strengthening of its associated elevated subsidence inversion over SoCAB.

(3) Resulting easterly upper level synoptic background winds influenced surface wind flow directions at inland sites, so that a surface frontal convergence zone resulted where the background easterly flow met the inland moving westerly onshore sea breeze flow. The maximum inland penetration of the convergence zone was to the San Gabriel Mountain peaks, and resulted in the location of the maximum daytime ozone-episode concentrations.

(4) The current MM5 simulations reproduced the main qualitative features of the evolution of the diurnal sea breeze cycle in the SoCAB with reasonable accuracy. The position of the sea breeze front during its daytime inland penetration and nighttime retreat could be determined from the simulated wind fields. In particular, MM5 showed reasonable skill in simulation of the diurnal variation of coastal temperature gradients that produce the diurnal sea breeze cycle, opposing easterly flow, inland movement of the sea breeze front, retreat of land breeze front, and spatial wind velocity distributions.

(5) The accuracy of predicted MM5 surface winds and temperatures over SoCAB were improved in the current simulations by the following sequential modifications of MM5 and/or its input parameters: use of the PSU MBLI scheme, use of the Gayno-Seaman turbulence scheme, analysis nudging with NCAR GDAS model output, accurate specification of deep-soil temperature, interpolation of predicted MM5 temperatures and

winds to SCOS97 observational levels, observational nudging with SCOS97 surface and upper level coarse RWP and rawinsonde winds and RASS temperatures, use of updated urban land-use patterns, use of corrected input ocean and urban surface roughness parameter values, and proper limitation of MM5 diagnosed mixing-depth values.

(6) The current MM5 simulations were less successful in the reproduction of some quantitative aspects of the diurnal evolution of the SoCAB sea breeze cycle, including low nighttime wind speeds, and the precise times and magnitudes of some sea and land breeze frontal wind shifts. Possible causes of these discrepancies include: errors in the early version of the2-7 August SCOS97 observational data set (version MET-0) supplied by CARB, errors in the NCAR GDAS wind fields, over nudging in the vertical of the SCOS97 (RWP RASS, and rawinsonde) winds, use of a too large lowest vertical grid spacing, Domain 4 lateral boundary too close to Ventura coastline, and/or too large Domain 4 horizontal grid spacing.

9.4 Recommendations for Future SoCAB Sea Breeze Research

Although the evaluations of the SCOS97 observations and MM5 model results summarized in this report indicate mostly positive results, it is clear that a complete understanding of the meteorology of the 3-7 August ozone episode requires additional data analysis and model simulations. The following future research is thus recommended:

(1) Now that higher QA-level SCOS97 upper air data sets are available, additional analyses of the 3-7 August episode should be carried out to refine our understanding of the complex interactions between the upper level synoptic and surface mesoscale meteorological forcings that produced the episode. Particular attention should be paid to possible terrain induced return flow regions within the strong elevated subsidence inversion, and their role in the fumigation of residual layer ozone to the surface during midmorning periods, as apparently observed in the hours before the afternoon episode. Such a run would require a more detailed analysis of MM5 upper air distributions than done in the current study.

(2) A review of the NCAR Reanalysis large scale model wind fields for this SCOS97 case revealed that its upper level nighttime winds were lower than those of the NCAR GDAS fields used as the initial conditions, boundary conditions, and analysis nudging fields in the current simulations. Although the latest version of the MM5 users manual recommends GDAS output, because of its more realistic coastal temperature gradients, it would be useful to carry out a simulation with Reanalysis model fields to see if this reduces the currently over predicted nighttime wind speeds.

(3) As the current simulations showed increased over-predicted nighttime wind speeds when SCOS97 upper air winds were used in the observational nudging scheme, it would be useful to carry out a simulation with a reduced vertical nudging coefficient. This change would reduce impacts from upper-level high-speed layers on over-predicted nighttime surface speeds. This run should be made if the updated (higher QA level) SCOS97 upper air data still produce over-predicted nighttime surface wind speeds.

(4) As the MM5 configuration for an optimum SoCAB sea breeze simulation involves several important formulation and input choices, sequential parametric MM5 simulations should be carried out to determine the optimum combination of: first vertical grid spacing (perhaps the 7 m value used in the current SJV study), westward movement of the Domain 4 lateral boundary position, reduced Domain 4 horizontal grid spacing (to perhaps 1.67 km), updated land use boundaries and parameters, and better determined deep soil temperatures. The proposed simulations will build upon the understanding and results obtained from the current effort. A more complete understanding will allow for more accurate simulations of the complex meteorological conditions that produced the 3-7 August 1997 SoCAB ozone episode, and those results will allow for more accurate air quality simulations.

REFERENCES

Arya, P., 1988: *Introduction to Micrometeorology*. Academic Press, New York, 307 pp.

Baxter, R. A., 1991: Determination of mixing heights from data collected during the 1985 SCCCAMP Field Program. *J. Appl. Meteor*., **30**, 598-606.

Benjamin, S. G., and N. L. Seaman, 1985: A simple scheme for objective analysis in curved flow. *Mon. Wea. Rev.,* **113**, 1184-1198.

Bettes, A. K., 1973: Non-precipitating cumulus convection and its parameterization. *Quart. J. Roy. Meteor. Soc*., **99**, 178-196.

Blackadar, A., 1979: High resolution models of the PBL. *Advances in Environ. Sci. and Engin*., J. Pfafflin and E. Ziegler, Eds, **1,** Gordon and breach, 50-85.

Bornstein, R. D., P. Thunis, P. Grossi, and G. Schayes, 1996: Development of the Topographic Vorticity-mode Mesoscale (TVM) Model: Part II--Evaluation. *J. Appl. Meteor.*, **35**, 1824-1834.

Bornstein, R., and D. Boucouvala, 2000: Preliminary meteorological analysis of a 1997: Southern California ozone study (SCOS'97) episode. *11th Joint AMS/AWMA Conf. on Applications of Air Pollution Meteor.,* 9-14 Jan, Long Beach: .70-73.

Boucouvala, D., and R. Bornstein, 2000: MM5 simulation of the meteorological conditions during a Southern California ozone study (SCOS'97) episode. NATO/ITM *Conf. on Air Pollution Modelling,* 15-19 Boulder, CO, 8 pp.

CARB, 2001: SCOS97-NARSTO data analysis conference. Abstracts. 13-15 Feb., Diamond Bar, CA., 21 pp.

Charnock, H., 1955: Wind stress on a water surface. *Q. J. R. Meteorol. Soc*., **81**, 639-640.

Daley, R., 1991: *Atmospheric Data Analysis*. Cambridge Univ. Press, Atmospheric and Space Sciences Series, No. 2, 457 pp.

Davies, H. C., and R. E. Turner, 1977: Updating prediction models by dynamical relaxation: An examination of the technique. *Quart. J. Roy. Meteor. Soc*., **103**, 225-245.

Deardorff, J., 1972: Parameterization of the PBL for use in general circulation models. *Mon. Wea. Rev.,* **100**, 93-106.

Douglas, S. G., and R. C. Kessler, 1991: Analysis of mesoscale airflow patterns in the South-Central Coast air basin during the SCCCAMP 1985 intensive measurement periods. *J. Appl. Meteor*., **30,** 607-631.

Dudhia, J., 1989: Numerical study of convection observed during the winter monsoon experiment using a mesoscale two-dimensional model. *J. Atmos. Sci.,* **46**, 3077-3107.

Dudhia, J., 1993: A nonhydrostatic version of the Penn State/NCAR mesoscale model: Validation tests and simulation of an Atlantic cyclone and cold front. *Mon. Wea. Rev.,* **121**, 1493-1513.

EPA, 1996: Guidance on the use of modeled results to demonstrate attainment of the ozone NAAQS. EPA-454/B-95-007.

Fitzner, C., et al., 1989: Measurement of ozone levels by ship along the eastern shore of Lake Michigan. *J. Air. Pollut. Control Assoc*., **39**, 727-8.

Fujita, E., et al., 2000: SCOS97 Southern California Ozone Study and Aerosol Study. Final report to CARB, Contract No. 93-326, DRI, Reno, NV, 225 pp.

Gayno, G. A., 1994: Development of a Higher-Order, Fog-Producing Boundary Layer Model Suitable for Use in Numerical Weather Prediction. M.S. Thesis, The Pennsylvania State Univ., 104 pp.

Gayno, G. A., N. L. Seaman, A .M. Lario, and D. R. Stauffer, 1994: Forecasting Visibility Using a 1.5-Order Closure Boundary Layer Scheme in a 12-km Non-Hydrostatic Model. 10th AMS Conf. on Num. Wea. Pred., Portland, OR, July 18-22, 18-20.

Gilliam, H., 1970: Weather of the San Francisco Bay Region. U. Calif. Press, Berkeley, 72 pp.

Glendening, J. W., 1990: A mixed-layer simulation of daytime boundary-layer variations within the Los Angeles Basin. *Mon. Wea. Rev*., **118,** 1531-1550.

Grell, G. A., J. Dudhia, and D. Stauffer, 1994: A Description of the Fifth Generation Penn State/ NCAR Mesoscale Model (MM5). NCAR Tech. Note, NCAR TN-398-STR, 138 pp.

Haagenson, P. L., J. Dudhia, G. A. Grell, and D .R. Stauffer, 1994: The Penn State/NCAR Meso-scale Model (MM5) Source Code Documentation. NCAR Tech. Note NCAR/TN-392+ STR, 172 pp.

Hegarty, J., M. Leidner, and M. Iakono, 1998: Modeling Air Pollution in the Los Angeles Basin using the MM5-SAQM modeling system. Part I: meteorological simulations. Preprints, *10th Joint Conference on the applications of Air Pollution Meteorology with A&WMA*, Phoenix, AZ, Amer. Meteor. Soc., J345-J348.

Holets, S., and R. N. Swanson, 1981: High-inversion fog episodes in central California. *J. Appl. Meteor.*, **20**, 890-899.

Kain, J. S., and J. M. Fritsch, 1990: A one-dimensional entraining/detraining plume model and its application in convective parameterization. *J. Atmos. Sci.,* **47**, 2784-2802.

Kain, J., and J. Fritsch, 1993: Convective parameterization for mesoscale models: The Kain-Fritch scheme. *The Representation of Cumulus Convection in Numerical Models,* K. Emanuel and D. Raymond Eds., Amer. Meteor. Soc., pages???????

Kessler, R. C., and G. Douglas, 1991: A numerical study of mesoscale eddy development over the Santa Barbara channel. *J. Appl. Meteor*., **30,** 633-651.

Kitaigorodski, S., 1970: The physics of air-sea interaction. Gidromet. Izdatel'stvo, Leningrad. (Israel Prog. Sci. Tranls., Jerusalem).

Lalas, D., et al., 1983: Sea-breeze circulation and photochemical pollution in Athens, Greece. *Atmos. Environment*, **17**, 1621-32.

Lawson, D. R., 1990: The southern California air quality study. *J. Air Waste Manage. Assoc.,* **40**, 156-165.

Leidner, S., D. Stauffer, and N. Seaman, 1999, Improving short-term numerical weather Prediction in the California coastal zone by dynamic initialization of the marine boundary layer, *Mon. Wea. Rev.,* submitted.

Lin, Q., 2000: Urban influences on summertime convective thunderstorms in Atlanta. M. S. Thesis, Dept. of Meteor., SJSU, San Jose, CA, 116 pp.

Lindsey, C. G., S. E. Ray, B. M. Schoell, T. S. Dye, and M. Arthur, 1996: Data collected by a network of radar profilers, rawinsonde sounding stations, and surface meteorological monitoring sites during IMS-95. Final Data Report STI-95080-1622-FDR, Sonoma Technology Inc., Santa Rosa, CA, 352 pp.

Lozej, C., and R. Bornstein, 1999: Comparison of nesting techniques within a meteorological model. *Air Pollution VII*, Southampton, UK, 1009-1021.

Lu, R., and R. P. Turco, 1995: Air pollutant transport in a coastal environment-II: Three-dimensional simulations over the Los Angeles Basin. *Atmos. Environ.,* **29**, 1499-1518.

Lu, R., and R. P. Turco, 1996: Ozone distributions over the Los Angeles Basin: Three-dimensional simulations with the SMOG model. *Atmos. Environ.,* **30**, 4155-4176.

Lu, R., R. P. Turco, and M. Jacobson, 1997: An integrated air pollution modeling system for urban and regional scales: Part 1. Structure and performance. *J. Geophys. Res.,* **102**, 663-6079.

McElroy, J. L., et al., 1983: Airborne downward looking LIDAR measurements during the San Diego oxidant transport study. TS-AMD-83612, US EPA, Las Vegas, NV.

McElroy, J. L., and T. B. Smith, 1986: Vertical pollutant distributions and boundary layer structure observed by airborne lidar near the complex Southern California coastline. *Atmos. Environ*., **20**, 1555-1566.

McElroy, J. L., and T. B. Smith, 1991: LIDAR Descriptions of Mixing-layer thickness characteristics in a complex terrain/coastal environment. *J. Appl. Meteor*., **30,** 585-597.

Mellor, G.L., and T. Yamada, 1974: A Hierarchy of Turbulence Closure Models for Planetary Boundary-Layers. *J. Atmos. Sci.,* **31**, 1791-1806.

Moore, G. E., and S. D. Reynolds, 1986: Meteorological and air quality analysis in support of the 1985 SCCCAMP monitoring program. Document SYSAPP-86/003, 116 pp. [Avail-able from Systems Applications Inc., San Rafael, CA 94903.]

Moore, G. E., S. G. Killus, R. C. Kessler, and J. P. Killus, 1991: Identification and tracking of polluted air masses in the south-central coast air basin. *J. Appl. Meteor*., **30**, 715-732.

Munoz, R. C., D. R. Stauffer, and N. L. Seaman, 2000: Treatment of buoyancy production at a cloudy-clear interface in a TKE model. 14th AMS Symp. on Bound. Layers and Turb. 7-11 August, Aspen, CO, 4 pp.

Pandis, S. N., and J. H. Seinfeld, 1989: Mathematical modeling of acid deposition due to radiation fog. *J. Geophys. Res.,* **94-D**, 12911-12923.

Scire, J. S., and J. C. Chang, 1991: Analysis of historical ozone episodes in the SCCCAMP region and comparison with SCCAMP 1985 monitoring study. MMS-89-0047, SYSAPP-88 /112. [Available from Systems Applications Inc., San Rafael, CA 94903.]

Seaman, N. L., and D. R. Stauffer, 1996: SARMAP Meteorological Model. Final Report, ENSR Subcontract No. 91219 and Alpine Geophysics Subcontract No. AG/90-TS05-SO2. Available from California Air Resources Board, Technical Support Division, Sacramento, CA. 174 pp.

Seaman, N. L., and D. R. Stauffer, 1998: The Use of the San Joaquin Valley Meteorological Model in Preparation of a Field Program in the south Coast Air Basin and Surrounding Regions of Southern California: Numerical modeling studies to support the design of the 1997 Southern California Ozone Study (SCOS97) field program. Final Report, Contract No. 94-730. Available from California Air Resources Board, Technical Support Division, Sacramento, CA. 145 pp.

Seaman, N. L., D. R. Stauffer, and A. M. Lario, 1995: A multiscale four- dimensional data assimilation system applied in the San Joaquin Valley during SARMAP. Part I: Modeling design and basic performance characteristics. *J. Appl. Meteor*., **34**, 1739-1761.

Shoran, P. C., N. L. Seaman, and G. A. Gayno, 2000: Evaluation of Numerical Predictions of Boundary-Layer Structure during the Lake Michigan Ozone Study (LMOS). *J. Appl. Meteor.,* **39**, 412-426.

Someria, G., and J. W. Deardorff, 1977: Subgrid-scale condensation in models of non-precipitating clouds. *J. Atmos. Sci.,* **34**, 344-355.

Smith, T. B., 1984: A conceptual model of the air quality environment in Ventura-Santa Barbara counties. Rep. for Western Oil and Gas Association, 12 pp. [Available from T.B. and Associates, Inc., Pasadena, CA.]

Smith, T. B., and D. E. Lehrman, 1987: Meteorological conditions associated with ozone exceedances in Santa Barbara County. Report For Western Oil and Gas Association, 45 pp. [Available from T. B. and Associates, Inc., Pasadena, CA.]

Stauffer, D. R., 2001: Personnel communication.

Stauffer, D. R., and N. L. Seaman, 1990: Use of four-dimensional data assimilation in a limited-area mesoscale model. Part I: Experiments with synoptic data. *Mon. Wea. Rev.,* **118**, 1250-1277.

Stauffer, D. R., and N. L. Seaman, 1994: On multi-scale four-dimensional data assimilation. *J. Appl. Meteor.,* **33**, 416-434.

Stauffer, D. R., N. L. Seaman, G. K. Hunter, S. M. Leidner, A. M. Lario-Gibbs, and S. Tanrikulu, 2000a: Field-Coherence Technique for Meteorological Field-Program Design for Air-Quality Studies. Part I: Description and Interpretation. . *J. Appl. Meteor.*, **39**, 297-316.

Stauffer, D. R., R. C. Munoz, and N. L. Seaman, 2000b: In-cloud turbulence and explicit microphysics in the MM5. 9th PSU/NCAR Mesoscale Model Users' Workshop. Boulder, CO, 23-25 June, 177-180.

Sterbis, C., 2000: An analysis of short-term mesoscale forecasts in the Los Angeles basin using SCOS97 data. M. S. Thesis, Dept. of Meteor., NPGS, Monterey, CA, 101 pp.

Taha, H., 1997: Modeling the impacts of large-scale albedo changes on ozone air quality in the South Coast Air Basin. *Atmos. Environ.,* **31**, 1667-1676.

Tanrikulu, S., D. R. Stauffer, N. L. Seaman, and A. J. Ranzieri, 2000: A Field-Program Design for Air-Quality Studies. Part II: Evaluation in the San Joaquin Valley. *J. App. Meteor.*, **39**, 317-334.

Tesche, T. W., 1991. Evaluation Procedures for Using Numerical Meteorological Models as Input to Photochemical Models. *7th Joint Conference on Applications of Air Pollution Meteorology*, AMS, New Orleans, LA, 14-18 January.

Tesche, T. W., 1994: Evaluation procedures for regional emissions, meteorological, and Photochemical models. *86th Annual Meeting of the Air and Waste Management Association,*14-18 June, Denver CO.

Tesche, T. W., and W. A. Lyons, 1991: Protocol for the LMOS meteorological model performance evaluation. Prepared for the Lake Michigan Air Directors Consortium, Des Plaines, IL. Prepared by Alpine Geophysics, LLC, and ASTeR, Inc.

Tesche, T. W., and P. M. Roth, 1998: Performance evaluation: needs and future directions. *Conference on Photochemical Modeling as a Tool for Decision-Makers,* California Air Resources Board, Sacramento, CA.

Tripoli, G. J, and W. R. Cotton, 1981: The use of ice-liquid potential temperature as a thermodynamic variable in deep atmospheric models. *Mon. Wea. Rev*., **109**, 1094-1102.

Ulrickson, B. L., and C. F. Mass, 1990a: Numerical investigation of mesoscale circulations over the Los Angeles Basin. Part I: A verification study. *Mon. Wea. Rev.,* **118**, 2138-2161.

Ulrickson, B. L., and C. F. Mass, 1990b: Numerical investigation of mesoscale circulations over the Los Angeles Basin. Part II: Synoptic Influences and Pollutant transport. *Mon. Wea. Rev.,* **118**, 2162-2184.

Wakimoto, R. M., 1987: The Catalina Eddy and its effect on Pollution over Southern California. *Mon. Wea. Rev*., **115**, 837-855.

Wakimoto, R. M., and J. L. McElroy, 1986: Lidar Observation of elevated pollution layers over Los ngeles. *J. Appl. Meteor.,* **25**, 1583-1599.

Wakamatsu, S., et al., 1983: Aircraft survey of the secondary photochemical pollutants covering the Tokyo metropolitan area. *Atmos. Environment*, **17**, 827-36.

Wolfe, D., and B. Weber, 1999: Data Management—Upper-Air Meteorological Network. Draft Final Report to CARB on Contract 96-323, NOAA ERL, Boulder, CO, 122 pp.

Wilmont, C., 1981: On the validation of models. *Phys. Geogr*. 2, 168.

Zhang, D. L., and R. A. Anthers, 1982: A high-resolution model of the planetary boundary layer. Sensitivity tests and comparisons with SESAME-79 data. *J. Appl. Meteor.,* **21**, 1594-1609.

Appendix A: List of Acronyms

AGL	Above Ground Level
BASIN	Basic Studies on Airflow, Smog, and Inversions (a SoCAB study)
CARB	California Air Resources Board
CSUMM	Colorado State University Mesoscale Model
ECMWF	European Center for Medium range Weather Forecast
FDDA	Four Dimensional Data Assimilation
GC	General Circulation
GDAS	Global Data Assimilation
MATLAB	A graphics software package
MBL	Marine Boundary Layer
MM5	Mesoscale Meteorological Model 5th generation
NAAQS	National Ambient Air Quality Standard
NCEP	National Center for Atmospheric Prediction
NCAR	National Center for Atmospheric Research
NOAA	National Oceanic and Atmospheric Administration
NWS	National Weather Service
PBL	Planetary Boundary Layer
PDT	Pacific Daylight Time
PM	Particulate matter
PSU	Pennsylvania State University
QA	Quality assurance
RWP	Radar wind profiler
RASS	Radio acoustic sounding system
SBL	Surface Boundary Layer
SCCCAMP	South-Central Coast Cooperative Aerometric Monitoring Program

SCAQS	Southern California Air Quality Study
SCOS97	1997 Southern California Ozone Study
SJSU	San Jose State University
SoCAB	South Coast Air Basin
SST	Sea surface temperature
SURFER	A graphics software package
TOGA	Tropical Ocean Global Atmospheres (an experiment)
UAM	Urban Airshed Model
UCLA	University of California, Los Angeles
UTC	Coordinated Universal Time
3-D	Three-dimensional

IMPROVEMENT AND EVALUATION OF THE MESOSCALE METEOROLOGICAL MODEL MM5 FOR AIR-QUALITY APPLICATIONS IN SOUTHERN CALIFORNIA AND THE SAN JOAQUIN VALLEY

APPENDIX B to Final Report: Modeling of the SCOS-97 Case of 26-30 September 1997

by

Robert D. Bornstein, Co. P. I.
Dimitra Boucouvala
James Wilkinson
Anil Yadav
Department of Meteorology
San Jose State University
San Jose, CA 95192-0104

Nelson L. Seaman, Co. P. I.
David R. Stauffer
Glenn K. Hunter
Department of Meteorology
Pennsylvania State University
University Park, PA 16802
(SJSU Foundation Subcontract No. 22-1505-7384)

Douglas Miller
Department of Meteorology
Naval Postgraduate School
University Park, PA 16802
(SJSU Foundation Subcontract No. 22-1505-7384)

Prepared for the

California Air Resources Board
and
California Environmental Protection Agency

2020 L Street
P.O. Box 2815
Sacramento CA 95812

under
Contract No. 97-310

27 April 2001

Disclaimer

The statements and conclusions in this Report are those of the contractors and not necessarily those of the California Air Resources Board. The mention of commercial products, their source, or their use in connection with material reported herein is not to be construed as actual or implied endorsement of such products.

List of Figures

Figure B1. Detail of NOAA EDAS (Eta data assimilation system) analysis of 500-mb heights (dm) and winds (kts) over western North America and the eastern Pacific Ocean at 1200 UTC, 26 September 1997. Heavy dashed line shows position of a 500 mb tilted trough.

Figure B2. Plot of surface observations over southern and central CA at 1200 UTC, 26 September 1997.

Figure B3. Detail of NOAA EDAS analysis for surface winds (kts) over southern CA and the CA Bight at 1800 UTC, 26 September 1997.

Figure B4. GOES-9 visible image at 1745 UTC, 26 September 1997.

Figure B5. GOES-9 visible image at 2000 UTC, 27 September 1997.

Figure B6. Detail of NOAA EDAS (Eta data assimilation system) analysis of 700-mb heights (dm) and winds (kts) over western North America and the eastern Pacific Ocean at 1200 UTC, 27 September 1997. Heavy dashed line shows position of a 700 mb tilted trough.

Figure B7. Detail of NOAA EDAS (Eta data assimilation system) sea-level pressure analysis (mb) and winds (kts) over western North America and the eastern Pacific Ocean at 1800 UTC, 27 September 1997. Heavy dashed lines shows position of major surface troughs.

Figure B8. Plot of surface observations over southern and central CA at 1800 UTC, 27 September 1997.

Figure B9. GOES-9 visible image at 1715 UTC, 28 September 1997.

Figure B10. Detail of NOAA EDAS analysis for surface winds (kts) over southern CA and the CA Bight at 1800 UTC, 28 September 1997.

Figure B11. GOES-9 visible image at 1800 UTC, 29 September 1997.

Figure B12. Detail of NOAA EDAS (Eta data assimilation system) analysis of 700-mb heights (dm) and winds (kts) over western North America and the eastern Pacific Ocean at 1200 UTC, 29 September 1997.

Figure B13. GOES-9 visible image at 2130 UTC, 30 September 1997.

Figure B14. Detail of NOAA EDAS analysis for surface winds (kts) over southern CA and the CA Bight at 1200 UTC, 30 September 1997.

Figure B15. MM5 terrain (m) on the innermost 5-km domain of the nested mesoscale model. Contour interval is 100 m.

Figure B16. MM5 simulated surface-layer winds (m s^{-1}) at 35 m AGL for 1800 UTC, 26 September 1997, after 6 h of model integration. Isotachs are shown at 1 m s^{-1}, 2 m s^{-1}, 5 m s^{-1}, and thereafter at intervals of 5 m s^{-1}.

Figure B17. Plot of surface observations over southern and central CA at 1800 UTC, 26 September 1997.

Figure B18. MM5 simulated cloud liquid water (g kg^{-1}) at about 300 m AGL (σ = 0.974) for 1800 UTC, 26 September 1997, after 6 h of model integration. Contour interval is 0.1 g kg^{-1}.

Figure B19. MM5 simulated cloud liquid water (g kg^{-1}) at about 550 m AGL (σ = 0.952) for 1800 UTC, 26 September 1997, after 6 h of model integration. Contour interval is 0.1 g kg^{-1}.

Figure B20. MM5 simulated surface-layer winds (m s^{-1}) at 35 m AGL for 1800 UTC, 27 September 1997, after 30 h of model integration. Isotachs are shown at 1 m s^{-1}, 2 m s^{-1}, 5 m s^{-1}, and thereafter at intervals of 5 m s^{-1}.

Figure B21. MM5 simulated surface-layer temperatures (C) at 35 m AGL for 1800 UTC, 27 September 1997, after 30 h of model integration. Isotherms are shown at 2 C intervals.

Figure B22. MM5 simulated cloud liquid water (g kg^{-1}) in the surface layer at about 35 m AGL (σ = 0.997) for 1800 UTC, 27 September 1997, after 30 h of model integration. Contour interval is 0.1 g kg^{-1}.

Figure B23. MM5 simulated surface-layer winds (m s^{-1}) at 35 m AGL for 1800 UTC, 28 September 1997, after 54 h of model integration. Isotachs are shown at 1 m s^{-1}, 2 m s^{-1}, 5 m s^{-1}, and thereafter at intervals of 5 m s^{-1}.

Figure B24. Plot of surface observations over southern and central CA at 1800 UTC, 28 September 1997.

Figure B25. MM5 simulated surface-layer temperatures (C) at 35 m AGL for 1800 UTC, 28 September 1997, after 54 h of model integration. Isotherms are shown at 2 C intervals.

Figure B26. MM5 simulated cloud liquid water (g kg^{-1}) in the surface layer at about 35 m AGL (σ = 0.997) for 1800 UTC, 28 September 1997, after 54 h of model integration. Contour interval is 0.1 g kg^{-1}.

Figure B27. MM5 simulated surface-layer winds (m s^{-1}) at 35 m AGL for 1800 UTC, 29 September 1997, after 78 h of model integration. Isotachs are shown at 1 m s^{-1}, 2 m s^{-1}, 5 m s^{-1}, and thereafter at intervals of 5 m s^{-1}.

Figure B28. Plot of surface observations over southern and central CA at 1800 UTC, 29 September 1997.

Figure B29. MM5 simulated cloud liquid water (g kg^{-1}) in the low levels at about 120 m AGL (σ = 0.990) for 1800 UTC, 29 September 1997, after 78 h of model integration. Contour interval is 0.1 g kg^{-1}.

Figure B30. MM5 simulated surface-layer winds (m s^{-1}) at 35 m AGL for 1800 UTC, 30 September 1997, after 102 h of model integration. Isotachs are shown at 1 m s^{-1}, 2 m s^{-1}, 5 m s^{-1}, and thereafter at intervals of 5 m s^{-1}.

Figure B31. Plot of surface observations over southern and central CA at 1800 UTC, 30 September 1997.

Figure B32. MM5 simulated cloud liquid water (g kg^{-1}) in the surface layer at about 35 m AGL (σ = 0.997) for 1800 UTC, 30 September 1997, after 102 h of model integration. Contour interval is 0.1 g kg^{-1}.

Figure B33. MM5 simulated cloud liquid water (g kg^{-1}) at about 300 m AGL (σ = 0.974) for 1800 UTC, 30 September 1997, after 102 h of model integration. Contour interval is 0.1 g kg^{-1}.

Figure B34. MM5 simulated cloud liquid water (g kg^{-1}) at about 550 m AGL (σ = 0.952) for 1800 UTC, 30 September 1997, after 102 h of model integration. Contour interval is 0.1 g kg^{-1}.

Figure B35. MM5 simulated mixed-layer depth (m) for 1800 UTC, 30 September 1997, after 102 h of model integration. Contour interval is 400 m.

Abstract

For this part of the study, conducted by the Pennsylvania State University (PSU), the *objective* was to investigate the ability of the MM5 mesoscale meteorological model for simulating a complex late-summer event involving coastal fog and stratus in the South Coast Air Basin (SoCAB). The particular event of interest was observed from 26-30 September 1997 as part of the Southern California Ozone Study of 1997 (SCOS-97). In this case, the general north-westerly surface flow along the Pacific coast, that is typical of warm-season winds in the Northeast Pacific high-pressure ridge, broke down over the SoCAB and was replaced on 27-28 September by a Santa Ana wind regime directed offshore (i.e., from the east-northeast). Flow reversal in the Santa Ana led to high wind speeds just above the boundary layer, warming and drying in many coastal areas, and rapid evaporation of the marine fog and stratus in the coastal environment. Later, on 29-30 September, the Santa Ana regime weakened and dissipated. As a result, westerly flow from the Pacific Ocean gradually returned to the coastal SoCAB. This gradual restoration of a more typical flow regime was accompanied by a return of marine fog and stratus, starting from northern Mexico and then filling much of the California Bight.

The methodology used for simulating the September SCOS-97 event was to apply an improved version of the MM5 that had been developed earlier for applications to fog events in the San Joaquin Valley. This MM5 version has been tested and evaluated by PSU as part of the same CARB-supported study conducted under SJSU Foundation Subcontract No. 22-1505-7384. The primary change introduced into the model related to fog formation involved extensions of the model's turbulent boundary-layer parameterization to account for the effects of saturation on the buoyant production of turbulent kinetic energy (TKE). At the time of this report, PSU had completed a preliminary set of simulations for the September SCOS-97 case on quadruple-nested grids (horizontal resolutions of 135, 45, 15, and 5 km) over the SoCAB using four-dimensional data assimilation (FDDA) based on analysis nudging. None of the special SCOS-97 observations were assimilated into this first experiment. Nevertheless, the preliminary numerical experiment provides an excellent testbed to evaluate the basic model performance and to determine whether further development work will be necessary before running the final experiment (with the SCOS-97 data included via observation-nudging FDDA).

MM5 results from the preliminary analysis-nudging experiment revealed good agreement with the overall evolution observed for the 26-30 September 1997 episode. The initial northwesterly surface flow was replaced in the model by a Santa Ana regime on 27-28 September. This wind reversal was accompanied by a rapid loss of fog and cloudiness in the model. Later, as the Santa Ana weakened, the model re-formed the marine coastal fog, beginning along Baja CA and then spreading rapidly north and westward. By 29 September, fog and stratus again covered wide areas of the Southern California Bight in the MM5. Thus, it is apparent that the model simulated successfully the evolution of the primary characteristics in this complex coastal event.

A future model experiment soon will include the special SCOS-97 data through observation nudging in an attempt to reduce the remaining errors in the model fields. More extensive model evaluations will be aimed at extending our understanding of vertical structure of wind, temperature, humidity and cloud/fog in the coastal regions and especially in the SoCAB as the flow regimes undergo the major changes observed throughout the episode.

B-1. Introduction

In 1998-2001, the California Air Resources Board (CARB) sponsored a numerical modeling study aimed at improving the MM5 meteorological model to allow applications for a wider variety conditions than had been possible in the past. That study, titled "Improvement and Evaluation of the Mesoscale Meteorological Model MM5 for Air-Quality Applications in Southern California and the San Joaquin Valley," included work by Penn State University (PSU) to upgrade the model's performance in cases having fog and low stratus clouds. In the Final Report already provided to CARB for this project (Bornstein et al. 2001), PSU described results from numerical simulations of fog in the San Joaquin Valley (SJV) using an advanced version of the MM5's turbulence parameterization.

The numerical study of SJV fog was conducted in wintertime, using a case from December 1995 that was characterized by a stagnant high-pressure system and very weak winds following passage of a cold front and rain showers. For that type of winter event, fog grows primarily as a result of radiational cooling. However, coastal fog and stratus in the South Coast Air Basin (SoCAB), including the adjoining offshore area of the Southern California Bight, present a much different challenge for a numerical model. First, fog and stratus are most extensive and common in the SoCAB during the warm season (especially in late summer and early autumn). Second, the fog in this region forms primarily due to the advection of relatively warm moist air in the marine boundary layer over the colder waters upwelling along the California coast, rather than through radiation flux divergence in a stagnant post-frontal air mass. (Although radiation flux divergence can play an important secondary role in maintaining marine fog and stratus, it is not the primary mechanism for its formation in the coastal region.) Third, accurate representation of these coastal events requires that a model be able to simulate rapidly changing mesoscale dynamics and thermodynamics in and around the SoCAB, including local circulations induced by the region's highly complex terrain. Therefore, the considerable success obtained in prior model simulations of fog and stratus in the SJV does not guarantee that the MM5 model is now suitable for studying these saturated features in the SoCAB.

The ***objective*** of this part of the study, conducted by the Pennsylvania State University (PSU), was to investigate the ability of the MM5 mesoscale meteorological model to simulate a complex late-summer event involving coastal fog and stratus in the South Coast Air Basin (SoCAB). The particular event that was the focus of the study was observed from 26-30 September 1997 as part of the Southern California Ozone Study of 1997 (SCOS-97). In this case, the general north-westerly flow along the Pacific coast, that is typical of the warm-season wind regime in the Northeast Pacific high-pressure ridge, broke down over the SoCAB and was replaced on 27-28 September by a *Santa Ana* wind regime directed offshore (i.e., winds from the east-northeast). This flow reversal in the Santa Ana led to high wind speeds just above the boundary layer, warming and drying in many coastal areas in the lee of the major mountain ranges, and rapid evaporation of the marine fog and stratus in the coastal regions. Later, on 29-30 September, the Santa Ana flow regime dissipated and west-northwesterly flow off the Pacific Ocean gradually returned to the coastal areas of the SoCAB. The end of the Santa Ana was accompanied by the return of marine fog and stratus, starting from northern Mexico and then filling the Southern California Bight, even though restoration of the strong Northeast Pacific Ridge and a typical northwesterly wind regime was delayed for several days.

In this report, Section B-2 gives a very brief review of the numerical modeling system applied for this SCOS-97 episode. Section B-3 gives a more detailed description of the meteorological event. Section B-4 discusses the results of the preliminary model experiment using the MM5. Section B-5 gives a brief summary of what has been learned thus far.

B-2. Numerical Model and Experiment Design

The methodology used for simulating the September SCOS-97 episode was based on the non-hydrostatic MM5 mesoscale meteorological model (Grell et al. 1994) used in the study of fog in the SJV. This version of the model was developed and tested earlier by PSU as part of this same CARB-supported project conducted under SJSU Foundation Subcontract No. 22-1505-7384 (see Final Report by Bornstein et al. 2001). For the September SCOS-97 episode, the SJV version of MM5 was reconfigured by simply placing the center of the domain over the LA Basin. The domain locations are exactly the same as for the episode of 4-7 August 1997 simulated by San Jose State University (SJSU) and described in the Final Report for this study. Model resolutions were also the same as those used by SJSU, with quadruple-nested grids having mesh sizes of 135-, 45-, 15-, and 5-km. In this application, there were 30 layers in the vertical direction.

The primary change made in the MM5 model to equip it for improved fog simulations was made by Penn State as part of the SJV fog study (Bornstein et al. 2001). It involved modifications to the model's turbulent boundary-layer parameterization to account for the effects of saturation on the buoyant production of turbulent kinetic energy (TKE). As a consequence, turbulence develops more easily in fog and cloud layers. Not only does such mixing change the thermal profile inside the cloud layer, but it can result in more rapid entrainment of dry air into a cloud layer. Thus, the evolution and vertical structure of the saturated layers are simulated more accurately. Initial conditions for the September 1997 episode were generated using a background (or, first guess) from the Medium Range Forecast (MRF) global-model analyses generated by the National Centers for Environmental Prediction (NCEP). The global analyses were enhanced by projecting them onto the MM5's outermost 135-km domain and then blending in National Weather Service surface and radiosonde observations in an objective analysis step. The same procedure was followed every 12 h throughout the 26-30 September episode to provide lateral boundary conditions for the MM5.

The sea-surface temperature used in the MM5 experiments was defined by direct interpolation from the MRF's sea-surface temperature fields. These global model analyses are based on ship and buoy observations and remotely sensed satellite data. They reflect the basic climatological pattern having colder waters along the CA coast, but they are unlikely to accurately represent finer details of the surface water temperatures in the 50-100 km closest to the shore (where the water is often coldest). Unfortunately, it is very difficult to find accurate and timely analyses of the fine-scale sea-surface temperatures for most cases due to the scarcity of direct measurements. However, water temperatures can have a very strong influence on the formation of fog and stratus over the study region. Thus, the uncertainty in the sea-surface temperature analyses represents a potentially important limiting factor that could affect the accuracy of subsequent numerical simulations. Past experience in this area suggests that the impact of this uncertainty is

usually not a major factor in most cases. Nevertheless, imperfect sea temperatures can adversely affect the timing of the sea breeze and the development of nocturnal land breezes in coastal areas and the LA Basin. Therefore, it is always important to monitor these sensitive flows in coastal applications of numerical models.

Finally, the initialization of the MM5 was completed by running the model with Penn State's Marine Boundary Layer Initialization (MBLI) scheme for the 12-h period from 0000 UTC to 1200 UTC on 26 September in order to generate a realistic marine boundary-layer structure over the Pacific Ocean. The purpose of the MBLI is to impose a climatologically realistic vertical structure for the marine boundary layer over the ocean near in the eastern Pacific Ocean, that is generally lacking in the coarse-resolution MRF analyses. This procedure was described in detail in Leidner et al. (2001) and was used by Bornstein et al. (2001) for the August SCOS-97 episode. The end of the MBLI period, 1200 UTC, 26 September 1997, was taken as the initial time for all subsequent numerical experiments with the MM5.

Two numerical experiments are planned for the September SCOS-97 event. The first experiment (AFDA-SC97) uses four-dimensional data assimilation (FDDA) based on analysis nudging. The analysis nudging is applied only on the 135-km, 45-km and 15-km domains. Therefore, the only influence of the FDDA on the 5-km innermost domain is felt through the lateral boundaries of the fine grid. In effect, the FDDA is used in this experiment only to provide accurate boundary conditions to the 5-km domain, which is then free to develop mesoscale solutions, based only on the model's physical and dynamical forcing. None of the special SCOS-97 observations are assimilated into Exp. AFDA-SC97. Nevertheless, this preliminary experiment provides an excellent testbed to evaluate the basic model performance and to determine whether further development work will be necessary. The second experiment (OBFDA-SC97) will include the special SCOS-97 meteorological data in the model's FDDA system through observation-nudging (Stauffer and Seaman 1994). These special data (wind, temperature and humidity) are assimilated on both the 12-km and 4-km domains.

Only the first experiment has been run at the time of this writing. The second experiment is scheduled for April 2001. Both experiments extend for 108 h following the MBLI, from 1200 UTC, 26 September, to 0000 UTC, 1 October 1997.

B-3. Case Description

The September SCOS-97 episode began on 26 September with northwesterly surface flow off the coast of CA. At 1200 UTC, this wind regime was supported by the Northeast Pacific Ridge, which had a central pressure of 1018 mb near33.5 N and 125.0 W (not shown). The high-pressure system and the northwesterly coastal winds it spawns are common features of the summer and early autumn climatology of the eastern Pacific. Generally lower pressures prevail over the heated interior of western North America. At the same time, a moderately strong 500-mb ridge was found above the surface ridge (Figure B1). The Pacific Ridge was separated from another upper-level anticyclonic center over northwestern Mexico by a positively tilted 500-mb trough. The trough extended from a weak upper low over the Pacific near 25 N, 122.5 W northeastward toward Salt Lake City, UT. This upper-level trough lay over the San Diego area

at the initial time, so that Figure B1 shows northerly upper-level flow covering most of the SoCAB. Because of the proximity of the trough, local surface observations over the SoCAB at 1200 UTC (Figure B2) indicated fairly widespread broken clouds and some coastal fog. There was even a rain shower reported in the mountains just east of the LA Basin, so the initial regime was comparatively moist.

The local pattern of the surface winds in the SoCAB, analyzed by NOAA's Eta data assimilation system (EDAS) at 1800 UTC, 26 September, are shown in Figure B3. Although the analysis is rather coarse (80-km resolution) compared to the resolution to be used in the MM5's inner domains, it provides a reasonable representation of the synoptic-scale wind pattern. Winds north and west of Point Conception averaged about 10 m s^{-1} at this time, but dropped to ~2-5 m s^{-1} in the CA Bight. Another EDAS analyses at this time, for the 900-mb winds, shows that directions through the lowest kilometer were mostly similar to those of the surface flow (not shown).

A visible satellite image (Figure B4) at 1745 UTC (1045 PDT), 26 September, indicates broad areas of broken clouds over the Pacific Ocean and SoCAB. On closer inspection, the cloud patterns can be understood as follows. First, the mostly cloudy areas south and west of Point Conception in Figure B4 are stratus and stratocumulus that correspond to the areas experiencing anticyclonic north or northwesterly winds in the Pacific Ridge, with advection of moist air over colder waters. Most of the California Bight, from the islands to the mainland coast, lies just west of the upper-level trough. Here, clouds have already dissipated or are clearing due to absorption of solar energy. Over land, Figure B4 shows that the coastal areas and western basins from Santa Barbara to northern Mexico have widespread clouds, with only a few breaks. These clouds are due to the above-normal moisture associated with the upper-level trough, combined with the effects of sensible heating in the daytime boundary layer. Three hours later, another visible satellite image at 2015 UTC (1345 PDT) reveals fewer clouds over the CA Bight due to continued absorption of solar energy in the marine boundary layer (not shown). This evolution of cloudiness over the Bight is typical for this coastal marine environment, with clouds evaporating in the afternoon due to absorption of solar energy and then reforming at night. However, the inland clouds are unusual at this time of year.

Next, Figure B5 shows a visible picture for the next afternoon (27 September, 2000 UTC). Almost the entire domain of the satellite image, over both land and water, had cleared by this time. The dramatic change can be understood by examining the EDAS upper-level analyses and the surface observations at 1200 UTC and 1800 UTC. By 1200 UTC on 27 September, the 500-mb trough had shifted ~300-400 km eastward, while the upper level Northeast Pacific Ridge had strengthened and built eastward into central CA (not shown). At 700 mb, Figure B6 shows that mid-level winds in the building Pacific Ridge had become northeasterly over the SoCAB. Meanwhile, Figure B7 reveals that the upper-level ridging over the West Coast induced a strong surface high-pressure system over OR at 1800 UTC, with surface ridging and north-northeasterly winds in central CA and the northern SoCAB. These deep northeasterly winds (from the surface to 500 mb) led to a moderately strong Santa Ana event in the SoCAB on 27-28 September. The coastal low-pressure trough shown in Figure B7 over the Channel Islands is a reflection of the strong adiabatic warming occurring in the downslope winds to the lee of the San Rafael Mountains. Of course, the EDAS analysis in Figure B7 is too coarse to resolve many of the mesoscale details in the region of interest. Figure B8, however, shows that temperatures

observed near San Luis Obispo and Santa Maria (west of the Coast Range Mountains) were in the mid-80s F (29-30 C) at 1800 UTC, with surface winds of ~10 m s^{-1} due to the Santa Ana adiabatic heating. These temperatures in the lee of the mountains were about 5 C warmer than at most other stations in the region that morning. In many Santa Ana events, even stronger winds are common a few hundred meters above the surface and downwind of the main passes and valleys through the mountains.

Together, Figures B5-B8 reveal the main features of a typical Santa Ana wind event. As dry continental air in the lowest 1-2 km was forced southwestward over the mountains surrounding the LA Basin and the other SoCAB mountain ranges by the high in OR, it descended rapidly and experienced adiabatic warming due to compression. Adiabatic heating lowered the relative humidity in the lee of the mountains and in the coastal marine regions, thus dissipating the clouds and fog, as shown in Figure B5.

The generally clear skies in Figure B9 suggest that the clear Santa Ana regime continued through 1800 UTC, 28 September. However, a long swath of coastal fog had re-formed from Baja CA to the waters off Long Beach, CA, suggesting that another important change was underway. The local EDAS surface-wind analysis at 1800 UTC, 28 September (Figure B10) shows that the low-level winds now formed a large cyclonic circulation centered on the Los Angeles Basin. At some sites in the Basin and also at San Luis Obispo and Santa Maria, surface temperatures at 1800 UTC rose to 33 C on this morning. Notice that the broadening cyclonic circulation has produced a wedge of light southerly winds along the coast in the area where the fog has reformed (compare coastal winds in Figures B7 and B10). This southerly coastal air-stream is least affected by the adiabatic warming associated with the Santa Ana and so is the first place where a saturated marine boundary layer can be re-established. Meanwhile, the easterly flow on the north side of the SoCAB from the surface to 700 mb has weakened over the past 12 h, suggesting that the Santa Ana regime is already beginning to break down.

The disappearance of the Santa Ana winds became more evident on 29 September. Indeed, by 1800 UTC, the satellite image in Figure B11 shows that fog and stratus cloud had once more become widespread over the Pacific Ocean, with some modest gaps. Comparison of the satellite picture with the EDAS surface wind analysis for this time (not shown) indicates that many of the gaps in the marine fog lie in the lee of the islands and headlands of the region. Surface winds over the CA Bight were mostly southwesterly at ~2 m s^{-1}, indicating that the dynamic forcing was unusual and weaker than normal. In fact, the 700-mb EDAS analysis at 1200 UTC, 29 September (Figure B12), reveals that the normal Northeast Pacific Ridge had weakened, while the anticyclone over northern Mexico had strengthened considerably. This condition produced widespread south-southeasterly upper-level winds over the SoCAB and CA Bight. While Figure B12 shows that average climatological conditions had not returned, the new wind pattern did signal the end of the Santa Ana event, since there was no longer any mid-level flow of continental air crossing the mountains into the SoCAB from the northeast.

Finally, a satellite image and the EDAS surface-wind analysis for 1200 UTC, 30 September (shown in Figures B13 and B14 respectively), indicate that the normal marine stratus and northwesterly surface-wind regime were gradually beginning to reassert themselves. Farther aloft, the Northeast Pacific Ridge was beginning to strengthen once more (not shown), but it had

not yet begun to dominate the winds above the CA Bight. Nevertheless, Figure B13 suggests that stratus and stratocumulus clouds are the dominant cloud types over the Pacific at this time. These clouds are identified by their speckled cellular patterns, which also implies that they were located relatively high above the surface (usually near 400-700 m MSL). Meanwhile, closer to the coast of the SoCAB, the clouds have very little fine structure, suggesting that the stratus is much lower (100-300 m) and may extend to the surface as fog in some areas. This sloping marine cloud layer, deep to the west and shallow near the coast, is normal for the CA Bight in summer and early autumn (Leidner et al. 2001). Last of all, note that a few small bright convective clouds can be seen in Figure B13 over the crests of the mountain ranges east of Los Angeles and southward into Baja CA. These very bright convective clouds appear distinctly different from the light-gray shades of the low-level stratus and fog, because the updrafts in convective plumes quickly produce more cloud droplets and much higher liquid-water contents than are normally found in marine stratus.

B-4. Results of the Preliminary FDDA Experiment

At present, PSU has completed simulations for Exp. AFDA-SC97 on the quadruple-nested grids (horizontal resolutions of 135, 45, 15, and 5 km) over the SoCAB using four-dimensional data assimilation (FDDA) based on analysis nudging. None of the special SCOS-97 observations were assimilated into this first model experiment. Nevertheless, the preliminary numerical experiment provides an excellent testbed to evaluate the basic model performance. All discussions of the experimental results in this report will focus on the high-resolution 5-km domain, which is anticipated to have the greatest detail in the meteorological solutions. Since orography is expected to exert an important influence on the model solutions, the terrain field on the 5-km MM5 domain is shown in Figure B15 for reference.

First, the MM5-simulated surface-layer wind field is shown at 1800 UTC, 26 September (+6 h in the Exp. AFDA-SC97 simulation) (Figure B16). For comparison, Figure B17 shows the surface observations over the SoCAB at the same time. A brief examination of these figures reveals that the MM5 has already adjusted to the local forcing and has produced almost all of the observed mesoscale details found in the data. For example, the modeled winds capture the cyclonic turning of the winds over the CA Bight, where winds are northwesterly at 7-8 m s^{-1} near San Nicolas Island, westerly at 6-7 m s^{-1} near San Clemente Island, and southwesterly at ~3 m s^{-1} along the coast from San Diego northward. The model has even reproduced the light southerly wind at Long Beach, the nearly calm winds in the West Basin of Los Angeles inland from Palo Verdes Hills, and many similar details farther inland.

At the same time, the MM5 generated a realistic field of cloud-liquid water similar to the observed clouds in Figure B4. The model's cloud field (Figures B18-B19) is characterized by many isolated pockets of saturation over the coastal mountains, the mountains surrounding the LA Basin and over the ocean. Nearly all of the cloud pockets over the ocean are rather shallow in depth. Close to the coast, the oceanic clouds are found mostly in the lower levels (~975 mb, or 300 m MSL) (Figure B18), while farther west from the coast, they are found at somewhat higher levels (~950 mb, or 550 m MSL) (Figure B19). This is consistent with the climatology of the sloping marine-layer inversion over the CA Bight described by Leidner et al. (2001). When

all model layers between the surface and 1 km MSL are examined (not shown), it is apparent that most of the marine area between San Diego and the west boundary of the 5-km domain has some cloud, although there are frequent breaks in the stratus deck. One extensive area that remains mostly cloud free in the model is the region from ~ 40 km south of the islands in Santa Barbara Channel, and from Pt. Conception to just west of Los Angeles. Figure B4 confirms the main aspects of this distribution of marine cloudiness near mid-day on 26 September. The shallow depth of the marine clouds and their height (most of them do not extend to the sea surface at this time) reveals them to be stratus clouds rather than fog.

Over land, the model produced cloud-water patterns that are repeated at all layers up to at least 1 km AGL, indicating deeper clouds than were found over the Pacific Ocean (e.g., compare Figures B18 and B19). These deeper clouds are consistent with those over land in the satellite picture (Figure B4). In fact, the MM5 also produced a few isolated heavy showers (~1-2 cm) about this time over some of the higher peaks surrounding the LA Basin, similar to the observed showers noted early in the period (see Figure B2).

Thus, the observations indicate that the model has done very well in reproducing nearly all of the important features found in the data at 18 UTC, 26 September (+6 h). Further evaluation is planned, including comparison of profiles of the model's winds to those measured from the special radar wind profilers deployed in the special SCOS-97 study. However, plots of those special data were not yet available at the time this report was completed.

Next, we examine the MM5 outputs at 1800 UTC, 27 September (+30 h), when the Santa Ana winds drastically had altered the earlier patterns. First, Figure B20 shows the surface-layer winds at this time. A number of significant changes can be detected by comparing winds in this figure to those from Figure B16 on the previous day. First, the winds west and southwest of the Point Conception have intensified and become more north-northwesterly. Comparison of Figures B20 and the EDAS analysis at this time (Figure B7) indicates that these high-speed winds are correct and are found on the oceanic side of the surface low-pressure trough induced by the Santa Ana flow. Figure B20 shows that the flow inside the CA Bight (east of the surface trough) is much weaker and variable in direction. Along the Pacific coast near San Diego, the model simulates westerly to west-northwesterly winds. Again, direct comparison with the surface observations shown in Figure B8 reveals that the model has done fairly well in replicating most aspects of the complex mesoscale wind patterns, even though some minor errors also are apparent.

Perhaps the most notable problem in the simulated flow shown in Figure B20 is the unverified area of high-speed northeasterly winds (10-14 m s^{-1}) over the San Rafael Mountains (north of the Santa Barbara Channel). It may be possible that these winds are accurate, and merely are unobserved by the data shown in Figure B8. However, a more detailed examination and comparison to the SCOS-97 special database will have to be made. One important piece of corroborating evidence is found in the MM5's surface-layer temperature field (Figure B21), that shows several patches of warm air in the lee of the mountains near Santa Maria, Santa Barbara, and in the LA Basin. Figure B8 shows that unusually warm temperatures were observed in most of these regions as the Santa Ana regime became established.

Figure B22 shows the MM5's surface-layer cloud-water field (fog) at 1800 UTC, 27 September. The figure reveals that the model-simulated fog is quite extensive from Los Angeles to San Diego and westward nearly to San Nicolas Island. However, the satellite picture in Figure B5 shows that the model's simulation of fog at this time is mostly wrong. Cloud water in the model's other layers between the surface and 1 km AGL (not shown) indicate that there is still a thin stratus layer at the sloping marine inversion at this time, even though Figure B5 indicates the actual clouds have mostly dissipated. Six hours later, at 0000 UTC, 28 September (+36 h), most of these clouds in the MM5 simulation also had dissipated, except for some remnants in the shear zone just the west of the offshore Santa Ana surface trough (not shown). This result suggests that the Santa Ana is probably a bit slow to develop in the model and it may actually be somewhat weaker than found in nature. However, the lack of direct observations over the ocean makes it difficult to prove this hypothesis.

By 1800 UTC, 28 September (+54 h), model's sea-level pressure had dropped about 5-6 mb from the initial values (not shown) as the broad cyclonic circulation developed in response to the widespread diabatic heating that accompanied the Santa Ana event. The 700 mb and 500 mb height analyses (not shown) also indicate that the Northeast Pacific Ridge was rapidly weakening on this day. Figure B23 shows the MM5-simulated surface-layer winds at 1800 UTC on the third day of the episode, which can be compared to the EDAS analysis in Figure B10. The model's winds show both general agreement with the analysis and also some apparent errors at this time. First, the model solution contains northwesterly winds to the west of Point Conception and westerly winds along the southern boundary of the domain. Also, north of Santa Barbara in the northern part of the model domain, winds are mostly from the east. These major features of the cyclonic circulation are correct and are confirmed in Figure B10. However, it appears that the 10-15 m s^{-1} northeasterly Santa Ana winds crossing the San Rafael Mountains are too strong in the model. These northeasterly winds extend from the Mojave Desert across the passes in the mountains, down to the coast near Santa Barbara, and from there westward across the Channel Islands. Although there is a 15-kt (7.5 m s^{-1}) northeasterly surface observation near Newhall Pass northeast of Santa Barbara (see Figure B24), there is no corroboration in the data downwind along the Channel to confirm the Santa Ana flow being so powerful or extensive. Elsewhere over land, the model solutions in Figures B23 and the local wind observations in Figure B24 tend to be chaotic in direction, or even calm (over Los Angeles). This is probably a result of local disruptions of the unusual cyclonic flow pattern by the Santa Ana winds. Since there were an unusual number of radar wind profilers deployed for the SCOS-97 study, it may be possible to control the model's tendency to over-predict the strength of the Santa Ana winds at this time in the future obs-nudging experiment (Exp. OBFDA-SC97).

Also at 1800 UTC (1100 PDT), 28 September, Figure B25 shows that the simulated surface-layer temperature field has a number of pockets in the lee of the mountains where the Santa Ana winds have caused strong adiabatic warming. Maximum temperatures simulated in these warm pockets are about 31 C near San Luis Obispo, 30 C near Santa Barbara, and 32-33 C in the LA Basin. The observations in Figure B24 confirm 91 F (32.8 C) at San Luis Obispo and 92 F in Los Angeles (33.3 C), but no hot temperatures at Santa Barbara. Meanwhile, in the desert east of Palm Springs, the model simulated a maximum of 33.6 C, while the maximum observation in this area is confirmed to be even hotter at 99 F (37 C). Thus, despite some distortions in the wind field, the MM5 has reproduced the pattern of the temperatures observed in this Santa Ana

event reasonably well, with the most serious error occurring in the vicinity of Santa Barbara. Also, note that the solutions in Figure B25 contain a swath of warm temperatures over the ocean west-southwestward (downwind) from Santa Barbara. There are no data over the ocean, but this warming is clearly associated with the swath of northeasterly Santa Ana winds shown earlier in Figure B23.

Lastly for this time, Figure B26 shows the fog pattern produced by the MM5 at 1800 UTC, 28 September. After dissipating almost all clouds at the peak of the Santa Ana (about 0000 UTC, 28 September), the model has begun reforming fog along the coast from Baja CA northward almost to Long Beach. This is in good agreement with the observed fog re-formation in Figure B9. However, as the figures show, the model also began spreading the fog westward about 12 h too soon. Nevertheless, the basic result of the re-formation of fog is generally correct and encouraging. The model does not produce any stratus cloud above the lowest couple of layers, suggesting that the marine boundary layer is very thin at this time. Further comparison of the wind fields in Figures B23 and B10 shows that the southerly winds that were observed along the coast near San Diego, where the fog was first observed to reform, had not yet developed in the model. Some southerly components are found in the MM5's winds along the coast in this area, but the simulated wind directions are predominantly from the west. This error is possibly a response to the over-development of the Santa Ana winds farther north over the Santa Barbara area. Early expansion of the fog could also be due, in part, to possible errors in the sea-surface temperature field.

Over the next 24 h, the EDAS 700-mb analysis (Figure B12) indicated that a broad southeasterly upper-level flow replaced the Santa Ana regime, which was accompanied by the return of widespread fog over the Pacific Ocean (Figure B11). At 1800 UTC, 29 September (+78 h), the MM5 produced mostly southwesterly flow over the Pacific Ocean (Figure B27). This unusual surface flow pattern is confirmed by the observations (shown in Figure B28) and by the EDAS surface analysis (not shown). Closer comparison between Figures B27 and B28 shows good agreement between the modeled and observed winds all along the coastline from San Diego to Long Beach and westward to Point Conception. The broad extent of the southwesterly winds over the ocean is confirmed by the observation at San Clemente Island in Figure B28. At the same time, the EDAS surface analysis (not shown) rejected the southeasterly wind observed at San Nicolas Island as unrepresentative. The observations in Figure B28 also confirm the model's simulation of nearly calm winds at this time over much of Los Angeles. Thus, the model wind field has successfully transitioned to the post-Santa Ana regime found in the observations.

Consistent with the post-Santa Ana flow from the Pacific, Figure B28 shows that temperatures are generally 2-4 C cooler at 1800 UTC, 29 September, than they were 24 h earlier (compare to Figure B24), although hot temperatures remain in the deserts of southeastern CA. The MM5 simulation at this time (not shown) reproduces this cooler temperature pattern quite well, with 20-22 C temperatures immediately along the coast due to the onshore flow. In the interior of the LA Basin, maximum temperatures simulated at this time are 31 C (88 F), while the maximum observed temperature in Figure B28 is 30 C (86 F). Finally, at this time, Figure B29 shows that the MM5 correctly expanded the fog over a wider area, practically filling the region south of 34 N, while preventing fog formation around the Channel Islands and Point Conception. Comparing the simulated fog field to the satellite picture in Figure B11 shows that the model has

done reasonably well, although the real fog pattern is far too complex for any model to capture in detail. Nevertheless, note that the MM5 has correctly simulated fog-free "halos" around San Clemente and Santa Catalina Islands. Thus, despite some inaccuracies, the model has reproduced some rather amazing details of the fog distribution, as well.

The final time at which the model was evaluated in this preliminary study of the September SCOS-97 episode was at 1800 UTC, 30 September (+102 h), just 6 h before the end of Exp. AFDA-SC97. Although the EDAS analysis at 1200 UTC (Figure B14) showed that light west to northwesterly surface winds were beginning to return to the CA Bight, the upper-level Northeast Pacific Ridge was still weak and had not yet re-asserted dominance over the region (not shown). The MM5 responded reasonably well to this transitional situation. Figure B30 shows that the model's surface-layer winds at 1800 UTC, 30 September, were west-northwesterly at 2 -4 m s^{-1} over the oceanic part of the domain, very nearly as observed. Meanwhile, the model simulation produced sea breezes in the coastal areas and lighter winds with chaotic directions farther inland. This pattern is confirmed by the observed winds over the SoCAB (Figure B31). The model-simulated temperatures in the SoCAB continued to cool toward average seasonal values (not shown), much like the observed temperatures in Figure B31.

The fog and stratus clouds produced by the MM5 at 1800 UTC, 30 September, also agree fairly well with the observed clouds in Figure B13. First, Figure B32 shows that the MM5 simulated some patches of fog right along the coastline from Baja to Los Angeles. As discussed in Section B-3, the texture of the clouds in Figure B13 imply that fog exists along the coast, which is confirmed by the coastal surface reports in Figure B31. However, the model's coastal fog appears to be somewhat more extensive than in the satellite picture, which shows a lengthy gap south of Long Beach (Figure B13). Next, Figures B33 and B34 show the MM5's cloud liquid-water distributions at about 975 mb (~300 m AGL) and 950 mb (550 m AGL), respectively. Note that Figures B32-B34 indicate two major areas of cloudiness. The first is a region of marine clouds and fog extending from the coastline (Los Angeles to Baja) to ~125 km westward near 119 W. The figures reveal that this cloud mass slopes strongly upward toward the west, away from the coast, and corresponds to the eastern marine-cloud region inside the CA Bight shown in the satellite picture (see Figure B13). Moreover, careful examination of the simulated eastern cloud area at all model levels (not shown) reveals that it contained numerous cloud-free patches, most notably to the lee (east) of islands and near Long Beach. These cloud-free patches are mostly similar to those observed in Figure B13. The second model-simulated cloud area lies west of 120 W and consists entirely of stratus centered near 950 mb (Figure B34). Figure B13 shows that there is an extensive stratus deck to the west, but in reality it lies ~100 km farther west than in the model, beginning at about 122 W (except for some cloud/fog patches near Point Conception and the Channel Islands). Thus, although the model failed to capture all aspects of the observed clouds correctly, the main cloud-field features were simulated reasonably well in this complex situation.

The boundary-layer depth has not been a major factor in the evaluation of this preliminary experiment because more work needs to be done to diagnose the observed depth of the mixed layer in the SoCAB as the episode evolves. The essence of the sloping marine boundary layer can be detected easily in the simulations from the height of the cloud layers (e.g., Figures B32-B34). However, Figure B35 directly confirms that basic pattern at 1800 UTC, 30 September.

West of Pt. Conception and 120 W, the marine layer is about 400 m deep in most areas. East of 120 W, it slopes downward toward the coastline, where it often becomes less than 100 m deep. As is well known, the boundary-layer depth in the Los Angeles Basin also remains rather shallow, with broad areas of the inner Basin having simulated depths of less than 400 m. Elsewhere, over the peaks of the surrounding mountain ranges and in the deserts of southeastern CA, the mixed-layer depth grows to 800-1200 m at this time.

As the model evaluations continue, cross sections of the turbulent mixed-layer depth and cloud-water profiles will be generated to provide a much more detailed understanding of the model's thermal and moisture structures. Radiosonde profiles in the SoCAB from the SCOS-97 database will provide accurate estimates of observed mixed-layer depth. Supplemental estimates based on radar wind-profiler data can also be used for this purpose. Although profiler-based estimates often are more ambiguous, the large volume of profiler data will make it a valuable resource for this purpose.

B-5. Summary

The MM5 mesoscale model has been run by Penn State for a preliminary experiment (AFDA-SC97) over the SoCAB to study the formation of coastal fog and stratus in the complex event of 26-30 September 1997. With an inner domain having a horizontal resolution of 5 km, this experiment used FDDA via analysis nudging on the coarser meshes of its nested-grid domains, but none of the special SCOS-97 data were assimilated. The four domains had resolutions of 135, 45, 15, and 5 km. All domains used 30 layers in the vertical direction. The MM5 was initialized using the NCEP MRF analyses and with standard surface and upper-air data from the National Weather Service. The model's initial conditions were completed by integrating for the first 12 h with the Penn State Marine Boundary-Layer Initialization (MBLI) scheme, beginning at 0000 UTC, 26 September 1997, to develop the vertical structure of the marine layer that is normally missing from global-model analyses. Finally, the model was run with analysis nudging for 108 h from 1200 UTC, 26 September to 0000 UTC, 1 October 1997.

Since the focus of the experimentation for this case was to determine how well the MM5 could simulate marine cloud and fog along the coast of the SoCAB, the model evaluations reported here reflect that primary objective. A key to simulating the development and dissipation of cloud and fog for the September SCOS-97 episode was to replicate the evolution of the winds in this very complex event. In particular, this case was characterized by the development and subsequent breakdown of a Santa Ana event in the middle of the simulation period. The model appeared to reproduce most aspects of the Santa Ana winds reasonably well, although there is still much work to be done to analyze the vertical structure of the event from the special SCOS-97 database and to quantify the fit of the model to the observations.

The onset of the Santa Ana, with its adiabatically warmed winds flowing over the SoCAB and the CA Bight from the northeast, led to rapid clearing of clouds on 27 September. This was a dramatic change from the extensive cloud fields that covered the region on 26 September. Although the model was perhaps 6-12 h too slow to complete the clearing, it did so correctly in response to the onset of Santa Ana winds in the simulation. The simulated temperatures rose

dramatically on 27-28 September in the lee of the mountain ranges and in the eastern deserts, very much as observed. However, it appears that the low-level Santa Ana winds simulated in the model may have become too strong in some areas, especially on 28 September. This led to some local distortions in the coastal wind patterns. Close attention will be given in the ongoing evaluations to comparisons of the model's wind structure in the vertical direction to observed radar wind-profiler data.

When the Santa Ana regime began to break down on 28 September, it was replaced by southeasterly 700-mb flow over the region of interest due to strengthening of an upper-level anticyclone over northern Mexico. The MM5 reproduced this reversal of the typical wind direction and the re-development of coastal fog and stratus that accompanied it. Despite some local inaccuracies, the model did a remarkably realistic job of capturing the timing, distribution and type of clouds (fog or stratus) as they developed. Remarkably, these characteristics of the cloud evolution were captured by the model, even though it had rather coarse vertical resolution in this experiment (compared to the SJV fog study, for which the MM5 had used 40 vertical levels).

Preliminary evaluations of this first model experiment for the September 1997 episode have been mostly qualitative to gain an overall impression of the mesoscale features simulated by the model compared to those found in the observations. At this point, other than the possible errors noted in the strength of the Santa Ana winds simulated downwind of the coastal mountain ranges, it appears that the model solutions in Exp. AFDA-SC97 are quite reasonable. The extensive wind profiler data in the SCOS-97 database will provide a good opportunity to correct the most serious wind errors in ongoing experimentation through obs-nudging FDDA. However, a more thorough evaluation of the vertical wind structure in the data and the solutions of Exp. AFDA-SC97 must be completed before beginning the second experiment. Plots showing vertical time-height sections of these profiler winds are being provided to PSU by Sonoma Technology, Inc., to assist in the model evaluations. Thus, PSU expects to be able to proceed with the final experiment very soon.

References

Bornstein, R.D., D. Boucouvala, J. Wilkinson, A. Yadav, N.L. Seaman, D.R. Stauffer, G.K. Hunter and D. Miller, 2001: Improvement and Evaluation of the Mesoscale Meteorological Model MM5 for Air-Quality Applications in Southern California and the San Joaquin Valley. Final Report to CA Air Resources Board, Contract No. 97-310, 197 pp.

Grell, G.A., J. Dudhia, and D.R. Stauffer, 1994: A description of the fifth-generation Penn State/NCAR Mesoscale Model (MM5). NCAR Tech. Note 398+SRT, 122 pp.

Leidner, S.M., D.R. Stauffer and N.L. Seaman, 2001: Improving short-term numerical weather prediction in the California coastal zone by dynamic initialization of the marine boundary layer. *Mon. Wea. Rev*., **129**, 275-294.

Stauffer, D.R. and N.L. Seaman, 1994: Multiscale four-dimensional data assimilation. *J. Appl. Meteor*., **33**, 416-434.

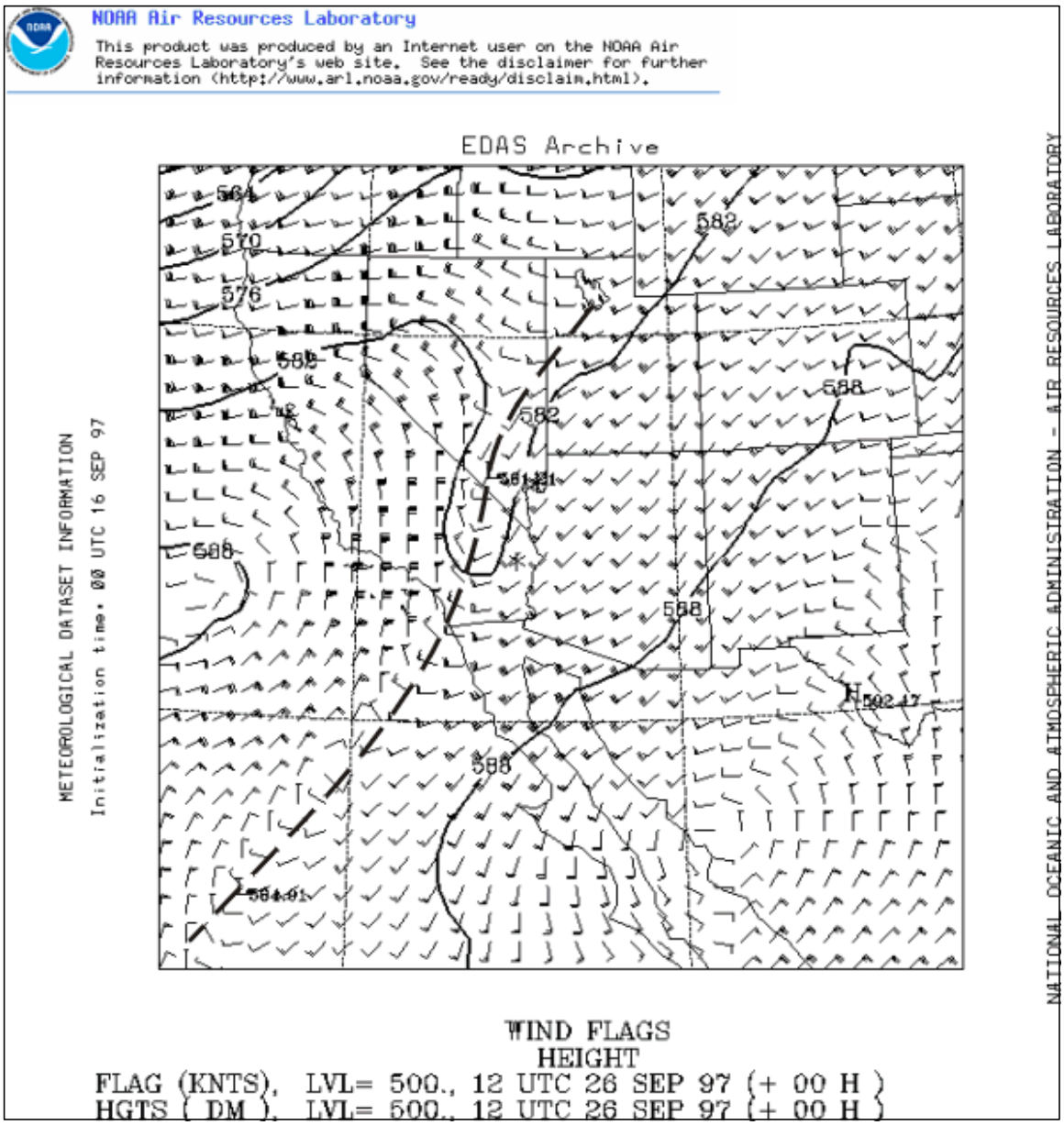

Figure 1. Detail of NOAA EDAS (Eta data assimilation system) analysis of 500-mb heights (dm) and winds (kts) over western North America and the eastern Pacific Ocean at 1200 UTC, 26 September 1997. Heavy dashed line shows position of a 500 mb tilted trough.

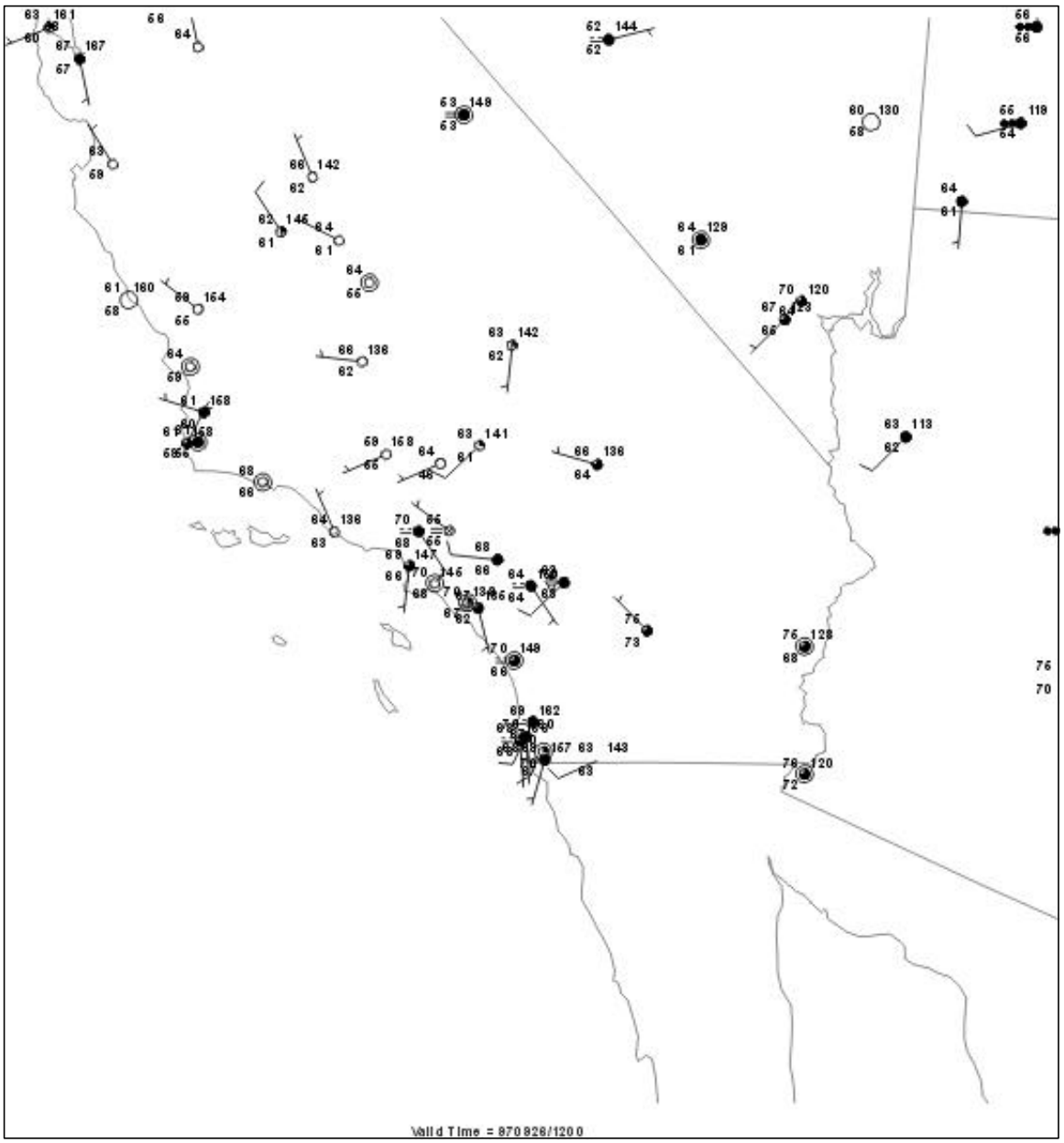

Figure 2. Plot of surface observations over southern and central CA at 1200 UTC, 26 September 1997.

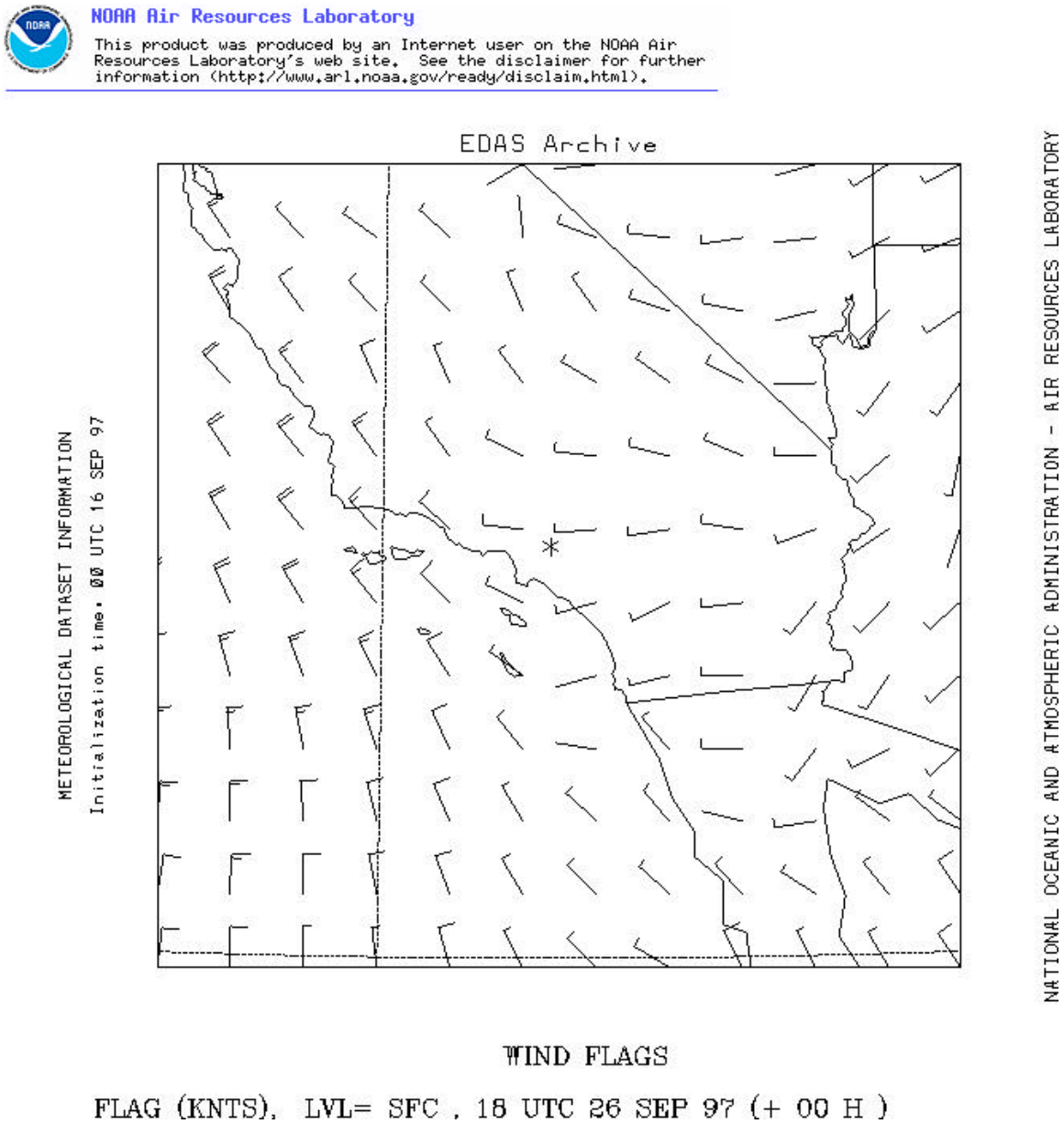

Figure 3. Detail of NOAA EDAS analysis for surface winds (kts) over southern CA and the CA Bight at 1800 UTC, 26 September 1997.

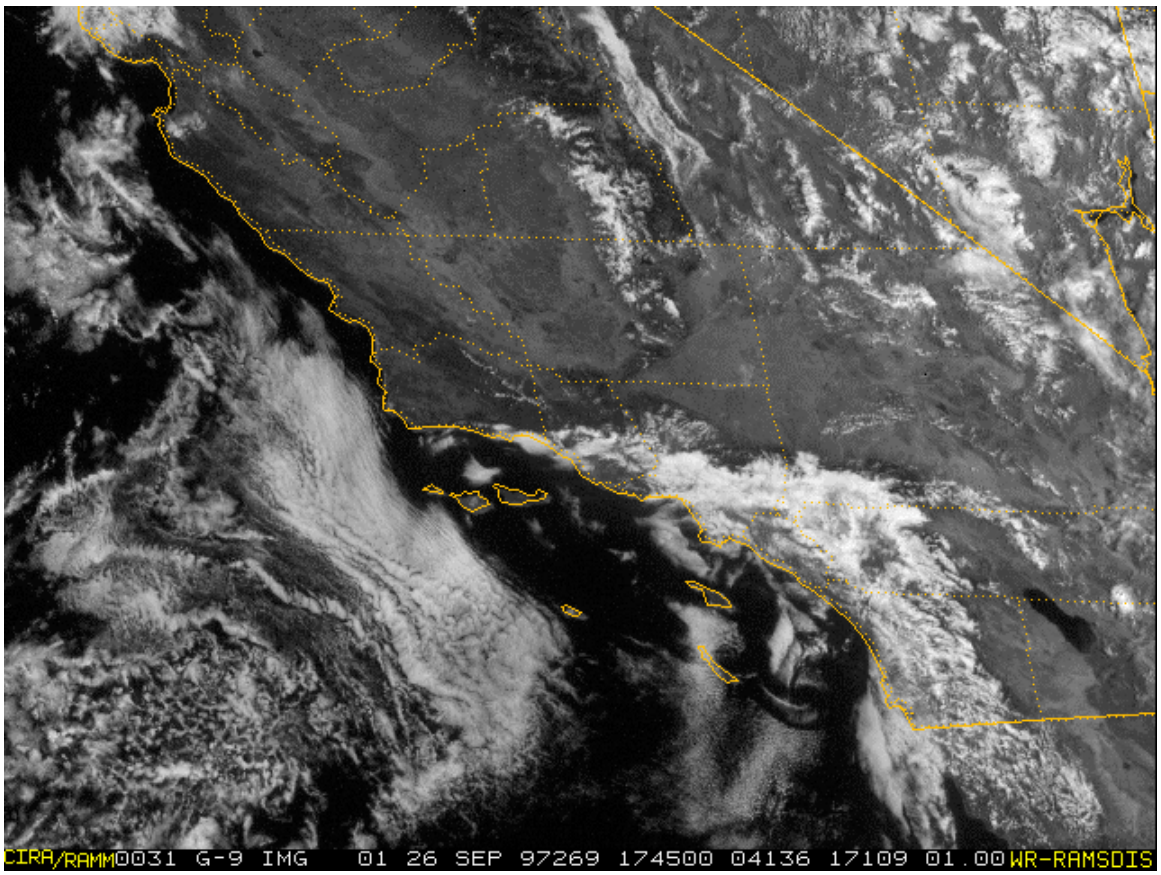

Figure 4. GOES-9 visible image at 1745 UTC, 26 September 1997.

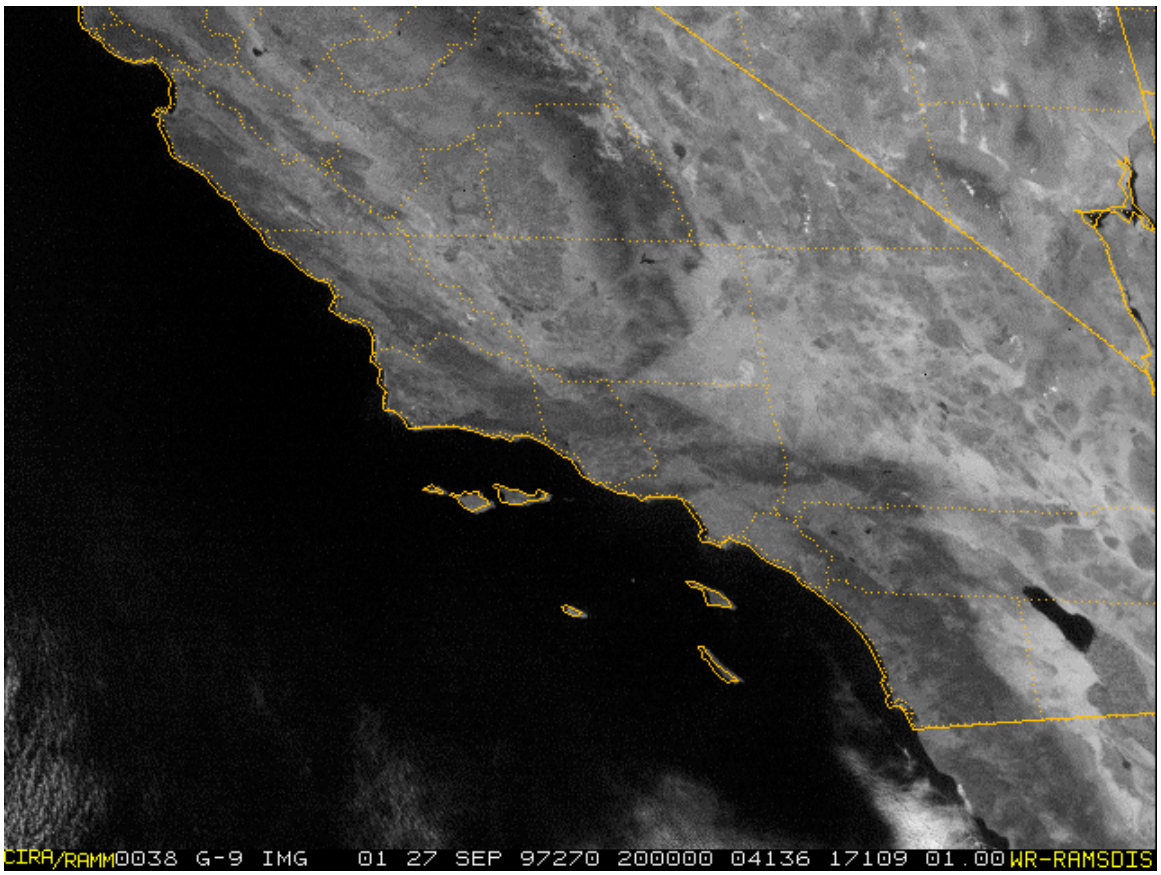

Figure 5. GOES-9 visible image at 2000 UTC, 27 September 1997.

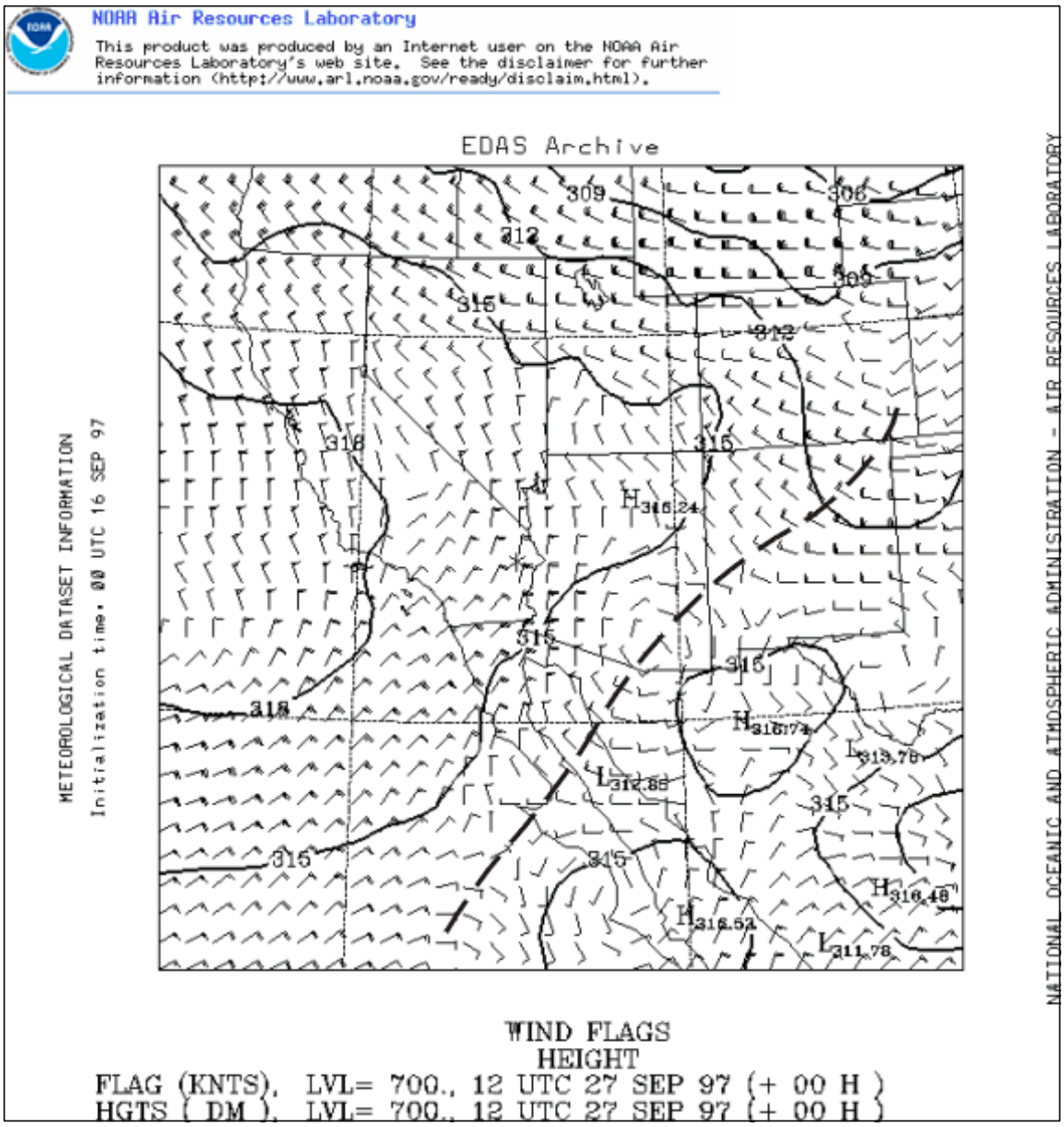

Figure 6. Detail of NOAA EDAS (Eta data assimilation system) analysis of 700-mb heights (dm) and winds (kts) over western North America and the eastern Pacific Ocean at 1200 UTC, 27 September 1997. Heavy dashed line shows position of a 700 mb tilted trough.

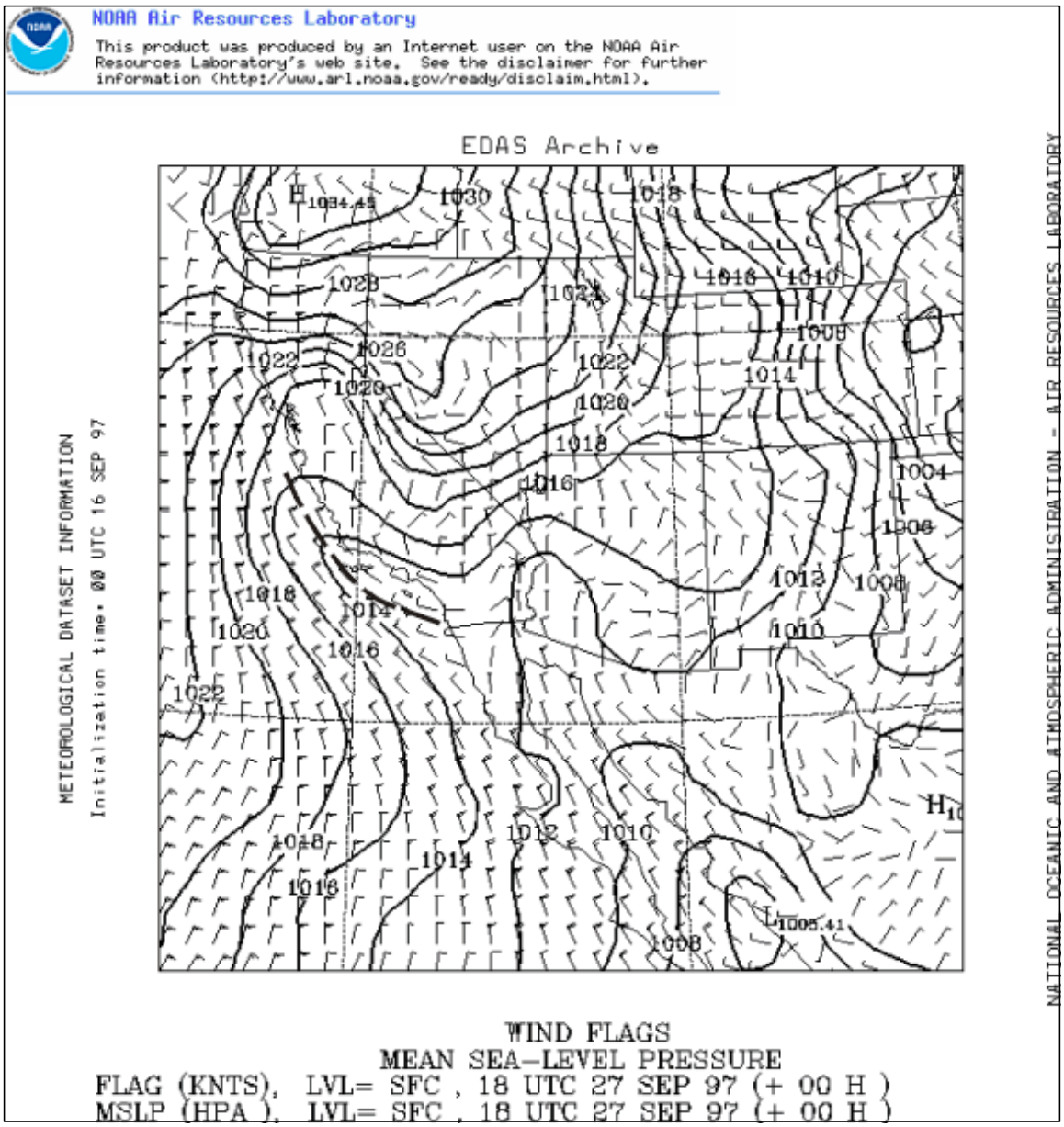

Figure 7. Detail of NOAA EDAS (Eta data assimilation system) sea-level pressure analysis (mb) and winds (kts) over western North America and the eastern Pacific Ocean at 1800 UTC, 27 September 1997. Heavy dashed lines shows position of major surface troughs.

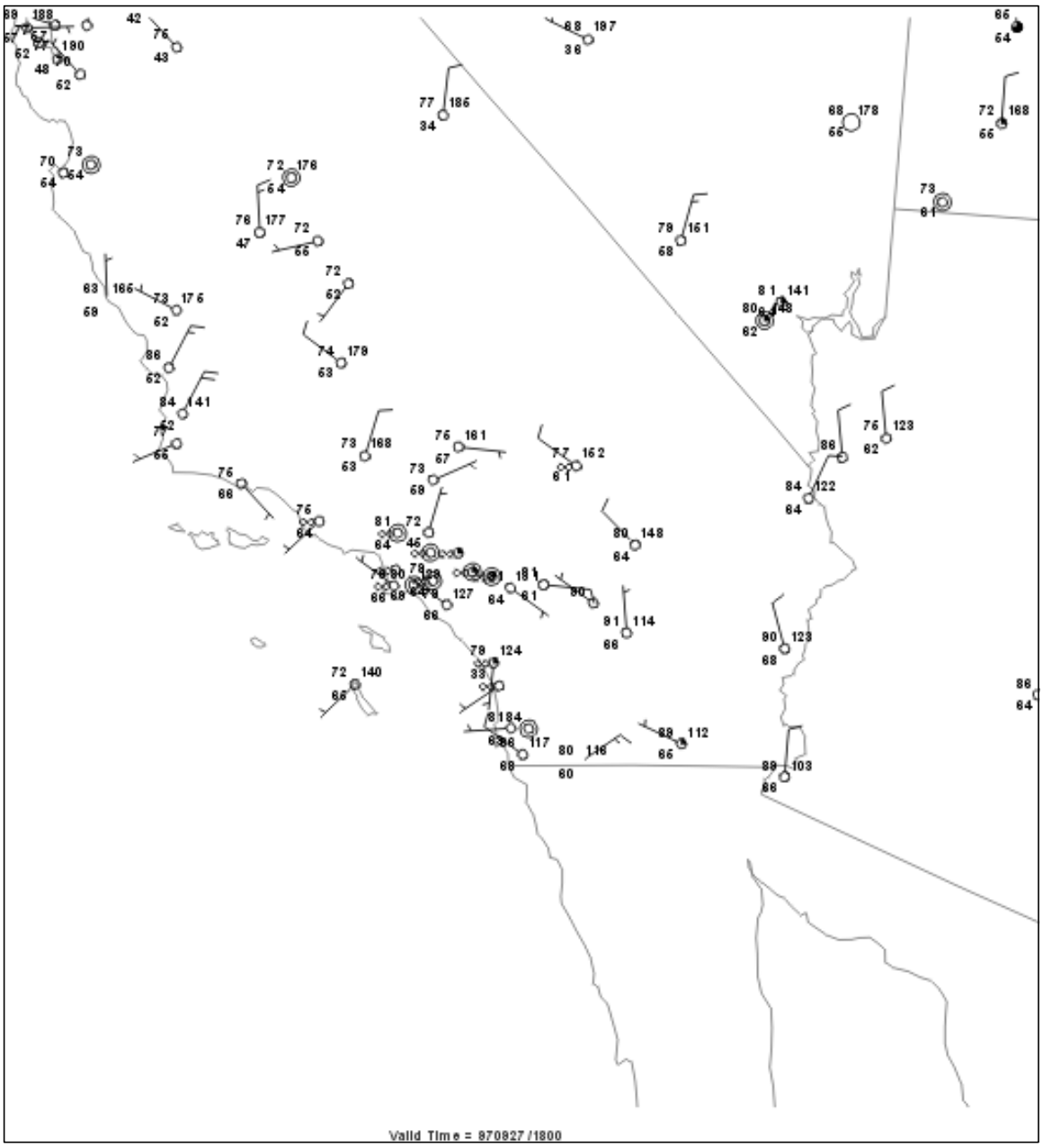

Figure 8. Plot of surface observations over southern and central CA at 1800 UTC, 27 September 1997.

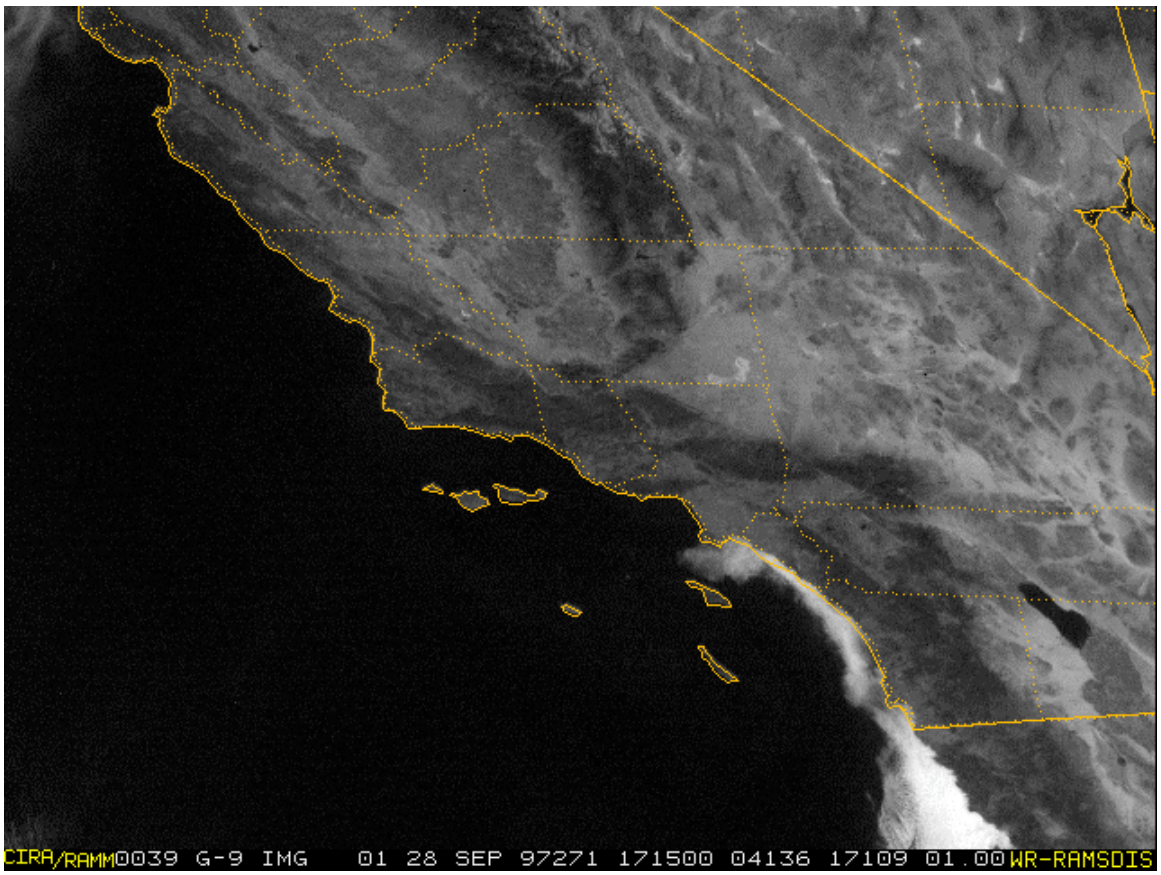

Figure 9. GOES-9 visible image at 1715 UTC, 28 September 1997.

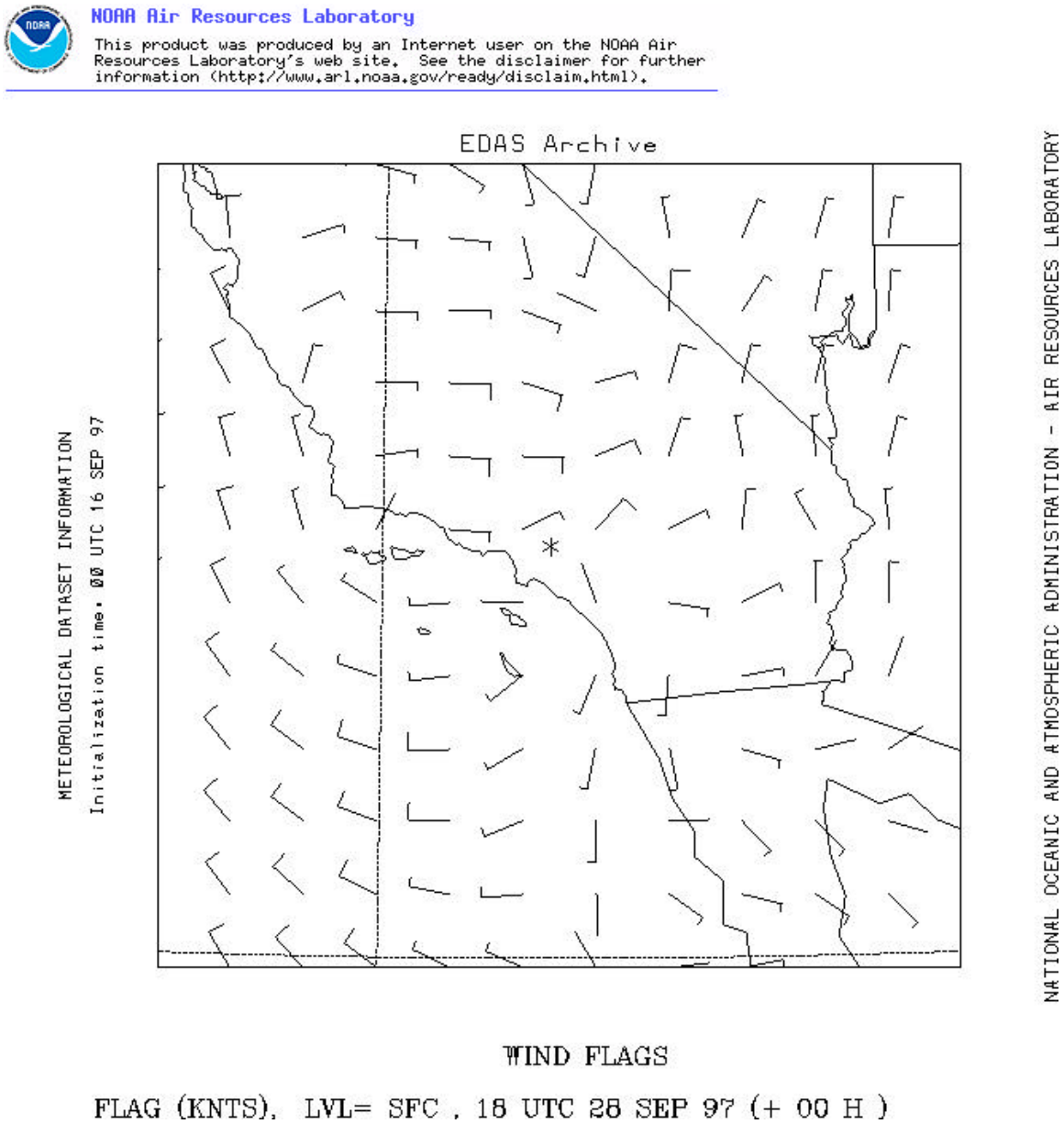

Figure 10. Detail of NOAA EDAS analysis for surface winds (kts) over southern CA and the CA Bight at 1800 UTC, 28 September 1997.

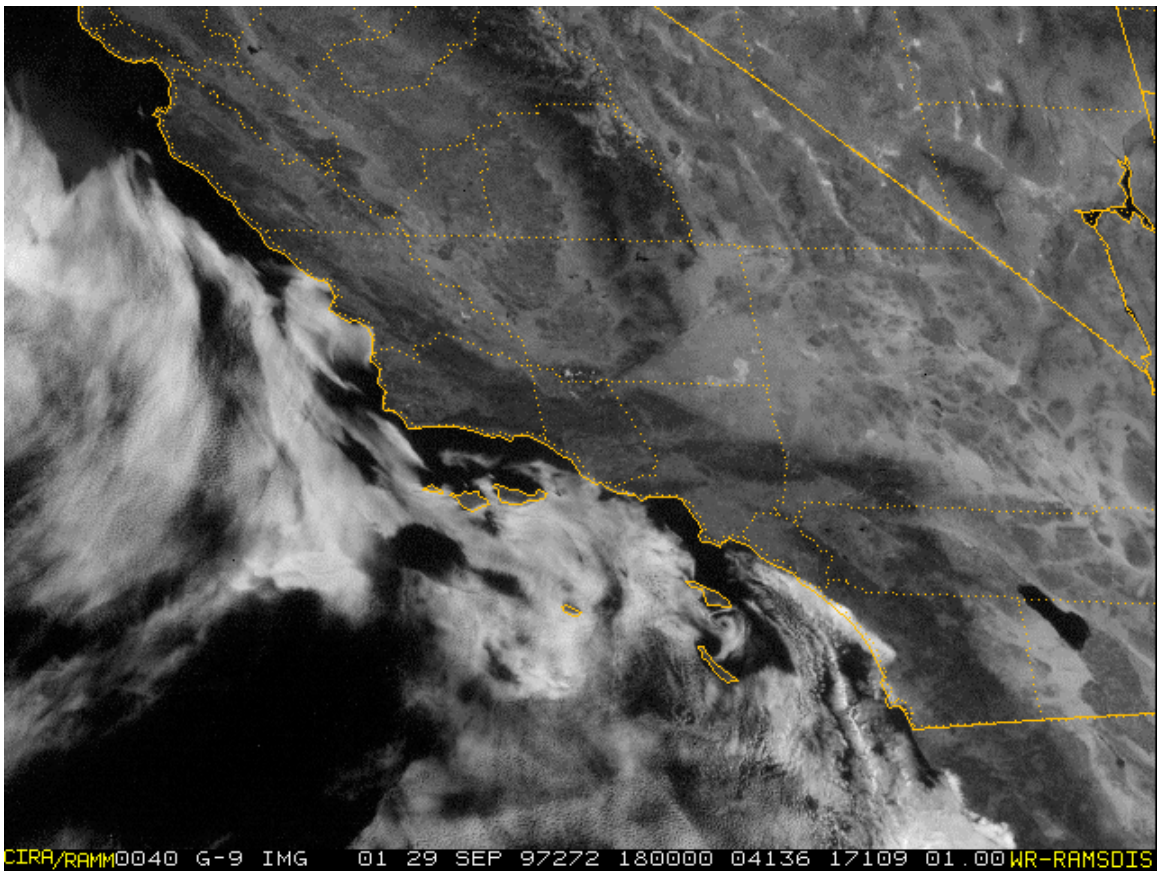

Figure 11. GOES-9 visible image at 1800 UTC, 29 September 1997.

NOAA Air Resources Laboratory
This product was produced by an Internet user on the NOAA Air Resources Laboratory's web site. See the disclaimer for further information (http://www.arl.noaa.gov/ready/disclaim.html).

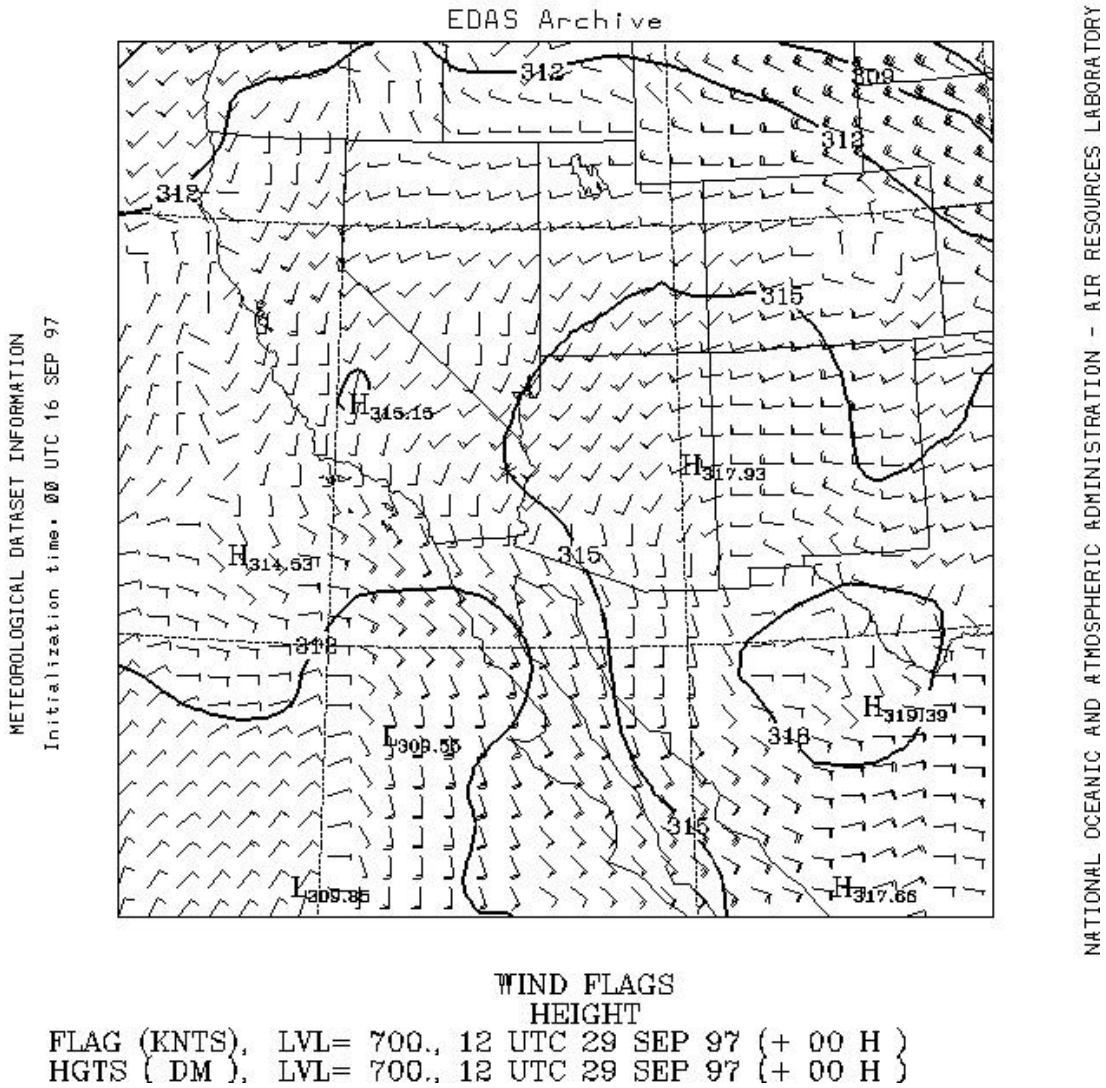

Figure 12. Detail of NOAA EDAS (Eta data assimilation system) analysis of 700-mb heights (dm) and winds (kts) over western North America and the eastern Pacific Ocean at 1200 UTC, 29 September 1997.

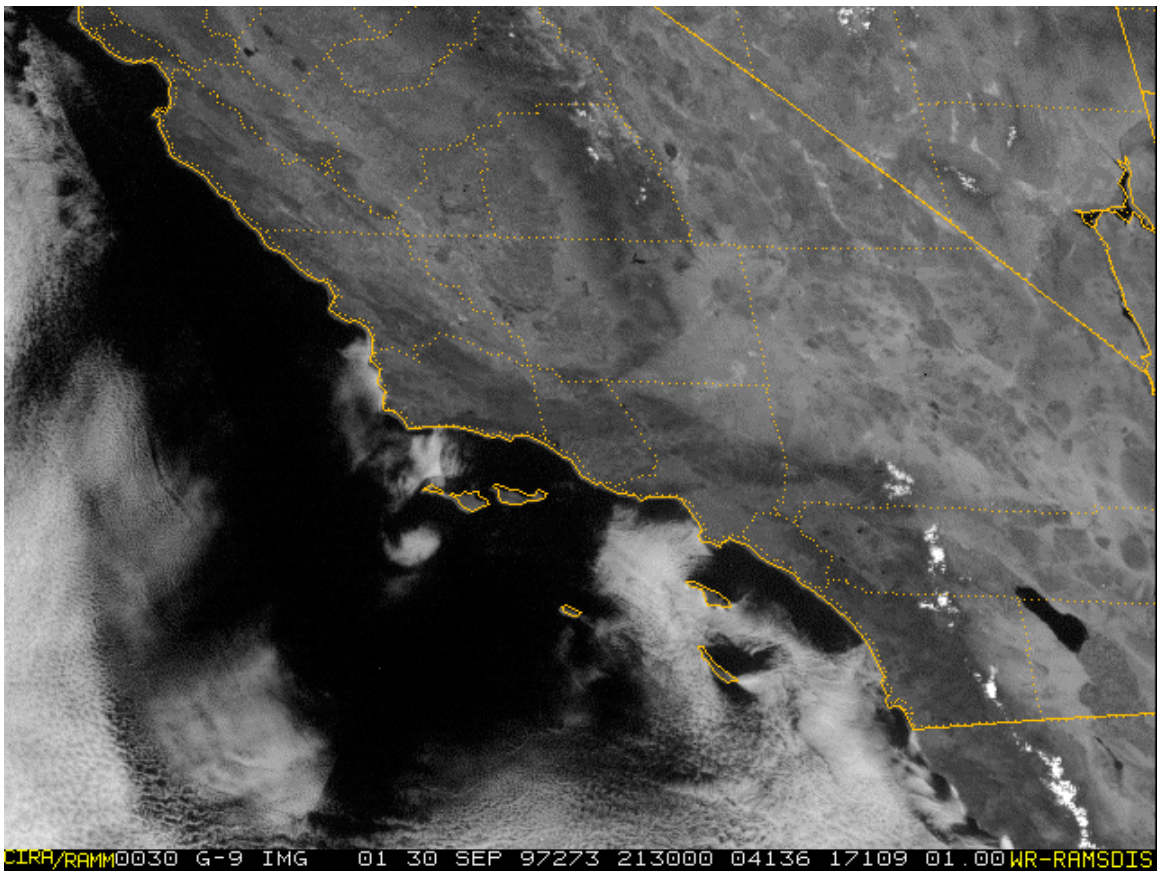

Figure 13. GOES-9 visible image at 2130 UTC, 30 September 1997.

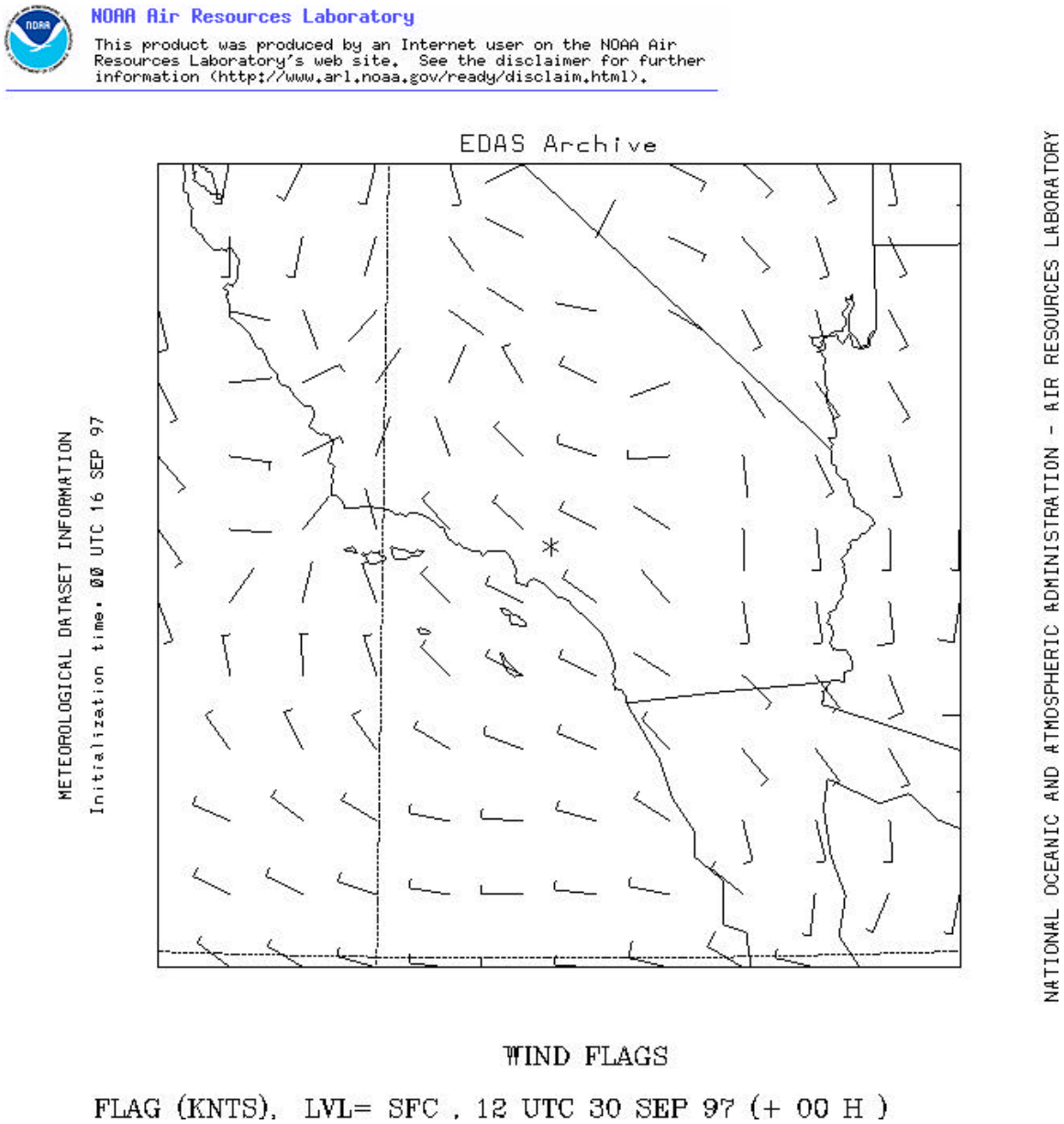

Figure 14. Detail of NOAA EDAS analysis for surface winds (kts) over southern CA and the CA Bight at 1200 UTC, 30 September 1997.

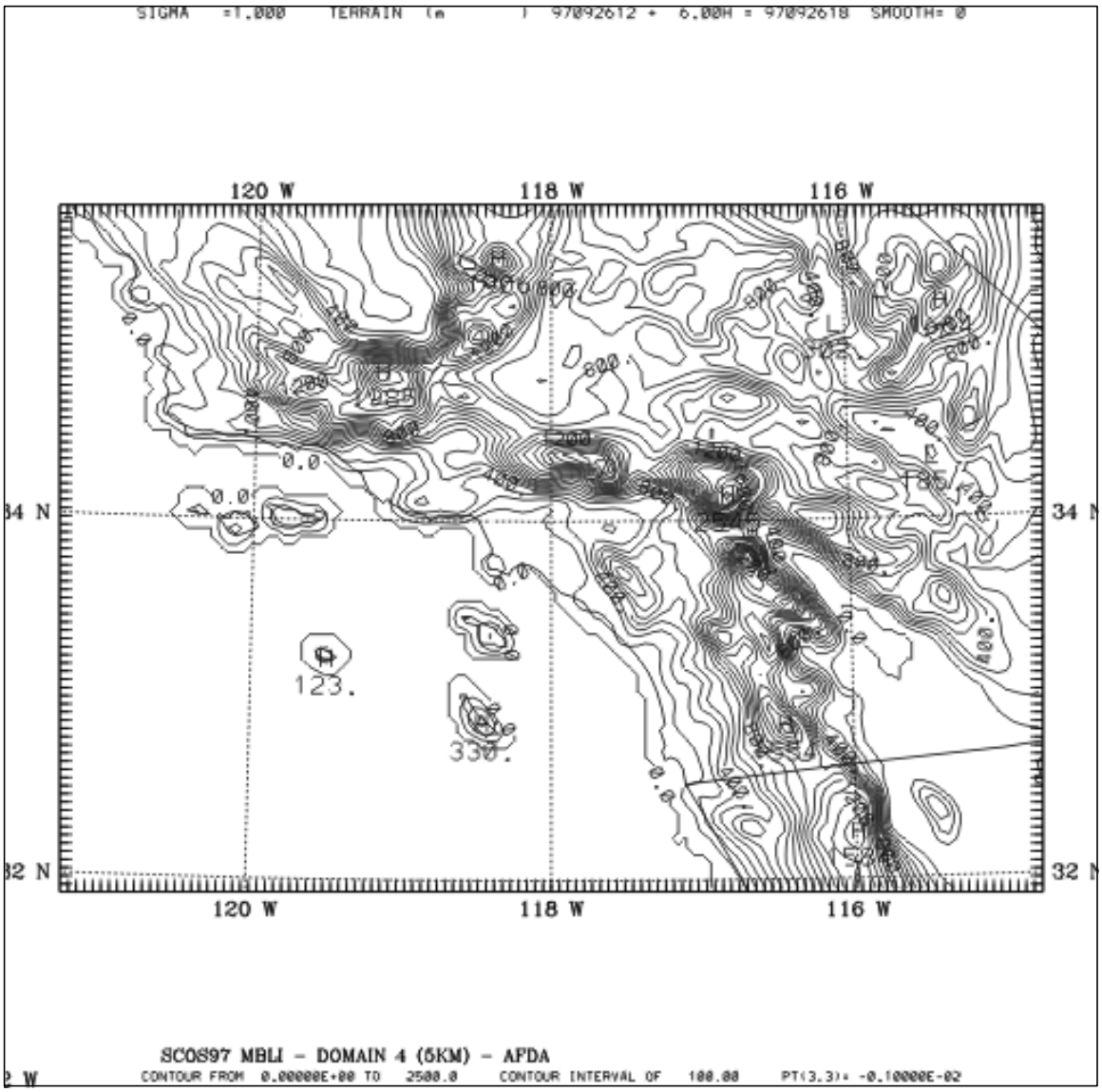

Figure 15. MM5 terrain (m) on the innermost 5-km domain of the nested mesoscale model. Contour interval is 100 m.

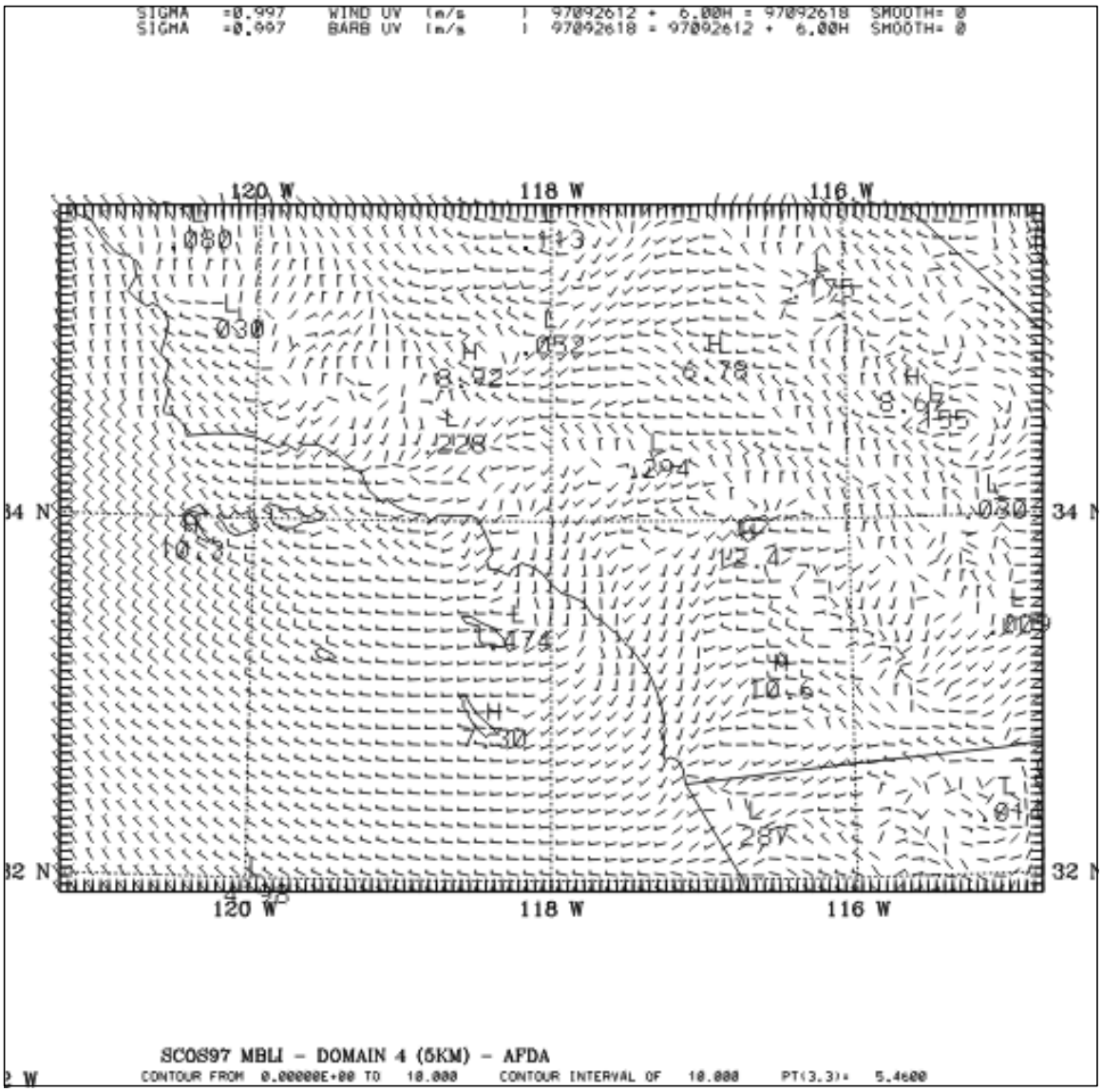

Figure 16. MM5 simulated surface-layer winds (m s^{-1}) at 35 m AGL for 1800 UTC, 26 September 1997, after 6 h of model integration. Isotachs are shown at 1 m s^{-1}, 2 m s^{-1}, 5 m s^{-1}, and thereafter at intervals of 5 m s^{-1}.

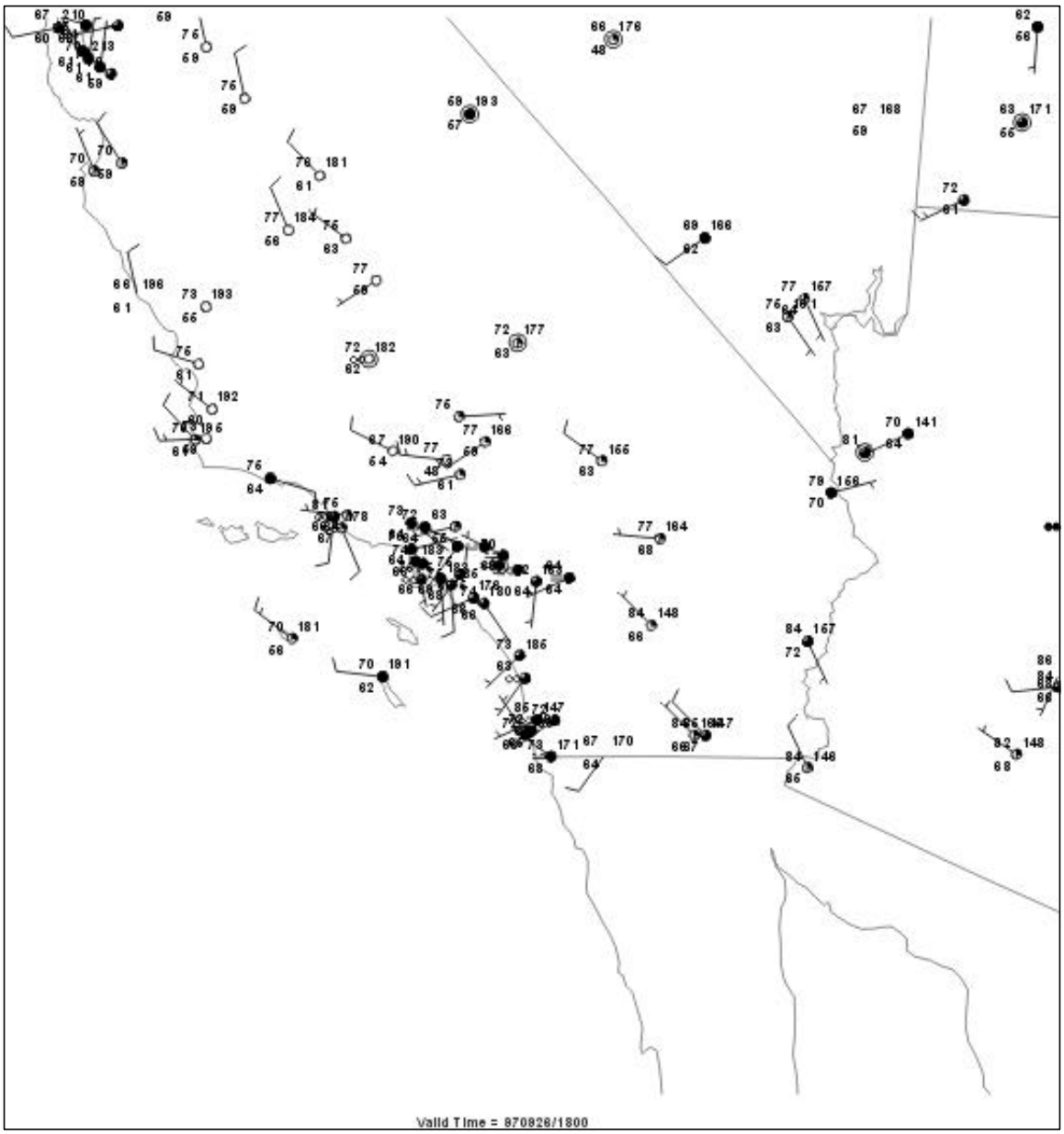

Figure 17. Plot of surface observations over southern and central CA at 1800 UTC, 26 September 1997.

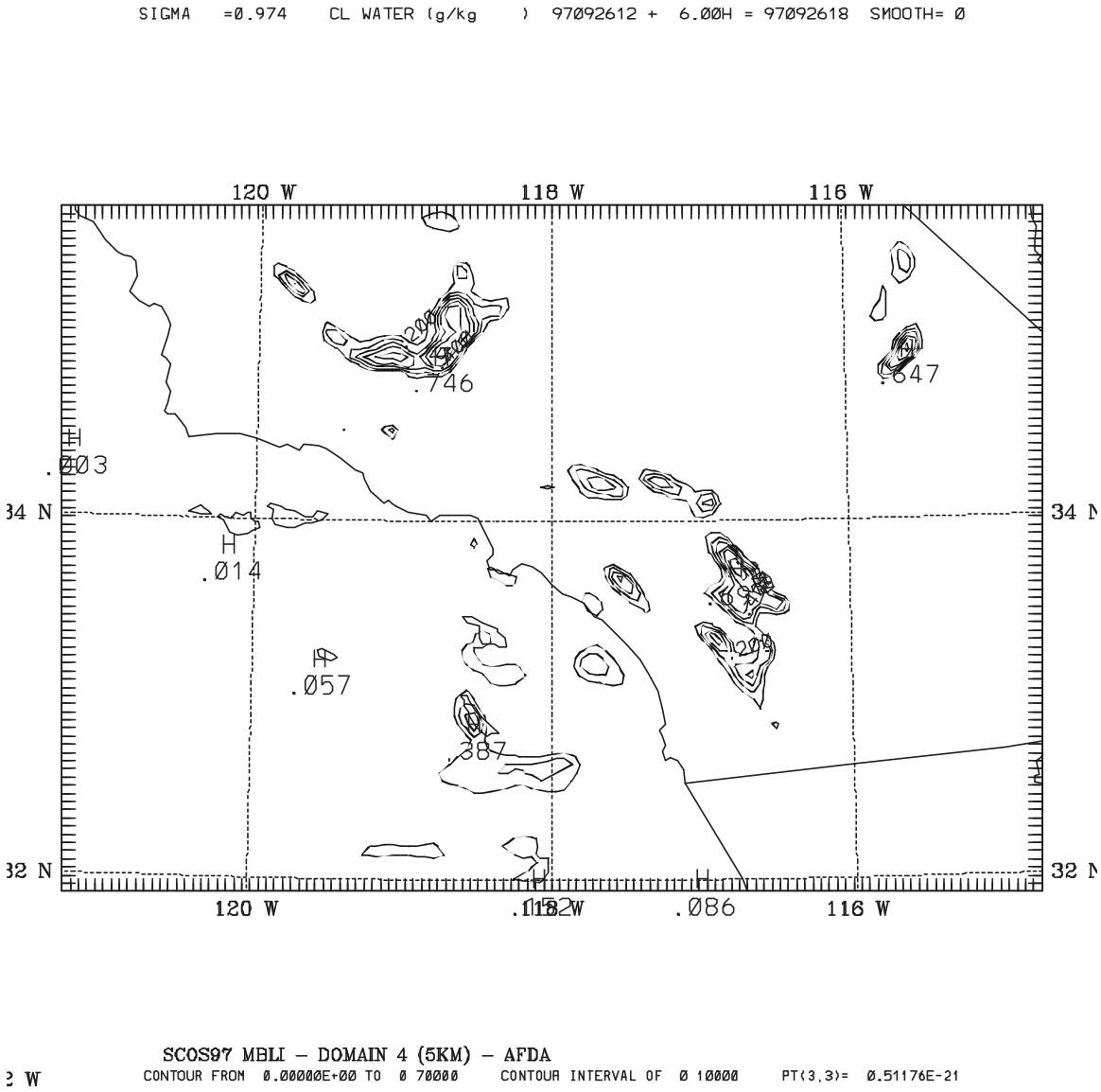

Figure 18. MM5 simulated cloud liquid water (g kg^{-1}) at about 300 m AGL (s = 0.974) for 1800 UTC, 26 September 1997, after 6 h of model integration. Contour interval is 0.1 g kg^{-1}.

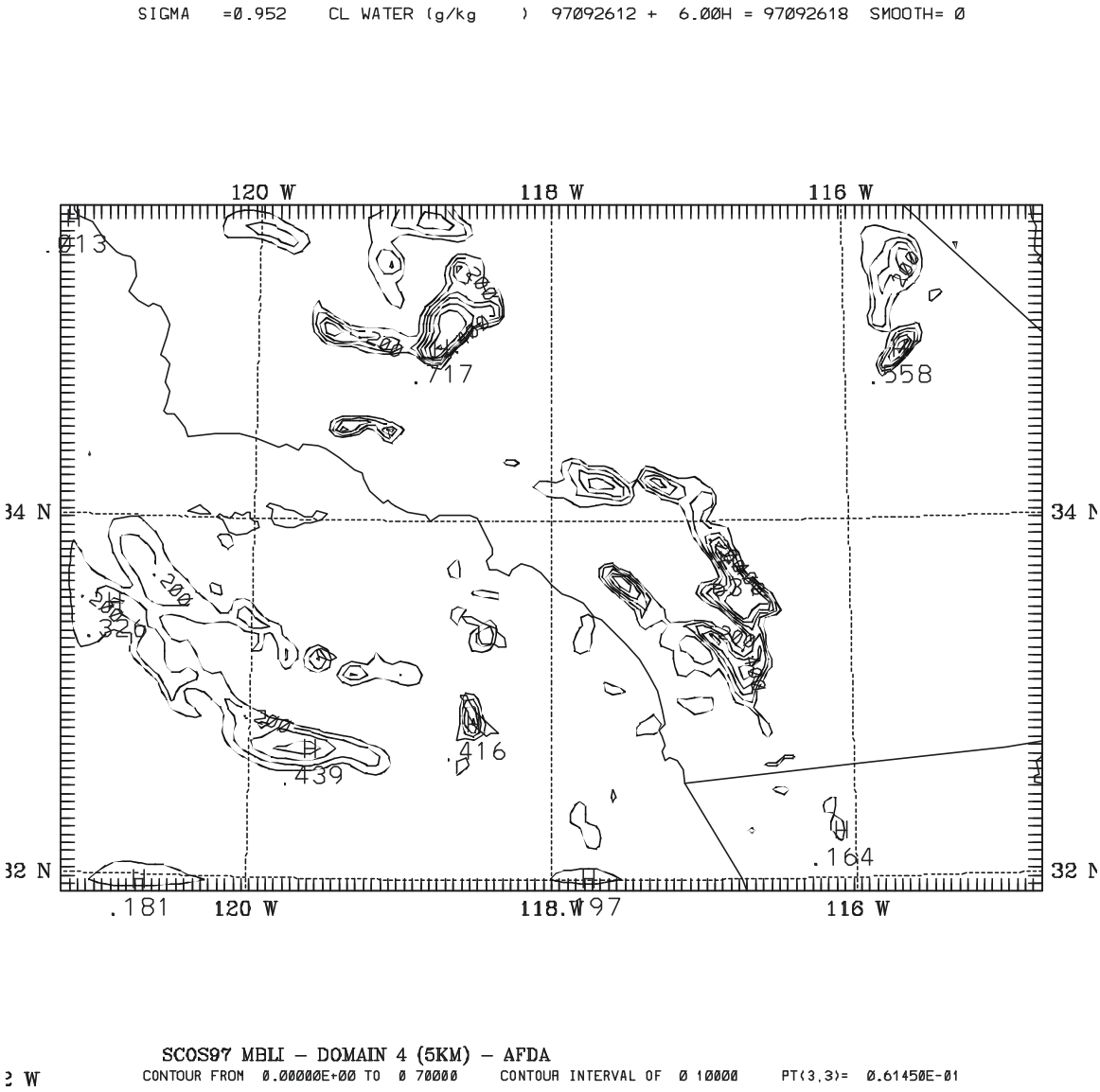

Figure 19. MM5 simulated cloud liquid water (g kg^{-1}) at about 550 m AGL (s = 0.952) for 1800 UTC, 26 September 1997, after 6 h of model integration. Contour interval is 0.1 g kg^{-1}.

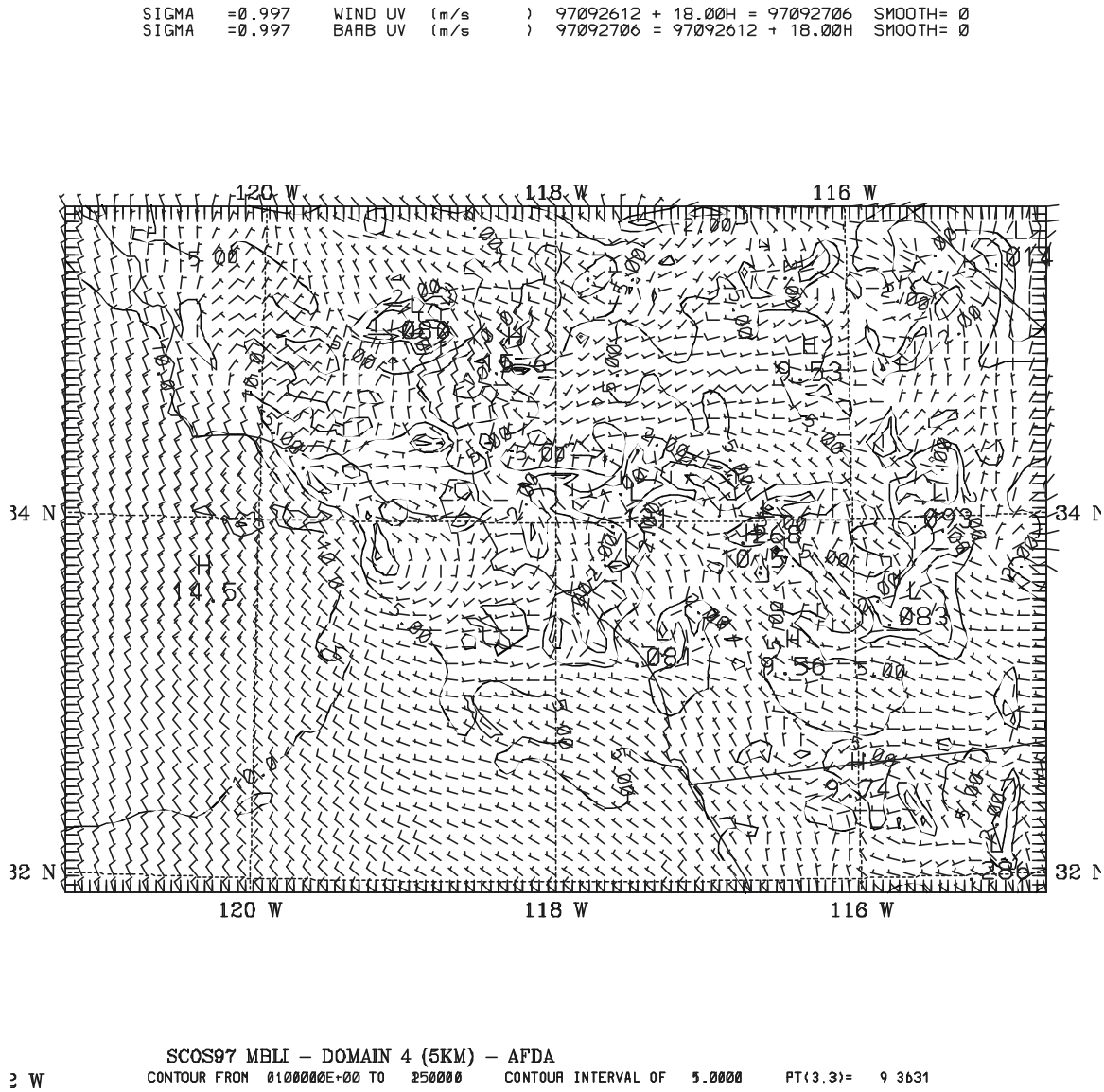

Figure 20. MM5 simulated surface-layer winds (m s^{-1}) at 35 m AGL for 1800 UTC, 27 September 1997, after 30 h of model integration. Isotachs are shown at 1 m s^{-1}, 2 m s^{-1}, 5 m s^{-1}, and thereafter at intervals of 5 m s^{-1}.

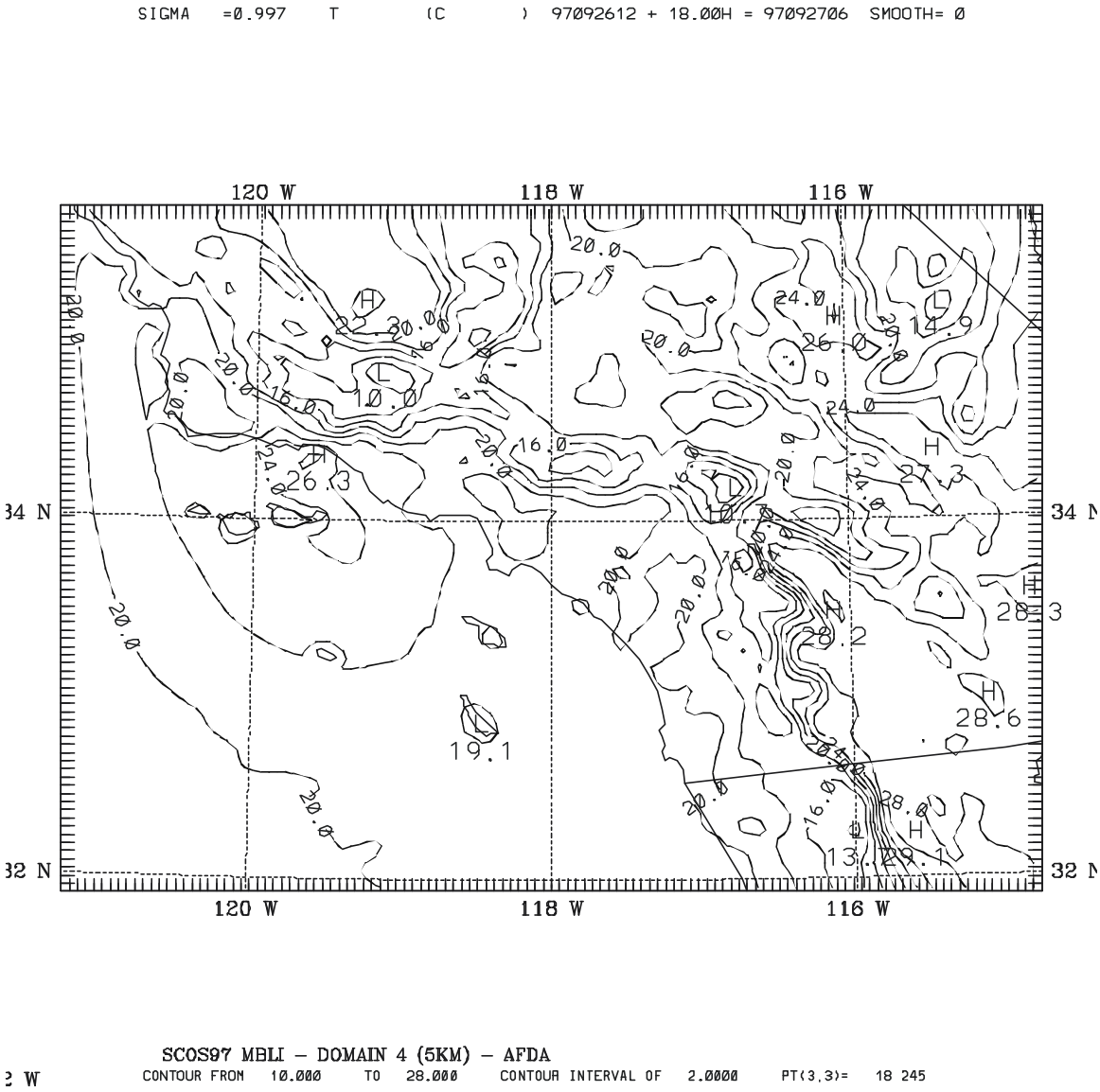

Figure 21. MM5 simulated surface-layer temperatures (C) at 35 m AGL for 1800 UTC, 27 September 1997, after 30 h of model integration. Isotherms are shown at 2 C intervals.

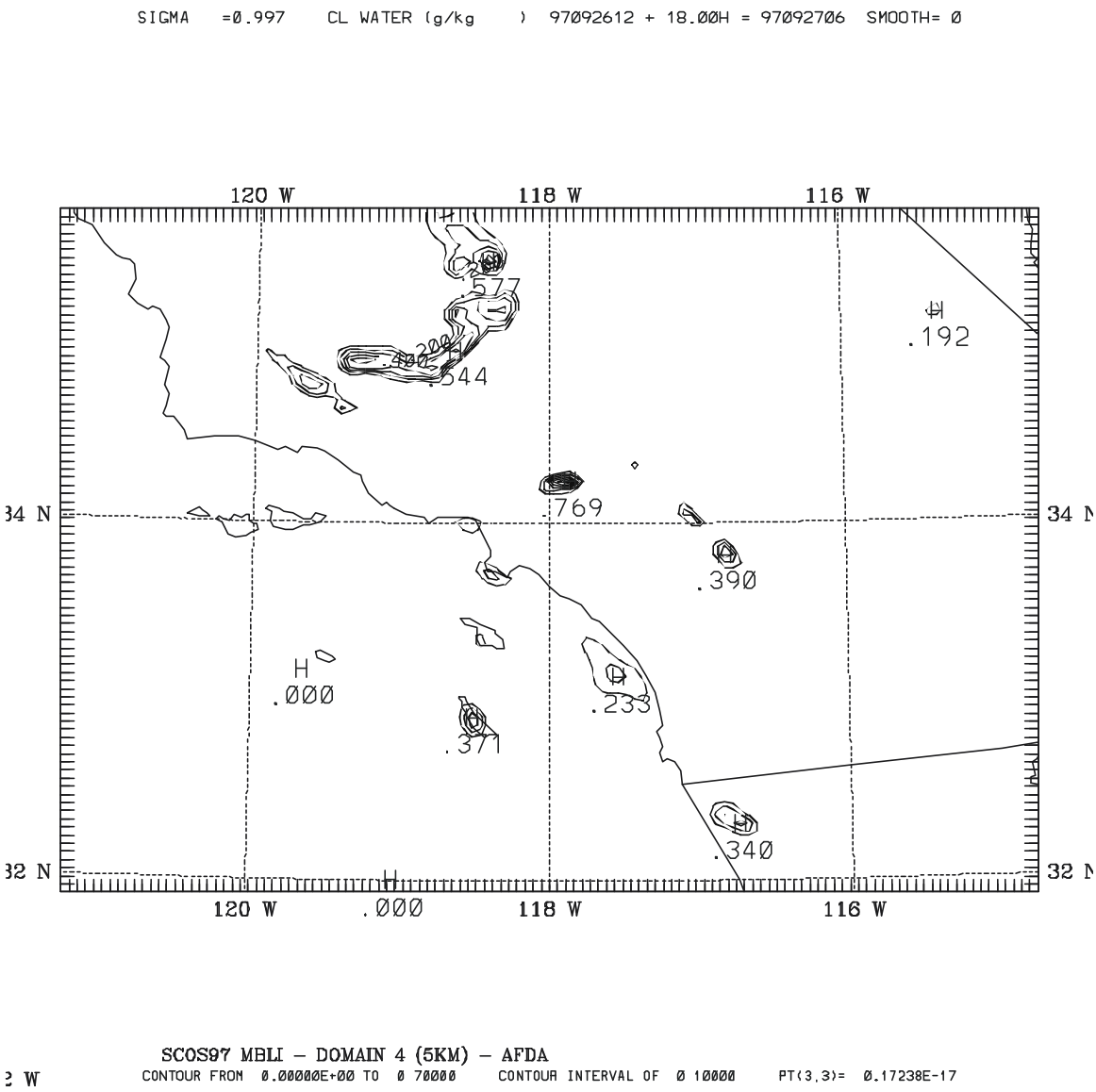

Figure 22. MM5 simulated cloud liquid water (g kg^{-1}) in the surface layer at about 35 m AGL (s = 0.997) for 1800 UTC, 27 September 1997, after 30 h of model integration. Contour interval is 0.1 g kg^{-1}.

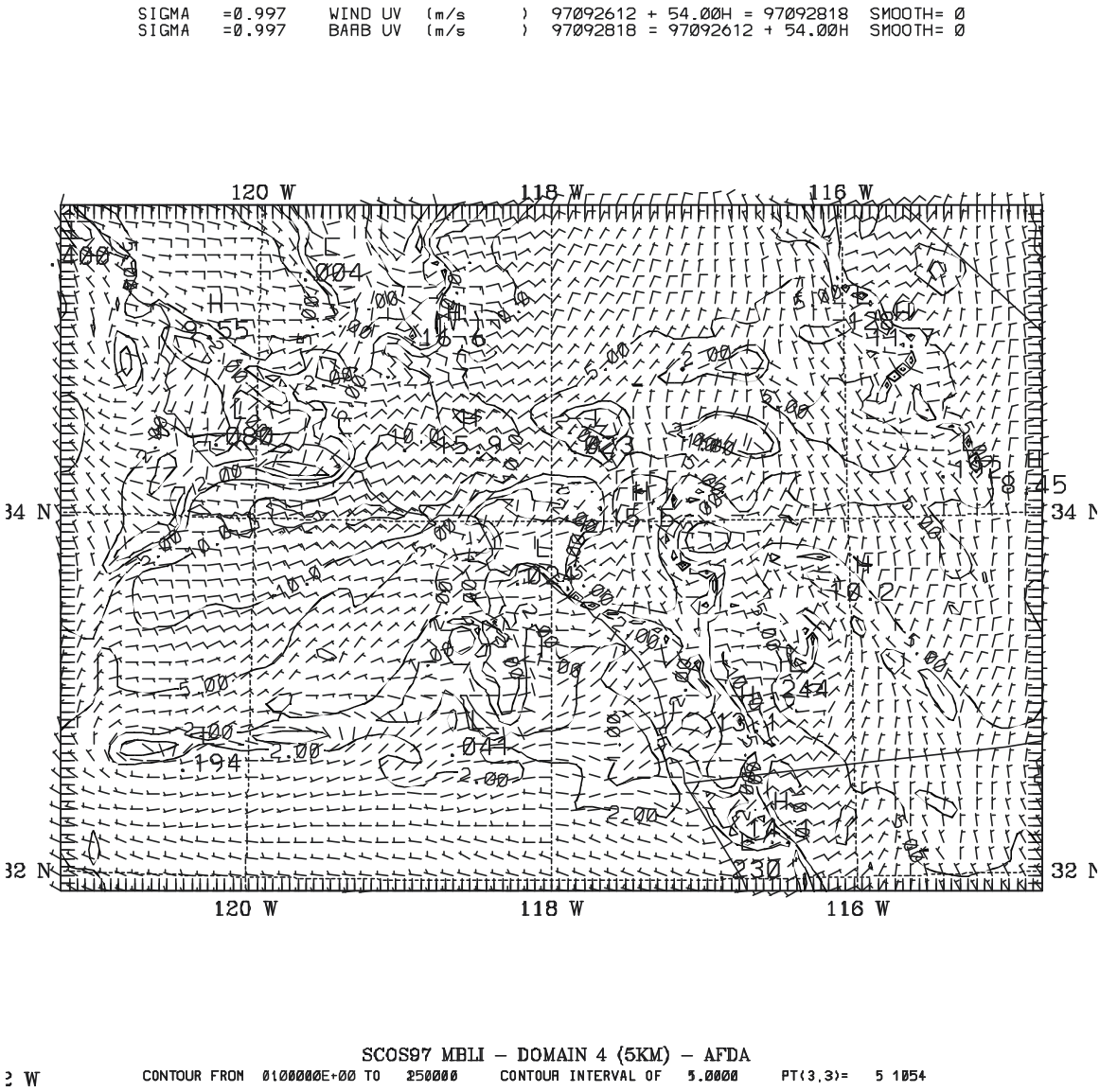

Figure 23. MM5 simulated surface-layer winds (m s^{-1}) at 35 m AGL for 1800 UTC, 28 September 1997, after 54 h of model integration. Isotachs are shown at 1 m s^{-1}, 2 m s^{-1}, 5 m s^{-1}, and thereafter at intervals of 5 m s^{-1}.

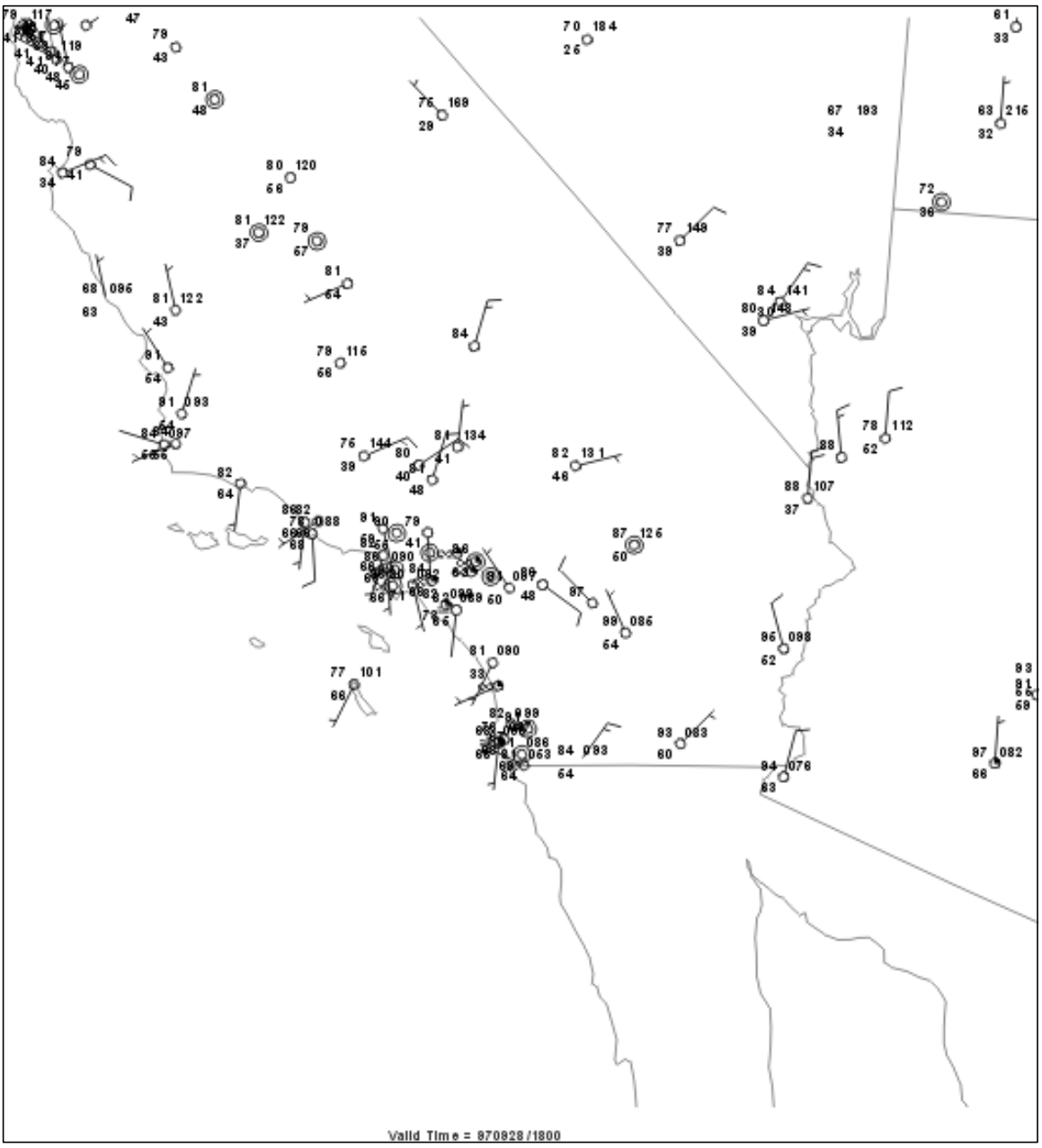

Figure 24. Plot of surface observations over southern and central CA at 1800 UTC, 28 September 1997.

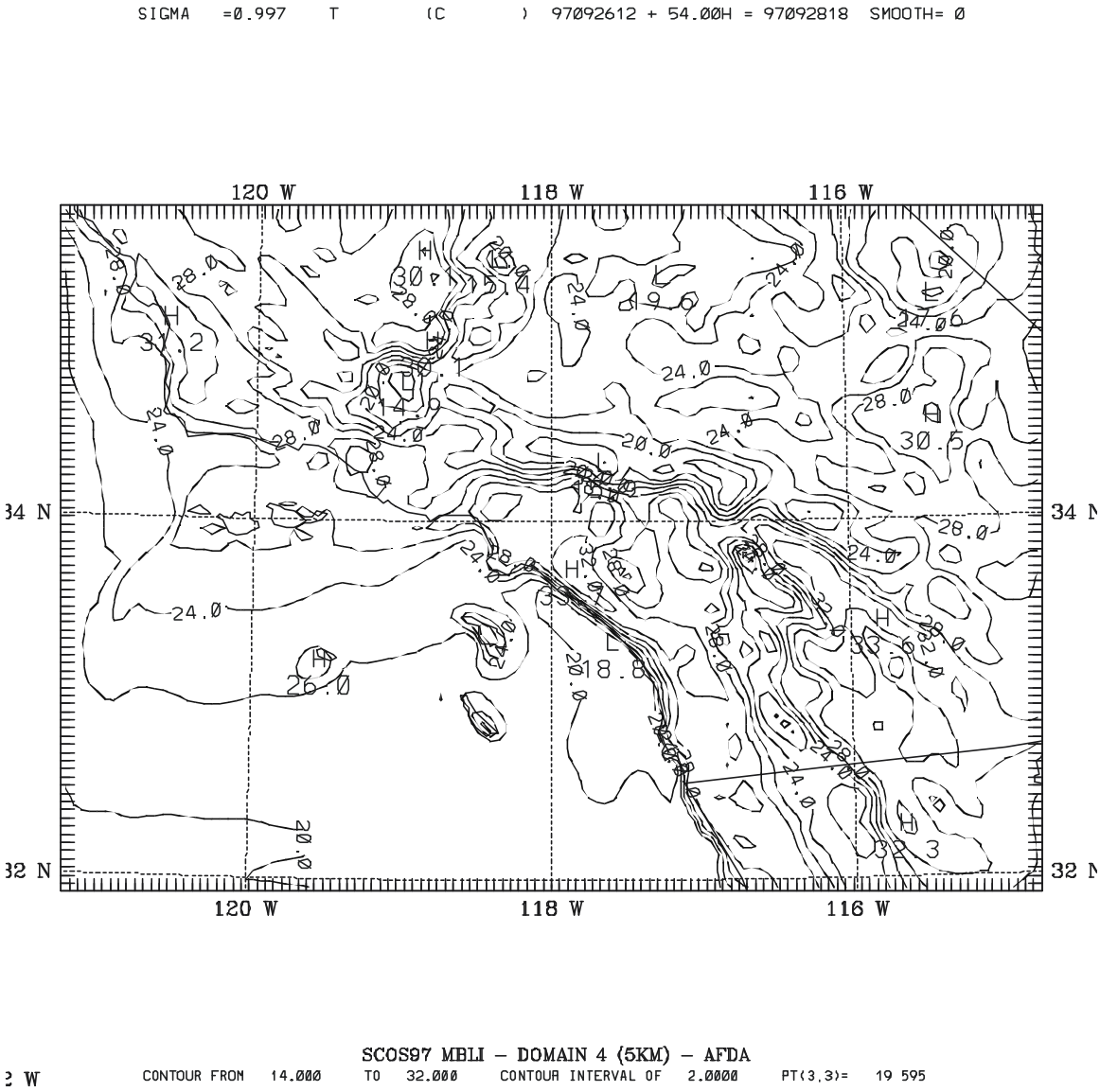

Figure 25. MM5 simulated surface-layer temperatures (C) at 35 m AGL for 1800 UTC, 28 September 1997, after 54 h of model integration. Isotherms are shown at 2 C intervals.

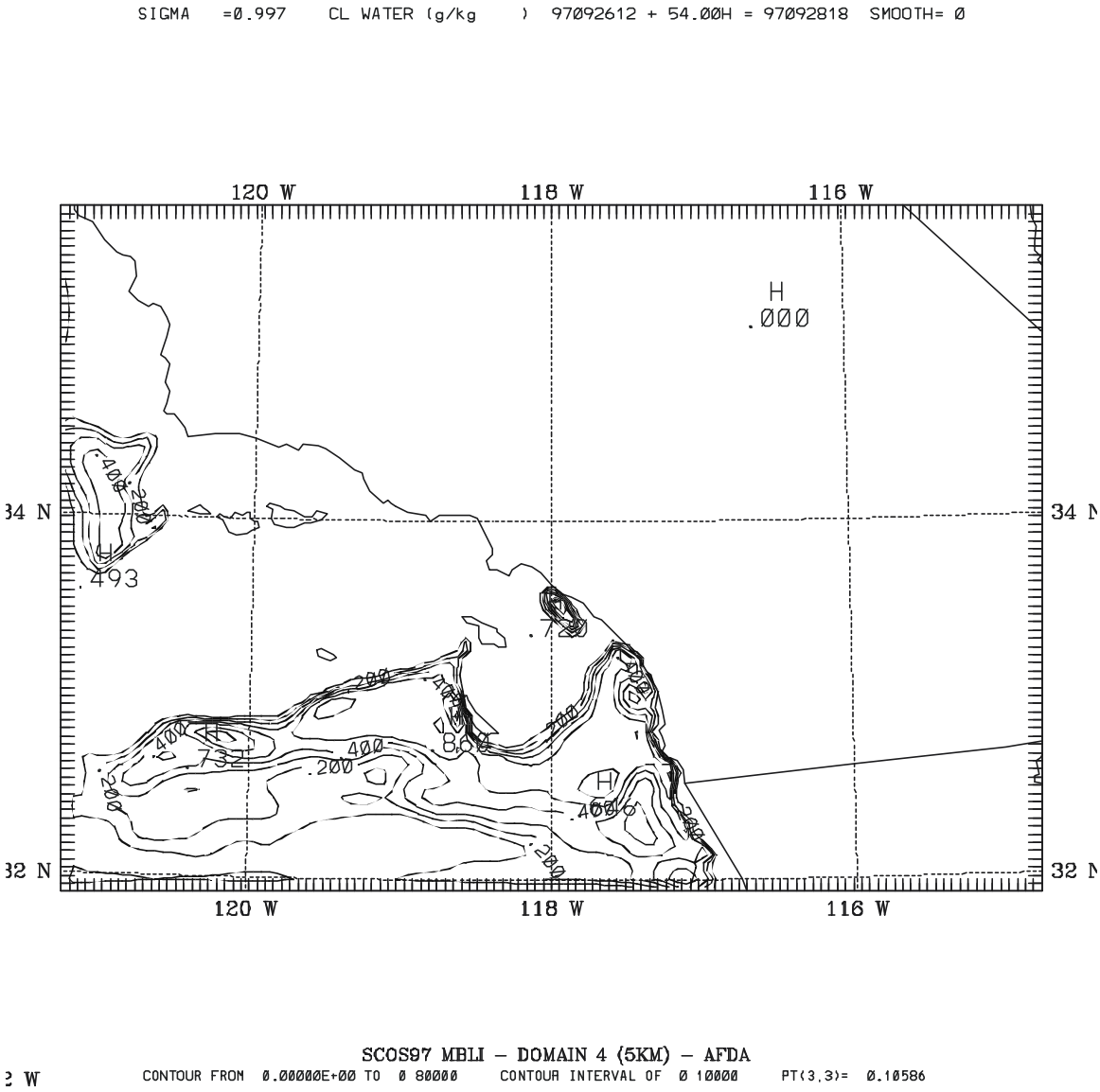

Figure 26. MM5 simulated cloud liquid water (g kg^{-1}) in the surface layer at about 35 m AGL (s = 0.997) for 1800 UTC, 28 September 1997, after 54 h of model integration. Contour interval is 0.1 g kg^{-1}.

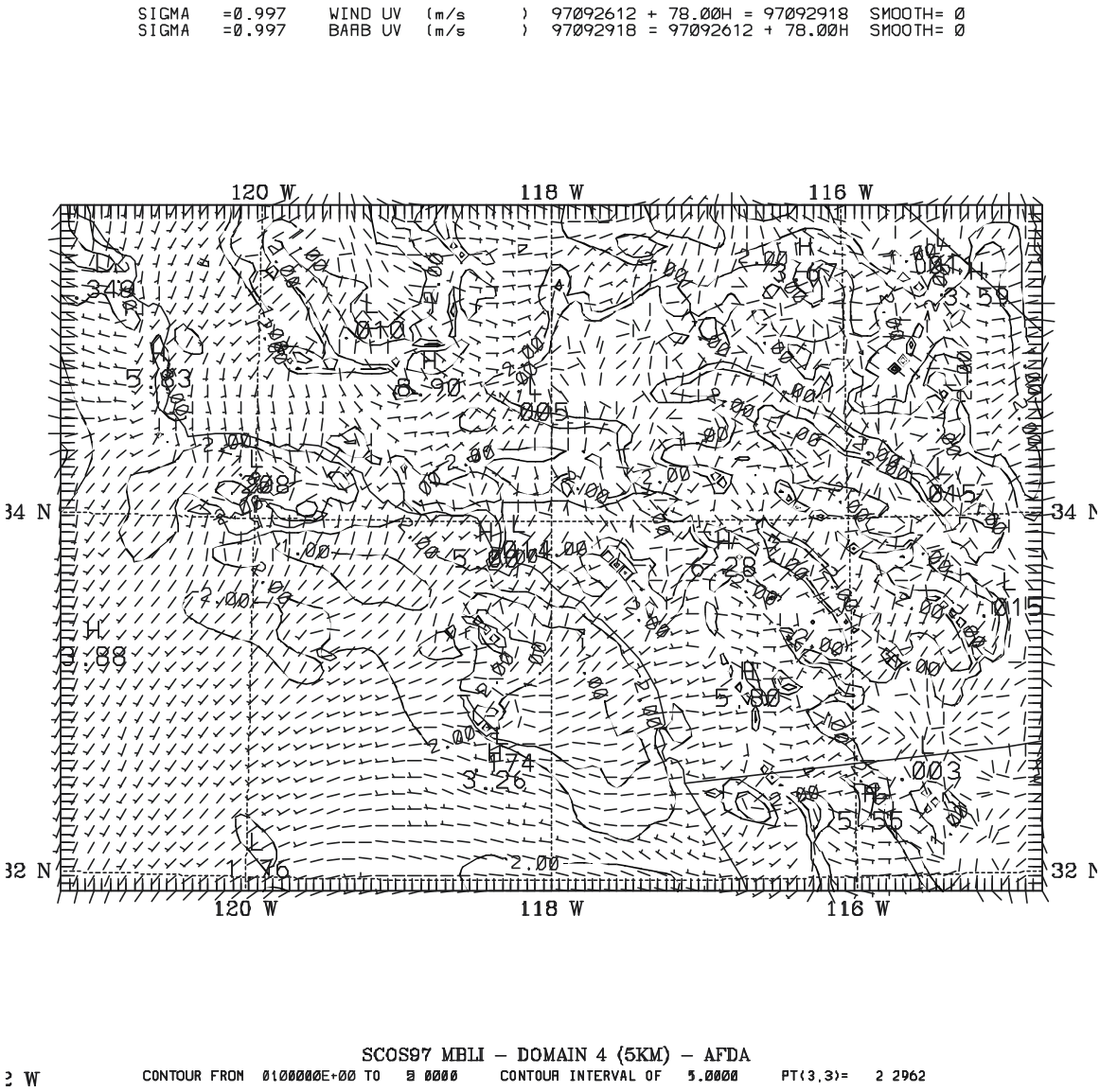

Figure 27. MM5 simulated surface-layer winds (m s^{-1}) at 35 m AGL for 1800 UTC, 29 September 1997, after 78 h of model integration. Isotachs are shown at 1 m s^{-1}, 2 m s^{-1}, 5 m s^{-1}, and thereafter at intervals of 5 m s^{-1}.

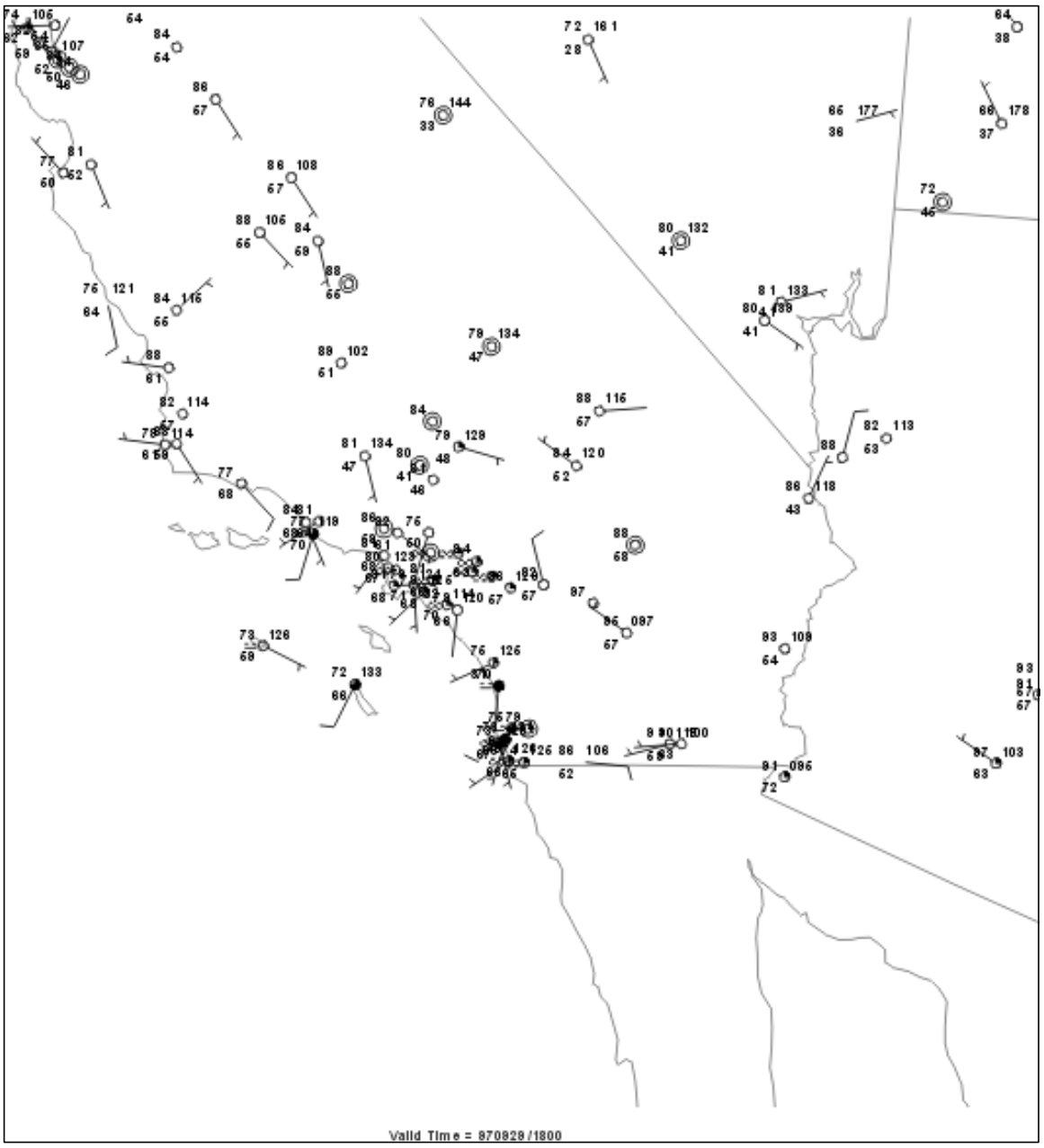

Figure 28. Plot of surface observations over southern and central CA at 1800 UTC, 29 September 1997.

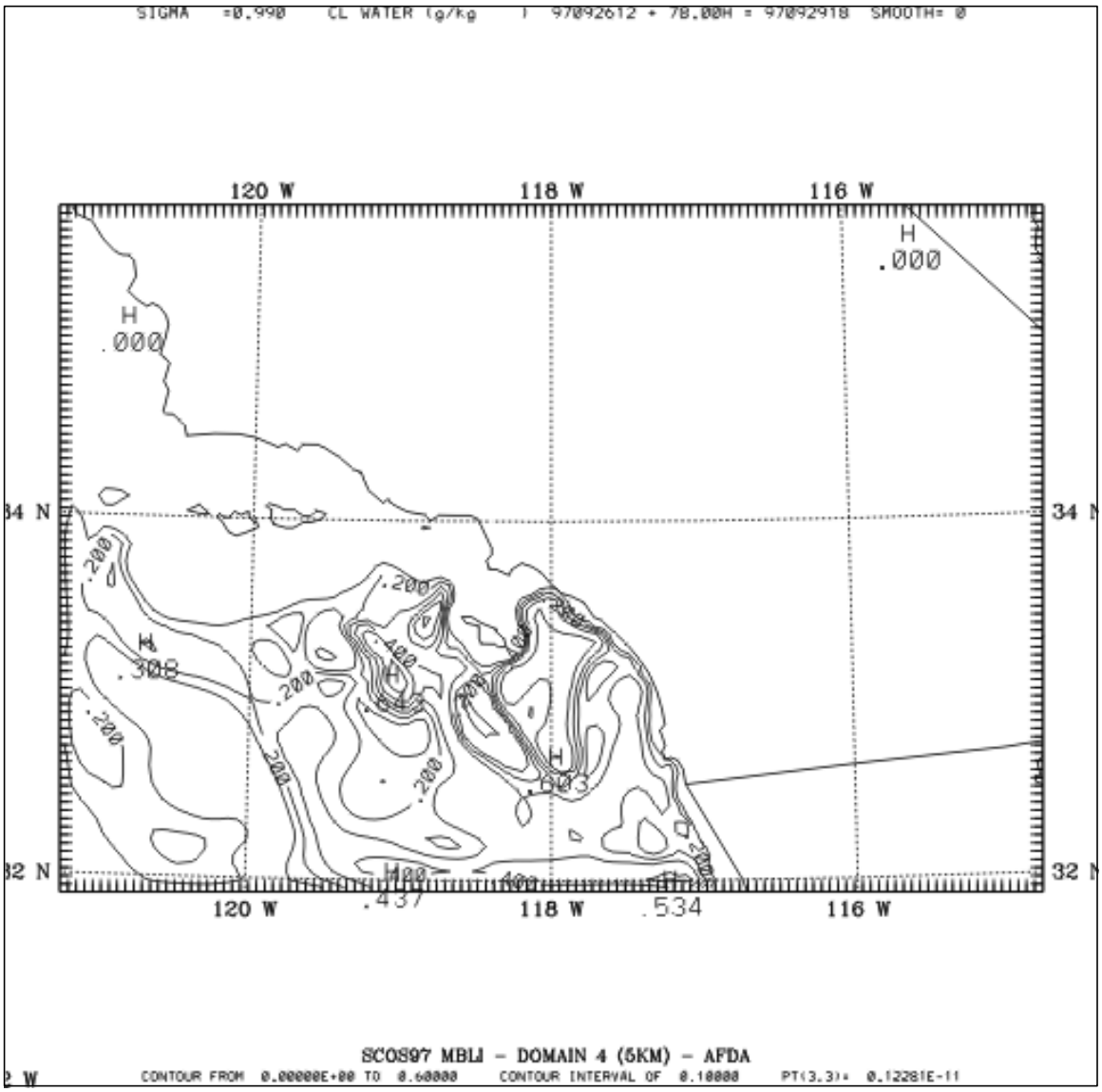

Figure 29. MM5 simulated cloud liquid water (g kg^{-1}) in the low levels at about 120 m AGL (s = 0.990) for 1800 UTC, 29 September 1997, after 78 h of model integration. Contour interval is 0.1 g kg^{-1}.

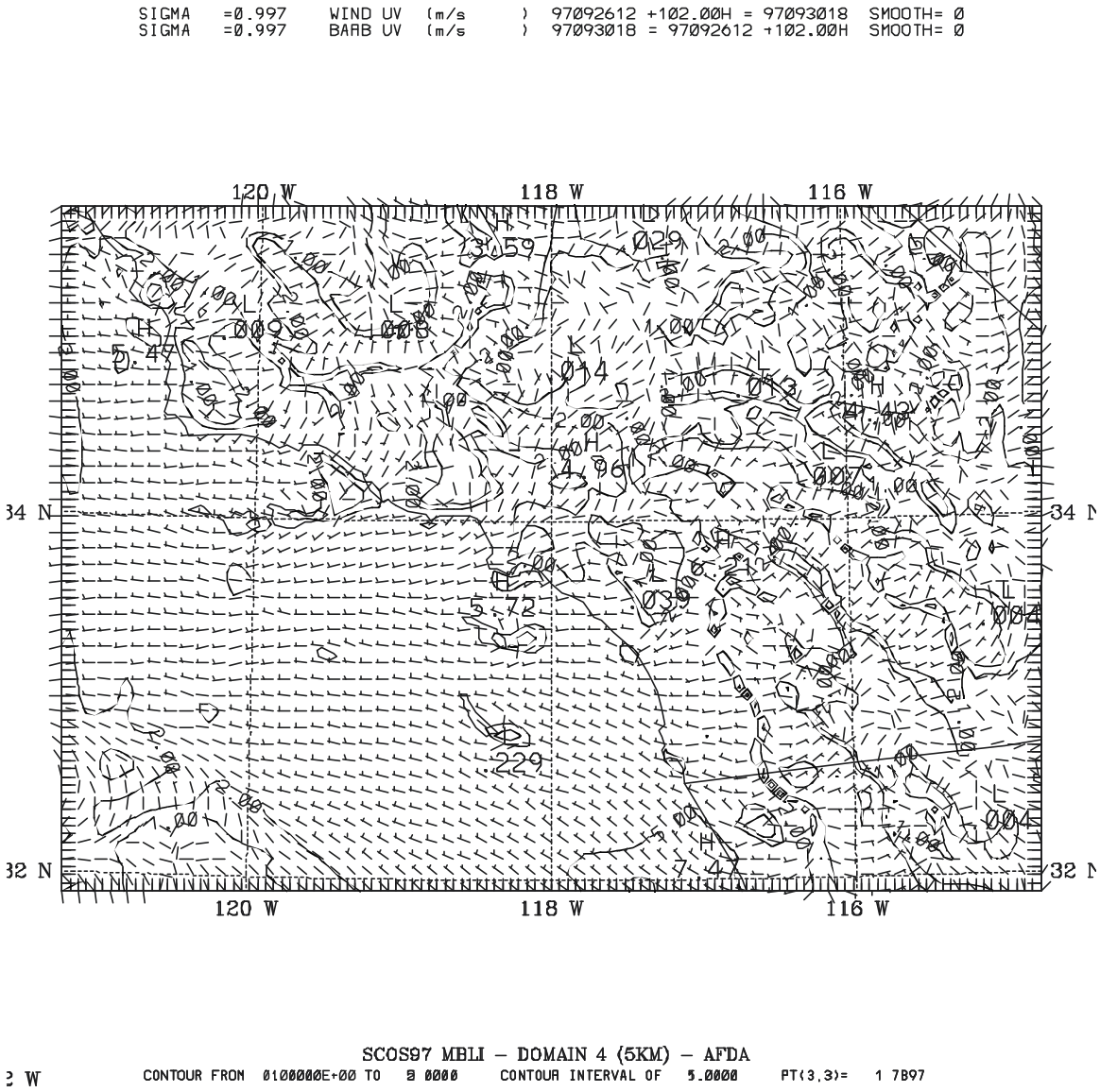

Figure 30. MM5 simulated surface-layer winds (m s^{-1}) at 35 m AGL for 1800 UTC, 30 September 1997, after 102 h of model integration. Isotachs are shown at 1 m s^{-1}, 2 m s^{-1}, 5 m s^{-1}, and thereafter at intervals of 5 m s^{-1}.

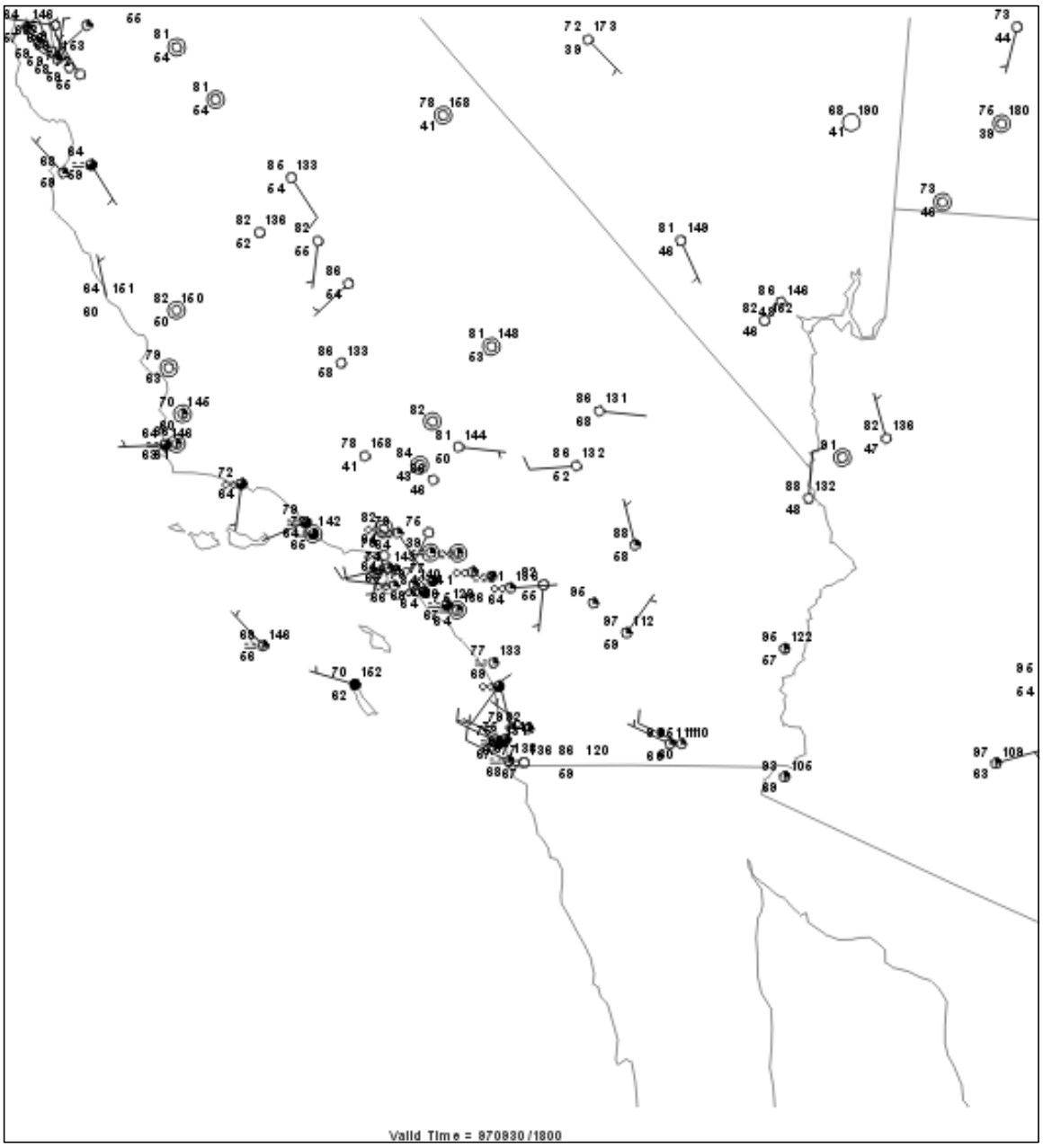

Figure 31. Plot of surface observations over southern and central CA at 1800 UTC, 30 September 1997.

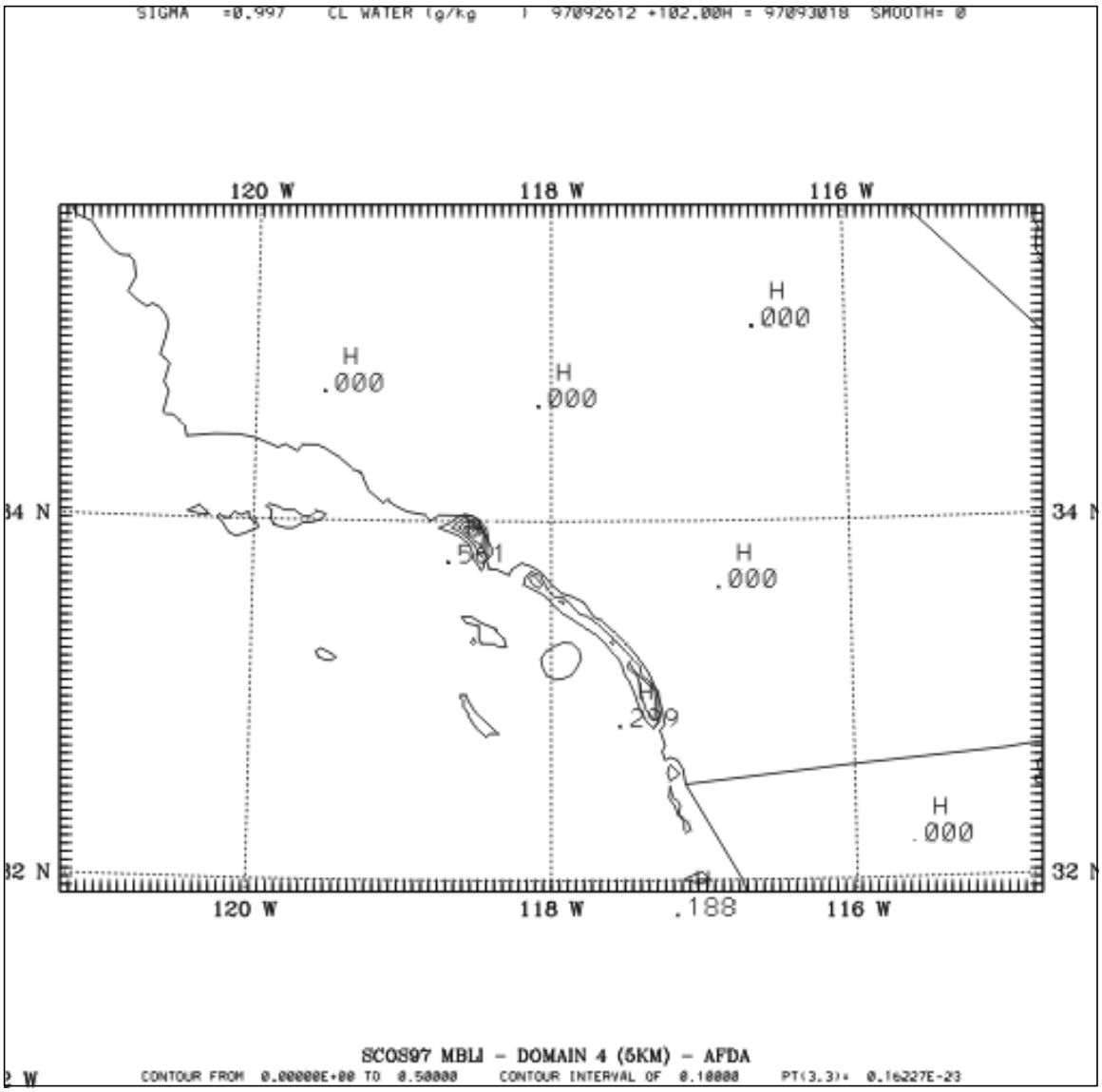

Figure 32. MM5 simulated cloud liquid water (g kg^{-1}) in the surface layer at about 35 m AGL (s = 0.997) for 1800 UTC, 30 September 1997, after 102 h of model integration. Contour interval is 0.1 g kg^{-1}.

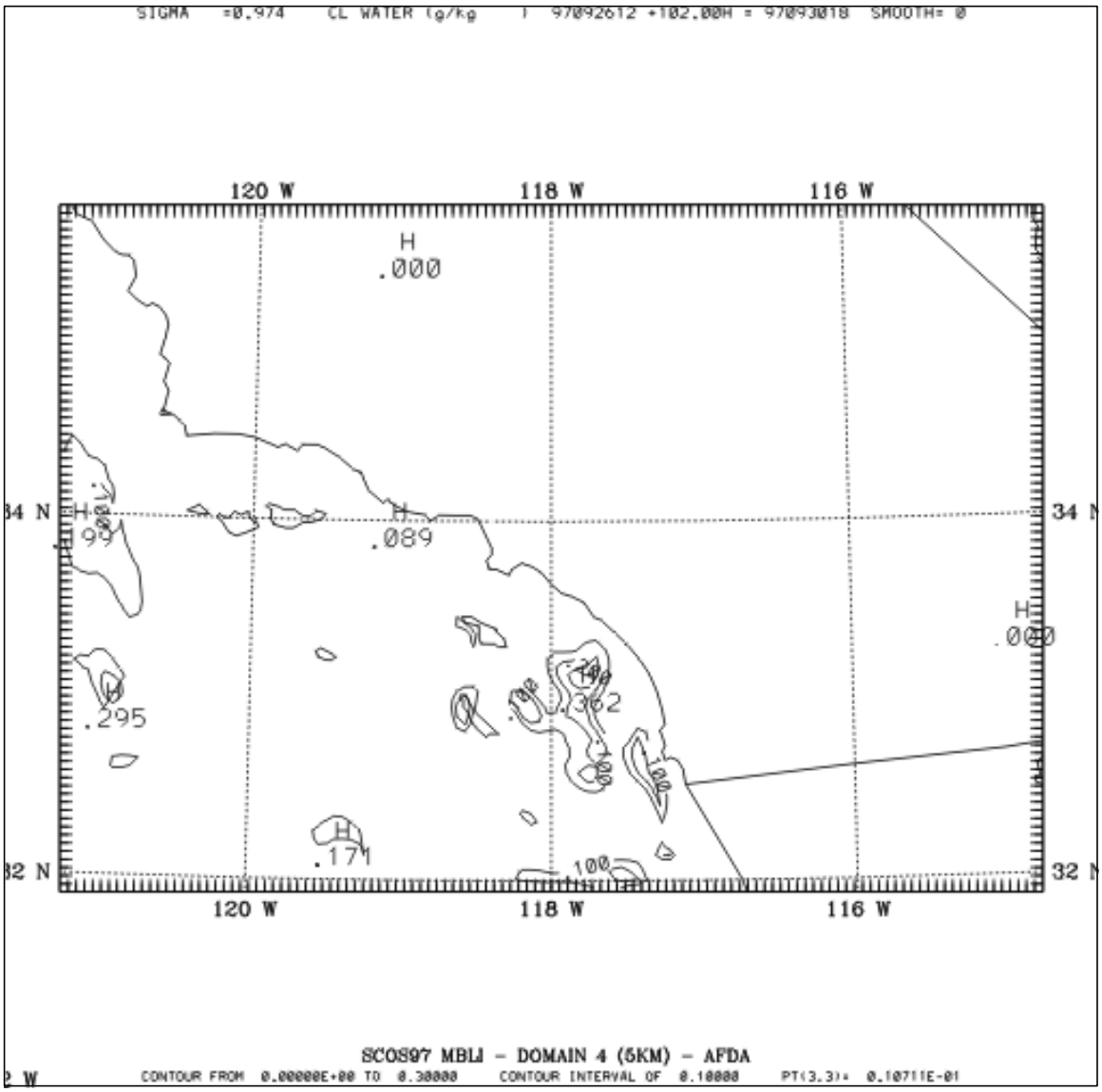

Figure 33. MM5 simulated cloud liquid water (g kg^{-1}) at about 300 m AGL (s = 0.974) for 1800 UTC, 30 September 1997, after 102 h of model integration. Contour interval is 0.1 g kg^{-1}.

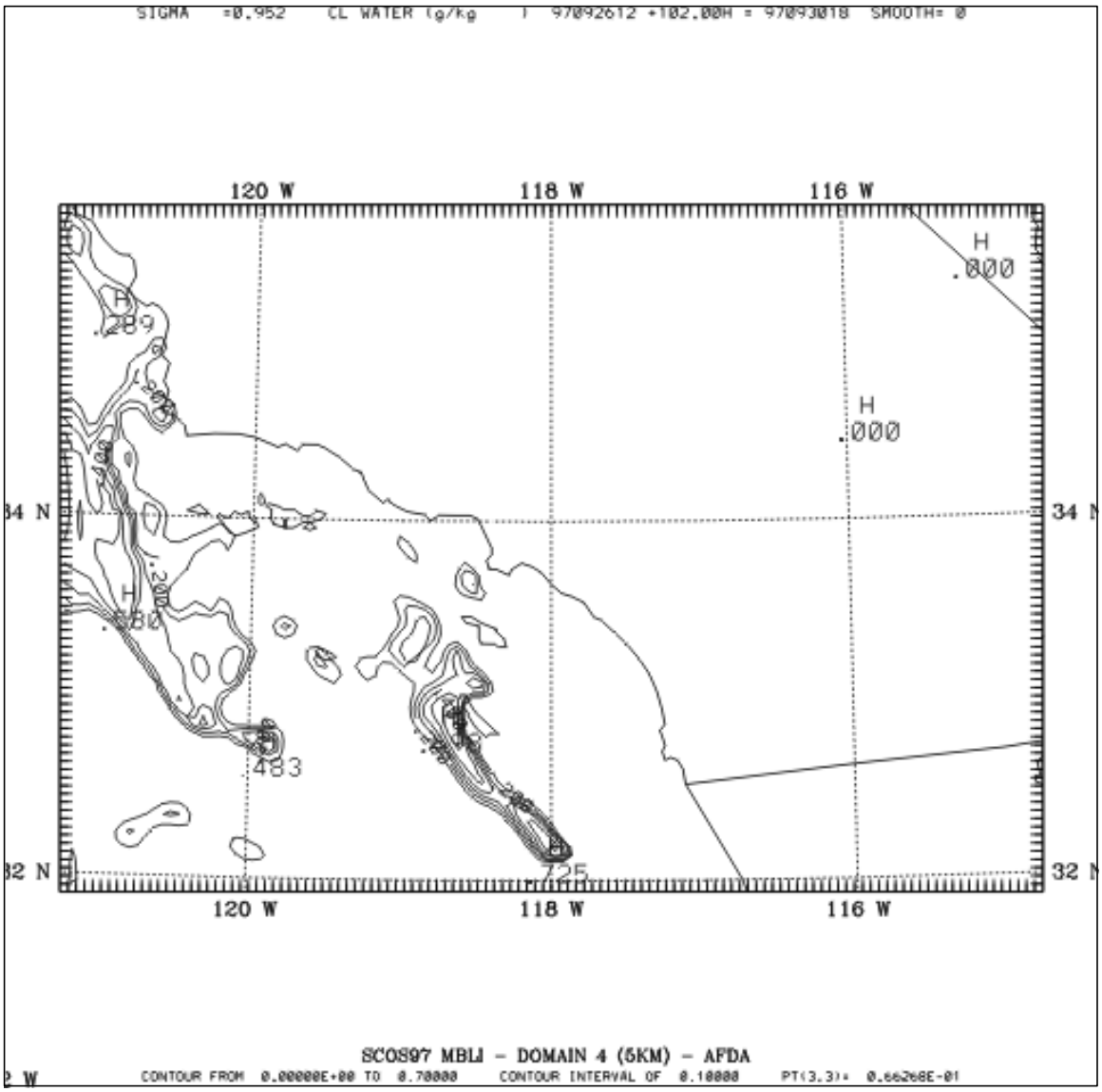

Figure 34. MM5 simulated cloud liquid water (g kg^{-1}) at about 550 m AGL (s = 0.952) for 1800 UTC, 30 September 1997, after 102 h of model integration. Contour interval is 0.1 g kg^{-1}.

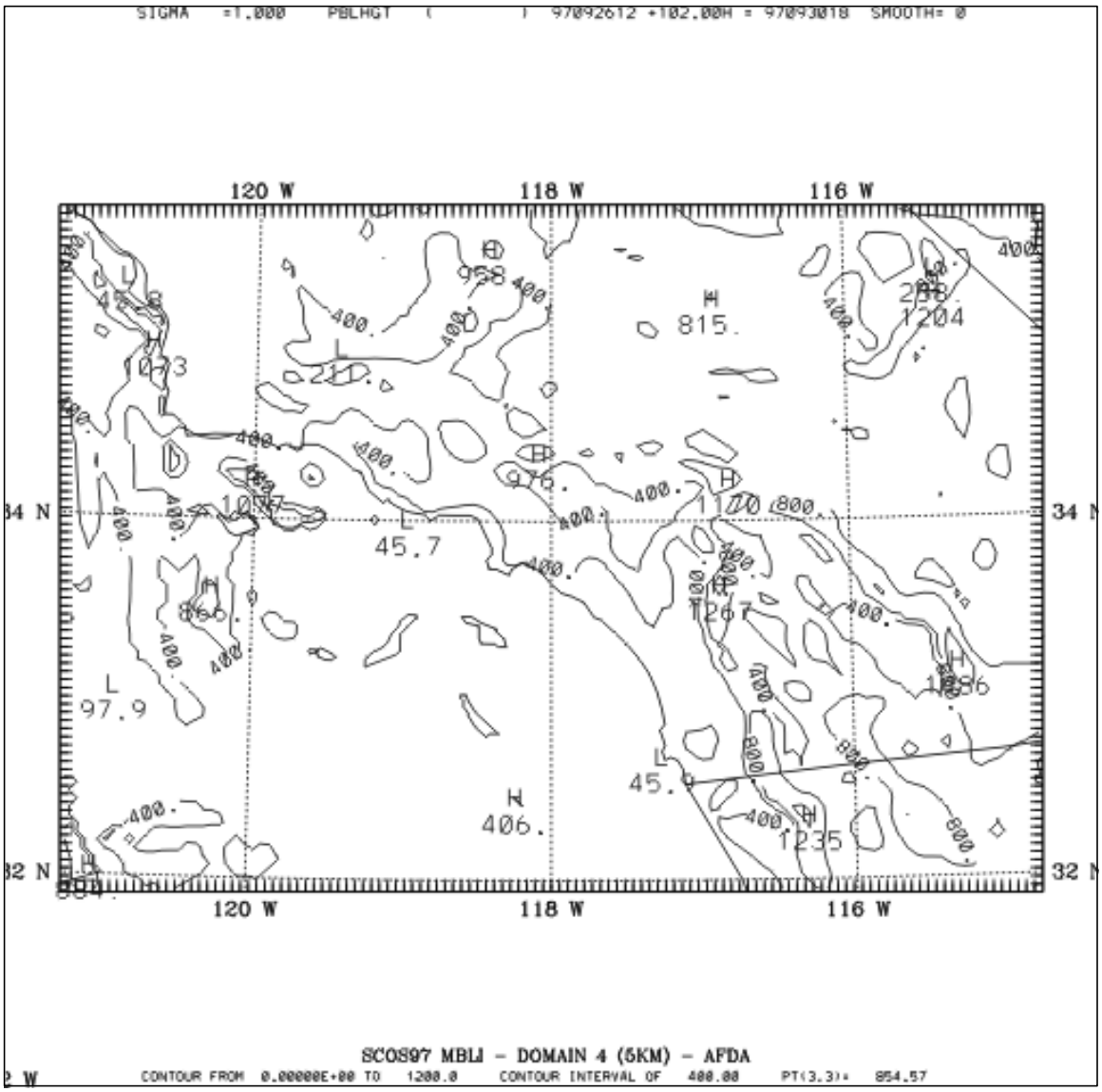

Figure 35. MM5 simulated mixed-layer depth (m) for 1800 UTC, 30 September 1997, after 102 h of model integration. Contour interval is 400 m.